

Doctoral Dissertation (Shinshu university)

Study on optimizing water harvesting through bioinspired
nanocomposites

バイオインスパイアされたナノ複合材料による水採取の
最適化に関する研究

March 2024

ZHANG YI

Abstract

Water is the lifeblood of our planet, and the adage "No water today, no tears tomorrow" underscores the profound importance of this invaluable resource. The rapid expansion of modern society and human civilization has further exacerbated the global water resource crisis, underscoring the pressing need for solutions. In this research, the focus has shifted not only to securing a direct source of clean water that is fog but also to the efficient utilization of existing water resources.

The turning point in our pursuit of innovative solutions came in the previous century when scientists stumbled upon a serendipitous discovery – the remarkable water collection abilities of beetles thriving in the arid Namib Desert. This revelation ignited a surge of research in the field of fog water harvesting, with the seminal article "Water capture by a desert beetle" published in *Nature* in 2001 acting as a catalyst. These unassuming desert dwellers unwittingly set off a wave of scholarly interest in biomimetic water collection. Their intricate behaviors and natural structures became a wellspring of inspiration, propelling extensive research and innovation in the realm of clean water production.

Simultaneously, atmospheric water harvesting (AWH) has emerged as a promising solution for mitigating the global clean water shortage by extracting fresh water from abundant airborne moisture. Capitalizing on the ubiquity of atmospheric moisture, AWH transcends geographical constraints, facilitating decentralized applications. AWH thus takes its place as a vital parallel or supplementary freshwater production method alongside conventional liquid water resource-based technologies.

Within the vast reservoir of atmospheric moisture, seawater, a fundamental component of Earth's water resources, has also garnered significant attention. Insights derived from studying the water collection strategies and mechanisms employed by plants and animals have informed the development of materials engineered for efficient water

harvesting. This, in turn, has steered our research toward materials designed to harness water resources in diverse and extreme conditions.

In this comprehensive study, we embarked on a multifaceted exploration that transitioned from developing biomimetic materials tailored exclusively for fog water collection to the creation of versatile materials capable of obtaining clean water in various scenarios. This evolution saw the shift from 2D membrane structures, as discussed in Chapter 2 and 3, to the intricate 3D hydrogels explored in Chapter 4.

Chapter 1 served as an introduction, outlining the research's background and significance, typical bionic prototypes, theoretical models, common material forms, and applications.

Chapter 2 delved into our observations of water collection abilities in various cultivated fungi. The results inspired the development of a streamlined, sandwich-like water collection material. Composed of a hydrophobic, hierarchical-structured polyurethane (PU) nanofiber membrane and hydrophilic filter paper, adhered by polyacrylamide (PAM), this material skillfully emulated the water-gathering prowess of fungal mycelium. It excelled at collecting water from fog, achieving an impressive water collection efficiency of $1018.6 \text{ mg cm}^{-2} \text{ h}^{-1}$ at $22 \pm 2^\circ\text{C}$ and $65 \pm 5\%$ relative humidity, offering a novel and efficient avenue for biomimetic water collection materials.

Chapter 3 marked an expansion of our biomimetic vision, integrating solar-driven photothermal seawater desalination. We designed a novel multi-biomimetic hierarchical membrane, ingeniously combining polyurethane nanofibers with hydrophilic carbon nanospheres and carbon nanotubes. This mesh-like membrane excelled in fog harvesting while harnessing solar energy for photothermal evaporation, culminating in an impressive water collection efficiency of $1666.2 \text{ mg cm}^{-2} \text{ h}^{-1}$ and a seawater evaporation rate of $1.05 \text{ kg m}^{-2} \text{ h}^{-1}$ under 1 sun. The chapter also introduced the construction of multi macro-micro-nanostructures, providing invaluable insights into biomimetic water harvesting materials applicable across various scenarios.

Chapter 4 ventured into the realm of 3D hydrogel materials in our pursuit of

enhanced water collection efficiency. We successfully crafted a versatile hydrogel matrix, incorporating polyvinyl alcohol (PVA), sodium alginate (SA), cross-linked by borax, and enriched with zeolitic imidazolate framework material 67 (ZIF-67) and graphene. This remarkable hydrogel demonstrated proficiency in water collection, achieving an average water harvesting ratio of 22.44 g g^{-1} under foggy conditions after 5 hours. Furthermore, it displayed an efficient water release capability, with a rate of $1.67 \text{ kg m}^{-2} \text{ h}^{-1}$ under 1 sun. Its seawater evaporation rate exceeded $1.89 \text{ kg m}^{-2} \text{ h}^{-1}$ under the same conditions, making it a promising resource for clean water production and a wide array of potential applications.

Chapter 5 offered general conclusions and outlook.

In summary, this doctoral thesis takes you on a journey into the world of multi-bioinspired materials for water collection, desalination, and harvesting. It offers fresh perspectives and innovative solutions to address the pressing global need for clean and sustainable water resources. Our work not only paves the way for a brighter future in water resource management but also ignites inspiration to produce clean water in diverse settings. The transition from developing materials for straightforward fog water collection in 2D structures to versatile materials adaptable to numerous scenarios in the form of 3D hydrogels marks our significant step forward in the quest for efficient clean water production.

Contents

Chapter 1: General introduction	2
1.1 Current situation of water scarcity and atmospheric water harvesting (AWH).....	2
1.2 Notable Examples of Bionics Applied in Water Harvesting.....	6
1.2.1 Mastering Water Collection: Desert beetles ‘ Ingenious Strategies	6
1.2.2 Biomimetic “Cactus Spine” for Enhanced Fog Collection	9
1.2.3 Spider Silk's Water Transportation	11
1.3 Theoretical basis	14
1.3.1 Young's Equation (Contact Angle Equilibrium)	15
1.3.2 Wenzel Model.....	16
1.3.3 Cassie-Baxter Model	16
1.3.4 Surface Energy Gradient Model.....	17
1.3.5 Laplace Pressure Equation.....	18
1.4 Manufacturing techniques for different AWH systems.....	19
1.4.1 Elements and processes of AWH.....	19
1.4.2 Common Forms of AWH Materials.....	26
1.4.3 Applications of AWHS	32
1.4.4 Solar-Driven Interfacial Desalination.....	34
1.5 Purpose and outline of this research.....	35
1.5.1 Research purpose.....	35
1.5.2 Research outline	36
Chapter 2	46
Bioinspired composite materials used for efficient fog harvesting with structures that consist of fungi-mycelia networks	46
Chapter 2: Bioinspired composite materials used for efficient fog harvesting with structures that consist of fungi-mycelia networks	47
2.1 Introduction.....	47
2.2 Experimental section.....	50
2.2.1 Materials	50
2.2.2 Fungi Cultivation.....	50
2.2.3 Fabrication of Hydrophobic Mesh-Like Membranes	51
2.2.4 Fabrication of Composite Amphipathic Materials.....	51
2.2.5 Characterization.....	52
2.2.6 Water-Collection Performance Measurements	52
2.3 Results and discussion	53
2.3.1 Morphological Features of Fungi	53
2.3.2 Analysis of the Water-Harvesting Structure of Fungi.....	55
2.3.3 Mimicking the Water-Harvesting System of Fungi.....	57
2.3.4 Morphology and Wettability of Hydrophobic Mesh Membranes.....	59
2.3.5 Surface Features and Wettability of Composite Amphipathic Materials.....	63
2.3.6 Water-Harvesting Properties of the Composite Materials	66

2.3.7 Water-Harvesting Behavior	70
2.4 Conclusion	72
Reference.....	73
Chapter 3.....	80
Multi-bioinspired hierarchical Janus membrane for fog harvesting and solar-driven seawater desalination	80
Chapter 3: Multi-bioinspired hierarchical Janus membrane for fog harvesting and solar-driven seawater desalination.....	81
3.1 Introduction	81
3.2 Experimental section.....	84
3.2.1 Materials	84
3.2.2 Fabrication of hydrophobic hierarchical mesh PU nanofiber membrane	85
3.2.3 Fabrication of carbon nanospheres (CNSs).....	86
3.2.4 Fabrication of different types of PU composite nanofiber membranes...	86
3.2.5 Culture and observation of fungi	87
3.2.6 Characterization.....	88
3.2.7 Water harvesting performance measurements	89
3.2.8 Preparation of the Janus membrane solar evaporation device and performance measurements	89
3.3 Results and discussion	90
3.3.1 Design and preparation of membranes	90
3.3.2 Structure characterizations and morphology of the membranes	92
3.3.3 Chemical composition and surface wettability of membranes.....	95
3.3.4 Fog harvesting properties	98
The wash fastness of HL-CNTs/CNSs/PUm was carried out with a commercial washing machine according to JIS L 1930. Each washing cycle was continued for 15min at room temperature. Samples can be obtained after 15 washing cycles. After washing, HL-CNTs/CNSs/PUm was dried at room temperature and the water harvesting property was evaluated.....	102
3.3.5 Fog harvesting mechanism of HL-CNTs/CNSs/Pum.....	104
3.3.6 Solar-heat conversion and evaporation performance	110
3.3.7 Practical applications of the HL-CNTs/CNSs/PUm device	115
3.4 Conclusion	119
Reference	120
Chapter 4.....	128
Multi-bioinspired hierarchical integrated hydrogel for passive fog harvesting and solar-driven seawater desalination.....	128
Chapter 4: Multi-bioinspired hierarchical integrated hydrogel for passive fog harvesting and solar-driven seawater desalination	129
4.1 Introduction	129
4.2 Experimental section.....	132
4.2.1 Materials	132

4.2.2	Fabrication of ZIF-67 nanocrystal powder	132
4.2.3	Treatment of graphene nanoplatelets	133
4.2.4	Preparation of different types of PVA/SA based hydrogels.....	133
4.2.5	Vacuum freeze-drying treatment for as-prepared hydrogels	134
4.2.6	Instruments and characterization	134
4.2.7	Water harvesting and release assessments	135
4.2.8	Preparation of the solar-driven seawater evaporation device system and performance measurements	137
4.3	Results and discussion	138
4.3.1	Design and synthesis of biomimetic hydrogel.....	138
4.3.2	Appearance, performance characteristics and microscopic hierarchical structure of functionalized hydrogels	141
4.3.3	Chemical composition and surface wettability of hydrogels in different hydration states	147
4.3.4	Photothermal conversion properties of hydrogels in different hydration states	150
4.3.5	Water harvesting and release performance	155
4.3.6	Solar-driven seawater evaporation performance	160
4.3.7	Practical application of GZPS evaporation device system.....	167
4.4.	Conclusion.....	171
	References.....	172
	Chapter 5.....	185
	Conclusion and outlook	185
	Chapter 5: Conclusion and outlook	186
	5.1 Conclusion	186
	5.2 Outlook.....	189
	Published papers.....	191
	Acknowledgments.....	193

Chapter 1

General introduction

Chapter 1: General introduction

1.1 Current situation of water scarcity and atmospheric water harvesting (AWH)

Water is the essence of life, a fundamental resource necessary for all living creatures on Earth. Yet, despite its undeniable significance, the world is grappling with an ever-worsening water crisis. Over three billion people across the globe lack access to adequate clean water, resulting in severe diseases and even deaths in less-developed regions. [1-3] The problem is exacerbated by the excessive use of water in agriculture and industries. [4-6] **Fig. 1-1** illustrates water stress levels by country and river basin in 1995 and 2055 in the absence of climate change.[7] In response to the challenges, researchers have embarked on a quest to revolutionize freshwater production, making it a critical focus within materials science and engineering. [8-11]

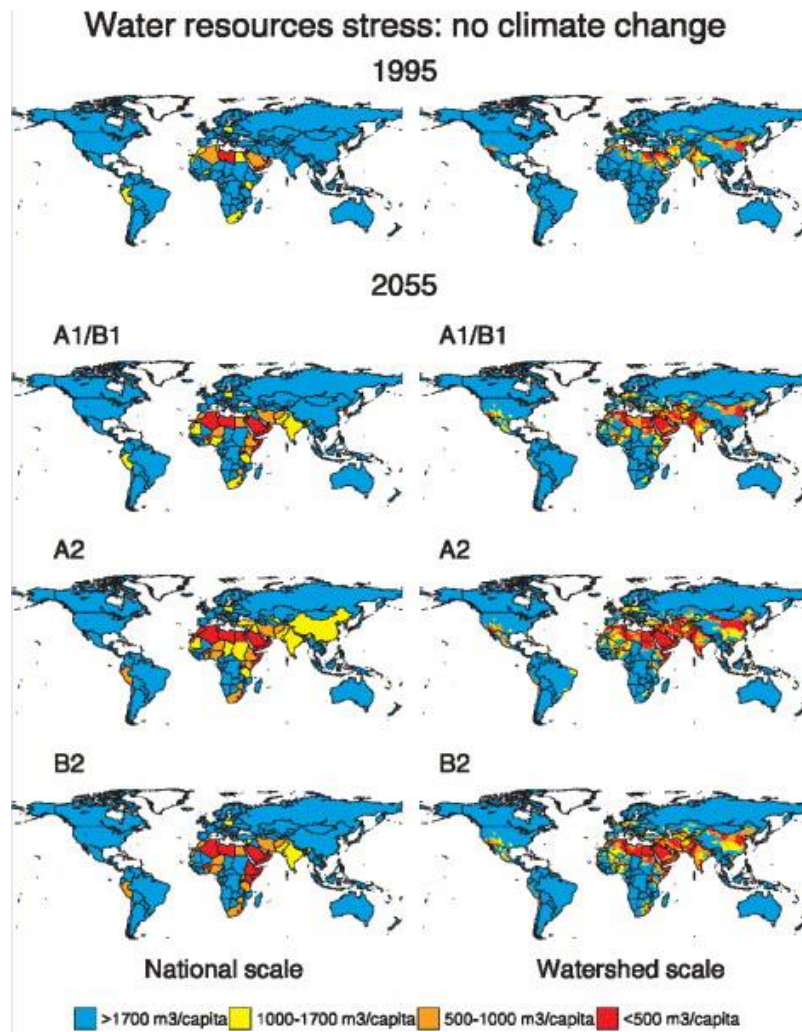


Fig. 1-1. Water resource stress levels across countries and watersheds: a comparison in the absence of climate change - 1995 vs. 2055. Reproduced with permission from ref [7] Copyright © 2004, Elsevier.

While traditional water purification techniques, like reverse osmosis and multi-stage flash evaporation, can generate freshwater from diverse liquid sources such as seawater or wastewater, their effectiveness is constrained by regional limitations arising from the uneven distribution of liquid water resources. [12-15] Additionally, these methods necessitate large, centralized infrastructures and frequent maintenance, rendering them impractical for certain developing or remote areas. This calls for alternative technologies for freshwater generation.

The majority of additional freshwater sources are found in ice caps, glaciers, and deep groundwater, posing challenges in terms of accessibility. **Fig. 1-2** provides an overview of global reservoirs and the associated limitations on access and utilization. [10] In this context, Atmospheric Water Harvesting (AWH) arises as a promising solution in addressing the worldwide scarcity of clean water. [16-17] AWH leverages the abundant moisture present in the atmosphere to produce fresh water, freeing it from geographical constraints and enabling decentralized applications.

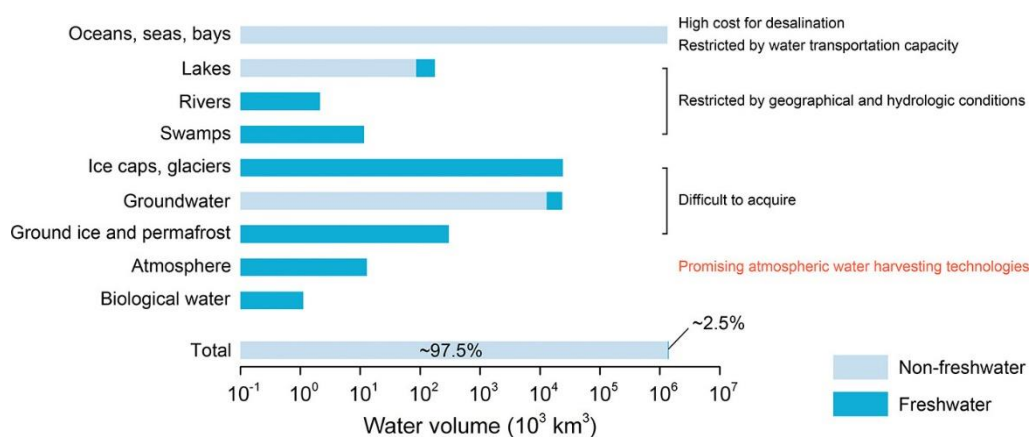


Fig. 1-2. Acquisition and utilization constraints of worldwide water reservoirs. Reproduced with permission from ref [10] Copyright © 2022 The Authors (Xiaoyi Liu, Danial Beysens, Tarik Bourouina). Published by American Chemical Society.

In certain extreme environments, particularly arid desert regions with minimal rainfall and sparse vegetation, life continues to thrive. Even in the face of limited precipitation in these desert areas, exceptional and distinctive flora and fauna are prevalent, especially along coastal desert regions. [18-21] The Namib Desert, in particular, has gained worldwide recognition for its mesmerizing fog formations, which have piqued substantial scientific interest. [22-24] This phenomenon also provides a tangible basis for further research in the field of fog collection, with potential applications in desert

environments. And the research on water harvesting has been hot for more than 20 years. In recent years, related research and development have continued. Some representative reports are shown in Fig. 1-3. [20, 25-29]

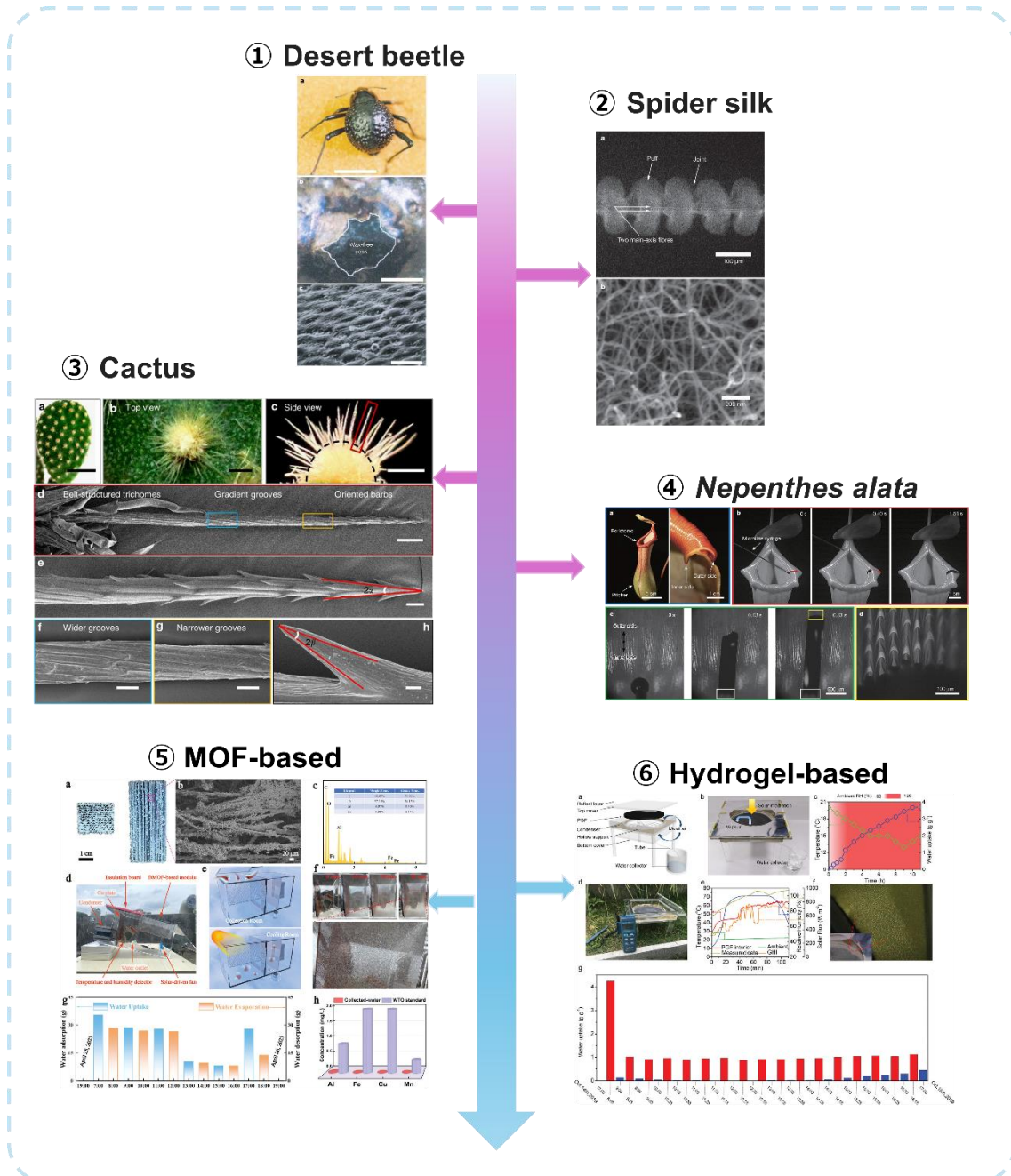


Fig. 1-3. Some representative reports on water harvesting research. Figure created by the author with the insets reproduced from [20, 25-29]. Reproduced with permission from

ref [20] Copyright ©2001, Springer Nature. Reproduced with permission from ref [25] Copyright © 2010, Springer Nature. Reproduced with permission from ref [26] Copyright © 2012, Springer Nature Reproduced with permission from ref [27] Copyright © © 2016, Springer Nature. Reproduced with permission from ref [28] Copyright © 2023, Wiley-VCH. Reproduced with permission from ref [29] Copyright © 2021, Elsevier.

1.2 Notable Examples of Bionics Applied in Water Harvesting

The natural world provides a myriad of valuable lessons in water collection. Through millions of years, plants and animals have developed ingenious strategies to thrive in the most arid environments. For example, desert beetles in the Namib Desert have developed a patterned surface with alternating hydrophobic and hydrophilic textures that allow them to condense and collect fog droplets. Likewise, cacti utilize evenly distributed clusters of spines and trichomes to guide water droplets to their roots. In contrast, the spider employs spindle-knots and joints to capture and merge tiny fogs into large droplets for sustenance. Understanding these natural mechanisms has inspired the development of high-efficiency biomimetic materials and devices for water harvesting. Gaining insights from these natural mechanisms has sparked the creation of highly efficient biomimetic materials and devices for water harvesting. Researchers are working to mimic and adapt nature's strategies, applying these principles into the development and production of water-harvesting materials. Below we will elaborate on some typical biological objects mentioned above.

1.2.1 Mastering Water Collection: Desert beetles ‘ Ingenious Strategies

Namib desert beetles, exemplified by the *Stenocara gracilipes* species, are true experts in the art of water collection from fog-laden winds. These remarkable insects have

developed distinct features on their elytra, featuring alternating hydrophobic wax-coated sections and nonhydrophobic, nonwaxy areas. These ingenious elytra design creates a superhydrophobic surface, reminiscent of the lotus leaf, which efficiently captures and transports fog droplets. On the beetle's back, the peaks of these bumpy structures harbor hydrophilic patches, which become shrouded in fog. Through the process of droplet coalescence, small droplets adhere to the hydrophilic portions. This mechanism enables droplets originating from the hydrophobic half to coalesce when blown or rebounded to the hydrophilic area. As these droplets grow, they gradually cover the hydrophilic region, enhancing the mass-to-surface ratio until surpassing attractive capillary forces. At this juncture, the droplets elegantly traverse the beetle's dorsal surface, directed by the hydrophobic peaks, as they make their way towards the beetle's mouth. [19-21] This extraordinary adaptation has not only captivated the attention of scientists but has also ignited a wellspring of inspiration for bionic research in the field of atmospheric water harvesting. [30, 31] Elisabeth Kostal et al. [30] mimicked the beetle's elytra through an innovative three-step fabrication process to enhance the fog-collection efficiency of glasses. Initially, a double-hierarchical surface structure was crafted on Pyrex wafers via femtosecond laser structuring, imparting superhydrophilicity to the surface (water contact angle $< 10^\circ$). Subsequently, a Teflon-like polymer $(CF_2)_n$ was plasma-deposited, transforming the laser-structured surface into a superhydrophobic state (water contact angle $> 150^\circ$). In the final step, selective removal of the Teflon-like coating through fs-laser ablation revealed superhydrophilic spots beneath the superhydrophobic surface, akin to the fog-collecting elytra of the Namib Desert beetle. **(Fig. 1-4, 1-5)** The final fog collection effect is also satisfactory.

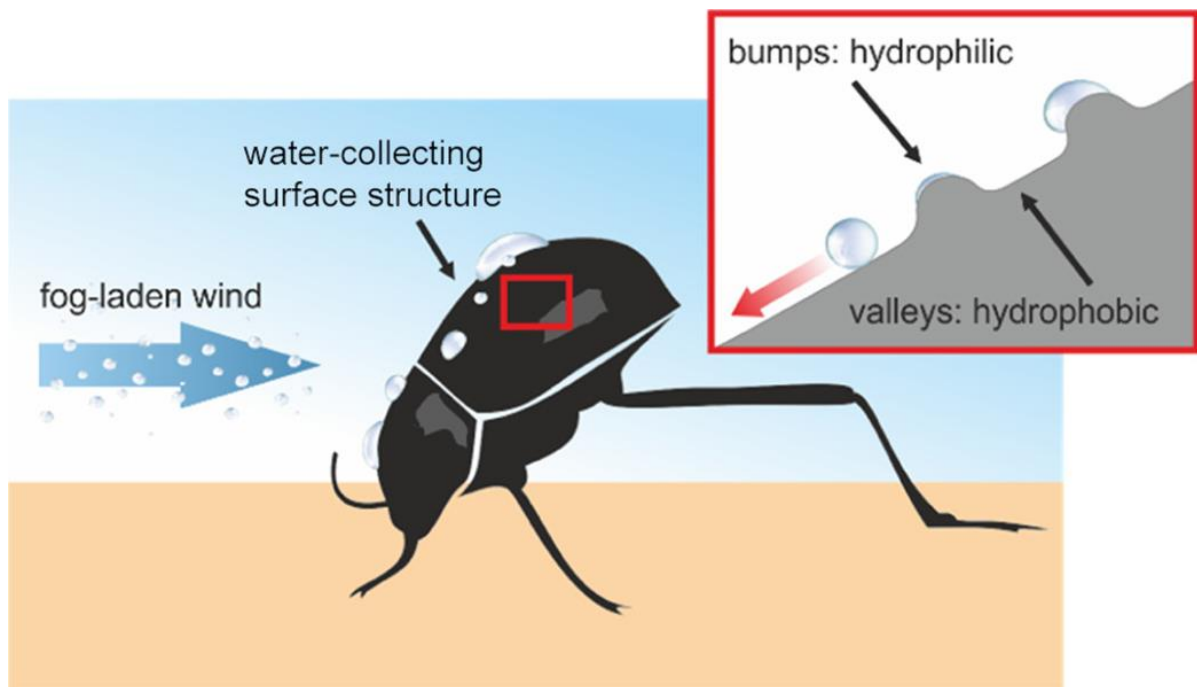


Fig. 1-4. Principle of Fog Collection by the Namib Desert Beetle: Droplets from fog-laden winds gather on the hydrophilic peaks, accumulating until reaching a critical size. Subsequently, they roll down the hydrophobic valleys, directed toward the beetle's mouth. Reproduced with permission from ref [30] Copyright © 2018, American Chemical Society.

a. Fabrication of double-hierarchical surface structures



b. Surface coating of laser-structured surfaces



c. Surface patterning by selective laser ablation



Fig. 1-5. Steps in the production of (a) superhydrophilic surfaces through fs-Laser structuring, (b) superhydrophobic surfaces via the deposition of a Teflon-like polymer layer, and (c) high-contrast micropatterns through selective laser ablation. Reproduced with permission from ref [30] Copyright © 2018, American Chemical Society.

1.2.2 Biomimetic “Cactus Spine” for Enhanced Fog Collection

Cacti, particularly the Cactaceae species, have mastered the art of fog collection and directional water droplet transportation in highly arid desert environments. This incredible adaptation is achieved through the synergy of conical structure and wettability gradient along the cactus spine, as depicted in **Fig. 1-6**. [26] The cactus surface is embellished with groupings of conical spines and trichomes, each with specific attributes contributing to the fog collection process. The tip of a spine contains oriented barbs,

where the angle (2β) plays a vital role in this mechanism. Meanwhile, the middle section features gradient grooves, while the base is adorned with belt-structured trichomes.

Inspired by the cactus, researchers have developed artificial conical structures employing various fabrication methods like magnetic particle-assisted molding, electrospinning, and 3D printing. [18, 32] These structures, with optimized apex angles and hydrophobic coatings, enhance fog capture and transportation efficiency. To further boost water collection, hierarchical conical spines with tiny barbs, oriented backward for optimal results, have been introduced.

The collective distribution of numerous conical spines plays a vital role, ensuring maximum contact with air. Clustered conical spines, as opposed to individual spines with discrete distribution, create a more turbulent flow field, enlarging the effective fog condensation area and improving water harvesting efficiency.

The scalability of conical water collectors inspired by cacti relies on the configuration of conical spines and the incorporation of water collection and storage materials. These closely arranged conical spines, whether positioned externally or internally on a spherical absorbing surface, efficiently condense and transport fog droplets toward the spherical surface, where collected water flows down for further usage. [33-35] This remarkable adaptation in cacti offers valuable insights for designing efficient fog-collection materials and devices.

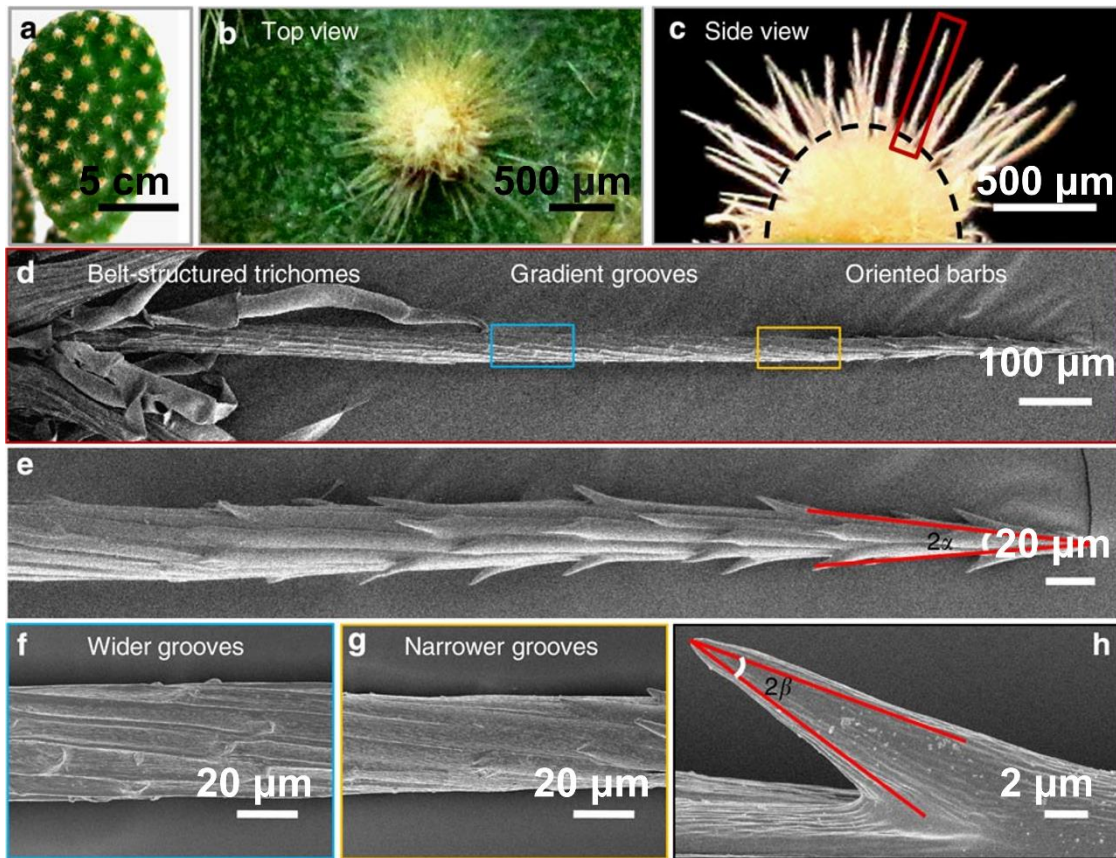


Fig. 1-6. Construction and surface features of the cactus. (a) An optical image reveals well-distributed clusters of spines and trichomes covering the cactus stem. (b) Magnified optical images show the top and (c) side views of a single cluster with spines growing from the trichomes. (d) SEM image displays a single spine divided into three regions: the tip (e) with an apex angle (2α) and oriented barbs, the middle (f, g) with gradient grooves, and the base with belt-structured trichomes. (h) Image of a single barb with an apex angle (2β) covering the tip of the spine (e). Reproduced with permission from ref [26] Copyright © 2012, Springer Nature.

1.2.3 Spider Silk's Water Transportation

Spider silk, a singularly dimensioned material with a diameter spanning from micrometers to millimeters, stands out as a valuable natural resource. Termed as "biological steel," spider silk exhibits attributes like high toughness, exceptional strength,

good elasticity, resistance to high temperatures, ultraviolet ray resistance, and effortless biodegradation. [36] These features have prompted its utilization in diverse applications, encompassing surgical sutures, parachute materials and body armor. [32, 37]

A fascinating discovery in the world of spider silk occurred in 2010 when researchers identified its exceptional water vapor condensation and collection capabilities, especially in spindle-shaped structures. [25] These spider silk structures exhibit unique features, consisting of periodic spindles and joints. Spindles are made up of randomly disordered nanofibers, while joints consist of neatly aligned nanofibers. In humid environments, spider silk undergoes structural changes, causing droplets to condense on the rebuilt silk. The surface energy gradient and Laplace pressure difference drive the directional movement of droplets, facilitating their collection on the spindle-knots. (**Fig. 1-7**) In the next section **1.3**, the relevant theory will be further explained.

This natural phenomenon has inspired the development of water-harvesting biomimetic materials. Different approaches, including dip-coating, electrodynamic techniques, microfluidics, and fluid-coating, have been employed to create materials that mimic the unique structure of spider silk.[38] These bio-inspired materials open up exciting possibilities for efficient water collection, influenced by the directional water-harvesting abilities of spider silk.

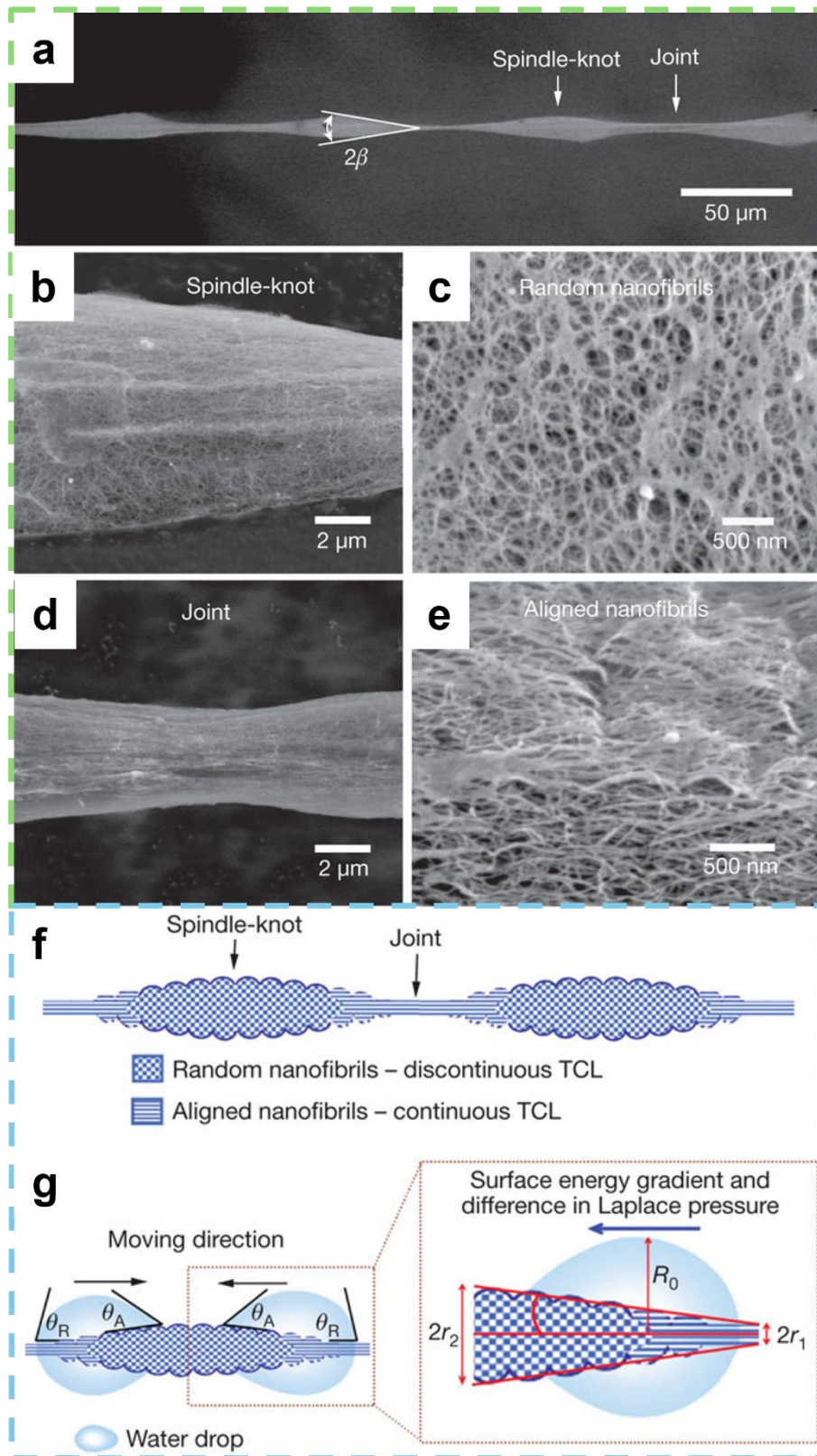


Fig. 1-7. Reconstructed wet spider silk structure: (a) Environmental SEM images depict periodic spindle-knots connected by slender joints. Low-magnification (b) and zoomed

(c) images illustrate the random interweaving of nanofibers within the spindle-knot. Low-magnification (d) and high-magnification (e) images capture the joint structure, comprised of nanofibrils aligned relatively parallel to the silk axis. (f, g) Mechanism of directional water collection on spider silk. Reproduced with permission from ref [25] Copyright © 2010, Springer Nature.

1.3 Theoretical basis

After examining various examples and related research on three types of organisms capable of collecting water in nature, it becomes evident that many water collection phenomena necessitate the establishment of robust theoretical foundations. This is essential to facilitate the development of functional materials for water harvesting and broaden their applications. The water collection process typically involves four key steps: "condensation," "coalescence," "transportation," and "absorption." [36] These steps are significantly influenced by the wetting behaviors and movements of water droplets.

To gain a deeper understanding of the intricate water harvesting processes, theoretical frameworks have been introduced to elucidate the phenomenon of fog harvesting. These theoretical models include Young's equation, the Wenzel model, and the Cassie model. [39] Each of these models helps in explaining how different surfaces interact with water droplets and the resulting wetting behaviors.

Additionally, the surface energy gradient model and the Laplace pressure equation are employed to provide insights into the transportation of water droplets. These models are essential in clarifying the forces and factors responsible for directing water droplets in the context of water collection.

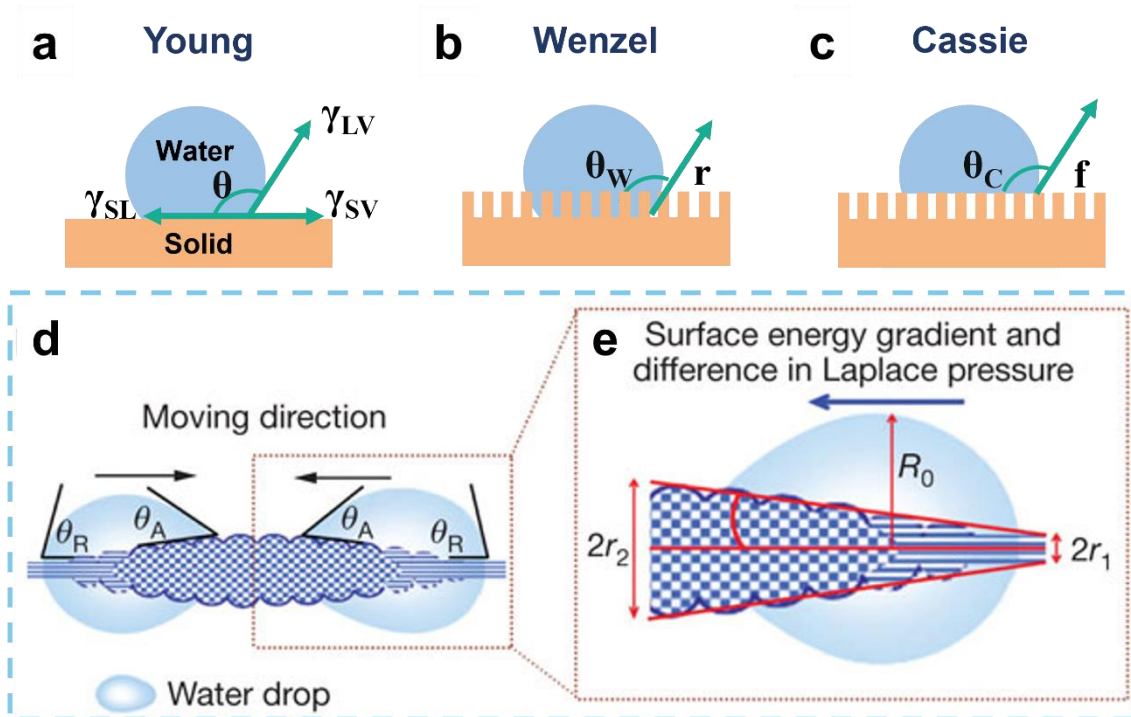


Fig. 1-8. Wetting characteristics of a water droplet on different solid surfaces. (a) Young's model, (b) Wenzel's model, and (c) Cassie's model. (d, e) Surface energy and roughness gradient model. Reproduced with permission from ref [25] Copyright © 2010, Springer Nature.

1.3.1 Young's Equation (Contact Angle Equilibrium)

T. Young first introduced the concept of contact angle equilibrium in 1805. [40] Young's equation relates the contact angle (θ_Y) of a liquid droplet on an ideal flat surface to the surface free energy of the solid material and the interfacial tensions of the system. It describes the thermodynamic equilibrium of surface free energy at the solid-liquid-vapor interface. (Fig. 1-8a) The apparent WCA in air is elucidated by Young's equation (1),

$$\cos\theta_Y = \frac{\gamma_{sv} - \gamma_{sl}}{\gamma_{lv}} \quad (1)$$

γ represents for the solid-vapor interface (sv), solid-liquid interface (sl), and liquid-vapor interface (lv). In the case of a hydrophilic surface, the energy required to create a liquid-vapor interface (lv) must be lower than that of a solid-vapor interface (sv). Consequently, this leads to contact angles measuring less than 90° on such surfaces. Conversely, for a hydrophobic surface, the opposite behavior is observed.

1.3.2 Wenzel Model

Wenzel proposed a model in 1936 to account for the influence of surface roughness on contact angle. [41] The Wenzel model states that the droplet completely fills the valleys of a relatively rough surface, leading to an apparent contact angle (θ_w) that depends on both the original contact angle (θ_Y) and the surface roughness factor (r). (**Fig. 1-8b**) The equation is as follows (2):

$$\cos\theta_w = r\cos\theta_Y \quad (2)$$

Surface roughness can influence wettability or anti-wetting characteristics, depending on the specific nature of the flat surface under consideration. For a smooth material with contact angle exceeding 90° , the inclusion of surface roughness will further accentuate the angle. Conversely, when the contact angle (θ) is less than 90° , surface roughness will diminish the angle.

1.3.3 Cassie-Baxter Model

Cassie and Baxter introduced a model to elucidate the impact of chemical heterogeneities on contact angles. [42] The model considers that liquids only make contact with the solid surface through the top of surface asperities, creating a composite surface with trapped air pockets. (**Fig. 1-8c**) The apparent contact angle (θ_c) is determined by the fractional areas (f_i) of the surface with different contact angles (θ_i).

The Cassie-Baxter model is valuable for estimating contact angles on heterogeneous surfaces.

$$\cos\theta_c = f_i(\cos\theta_i + 1) - 1 \quad (3)$$

It can be seen from the above equation that when there is an air layer at the contact interface between the liquid and the solid, and the larger the contact area between the liquid and the gas filling the groove, the apparent contact angle θ_c between the droplet and the rough surface will be greatly increased.

1.3.4 Surface Energy Gradient Model

The concept of surface energy gradient is used to explain directional water drop movement on surfaces with varying wetting properties. This gradient is generated by differences in surface roughness and local surface energy. Water droplets are driven from less hydrophilic regions to more hydrophilic regions due to the surface energy gradient. This model helps to elucidate the role of surface roughness in wettability. [43-45] The specific equation can be explained as:

$$F = \int_{L_j}^{L_k} \gamma(\cos\theta_A - \cos\theta_R) dl \quad (4)$$

γ denotes water's surface tension, while θ_A and θ_R represent advancing and receding angles of droplets on spider silk respectively, with the condition that θ_A is less than θ_R as per equation (1). The variable dl serves as an integrating factor along the length spanning from the joint (L_j) to the spindle-knot (L_k).

This theory is instrumental in elucidating the phenomenon of water droplet transportation by spider silk, as introduced in section 1.2.3. The spindle-knot, owing to its more extensive axial-parallel roughness, exhibits a smaller water contact angle compared to the joint. (Fig. 1-8d) Consequently, the joint is relatively more hydrophobic and possesses a lower apparent surface energy than the spindle-knot. Following the departure of water drops from the joints to the spindle-knots, a new cycle of water

condensation and directional transport can commence on joints.

1.3.5 Laplace Pressure Equation

Laplace pressure difference, determined by variations in curvature, is another driving force for directional droplets movement. It explains the differences in pressure experienced by water drops on regions with varying curvatures. When the Laplace pressure is higher in one area, it propels water drops to move towards the lower pressure region. The Laplace pressure equation complements the surface energy gradient model like the followings:

$$\Delta P = \int_{r_1}^{r_2} \frac{2\gamma}{(r+R_0)^2} \sin\beta \, dz \quad (4)$$

where r and R_0 refer to the local radius and the drop radius, respectively. β and z are used to represent the half apex-angle of the spindle-knot and the integrating variable along the diameter of the spindle-knot, respectively. The Laplace pressure within a water drop differs between areas with low and high curvatures. Specifically, the spindle-knot with a local radius of r_2 experiences lower Laplace pressure compared to the joint with a local radius of r_1 . This pressure differential results from the fact that r_2 is smaller than r_1 , thus creating a non-equilibrium Laplace pressure difference within droplet. [46] This difference acts as a propelling force, compelling the drop to move from the joint to the spindle-knot. The combined influence of the surface energy gradient and Laplace pressure is the critical factor driving the water droplets' transportation. (**Fig. 1-8e**)

In summary, these theoretical models and concepts provide a framework for understanding how factors such as surface roughness, surface energy, and chemical heterogeneities influence the wetting behavior of solid surfaces, which is crucial for designing functional materials with tailored wettability properties.

1.4 Manufacturing techniques for different AWH systems

After mastering the relevant basic theoretical knowledge, it becomes crucial to grasp the components, procedures, primary methodologies, and material properties vital for advancing material development.

This section will deliver an overview of the elements and processes within the Atmospheric Water Harvesting (AWH) system. It will categorize common material configurations into 1D, 2D, and 3D structures, providing a short introduction to each, and present preliminary research findings to comprehensively explore the attributes of water collection materials. Additionally, we'll briefly delve into the research on light-driven seawater desalination, reinforcing the groundwork for this study.

1.4.1 Elements and processes of AWH

The water harvesting process encompasses a series of critical steps illustrated in **Fig. 1-9**. These steps involve capturing water or fog, coalescing small droplets, guiding the collected droplets in a specific direction, and ultimately collecting and storing the harvested water. It's essential to acknowledge that, alongside the choice of materials, external environmental conditions play a significant role in determining the overall harvesting efficiency.

To optimize the performance of Atmospheric Water Harvesting (AWH) technologies, it is paramount to gain a deep understanding of the fundamental AWH processes. AWH's essence lies in the extraction of free water molecules or minute water droplets from the atmosphere, transforming them into substantial, usable water resources. This entails harnessing materials engineering techniques to fine-tune interactions between water and materials. By doing so, a range of water evolution processes (depicted in **Fig. 1-10**) [3] can be facilitated. These processes encompass the rapid nucleation of droplets (for dew

harvesting), efficient droplet growth, and the effective departure of droplets (for fog or dew harvesting), as well as the proficient capturing of vapor and energy-efficient release of water (for sorbent-based AWH). For instance, the incorporation of a hydrophilicity-switchable polymer into sorbent-based AWH materials can greatly ease the release of liquid water with minimal energy input. [3, 47,48]

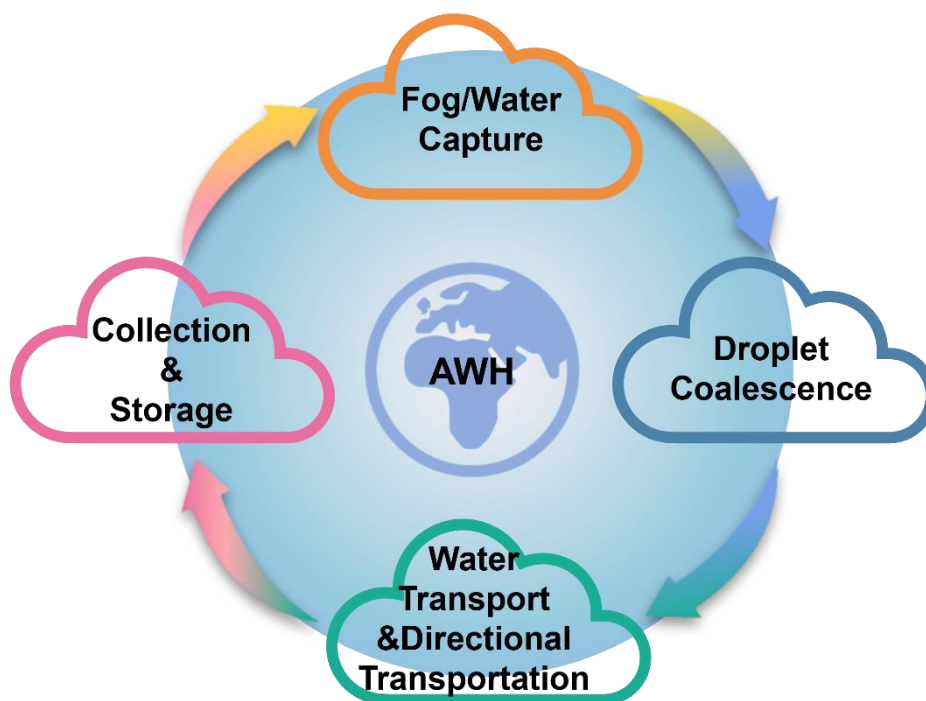


Fig. 1-9. Critical phases of the water harvesting process involve four key aspects. Inspired by ref [47].

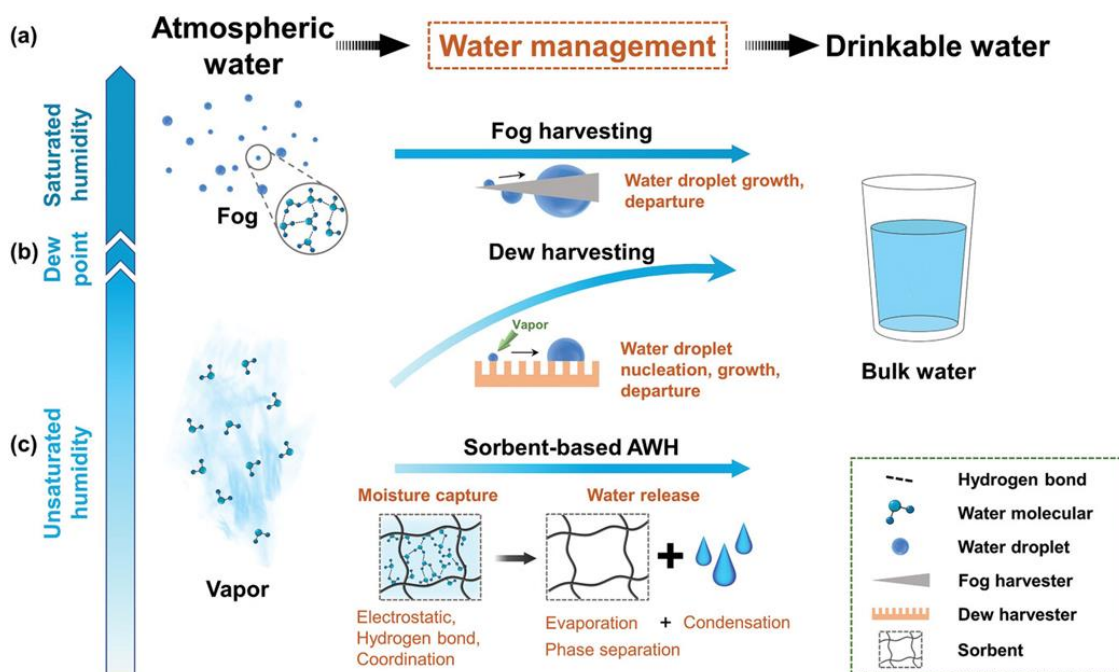


Fig. 1-10. AWH technologies. (a, b) AWH under saturated humidity, involving effective methods such as fog harvesting and dew harvesting. Key water management stages for dew and fog water include nucleation, growth, and departure of water droplets. (c) AWH under unsaturated humidity, employing sorbent-based methods to capture water molecules. Key water management steps for sorbent based AWH involve moisture capture and water release. Reproduced with permission from ref [3] Copyright © 2022, Wiley-VCH.

1.4.1.1 Fog/Water capture

Sorption plays a crucial role in condensing water molecules on solid surfaces. The interaction between the material's surface and water molecules is crucial. Water, as a polar triatomic molecule, exhibits distinct behavior when it encounters different surface polarities. The material's surface uses the van der Waals (vdW) force to attract water molecules. Surfaces with strong polarity, typically characterized by polar and hydrophilic terminal groups, favor the condensation of water molecules. In contrast, surfaces with

non-polar and hydrophobic characteristics hinder water molecule condensation. Notably, hybrid surfaces that combine hydrophilic and hydrophobic terminal groups could achieve comparable condensation abilities when these groups are carefully proportioned. The water condensation abilities on solid surfaces with distinct terminal groups vary, with rapid condensation occurring on surfaces terminated with polar and hydrophilic groups, while slower condensation happens on surfaces terminated with nonpolar and hydrophobic groups.

1.4.1.2 Droplet coalescence

Droplet coalescence involves the vapor-to-liquid phase transition occurring on the condensing surfaces. The initial stage of this process is known as nucleation, which is the formation of the tiniest droplet nuclei. Achieving a relatively high nucleation density is critical for condensing efficiently. Notably, hydrophilic surfaces exhibit higher nucleation densities compared to hydrophobic surfaces, making them the preferred choice for nucleation. [49]

For instance, **Fig. 1-11** provides visual representations of the initial nucleation process on two distinct surfaces. **Fig. 1-11a** portrays the nucleation on a superhydrophobic surface, while **Fig. 1-11b, c and d** depict the nucleation on compound amphiphilic surfaces composed of a superhydrophobic substrate and hydrophilic nano sites. Notably, the nucleation density on the amphiphilic surface could be meticulously controlled by adjusting the density of hydrophilic sites, resulting in a remarkable water collection rate increase of approximately up to 349% compared to the superhydrophobic surface. [50]

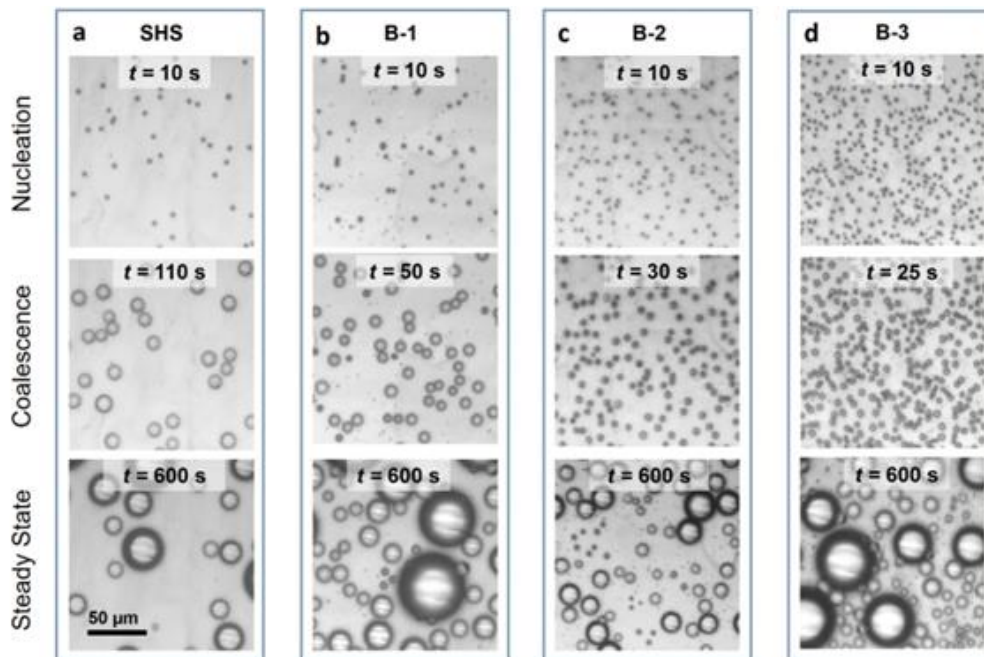


Fig. 1-11. Condensation and nucleation analysis. (a) Visual representation of the initial nucleation on a superhydrophobic surface. (b-d) Visualization of the initial nucleation on amphiphilic surfaces. Reproduced with permission from ref [50] Copyright © 2018, American Chemical Society.

1.4.1.3 Water Transport and Directional Transportation

In the realm of water harvesting, effective water transport is vital to timely collect and prevent the evaporation of collected water droplets from fog. Surfaces with chemical gradients induce liquid movement toward regions with higher surface energy, generating forces to direct water drops across the surface. [25] This gradient arises not only from material chemistry but also surface roughness. [25,26] Surface roughness gives rise to wettability gradients, resulting in a surface energy gradient. Furthermore, differences in curvature create a Laplace pressure differential, enabling directional transport. [25] Capillary action, governed by the interplay of surface tension, viscous drag, and gravity, also plays a role in continuous water motion. [51] Natural examples include the *Moloch*

horridus, which employs its semi-tubular skin texture for capillary water transport, and hygrosopic lizards with a skin channel network that uses capillary action to prevent extensive wetting. [52,53]

Efficient water collection via gravity is often a bottleneck issue in dropwise and filmwise condensation processes. [10] Rapid liquid transport and removal are essential to prevent evaporation and reduce thermal resistance, even with active cooling. To address this, researchers have explored engineered microstructures and metasurfaces to enhance water collection. Examples include modified mesh frameworks [54], hydrophobic/hydrophilic Janus fibrous membranes [55], and optimized fog harps that significantly improve water yield, even under light fog conditions. [56] Groove-filling imbibition phenomena, spindle patterns, and superhydrophobic–superhydrophilic hybrid meta surfaces with optimized triangle patterns have been adopted, further enhancing dew harvesting capabilities. [57-59] These concepts draw inspiration from natural organisms and plants to design structured surfaces that increase water harvesting capacity. [60-64] A comparison of water transport for some typical structures is shown in the **Table 1-1**. [47]

Table 1-1. Conclusion of mechanisms and transport speeds in different developed structures for water droplet Transport. Reproduced with permission from ref [47] Copyright © 2021, Elsevier.

Surfaces	Mechanism for directional transportation	Transportation speed
Janus porous surface	Capillary effect	++
Self-pumped surface	Capillary effect	+
Conical spine	Difference in Laplace pressure	+
Slippery asymmetric bumpy surface	Difference in Laplace pressure	+
Chemical gradient surface	Surface energy	+++

In summary, water transport plays a crucial role in facilitating water collection, with directional transportation methods offering innovative solutions to overcome gravity-related limitations.

1.4.1.4 Collection and Storage

Water collection and storage play pivotal roles in the survival of diverse organisms facing arid conditions. These natural systems have evolved remarkable mechanisms and structural adaptations to ensure the retention of this precious resource.

In addition to the principles observed in biological organisms, the properties of materials and the design of equipment also significantly impact water collection and storage. These factors influence the methods and efficiency of accumulation. In this section, we will provide a brief overview of biological water storage through two examples. In subsequent sections **1.4.2** and **1.4.3**, we will introduce the water storage methods of several adsorbent materials which have become popular in recent years and some water collection relevant application devices.

Lizards exhibit impressive water-holding capacity, attributed to their hierarchical skin structures and dense skin channels. The amount of water these structures can store is known as cortical water-holding capacity. This hierarchical skin arrangement allows them to store substantial amounts of water. [65,66] In arid regions, some plants have developed remarkable water storage and accumulation mechanisms. For instance, *Lychnis sibirica*, thriving in the arid steppe region of Mount Fuji, possesses tapered hair with internal microfibers which was studied by our lab before. In dry conditions, these hairs transform into vertically twisted crush plates. Microfibers within the hair play a key role in storing and releasing water. The morphological change of hair depends on humidity levels, and the hair can store and release water to survive in changing environmental conditions. [63, 67]

1.4.2 Common Forms of AWH Materials

In addition to the previously mentioned one-dimensional(1D) water-collecting fiber materials, which mimic spider silk (1.2.3), water harvesting materials can come in the form of either 2D structured film-like materials or 3D porous materials. While their water-harvesting mechanisms may differ, both of them are able to capture moisture from the atmosphere and release water for subsequent harvesting and storage.

1.4.2.1 2D AWH Materials

A commonly employed method for harvesting fog water entails the placement of a substrate, typically composed of materials such as polymer materials or metal meshes, oriented perpendicularly to the air flow. During foggy conditions, water droplets suspended in the air flow collide with the solid substrate, where they gradually accumulate through a series of collisions and coalescence. Over time, these droplets increase in size until they attain sufficient mass to descend under the pull of gravity, ultimately being collected in a tank. [3]

Recent advancements in water harvesting have led to the development of hybrid surfaces featuring a contrast between hydrophilic and hydrophobic properties, attracting significant attention for use in crafting water collection materials on diverse substrates, including textiles [68], cellulose films [69], composite meshes [70], copper sheets [71], stainless steel meshes [72], and more [73,74]. These hybrid surfaces have been the subject of extensive study, focusing on both the design of their surface structures and the regulation of their surface chemistry. [75,76]

The efficiency of water harvesting can be significantly affected by the distribution and configuration of hydrophilic and hydrophobic regions on smooth macro surfaces. [77]

For instance, researchers have investigated nanostructured surfaces with a range of pattern shapes, including pure superhydrophilic and superhydrophobic surfaces, circular patterns, and star-shaped patterns (as illustrated in **Fig. 1-12 (a)**). Among these, the star-shaped pattern has demonstrated the highest water harvesting capability, with star patterns sporting five points surpassing those with varying numbers of points. Moreover, the size of the pattern itself plays a pivotal role, with smaller patterns leading to more noticeable enhancements while maintaining the star-shaped structure and the overall hydrophilic region constant.

To further elevate water harvesting efficiency and facilitate precise droplet transportation, Ruan et al. in their research [78], devised a hierarchical cone structure with a tree-like and branched configuration on a superhydrophobic film (**Fig. 1-12 (b)**). This patterned film enhances the accuracy of directional droplet transport, resulting in a substantial improvement in harvesting efficiency.

Despite its considerable water yield, it is important to note that fog collection is inherently constrained by its reliance on foggy atmospheric conditions.

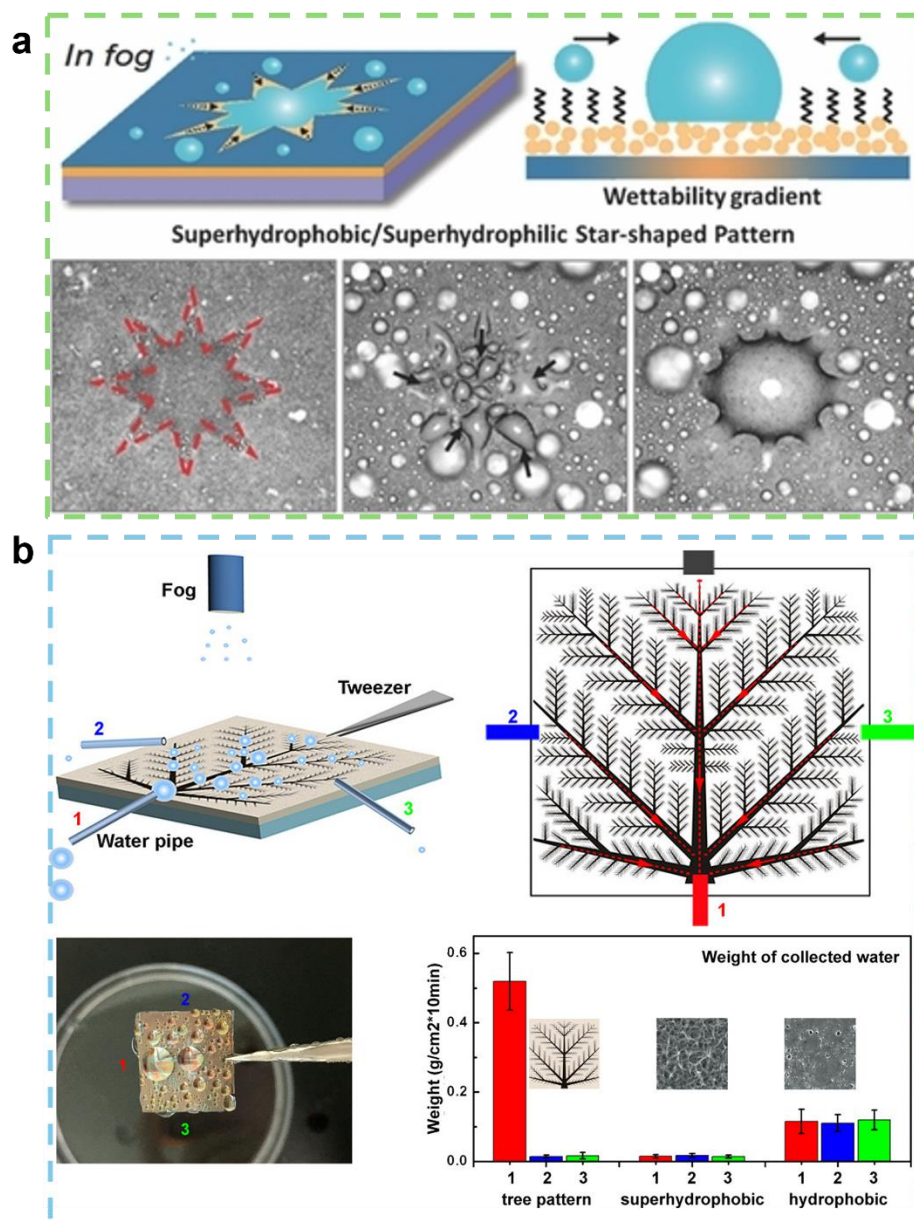


Fig. 1-12. (a) Developed a novel surface with star-shaped wettable patterns, combining wettability and shape gradients for enhanced water collection efficiency compared to circular patterns and uniformly superhydrophilic or superhydrophobic surfaces. Reproduced with permission from ref [77] Copyright © 2014, Wiley-VCH. (b) Schematic illustrating the fog harvesting process on the surface inspired by leaf veins, depicting the patterned film collecting water. It also includes the fog-collection efficiency comparison at locations 1, 2, and 3 on different surfaces. Reproduced with permission from ref [78] Copyright © 2017, American Chemical Society.

1.4.2.2 3D AWH Materials

The process of water harvesting using adsorbent materials operates in a cyclical fashion, involving the collection and absorption of fog, followed by the release of water through desorption and subsequent condensation. Desorption usually necessitates an external energy source, and currently, sustainable and economical options for this purpose center around solar and wind energy due to their renewable attributes. [17,47] In the development of effective adsorbent materials for water harvesting, it is necessary for the material to exhibit high hygroscopicity. Moreover, the material's surface should be modified with stable compounds featuring polar and hydrophilic groups. To further enhance the fog capture efficiency, the surface should be engineered to be porous and structured, leading to a substantial specific surface area. **Fig. 1-13** Given that many adsorbent materials rely on solar energy, they are frequently coated with solar-absorbing substances to enhance photothermal conversion efficiency. [79]

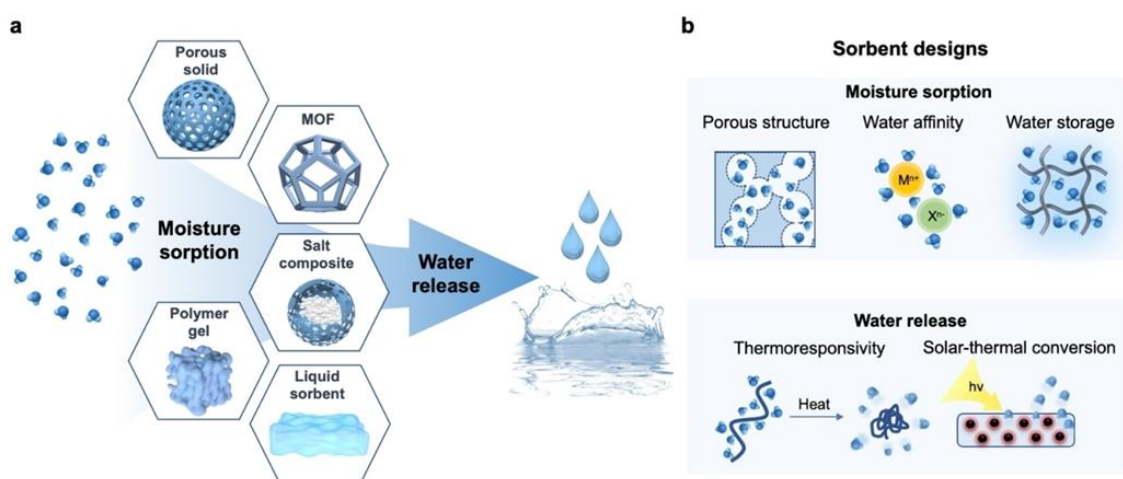


Fig. 1-13. (a) Sorbent materials in AWH, encompassing water sorption and release processes. (b) Properties crucial for designing a high-performance AWH sorbent. Reproduced with permission from ref [79] Copyright © 2022, Wiley-VCH.

The selection of materials for water harvesting plays a pivotal role in determining the performance of absorption and desorption-based Atmospheric Water Harvesting Systems (AWHS). Key factors to consider include the equilibrium water sorption mass, which reflects adsorption capacity, and the energy consumption during the desorption process, signifying desorption capacity. Additionally, the speed of two processes significantly affects the duration of the water harvesting cycle, making the performance of adsorbent a critical factor in absorption and desorption-based AWHS. [80,81]

Water harvesting with adsorbent materials is intricately linked to daily fluctuations in ambient temperature and humidity. [82-84] During the nighttime adsorption phase, characterized by higher humidity and lower temperatures, a substantial amount of water is captured and stored. In contrast, the daytime desorption phase occurs in a drier environment with elevated temperatures, promoting the release of stored water.

Different adsorbents exhibit varying sorption-desorption properties, closely tied to their structural composition and topography. In the quest for high-performance adsorbents, extensive research has been conducted, leading to substantial progress. Four categories of adsorbents were often being researched: classic adsorbents, metal-organic frameworks (MOF), and polymeric gels.

(1) Classic Adsorbents:

Classic adsorbents encompass materials such as zeolite, silica gel, hydrogel, molecular sieves, activated carbon, hygroscopic salts, manganese dioxide (MnO_2), and more. [82,85-87] These materials rely on physical or chemical sorption mechanisms for water absorption. While the water adsorption of the first mentioned five materials is primarily attributed to physical adsorption, hygroscopic salts and MnO_2 adsorb water through both physical and chemical adsorption processes. [17,81]

(2) Metal-Organic Frameworks (MOFs):

MOFs represent a unique class of materials characterized by their porous structures, which provide an extensive surface area for adsorption. The selection of metal nodes and organic linkers can be tailored to achieve specific water sorption characteristics. [82,88]

(3) Polymeric gels:

Polymeric gels are emerging as a promising host matrix for hygroscopic salts in water harvesting. While the moisture capture capacity and stability for utilization have seen improvements through various methods, molecular engineering, such as using hydrophilicity-controllable polymers, offers a versatile approach. Through the molecular-level combination of hygroscopic materials and hydrophilicity-controllable polymers, water release can take place via the phase separation process, eliminating energy-intensive desorption. This molecular-level water regulation, often using hydrogels, presents innovative opportunities for Atmospheric Water Harvesting due to its high hydrophilicity and water storage capabilities like the system shown in **Fig. 1-14** [17,47,81,83, 89, 90]

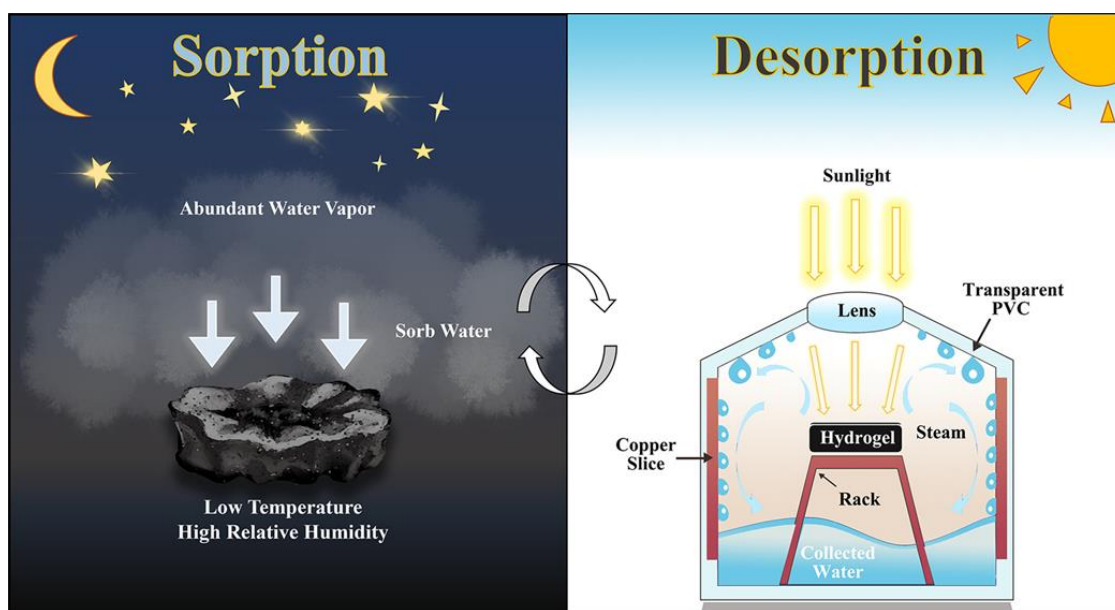


Fig. 1-14. The diagram depicts the dual processes of the hydrogel in water harvesting. Initially, the hydrogel absorbs moisture from the air during the night when temperatures are low, and relative humidity is high. Subsequently, in a homemade device heated by sunlight, desorption occurs. Then the water can be collected in the homemade device. Reproduced with permission from ref [89] Copyright © 2022, American Chemical Society.

The choice of adsorbent material depends on the specific requirements of the AWHS, with considerations including sorption capacity, desorption efficiency, and suitability for the prevailing environmental conditions.

1.4.3 Applications of AWHS

Atmospheric Water Harvesting (AWH) technologies have found diverse applications. They primarily focus on addressing the shortage of freshwater in remote and arid regions. These applications range from providing drinking water for humans in such regions to supporting sustainable agriculture through plant and crop irrigation.

AWH devices have demonstrated significant potential in generating portable drinking water. For instance, a 1 m² dew condensation panel can produce over 1 L of drinkable water one night. [91] Additionally, materials like MOF-801 can even generate 2.8 L of water one day in arid environments, even meeting the water needs of adults in desert conditions. [92] Beyond personal hydration, AWH technologies are applied to autonomously irrigate plants and crops, promoting sustainable future agriculture. **Fig. 1-15** [93,94] This is exemplified by systems like the Smart-Farm, where moisture is captured from the air and released into the soil for irrigation, offering a solution to food and water scarcity.

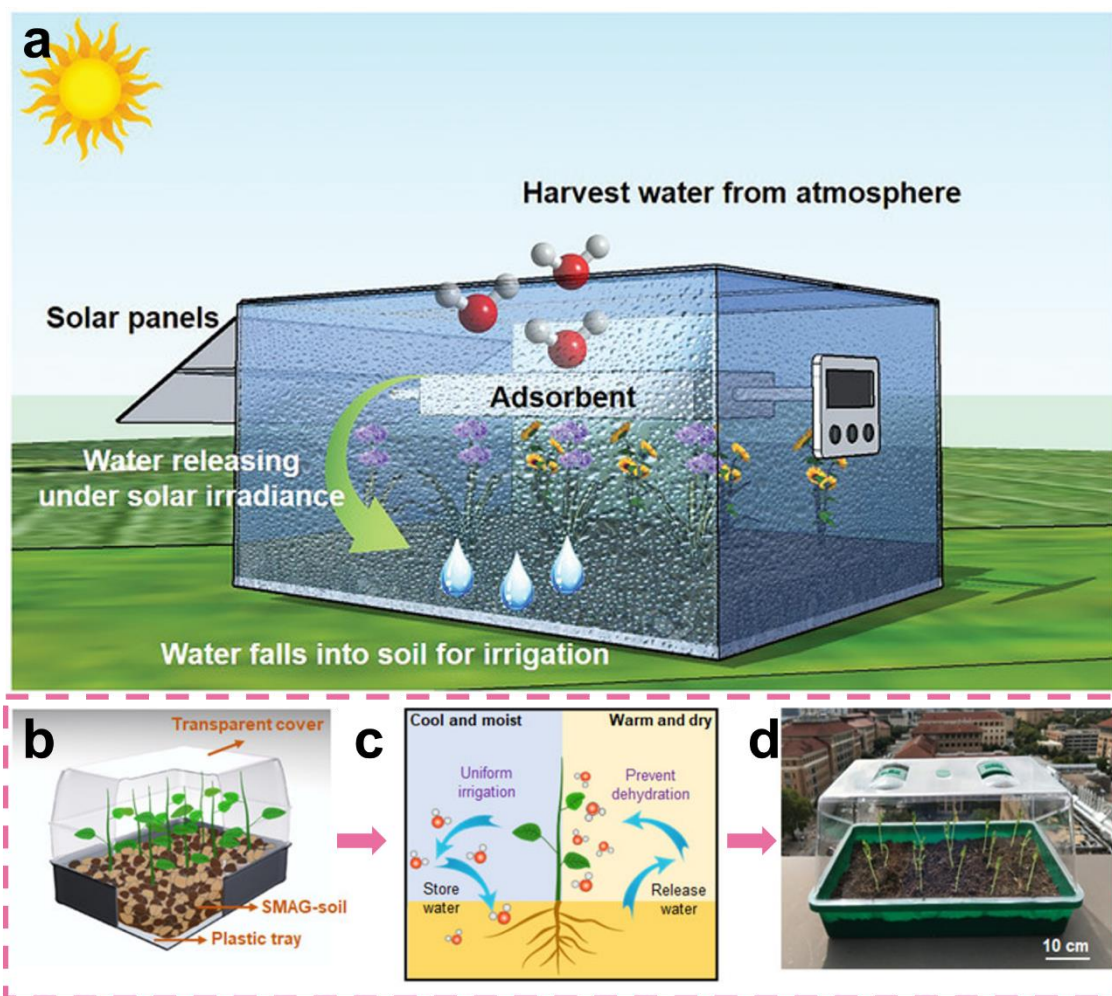


Fig. 1-15. (a) SmartFarm device schematic: adsorbent captures atmospheric water, triggered release via solar irradiance for soil irrigation. (b) Atmospheric water irrigation system schematic based on SMAG-soil for plant growth. (c) SMAG-soil moisture capture and release cycles. (d) Photograph of SMAG-soil device with growing radish plants. Reproduced with permission from ref [93] Copyright © 2020, Wiley-VCH. Reproduced with permission from ref [94] Copyright © 2020, American Chemical Society.

Commercial AWH devices and projects like FogQuest, SkyWater, AirDrop, and WaterSeer are already in use to address freshwater shortages. [10,95] For instance, the AirDrops device utilizes a solar panel and underground copper condenser to generate water through condensation. [96] These technologies represent a step towards addressing

limited and uneven freshwater sources.

In sum, AWH technologies are vital for alleviating freshwater scarcity in different regions and weather conditions. These technologies are self-sustainable and have potential commercial applications. While progress has been made, there is still room for materials optimization and system development to cater to specific weather conditions and locations.

1.4.4 Solar-Driven Interfacial Desalination

Solar-powered desalination is a rapidly evolving field, driven by the need for increased water supply and the transition to renewable energy sources. Solar energy, in particular, offers an attractive solution for desalination, aligning with regions facing both freshwater scarcity and ample solar irradiation. Recent developments have introduced novel materials and technologies to enhance the desalination process. [97]

One significant approach is direct solar desalination, which utilizes advanced photothermal materials like graphene-based and metal/ceramic nanostructures to facilitate evaporation through localized heating.[98] This method is gaining attention for its potential to harness solar energy efficiently for desalination.

Another promising avenue is solar-powered membrane distillation (SPMD), which combines solar collectors and photovoltaic panels with membrane distillation technology. SPMD systems have been developed for small-scale applications in remote areas lacking conventional water and electricity infrastructure. While technically feasible, further advancements are needed to make SPMD a cost-effective and long-lasting desalination solution. [99]

However, solar-driven interfacial desalination (SDID), which relies on localized heating and interfacial evaporation, presents its own challenges, such as salt accumulation on the evaporator's surface. In a standard SDID system, as depicted in **Fig. 1-16** [100], incoming sunlight is absorbed and transformed into heat through photothermal materials.

Innovative strategies are being explored to address salt mitigation through material design and structural engineering. These advancements aim to enhance the energy efficiency and long-term stability of SDID devices for large-scale use, particularly in remote and underprivileged areas. [101, 102]

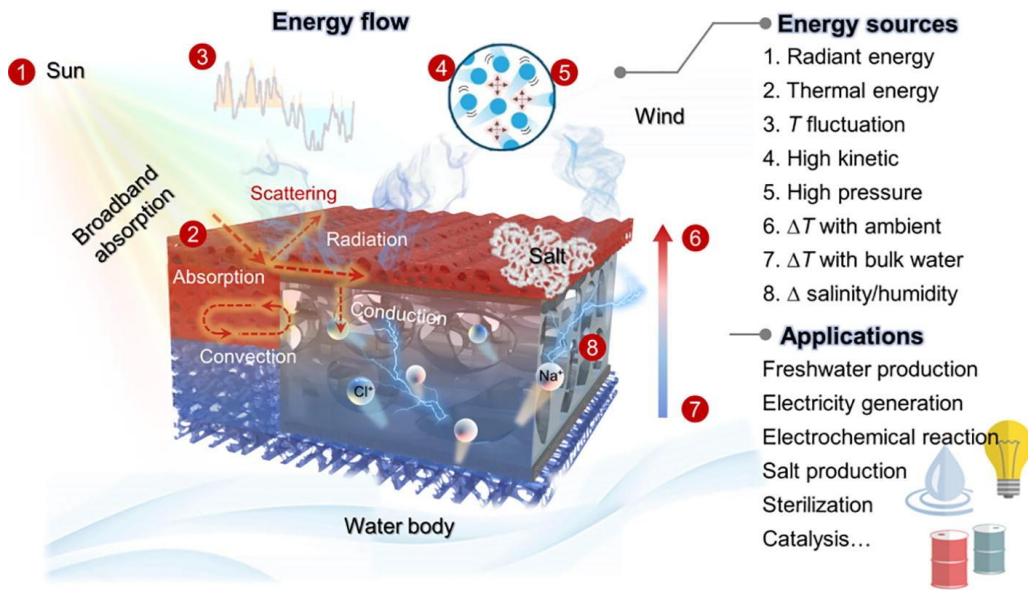


Fig. 1-16. Schematic illustrating the energy transfer process and potential energy sources in the solar-driven interfacial desalination (SDID) system. Reproduced with permission from ref [100] Copyright © 2021, Elsevier.

Overall, solar-driven desalination technologies hold great promise for addressing freshwater scarcity, offering sustainable and environmentally friendly solutions. Progress in materials, efficiency, and cost reduction is essential to make these technologies more accessible and effective, potentially transforming water availability in various regions.

1.5 Purpose and outline of this research

1.5.1 Research purpose

As society continues to progress, the importance of ensuring access to clean water

remains paramount. Traditional methods and technologies for obtaining clean water are often accompanied by exorbitant costs and inherent limitations. Drawing inspiration from the remarkable adaptations of various plants and animals thriving in arid environments, atmospheric water harvesting (AWH) has gained profound significance for the sustainable management of water resources in our modern world.

Consequently, the exploration of viable atmospheric water harvesting from fog has emerged as a promising field of research. In line with this, our research endeavors to develop functional materials inspired by the water collection mechanisms observed in nature. Our primary objective is to employ these biomimetic materials not only in foggy environments but also to expand their application to solar-driven interfacial seawater evaporation. This multifaceted approach aims to broaden the scope of material application scenarios, thereby providing a sustainable source of clean and accessible water resources.

1.5.2 Research outline

In Chapter 2, our research was dedicated to the exploration of water collection abilities in various cultivated fungi. Inspired by their proficiency in water collection, we closely examined these fungi, focusing on variations in mycelia diameter and hierarchical structural arrangements. Notably, we observed that these adept water-collecting fungi displayed characteristics of being both hydrophobic and hydrophilic. Armed with these insights, we set out to create diverse sandwich-like composite materials that effectively mimicked the observed mycelia, resulting in a composite material with an impressive ability to collect fog droplets.

Chapter 3 marked an expansion of our research horizons. Here, for the first time, we introduced the concept of solar-driven interfacial evaporation for seawater desalination, aiming to maximize the versatility of our materials across diverse environmental conditions for clean water production. In contrast to the intricate three-

layer structure explored in the previous chapter, we successfully fabricated a hierarchical multi-bioinspired Janus membrane using a practical and scalable process that combined electrospinning and ultrasonication. Remarkably, this Janus composite membrane excelled not only in fog collection but also in solar-thermal water evaporation and seawater desalination.

Addressing the inherent limitations of composite membranes, including their shape-dependent constraints on water collection, was the goal of **Chapter 4**. In overcoming this limitation, we developed a multifunctional 3D morphological hydrogel. Building upon its successful application in seawater desalination in the previous stage, we harnessed the versatility of hydrogels in both dry and wet states, adapting them for various scenarios. This innovative approach yielded remarkable outcomes, enabling the efficient collection of clean water in foggy environments and during seawater evaporation.

In summary, **Chapter 2** focused on emulating water collection abilities observed in fungi, leading to the development of a bioinspired water-harvesting material that effectively collects fog droplets. **Chapter 3** expanded the research to include solar-driven seawater desalination through a multi-biomimetic hierarchical membrane. **Chapter 4** explored 3D hydrogel materials, resulting in a versatile hydrogel with exceptional water collection, release, and seawater desalination capabilities. A graphical abstract outlining our research is presented in **Fig. 1-17**.

Finally, **Chapter 5** provided general conclusions and insights into future prospects for this research.

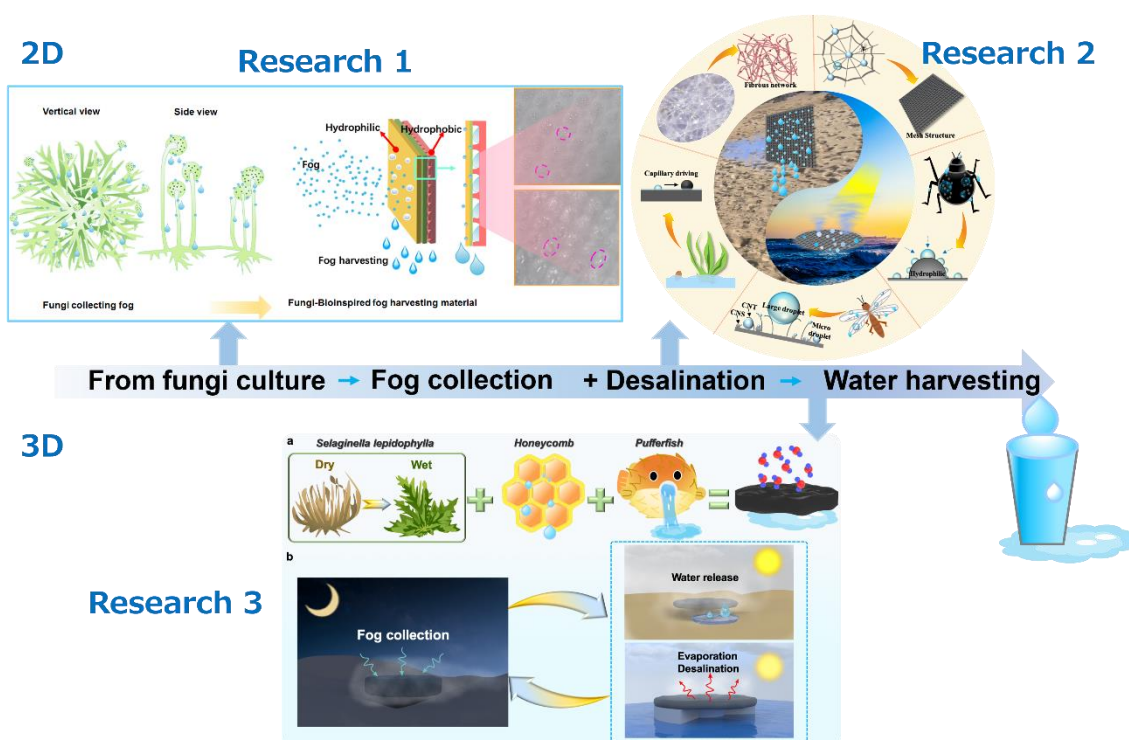


Fig. 1-17. A graphical abstract outlining our research.

Reference

- [1] M.M. Mekonnen, A.Y. Hoekstra, Four billion people facing severe water scarcity, *Science Advances* 2(2) e1500323. <https://doi.org/10.1126/sciadv.1500323>.
- [2] F. Zhao, Y. Guo, X. Zhou, W. Shi, G. Yu, Materials for solar-powered water evaporation, *Nature Reviews Materials* 5(5) (2020) 388-401. <https://doi.org/10.1038/s41578-020-0182-4>.
- [3] H. Lu, W. Shi, Y. Guo, W. Guan, C. Lei, G. Yu, Materials Engineering for Atmospheric Water Harvesting: Progress and Perspectives, *Advanced Materials* 34(12) (2022) 2110079. <https://doi.org/10.1002/adma.202110079>.
- [4] C.J. Vörösmarty, P. Green, J. Salisbury, R.B. Lammers, Global Water Resources: Vulnerability from Climate Change and Population Growth, *Science* 289(5477) (2000) 284-288. <https://doi.org/10.1126/science.289.5477.284>.
- [5] C. He, Z. Liu, J. Wu, X. Pan, Z. Fang, J. Li, B.A. Bryan, Future global urban water scarcity and potential solutions, *Nature Communications* 12(1) (2021) 4667. <https://doi.org/10.1038/s41467-021-25026-3>.
- [6] X. Zhou, Y. Guo, F. Zhao, G. Yu, Hydrogels as an Emerging Material Platform for Solar Water Purification, *Accounts of Chemical Research* 52(11) (2019) 3244-3253. <https://doi.org/10.1021/acs.accounts.9b00455>.
- [7] N.W. Arnell, Climate change and global water resources: SRES emissions and socio-economic scenarios, *Global Environmental Change* 14(1) (2004) 31-52. <https://doi.org/10.1016/j.gloenvcha.2003.10.006>.

- [8] Y. Guo, G. Yu, Engineering Hydrogels for Efficient Solar Desalination and Water Purification, *Accounts of Materials Research* 2(5) (2021) 374-384. <https://doi.org/10.1021/accountsmr.1c00057>.
- [9] M. Gao, L. Zhu, C.K. Peh, G.W. Ho, Solar absorber material and system designs for photothermal water vaporization towards clean water and energy production, *Energy & Environmental Science* 12(3) (2019) 841-864. <https://doi.org/10.1039/C8EE01146J>.
- [10] X. Liu, D. Beysens, T. Bourouina, Water Harvesting from Air: Current Passive Approaches and Outlook, *ACS Materials Letters* 4(5) (2022) 1003-1024. <https://doi.org/10.1021/acsmaterialslett.1c00850>.
- [11] M.A. Shannon, P.W. Bohn, M. Elimelech, J.G. Georgiadis, B.J. Mariñas, A.M. Mayes, Science and technology for water purification in the coming decades, *Nature* 452(7185) (2008) 301-310. <https://doi.org/10.1038/nature06599>.
- [12] N.A. Moharram, S. Bayoumi, A.A. Hanafy, W.M. El-Maghlany, Hybrid desalination and power generation plant utilizing multi-stage flash and reverse osmosis driven by parabolic trough collectors, *Case Studies in Thermal Engineering* 23 (2021) 100807. <https://doi.org/https://doi.org/10.1016/j.csite.2020.100807>.
- [13] E. Ali, J. Orfi, H. AlAnsary, A.S. Alsaadi, N. Ghaffour, Novel multistage flash reversal Concept: Modelling and analysis, *Applied Thermal Engineering* 217 (2022) 119223. <https://doi.org/https://doi.org/10.1016/j.applthermaleng.2022.119223>.
- [14] G. Crini, E. Lichtfouse, Advantages and disadvantages of techniques used for wastewater treatment, *Environmental Chemistry Letters* 17(1) (2019) 145-155. <https://doi.org/10.1007/s10311-018-0785-9>.
- [15] M.A. Darwish, N.M. Al-Najem, Energy consumption by multi-stage flash and reverse osmosis desalters, *Applied Thermal Engineering* 20(5) (2000) 399-416. [https://doi.org/https://doi.org/10.1016/S1359-4311\(99\)00032-0](https://doi.org/https://doi.org/10.1016/S1359-4311(99)00032-0).
- [16] Y. Tu, R. Wang, Y. Zhang, J. Wang, Progress and Expectation of Atmospheric Water Harvesting, *Joule* 2(8) (2018) 1452-1475. <https://doi.org/https://doi.org/10.1016/j.joule.2018.07.015>.
- [17] X. Zhou, H. Lu, F. Zhao, G. Yu, Atmospheric Water Harvesting: A Review of Material and Structural Designs, *ACS Materials Letters* 2(7) (2020) 671-684. <https://doi.org/10.1021/acsmaterialslett.0c00130>.
- [18] G. He, C. Zhang, Z. Dong, Survival in desert: Extreme water adaptations and bioinspired structural designs, *iScience* 26(1) (2023) 105819. <https://doi.org/https://doi.org/10.1016/j.isci.2022.105819>.
- [19] W.J. Hamilton, M.K. Seely, Fog basking by the Namib Desert beetle, *Onymacris unguicularis*, *Nature* 262(5566) (1976) 284-285. <https://doi.org/10.1038/262284a0>.
- [20] A.R. Parker, C.R. Lawrence, Water capture by a desert beetle, *Nature* 414(6859) (2001) 33-34. <https://doi.org/10.1038/35102108>.
- [21] T. Nørgaard, M. Dacke, Fog-basking behaviour and water collection efficiency in Namib Desert Darkling beetles, *Frontiers in Zoology* 7(1) (2010) 23. <https://doi.org/10.1186/1742-9994-7-23>.
- [22] D. Mitchell, J.R. Henschel, R.S. Hetem, T.D. Wassenaar, W.M. Strauss, S.A. Hanrahan, M.K. Seely, Fog and fauna of the Namib Desert: past and future, *Ecosphere* 11(1) (2020) e02996. <https://doi.org/https://doi.org/10.1002/ecs2.2996>.
- [23] S.E. Evans, M.E. Dueker, J.R. Logan, K.C. Weathers, The biology of fog: results from coastal

- Maine and Namib Desert reveal common drivers of fog microbial composition, *Science of The Total Environment* 647 (2019) 1547-1556. <https://doi.org/https://doi.org/10.1016/j.scitotenv.2018.08.045>.
- [24] F.D. Eckardt, R.S. Schemenauer, Fog water chemistry in the Namib desert, Namibia, *Atmospheric Environment* 32(14) (1998) 2595-2599. [https://doi.org/https://doi.org/10.1016/S1352-2310\(97\)00498-6](https://doi.org/https://doi.org/10.1016/S1352-2310(97)00498-6).
- [25] Y. Zheng, H. Bai, Z. Huang, X. Tian, F.-Q. Nie, Y. Zhao, J. Zhai, L. Jiang, Directional water collection on wetted spider silk, *Nature* 463(7281) (2010) 640-643. <https://doi.org/10.1038/nature08729>.
- [26] J. Ju, H. Bai, Y. Zheng, T. Zhao, R. Fang, L. Jiang, A multi-structural and multi-functional integrated fog collection system in cactus, *Nature Communications* 3(1) (2012) 1247. <https://doi.org/10.1038/ncomms2253>.
- [27] H. Chen, P. Zhang, L. Zhang, H. Liu, Y. Jiang, D. Zhang, Z. Han, L. Jiang, Continuous directional water transport on the peristome surface of *Nepenthes alata*, *Nature* 532(7597) (2016) 85-89. <https://doi.org/10.1038/nature17189>.
- [28] F. Luo, X. Liang, W. Chen, S. Wang, X. Gao, Z. Zhang, Y. Fang, Bimetallic MOF-Derived Solar-Triggered Monolithic Adsorbent for Enhanced Atmospheric Water Harvesting, *Small* 19(48) (2023) 2304477. <https://doi.org/https://doi.org/10.1002/smll.202304477>.
- [29] H. Yao, P. Zhang, Y. Huang, H. Cheng, C. Li, L. Qu, Highly Efficient Clean Water Production from Contaminated Air with a Wide Humidity Range, *Advanced Materials* 32(6) (2020) 1905875. <https://doi.org/https://doi.org/10.1002/adma.201905875>.
- [30] E. Kostal, S. Stroj, S. Kasemann, V. Matylitsky, M. Domke, Fabrication of Biomimetic Fog-Collecting Superhydrophilic–Superhydrophobic Surface Micropatterns Using Femtosecond Lasers, *Langmuir* 34(9) (2018) 2933-2941. <https://doi.org/10.1021/acs.langmuir.7b03699>.
- [31] B.T.W. Ang, C.H. Yap, W.S. Vincent Lee, J. Xue, Bioinspired Dual-Tier Coalescence for Water-Collection Efficiency Enhancement, *Langmuir* 34(44) (2018) 13409-13415. <https://doi.org/10.1021/acs.langmuir.8b02474>.
- [32] S. Zhang, J. Huang, Z. Chen, Y. Lai, Bioinspired Special Wettability Surfaces: From Fundamental Research to Water Harvesting Applications, *Small* 13(3) (2017) 1602992. <https://doi.org/https://doi.org/10.1002/smll.201602992>.
- [33] M. Cao, J. Ju, K. Li, S. Dou, K. Liu, L. Jiang, Facile and Large-Scale Fabrication of a Cactus-Inspired Continuous Fog Collector, *Advanced Functional Materials* 24(21) (2014) 3235-3240. <https://doi.org/https://doi.org/10.1002/adfm.201303661>.
- [34] S. Yi, J. Wang, Z. Chen, B. Liu, L. Ren, L. Liang, L. Jiang, Cactus-Inspired Conical Spines with Oriented Microbarbs for Efficient Fog Harvesting, *Advanced Materials Technologies* 4(12) (2019) 1900727. <https://doi.org/https://doi.org/10.1002/admt.201900727>.
- [35] F. Bai, J. Wu, G. Gong, L. Guo, Biomimetic “Cactus Spine” with Hierarchical Groove Structure for Efficient Fog Collection, *Advanced Science* 2(7) (2015) 1500047. <https://doi.org/https://doi.org/10.1002/advs.201500047>.
- [36] H. Zhu, Z. Guo, W. Liu, Biomimetic water-collecting materials inspired by nature, *Chemical Communications* 52(20) (2016) 3863-3879. <https://doi.org/10.1039/C5CC09867J>.
- [37] K. Schacht, T. Scheibel, Processing of recombinant spider silk proteins into tailor-made materials for biomaterials applications, *Current Opinion in Biotechnology* 29 (2014) 62-69.

<https://doi.org/https://doi.org/10.1016/j.copbio.2014.02.015>.

- [38] K. Wan, X. Gou, Z. Guo, Bio-inspired Fog Harvesting Materials: Basic Research and Bionic Potential Applications, *Journal of Bionic Engineering* 18(3) (2021) 501-533. <https://doi.org/10.1007/s42235-021-0040-0>.
- [39] S. Kwangseok, K. Minyoung, K. Do Hyun, Re-derivation of Young's Equation, Wenzel Equation, and Cassie-Baxter Equation Based on Energy Minimization, in: A. Mahmood (Ed.), *Surface Energy*, IntechOpen, Rijeka, 2015, p. Ch. 1. <https://doi.org/10.5772/61066>.
- [40] T. Young, An essay on the cohesion of fluids, *Abstracts of the Papers Printed in the Philosophical Transactions of the Royal Society of London* 1 (1997) 171-172. <https://doi.org/10.1098/rspl.1800.0095>.
- [41] R.N. Wenzel, RESISTANCE OF SOLID SURFACES TO WETTING BY WATER, *Industrial & Engineering Chemistry* 28(8) (1936) 988-994. <https://doi.org/10.1021/ie50320a024>.
- [42] A.B.D. Cassie, S. Baxter, Wettability of porous surfaces, *Transactions of the Faraday Society* 40(0) (1944) 546-551. <https://doi.org/10.1039/TF9444000546>.
- [43] K. Liu, Y. Tian, L. Jiang, Bio-inspired superoleophobic and smart materials: Design, fabrication, and application, *Progress in Materials Science* 58(4) (2013) 503-564. <https://doi.org/https://doi.org/10.1016/j.pmatsci.2012.11.001>.
- [44] M.K. Chaudhury, G.M. Whitesides, How to Make Water Run Uphill, *Science* 256(5063) (1992) 1539-1541. <https://doi.org/10.1126/science.256.5063.1539>.
- [45] S. Daniel, M.K. Chaudhury, J.C. Chen, Fast Drop Movements Resulting from the Phase Change on a Gradient Surface, *Science* 291(5504) (2001) 633-636. <https://doi.org/10.1126/science.291.5504.633>.
- [46] É. Lorenceau, D. QuÉRÉ, Drops on a conical wire, *Journal of Fluid Mechanics* 510 (2004) 29-45. <https://doi.org/10.1017/S0022112004009152>.
- [47] B. Wang, X. Zhou, Z. Guo, W. Liu, Recent advances in atmosphere water harvesting: Design principle, materials, devices, and applications, *Nano Today* 40 (2021) 101283. <https://doi.org/https://doi.org/10.1016/j.nantod.2021.101283>.
- [48] F. Zhao, X. Zhou, Y. Liu, Y. Shi, Y. Dai, G. Yu, Super Moisture-Absorbent Gels for All-Weather Atmospheric Water Harvesting, *Advanced Materials* 31(10) (2019) 1806446. <https://doi.org/https://doi.org/10.1002/adma.201806446>.
- [49] X. Dai, N. Sun, S.O. Nielsen, B.B. Stogin, J. Wang, S. Yang, T.-S. Wong, Hydrophilic directional slippery rough surfaces for water harvesting, *Science Advances* 4(3) eaaq0919. <https://doi.org/10.1126/sciadv.aaq0919>.
- [50] Y. Hou, Y. Shang, M. Yu, C. Feng, H. Yu, S. Yao, Tunable Water Harvesting Surfaces Consisting of Biphilic Nanoscale Topography, *ACS Nano* 12(11) (2018) 11022-11030. <https://doi.org/10.1021/acsnano.8b05163>.
- [51] H. Dai, Z. Dong, L. Jiang, Directional liquid dynamics of interfaces with superwettability, *Science Advances* 6(37) eabb5528. <https://doi.org/10.1126/sciadv.abb5528>.
- [52] P. Comanns, G. Buchberger, A. Buchsbaum, R. Baumgartner, A. Kogler, S. Bauer, W. Baumgartner, Directional, passive liquid transport: the Texas horned lizard as a model for a biomimetic 'liquid diode', *Journal of The Royal Society Interface* 12(109) (2015) 20150415. <https://doi.org/10.1098/rsif.2015.0415>.

- [53] W.C. Sherbrooke, A.J. Scardino, R. de Nys, L. Schwarzkopf, Functional morphology of scale hinges used to transport water: convergent drinking adaptations in desert lizards (*Moloch horridus* and *Phrynosoma cornutum*), *Zoomorphology* 126(2) (2007) 89-102. <https://doi.org/10.1007/s00435-007-0031-7>.
- [54] X. Gou, Z. Guo, Hybrid Hydrophilic–Hydrophobic CuO@TiO₂-Coated Copper Mesh for Efficient Water Harvesting, *Langmuir* 36(1) (2020) 64-73. <https://doi.org/10.1021/acs.langmuir.9b03224>.
- [55] J. Wu, H. Zhou, H. Wang, H. Shao, G. Yan, T. Lin, Novel Water Harvesting Fibrous Membranes with Directional Water Transport Capability, *Advanced Materials Interfaces* 6(5) (2019) 1801529. <https://doi.org/https://doi.org/10.1002/admi.201801529>.
- [56] W. Shi, T.W. van der Sloot, B.J. Hart, B.S. Kennedy, J.B. Boreyko, Harps Enable Water Harvesting under Light Fog Conditions, *Advanced Sustainable Systems* 4(6) (2020) 2000040. <https://doi.org/https://doi.org/10.1002/adsu.202000040>.
- [57] P.-B. Bintein, H. Lhuissier, A. Mongruel, L. Royon, D. Beysens, Grooves Accelerate Dew Shedding, *Physical Review Letters* 122(9) (2019) 098005. <https://doi.org/10.1103/PhysRevLett.122.098005>.
- [58] B.T.W. Ang, J. Zhang, G.J. Lin, H. Wang, W.S.V. Lee, J. Xue, Enhancing Water Harvesting through the Cascading Effect, *ACS Applied Materials & Interfaces* 11(30) (2019) 27464-27469. <https://doi.org/10.1021/acsami.9b08460>.
- [59] K. Hou, X. Li, Q. Li, X. Chen, Tunable Wetting Patterns on Superhydrophilic/Superhydrophobic Hybrid Surfaces for Enhanced Dew-Harvesting Efficacy, *Advanced Materials Interfaces* 7(2) (2020) 1901683. <https://doi.org/https://doi.org/10.1002/admi.201901683>.
- [60] Z. Yu, F.F. Yun, Y. Wang, L. Yao, S. Dou, K. Liu, L. Jiang, X. Wang, Desert Beetle-Inspired Superwetable Patterned Surfaces for Water Harvesting, *Small* 13(36) (2017) 1701403. <https://doi.org/https://doi.org/10.1002/sml.201701403>.
- [61] F.T. Malik, R.M. Clement, D.T. Gethin, W. Krawszik, A.R. Parker, Nature's moisture harvesters: a comparative review, *Bioinspiration & Biomimetics* 9(3) (2014) 031002. <https://doi.org/10.1088/1748-3182/9/3/031002>.
- [62] F.T. Malik, R.M. Clement, D.T. Gethin, M. Kiernan, T. Goral, P. Griffiths, D. Beynon, A.R. Parker, Hierarchical structures of cactus spines that aid in the directional movement of dew droplets, *Philosophical Transactions of the Royal Society A: Mathematical, Physical and Engineering Sciences* 374(2073) (2016) 20160110. <https://doi.org/10.1098/rsta.2016.0110>.
- [63] Z. Pan, W.G. Pitt, Y. Zhang, N. Wu, Y. Tao, T.T. Truscott, The upside-down water collection system of *Syntrichia caninervis*, *Nature Plants* 2(7) (2016) 16076. <https://doi.org/10.1038/nplants.2016.76>.
- [64] F.T. Malik, R.M. Clement, D.T. Gethin, D. Beysens, R.E. Cohen, W. Krawszik, A.R. Parker, Dew harvesting efficiency of four species of cacti, *Bioinspiration & Biomimetics* 10(3) (2015) 036005. <https://doi.org/10.1088/1748-3190/10/3/036005>.
- [65] P. Comanns, C. Effertz, F. Hischen, K. Staudt, W. Böhme, W. Baumgartner, Moisture harvesting and water transport through specialized micro-structures on the integument of lizards, *Beilstein Journal of Nanotechnology* 2 (2011) 204-214. <https://doi.org/10.3762/bjnano.2.24>.
- [66] W. Sherbrooke, Integumental water movement and rate of water ingestion during rain harvesting

- in the Texas horned lizard, *Phrynosoma cornutum*, *Amphibia-Reptilia* 25(1) (2004) 29-39. <https://doi.org/https://doi.org/10.1163/156853804322992814>.
- [67] F. Ito, S. Komatsubara, N. Shigezawa, H. Morikawa, Y. Murakami, K. Yoshino, S. Yamanaka, Mechanics of water collection in plants via morphology change of conical hairs, *Applied Physics Letters* 106(13) (2015) 133701. <https://doi.org/10.1063/1.4916213>.
- [68] Y. Wang, X. Wang, C. Lai, H. Hu, Y. Kong, B. Fei, J.H. Xin, Biomimetic Water-Collecting Fabric with Light-Induced Superhydrophilic Bumps, *ACS Applied Materials & Interfaces* 8(5) (2016) 2950-2960. <https://doi.org/10.1021/acsami.5b08941>.
- [69] C. Xu, R. Feng, F. Song, X.-L. Wang, Y.-Z. Wang, Desert Beetle-Inspired Superhydrophilic/Superhydrophobic Patterned Cellulose Film with Efficient Water Collection and Antibacterial Performance, *ACS Sustainable Chemistry & Engineering* 6(11) (2018) 14679-14684. <https://doi.org/10.1021/acssuschemeng.8b03247>.
- [70] J. Knapczyk-Korczak, D.P. Ura, M. Gajek, M.M. Marzec, K. Berent, A. Bernasik, J.P. Chiverton, U. Stachewicz, Fiber-Based Composite Meshes with Controlled Mechanical and Wetting Properties for Water Harvesting, *ACS Applied Materials & Interfaces* 12(1) (2020) 1665-1676. <https://doi.org/10.1021/acsami.9b19839>.
- [71] Z. Zhu, J. Li, H. Peng, D. Liu, Nature-Inspired Structures Applied in Heat Transfer Enhancement and Drag Reduction, *Micromachines*, 2021.
- [72] D. Sarkar, A. Mahapatra, A. Som, R. Kumar, A. Nagar, A. Baidya, T. Pradeep, Patterned Nanobrush Nature Mimics with Unprecedented Water-Harvesting Efficiency, *Advanced Materials Interfaces* 5(19) (2018) 1800667. <https://doi.org/https://doi.org/10.1002/admi.201800667>.
- [73] W. Liu, P. Fan, M. Cai, X. Luo, C. Chen, R. Pan, H. Zhang, M. Zhong, An integrative bioinspired venation network with ultra-contrasting wettability for large-scale strongly self-driven and efficient water collection, *Nanoscale* 11(18) (2019) 8940-8949. <https://doi.org/10.1039/C8NR10003A>.
- [74] M. Chen, Z. Yi, S. Tao, S. Wang, Z. Fang, C. Lu, Z. Xu, A Pragmatic Device Based on a Double-Sided Functional Structure for Efficient Water Harvesting, *Global Challenges* 4(5) (2020) 1900094. <https://doi.org/https://doi.org/10.1002/gch2.201900094>.
- [75] L. Zhang, J. Wu, M.N. Hedhili, X. Yang, P. Wang, Inkjet printing for direct micropatterning of a superhydrophobic surface: toward biomimetic fog harvesting surfaces, *Journal of Materials Chemistry A* 3(6) (2015) 2844-2852. <https://doi.org/10.1039/C4TA05862C>.
- [76] Y. Xing, W. Shang, Q. Wang, S. Feng, Y. Hou, Y. Zheng, Integrative Bioinspired Surface with Wettability Patterns and Gradient for Enhancement of Fog Collection, *ACS Applied Materials & Interfaces* 11(11) (2019) 10951-10958. <https://doi.org/10.1021/acsami.8b19574>.
- [77] H. Bai, L. Wang, J. Ju, R. Sun, Y. Zheng, L. Jiang, Efficient Water Collection on Integrative Bioinspired Surfaces with Star-Shaped Wettability Patterns, *Advanced Materials* 26(29) (2014) 5025-5030. <https://doi.org/https://doi.org/10.1002/adma.201400262>.
- [78] D. Seo, C. Lee, Y. Nam, Influence of Geometric Patterns of Microstructured Superhydrophobic Surfaces on Water-Harvesting Performance via Dewing, *Langmuir* 30(51) (2014) 15468-15476. <https://doi.org/10.1021/la5041486>.
- [79] W. Shi, W. Guan, C. Lei, G. Yu, Sorbents for Atmospheric Water Harvesting: From Design Principles to Applications, *Angewandte Chemie International Edition* 61(43) (2022) e202211267. <https://doi.org/https://doi.org/10.1002/anie.202211267>.

- [80] N. Asim, M. Badiei, M.A. Alghoul, M. Mohammad, N.A. Samsudin, N. Amin, K. Sopian, Sorbent-based air water-harvesting systems: progress, limitation, and consideration, *Reviews in Environmental Science and Bio/Technology* 20(1) (2021) 257-279. <https://doi.org/10.1007/s11157-020-09558-6>.
- [81] Z. Chen, S. Song, B. Ma, Y. Li, Y. Shao, J. Shi, M. Liu, H. Jin, D. Jing, Recent progress on sorption/desorption-based atmospheric water harvesting powered by solar energy, *Solar Energy Materials and Solar Cells* 230 (2021) 111233. <https://doi.org/https://doi.org/10.1016/j.solmat.2021.111233>.
- [82] L.G. Gordeeva, Y.D. Tu, Q. Pan, M.L. Palash, B.B. Saha, Y.I. Aristov, R.Z. Wang, Metal-organic frameworks for energy conversion and water harvesting: A bridge between thermal engineering and material science, *Nano Energy* 84 (2021) 105946. <https://doi.org/https://doi.org/10.1016/j.nanoen.2021.105946>.
- [83] R. Li, Y. Shi, M. Alsaedi, M. Wu, L. Shi, P. Wang, Hybrid Hydrogel with High Water Vapor Harvesting Capacity for Deployable Solar-Driven Atmospheric Water Generator, *Environmental Science & Technology* 52(19) (2018) 11367-11377. <https://doi.org/10.1021/acs.est.8b02852>.
- [84] Z. Zhang, Y. Wang, Z. Li, H. Fu, J. Huang, Z. Xu, Y. Lai, X. Qian, S. Zhang, Sustainable Hierarchical-Pored PAAS–PNIPAAm Hydrogel with Core–Shell Structure Tailored for Highly Efficient Atmospheric Water Harvesting, *ACS Applied Materials & Interfaces* 14(49) (2022) 55295-55306. <https://doi.org/10.1021/acsami.2c19840>.
- [85] D.T. Bui, A. Nida, Kim C. Ng, Kian J. Chua, Water vapor permeation and dehumidification performance of poly(vinyl alcohol)/lithium chloride composite membranes, *Journal of Membrane Science* 498 (2016) 254-262. <https://doi.org/https://doi.org/10.1016/j.memsci.2015.10.021>.
- [86] J. Wang, Y. Dang, A.G. Meguerdichian, S. Dissanayake, T. Kankanam-Kapuge, S. Bamonte, Z.M. Tobin, L.A. Achola, S.L. Suib, Water Harvesting from the Atmosphere in Arid Areas with Manganese Dioxide, *Environmental Science & Technology Letters* 7(1) (2020) 48-53. <https://doi.org/10.1021/acs.estlett.9b00713>.
- [87] H.-T. Oh, S.-J. Lim, J.H. Kim, C.-H. Lee, Adsorption Equilibria of Water Vapor on an Alumina/Zeolite 13X Composite and Silica Gel, *Journal of Chemical & Engineering Data* 62(2) (2017) 804-811. <https://doi.org/10.1021/acs.jced.6b00850>.
- [88] F. Fathieh, M.J. Kalmutzki, E.A. Kapustin, P.J. Waller, J. Yang, O.M. Yaghi, Practical water production from desert air, *Science Advances* 4(6) eaat3198. <https://doi.org/10.1126/sciadv.aat3198>.
- [89] T. Lyu, Z. Wang, R. Liu, K. Chen, H. Liu, Y. Tian, Macroporous Hydrogel for High-Performance Atmospheric Water Harvesting, *ACS Applied Materials & Interfaces* 14(28) (2022) 32433-32443. <https://doi.org/10.1021/acsami.2c04228>.
- [90] A.M.K. El-Ghonemy, RETRACTED: Fresh water production from/by atmospheric air for arid regions, using solar energy: Review, *Renewable and Sustainable Energy Reviews* 16(8) (2012) 6384-6422. <https://doi.org/10.1016/j.rser.2012.06.029>.
- [91] X. Liu, J. Trosseille, A. Mongruel, F. Marty, P. Basset, J. Laurent, L. Royon, T. Cui, D. Beysens, T. Bourouina, Tailoring silicon for dew water harvesting panels, *iScience* 24(7) (2021). <https://doi.org/10.1016/j.isci.2021.102814>.
- [92] H. Kim, S. Yang, S.R. Rao, S. Narayanan, E.A. Kapustin, H. Furukawa, A.S. Umans, O.M. Yaghi, E.N. Wang, Water harvesting from air with metal-organic frameworks powered by natural sunlight,

- Science 356(6336) (2017) 430-434. <https://doi.org/10.1126/science.aam8743>.
- [93] J. Yang, X. Zhang, H. Qu, Z.G. Yu, Y. Zhang, T.J. Eey, Y.-W. Zhang, S.C. Tan, A Moisture-Hungry Copper Complex Harvesting Air Moisture for Potable Water and Autonomous Urban Agriculture, *Advanced Materials* 32(39) (2020) 2002936. <https://doi.org/https://doi.org/10.1002/adma.202002936>.
- [94] X. Zhou, P. Zhang, F. Zhao, G. Yu, Super Moisture Absorbent Gels for Sustainable Agriculture via Atmospheric Water Irrigation, *ACS Materials Letters* 2(11) (2020) 1419-1422. <https://doi.org/10.1021/acsmaterialslett.0c00439>.
- [95] F. Rojas, V. Carter, M. Rosato, Fog Collection Technology Transfer and Co-Creation Projects in Falda Verde, Chile and Tojquia, Guatemala, in: J.-C. Bolay, S. Hostettler, E. Hazboun (Eds.) *Technologies for Sustainable Development*, Springer International Publishing, Cham, 2014, pp. 275-286.
- [96] N. Shafeian, A.A. Ranjbar, T.B. Gorji, Progress in atmospheric water generation systems: A review, *Renewable and Sustainable Energy Reviews* 161 (2022) 112325. <https://doi.org/https://doi.org/10.1016/j.rser.2022.112325>.
- [97] F.E. Ahmed, R. Hashaikeh, N. Hilal, Solar powered desalination – Technology, energy and future outlook, *Desalination* 453 (2019) 54-76. <https://doi.org/https://doi.org/10.1016/j.desal.2018.12.002>.
- [98] J. Kim, S. Hong, A novel single-pass reverse osmosis configuration for high-purity water production and low energy consumption in seawater desalination, *Desalination* 429 (2018) 142-154. <https://doi.org/https://doi.org/10.1016/j.desal.2017.12.026>.
- [99] M.R. Qtaishat, F. Banat, Desalination by solar powered membrane distillation systems, *Desalination* 308 (2013) 186-197. <https://doi.org/https://doi.org/10.1016/j.desal.2012.01.021>.
- [100] T. Ding, Y. Zhou, W.L. Ong, G.W. Ho, Hybrid solar-driven interfacial evaporation systems: Beyond water production towards high solar energy utilization, *Materials Today* 42 (2021) 178-191. <https://doi.org/https://doi.org/10.1016/j.mattod.2020.10.022>.
- [101] K. Xu, C. Wang, Z. Li, S. Wu, J. Wang, Salt Mitigation Strategies of Solar-Driven Interfacial Desalination, *Advanced Functional Materials* 31(8) (2021) 2007855. <https://doi.org/https://doi.org/10.1002/adfm.202007855>.
- [102] X. Liu, D.D. Mishra, X. Wang, H. Peng, C. Hu, Towards highly efficient solar-driven interfacial evaporation for desalination, *Journal of Materials Chemistry A* 8(35) (2020) 17907-17937. <https://doi.org/10.1039/C9TA12612K>.

Chapter 2

Bioinspired composite materials used for efficient fog harvesting with structures that consist of fungi-mycelia networks

Chapter 2: Bioinspired composite materials used for efficient fog harvesting with structures that consist of fungi-mycelia networks

2.1 Introduction

Water is the source of life for all living things and human activities. Climate change may influence the way the water cycle works in part, but it is not the most urgent current threat to global water resources. The direst problem is that the demand for water by all living creatures is excessive. The ever-increasing human population, especially persons with water-wasting lifestyles, has increased water demand until it has reached the upper limit of the available supply. [1] The issue of the scarcity of water is becoming a major global concern. Currently, there are about 1.1 billion people in the world who lack access to safe water, and approximately 2.7 billion people must deal with scarce water supplies for at least one month of the year. [2, 3] Thus, obtaining new sources of water is an essential and momentous challenge. Despite some current practical technologies that have been explored to address this crisis, such as wastewater disposal and the desalination of seawater, [4, 5] these approaches are still far from adequate because they are relatively inefficient, intricate, and costly. However, fog, as a latent and available source of freshwater, has shown outstanding potential to meet the expected demand, especially in arid and semiarid tropical and subtropical climate zones, where fog occurs frequently but freshwater is scarce. [6] In the natural world, many flora and fauna have evolved optimized structures to collect freshwater from fog for their survival. [7] In fact, the atmosphere air is a large water reservoir that contains about 1.4×10^7 tons of water. Even in the desert, the moisture content per unit volume in the atmosphere is more than $10 \text{ g} \cdot \text{m}^{-3}$. [8] Therefore, the idea of harvesting water from fog is an innovative, reproducible, and eco-friendly technical method.

Recently, the research and development activities of related biologically inspired

materials with water-collection capacity have become a hot topic. There are many plants and creatures in nature that can collect water from fog, such as cactus and Namib grass and spiders and desert beetles. [9, 10] These known plants and animals with water-harvesting capacity have provided inspiration and model prototypes for many relevant studies. [11-13] Perhaps we can learn from nature and create composite materials with special structures and properties that can achieve the goal of harvesting water from fog.

Previous studies in this area [14, 15] have focused mostly on animals and plants that can collect water from fog while living in regions where the environment is extreme and oppressive. Some researches have been conducted on spider webs that can collect water effectively. [16, 17] Also, some fungi can collect water, and they are a species that we often see in our daily activities. There are many types and forms of fungi, and in people's observation of fungi, it unexpectedly was found that the structure and appearance of certain fungi are very similar to spiders' webs. [18-20]

Collecting water from the air is divided into four main steps, i.e., (1) grab the tiny water droplets in the air and then condense them; (2) the water droplets condense and grow larger; (3) transport the large water droplets; and (4) water collection and storage. Due to the low nucleation energy barrier, the hydrophilic surface owns a better water-harvesting capacity. However, the collected water would spread on the surface and could not maintain a spherical shape, thus hindering the subsequent process of water harvesting. Hydrophobic surfaces enable better condensation and collection of water droplets due to their higher water contact angle and lower contact angle hysteresis. [21] Combined with previous research, when both hydrophilic and hydrophobic materials are present in composite materials, the composite materials will have better water-collection performance than a material that is merely hydrophilic or hydrophobic. The hydrophilic parts can more easily attract water droplets in the air compared to a hydrophobic area, [22] and the hydrophobic surface can make the water droplets move smoothly and converge into larger water droplets. [23]

To date, most of the related studies mentioned above have achieved excellent

performance in harvesting water, but the materials used are expensive and the manufacturing process is complicated. Therefore, different from the general direct biomimic material fabrication and water-collection research, the surface morphology and water-collection properties of fungi were first investigated in this study. The culture, observation, and identification of three common filamentous fungi (*Rhizopus delemar*, *Mucor hiemalis* f. *hiemalis*, and *Monascus purpureus*) were carried out. *Rhizopus delemar* and *Mucor hiemalis* f. *hiemalis* are very common fungi that appear on the surface of moist organic matter. [19] Fermented products of *Monascus purpureus* have been used in food, medicine, and industry in Asian countries for more than a thousand years. [24]

The hydrophilic water-absorbing layer-filter paper, the hydrophobic water-conducting layer-polyacrylamide (PAM), and the hydrophobic drainage layer-polyurethane (PU) nanofiber membrane were utilized then through a simple, facile, and economical manufacturing process; a water-collecting material similar to a sandwich structure was fabricated. It owns a water-harvesting ability that mimics the characteristics of fungi mycelia, which can collect water from the air. Filter paper is a facile, economical, and efficient commercially available porous material. The main component of the filter paper is cellulose, and it is rich in hydroxyl groups, which results in a strong affinity for water molecules. [25, 26] In addition, cellulose is biocompatible, renewable, biodegradable, nontoxic, and environmentally friendly. Its high specific surface area and good adsorption have been applied in the fabrication and modification of superwetting materials by many studies. [27, 28] PAM is a general-purpose enhancer of the strength of paper, and it is used often to increase osmosis; also it can act as a flocculant to purify drinking water. [29, 30] The production process of this material is more convenient and more efficient than has been reported in previous studies. [31] The results of the water-harvesting test showed that the material fabricated in this study has great potential for use in water-harvesting systems.

2.2 Experimental section

2.2.1 Materials

Difco potato dextrose agar (213400) was provided by Becton, Dickinson and Company. Nile red, fluoresce, and ethanol (95) were provided by FUJIFILM Wako Pure Chemical Corporation. Three different fungi (*Rhizopus delemar* (NBRC 4773), *Mucor hiemalis* f. *hiemalis* (NBRC 5834), and *Monascus purpureus* (NBRC 4485)) were provided by the NITE Biological Resource Center (NBRC), National Institute of Technology and Evaluation. *Rhizopus delemar* and *Mucor hiemalis* f. *hiemalis* belong to Mucoromycota. *Monascus purpureus* belongs to ascomycota. Ethanol (95) and *N, N*-dimethylformamide (DMF) were provided by FUJIFILM Wako Pure Chemical Corporation. Polyurethane (PU, molecular weight of $\sim 110,000$ g mol⁻¹) was obtained from Sigma-Aldrich Co. LLC. Polyacrylamide (PAM) with a viscosity of 2000–7000 mPa s (25 °C) was provided by Arakawa Chemical Industries, Ltd. Filter paper was purchased from TOYO ROSHI KAISHA, Ltd. The stainless steel meshes were purchased from Q-ho Metal Works.

2.2.2 Fungi Cultivation

The cultivation of fungi included several steps. First, the inoculum was prepared as follows. Difco potato dextrose agar powder (11.7 g) and 300 mL of distilled water were stirred for 3 min in a cone glass bottle; then, the mixture was sterilized at 120 °C for 1.5 h, after which it was allowed to cool to 60 °C. Subsequently, 10 mL of the inoculum that was obtained was poured into a Petri dish for cultivation under ultraviolet light (for sterilization), wrapped, and then placed in a 2 °C environment for 24 h as a culture medium for later use.

The above thawed fungi strains were transplanted separately onto the culture media. After the transplantation, all the cultured fungi grew naturally in a temperature incubator

at 28 °C for 1 week. **Fig. 2-1** shows what the fungi look like a week after being in cultivation.

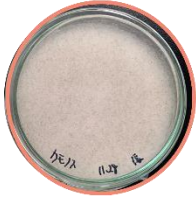
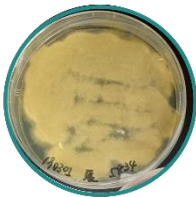

Strain	<i>Rhizopus delemar</i>	<i>Mucor hiemalis</i> f. <i>hiemalis</i>	<i>Monascus purpureus</i>
NBRC No.	NBRC 4773	NBRC 5834	NBRC 4485
Optical images			

Fig. 2-1. Optical images of fungi.

2.2.3 Fabrication of Hydrophobic Mesh-Like Membranes

Mesh-like materials have been proven to facilitate the efficiency of harvesting water. [32] However, in order to mimic and fabricate the hydrophobic mesh-like membrane layer with different fiber fineness, stainless steel meshes were used as the receiver in the electrospinning device for the hydrophobic membrane. A 20 wt % PU solution in DMF was used for electrospinning. The voltage was fixed at 15 kV. The distance between the needle and collector was fixed at 15 cm. At 20 ± 2 °C, $60 \pm 5\%$ RH, four kinds of samples were fabricated by changing the flow rate to 0.5 and 1.0 mL h⁻¹, as well as the mesh density for 40 and 60 per inch, respectively. The PU mesh-like membranes were identified as M_{0.5-40}, M_{0.5-60}, M₁₋₄₀, and M₁₋₆₀, where the 0.5 and 1 represent the flow rate, while 40 and 60 represent the density of the stainless steel mesh.

2.2.4 Fabrication of Composite Amphipathic Materials

Four kinds of fabricated PU membranes were combined with hydrophilic filter paper by a prepared PAM (50 wt % in water solution). PAM was spread on mesh-like PU nanofiber membranes as the water-conducting layer and the intermediate bonding to fix the hydrophilic commercial filter paper. The composite amphipathic materials were

defined as C_{0.5-40}, C_{0.5-60}, C₁₋₄₀, and C₁₋₆₀, corresponding to the PU membranes mentioned above. Finally, the composite materials were made into a size of 4 × 4 cm².

2.2.5 Characterization

Morphological investigation was performed by a Stereomicroscope (SZX7, Olympus Corporation), a digital microscope (VHX-900, Keyence Corporation), and scanning electron microscopy ((SEM, JSM-6010LA, JEOL Ltd.). The surface wetting properties of the samples were measured using a contact angle measuring instrument (DMs-400, Kyowa Interface Science Co., Ltd.) with 1 μL of deionized water as the liquid medium. For each fungi sample, seven parallel tests were conducted to give average results. Each membrane sample and composite material was tested 10 times in different parts, and the average value and standard deviation were obtained. Stained fungi specimens were observed with a fluorescence microscope (ECLIPSE E600, Nikon Corporation) to identify whether they were hydrophilic or hydrophobic. 3D topographical images were determined by laser scanning confocal microscopy (LSCM, OLS3000MS, OLYMPUS CORPORATION). The behavior of the water droplets was recorded by an industrial camera system (PL3-05, Shinano Kenshi Co., Ltd.). A digital single lens reflex camera (EOS 70D(w), Canon Inc.) was used to record the process of the fog-harvesting behavior. Infrared thermography (875-2isetV3, Testo SE & Co. KGaA) was used to photograph and record temperature changes of the sample during the water-collection experiment.

2.2.6 Water-Collection Performance Measurements

A humidifier (HTJS-007J-WH, MODERN DECO Co., Ltd.) was placed 5 cm away from the samples. The fog flow velocity was 40–50 cm s⁻¹ (tested by an anemometer, Model 6541-01, KANOMAX). The fog-collection performance of the PU mesh-like membranes, composite amphipathic materials, and filter paper was evaluated at 22 ± 2 °C

and $65 \pm 5\%$ RH. The mass of each sample was determined before and after every 20 min of fog collection, which lasted for 1 h. The mass of collected water (Δm_t , mg) was calculated based on formula (1). Water-collection efficiency η ($\text{mg cm}^{-2} \text{h}^{-1}$) can be obtained by calculation using formula (2):

$$\Delta m_t = m_t - m_0 \quad (1)$$

$$\eta = \Delta m_t / st \quad (2)$$

where m_t refers to the mass of composite material including collected water (mg), m_0 is the mass of composite material before the collection of fog (mg). In addition, s is the surface area of the sample (cm^2), and t is the time to collect water (h).

2.3 Results and discussion

2.3.1 Morphological Features of Fungi

According to the images taken with a stereomicroscope (**Fig. 2-1(a)**), it was found that many water droplets were strung out on the mycelia of *Rhizopus delemar*. The mycelia of *Mucor hiemalis* f. *hiemalis* and *Monascus purpureus* were shorter, [33, 34] and there were a few small water droplets. As shown in **Fig. 2-1(b)**, according to the ordinary images viewed through the digital microscope, water droplets were collected by each fungus during the process of growth. According to the surface observation, there were obvious water droplets on the surface of *Rhizopus delemar*. The common feature of both *Rhizopus delemar* and *Mucor hiemalis* f. *hiemalis* is that there were many fiber-like mycelia on the surfaces. The structure is intertwined, much like the structure of a spider web, and both thick and thin mycelia coexisted. Basically, the uppermost layer is composed of thin mycelial fibers and spores, and the middle and bottom layers are the thicker fibers, which are related to the growth of the fungi. The upper layers are immature fibrous mycelia, and the middle and bottom layers are thicker mycelia and mycorrhizae

that are mature and senescent. Among them, *Rhizopus delemar* can grow longer mycelia, and the mesh-like structure of the mycelia can be seen clearly, while those of *Mucor hiemalis* f. *hiemalis* and *Monascus purpureus* were short. [33-35] SEM images of the fungi (**Fig. 2-1(c)**) showed that they had both thick and thin mycelia, and the spherical nodules are spores. The *Mucor hiemalis* f. *hiemalis* mycelia were finer than that of *Rhizopus delemar*.

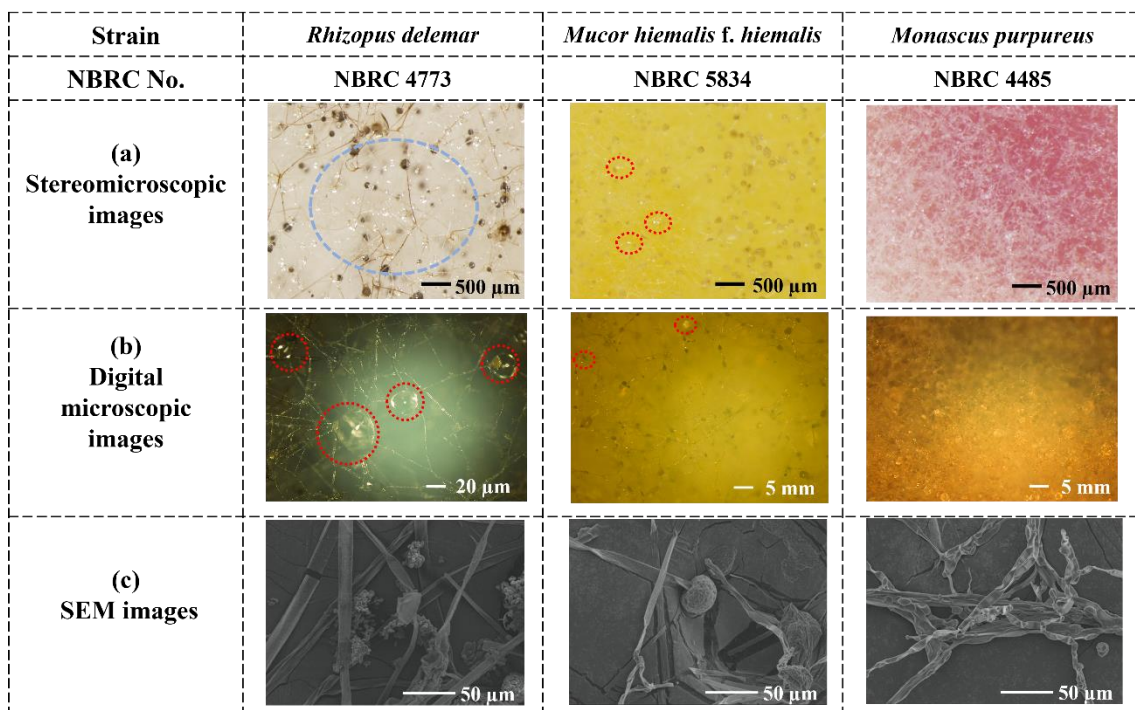


Fig. 2-2. Morphologies of fungi: (a) stereomicroscopic images of fungi, (c) light microscopic images of fungi, and (d) SEM images of fungi.

According to the observation of the experiments, water droplets rarely were seen on *Monascus purpureus*, but the SEM images show the special structure of conidia on the spores. Also, it is clear that an effective water-collection structure is a mesh-like structure. The cultivation of fungi can grow mycelia and form a complex mesh-like structure with both thick and thin fibers to achieve the harvesting of fog.

2.3.2 Analysis of the Water-Harvesting Structure of Fungi

In order to better mimic and manufacture water-harvesting materials, it is necessary to identify whether the fungi are hydrophilic or hydrophobic. This was determined through fluorescence staining technology and the water contact angle (WCA) tests.

A fluorescence staining experiment was performed to verify the wettability of the fungi stereoscopically. Nile red dye was an excellent vital stain due to its hydrophobic property, using a 510–560 nm band-pass exciter filter and 590 nm for an absorption filter. The condition of these hydrophobic excitation filters combined together was called G-2A. The fluorescein stain was for hydrophilic observation, using a 450–490 nm band-pass excitation filter and 520 nm for an absorption filter. The condition of these hydrophilic excitation filters combined together is called B-2A. The cultivated fungi were stained. Fluorescein and Nile red were dissolved in ethanol with concentrations of 2×10^{-4} and 1.25×10^{-4} wt %. The fungi samples were immersed in the Fluorescein staining solution for 15 min, washed with water and dried at room temperature for 1 h. The same procedure was performed with Nile red. And, it is worth mentioning that *Monascus purpureus* could not be stained because their structure and texture are relatively fragile, presenting as a powdery shape that cannot be sampled with tweezers. In further study, *Monascus purpureus* was excluded. The results of *Rhizopus delemar* and *Mucor hiemalis* f. *hiemalis* are shown in **Fig. 2-3**. *Rhizopus delemar* showed red under the G-2A, indicating that it is hydrophobic overall. However, when it was exposed under B-2A, there were still some green parts, which means that *Rhizopus delemar* also owned hydrophilicity parts. *Mucor hiemalis* f. *hiemalis* overall is embodied in a hydrophilic structure, but some thick mycelia also reflected hydrophobicity. Thus, *Mucor hiemalis* f. *hiemalis*' mycelia were amphiphilic. [31]

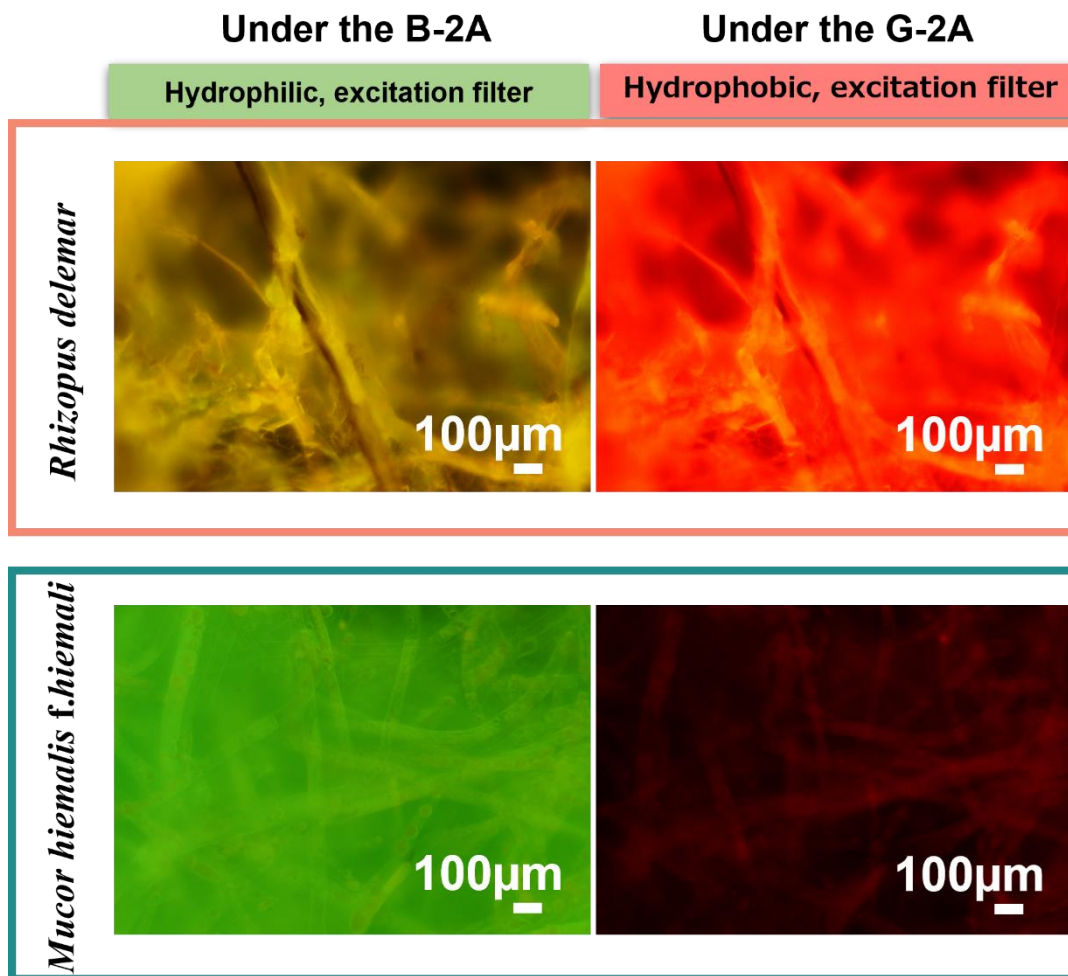


Fig. 2-3. Fluorescent staining images.

WCA tests were conducted to evaluate the wettability of the surface of the fungi when exposed to liquid water. Each sample generally was selected from seven different test points, and the data were averaged. Relevant tests were evaluated at 22 ± 2 °C and 65 ± 5 % RH. According to **Fig. 2-4**, the WCA of *Rhizopus delemar* is larger than 90° and shows hydrophobic properties, while the WCA of *Mucor hiemalis f. hiemalis* is less than 90° , which shows hydrophilic properties. Although *Rhizopus delemar* was found generally to be hydrophobic through WCA experiments, combining with the results of fluorescent staining, it can be found that its hydrophobic structure is the majority and hydrophilic parts also existed. Similarly, *Mucor hiemalis f. hiemalis* was hydrophilic

overall but also had obvious hydrophilic mycelia. The results mentioned above showed that both of them were amphiphilic.

Hydrophilic *Mucor hiemalis* f. *hiemalis* could capture tiny water droplets, but it also had the diffusion of the water droplets on its surface, which hindered the formation of larger water droplets, and the tiny water droplets that were captured were easily dispersed. *Rhizopus delemar* showed some hydrophilic property, which ensures that it can capture tiny water droplets. The overall water-collection system of *Rhizopus delemar* was hydrophobic, and its surface is more likely to aggregate captured tiny water droplets and creates bigger water droplets. As a result, the agminated large water droplets appeared easier on *Rhizopus delemar*.

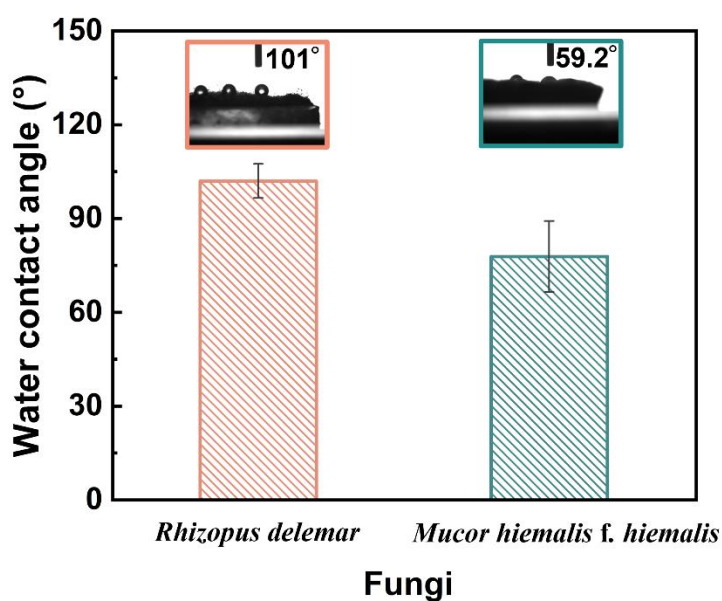


Fig. 2-4. Water contact angle results.

2.3.3 Mimicking the Water-Harvesting System of Fungi

Since the growth of fungi requires a period of time during which the nutrients of the medium are consumed gradually, fungi will have both senescent and neonatal parts after a period of growth. The growth of fungi will have several stages, and the characteristics of each stage also will be somewhat different; hence, the quantitative-qualitative analysis

could not be carried out smoothly. Moreover, considering that the productivity of fungi is very low and considering that the cultivation of fungi will be restricted by many external factors, the growth of fungi also has corresponding requirements for the environment. For the reasons stated above, it is difficult to apply fungi directly as raw materials for fabricating water-collection materials, so it is necessary to propose a water-collection material that can replace fungi, along with a long-term, effective, and controllable fabrication method.

The same as the analysis of fungi, prior research related to mesh-like water-harvesting materials also has shown that, compared with smooth homogeneous fiber membranes, hierarchical hydrophilic–hydrophobic fiber membranes have better water-harvesting capacity. [32] Based on the characteristics of fungi discussed above, the hierarchical structure referred to the upper surface for fog deposition combined with the bottom surface for water drainage, where the fiber fineness is inhomogeneous, such as with the mycelia of *Rhizopus delemar*, which greatly improves the efficiency of the collection of water. [36, 37] Nanofiber membranes are used in many water-collection materials due to their large specific surface area, excellent flexibility, and good permeability. [38-41] If the advantages of the mesh-like structure and nanofiber materials are combined, the water-collection effect would increase, but most nanomaterials are only sprayed or spread directly on the mesh-like materials. [32] There are a few materials that can directly shape the nanomaterials into macroscopic, mesh-like structures. To create a mesh-like hydrophobic membrane with a hierarchical structure as well as the coexistence of coarse and fine fibers, using the electrospinning method with the mesh-like material as the receiving device was a novel choice.

Based on previous studies related to harvesting water and biomimic of fungi, a material with a sandwich-like structure was proposed in this study. The surface layer of the water-collecting material is a hydrophilic layer (filter paper), the middle layer is a water-conducting transmission layer (PAM), and the lower layer is a water-collection and drainage layer (PU membrane).

2.3.4 Morphology and Wettability of Hydrophobic Mesh Membranes

The WCA test was performed on the electrospun PU mesh membranes to evaluate the difference in hydrophobicity of the membranes obtained under different electrospinning conditions, such as mesh density and flow rate. **Fig. 2-5** shows the device for producing hydrophobic nanofiber membranes with special mesh structures. The significant difference was statistically analyzed at a 5% (*) or 1% (**) probability level. From the results of the WCA test shown in **Fig. 2-6**, all four samples are hydrophobic. It can be seen clearly that $M_{0.5-60}$ and M_{1-60} show higher hydrophobicity than $M_{0.5-40}$ and M_{1-40} . In this study, a higher mesh density, such as 60 per inch demonstrated a higher WCA than that of the lower mesh density. The reason for this was considered to be the roughness of the surfaces of the two kinds of membranes, which was a mesh structure. Surfaces were further scanned, and the corresponding height profile to the x -axis and y -axis distribution maps were plotted (**Fig. 2-7**), which showed the mesh-like membrane morphology and the corresponding surface roughness to a certain extent. [42-44]

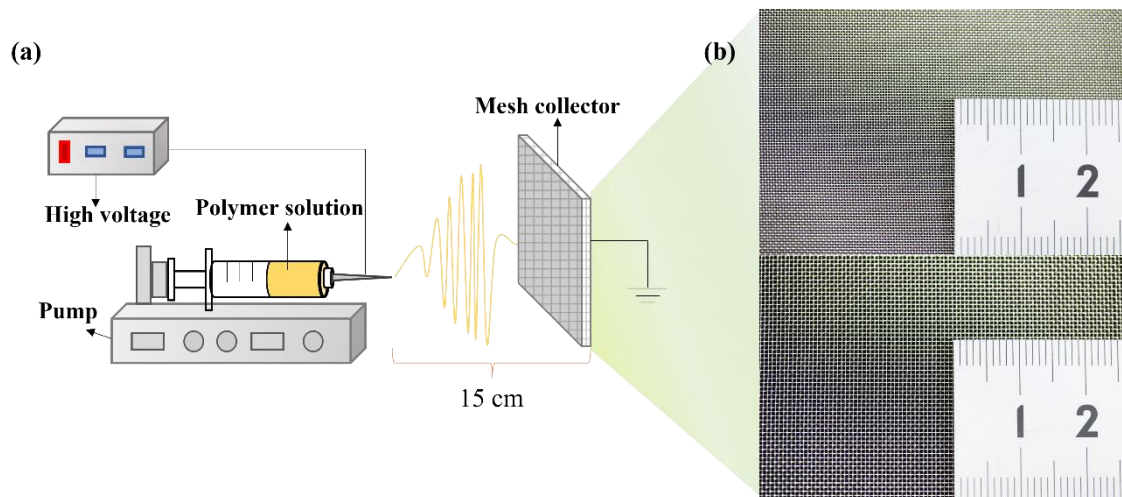


Fig. 2-5. Apparatus for PU mesh nanofiber membranes (a) electrospinning apparatus, (b) utilized meshes.

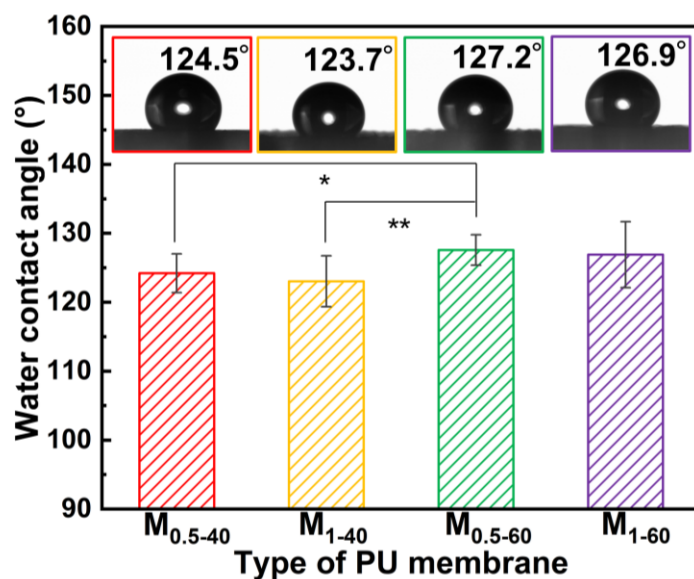


Fig. 2-6. Water contact angle results of different PU mesh nanofiber membrane.

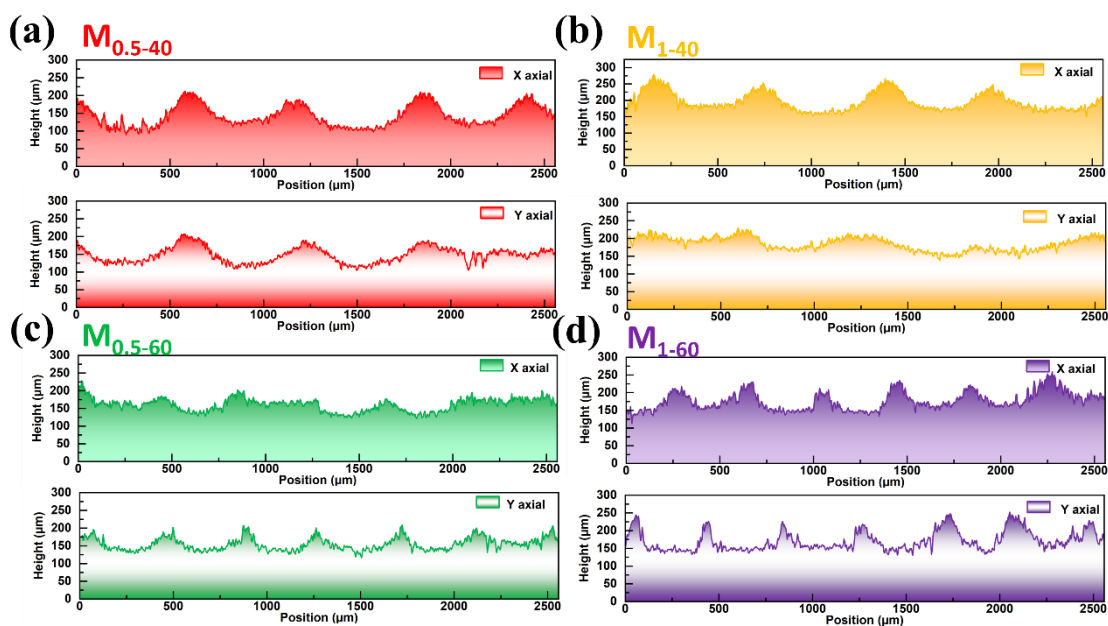


Fig. 2-7. Height profile corresponding to the x-axis and y-axis for (a) M_{0.5-40}, (b) M₁₋₄₀, (c) M_{0.5-60}, (d) M₁₋₆₀.

Fig. 2-8 shows the SEM images and fiber diameter distributions of the four membranes. The mesh structure for each membrane can be seen clearly. Moreover, the fibers on the crossed mesh showed accumulation compared to the surroundings, which

made the membrane a hierarchical structure on a macro scale. Along with the different flow rates and mesh densities, the diameters of the nanofibers also were different. A high flow rate resulted in a coarse fiber diameter because of the lack of fibers stretching and solvent evaporation. Furthermore, the density of the mesh increased from 40 to 60 per inch, with a slight increase also found in the diameter of the fiber due to the influence of the electric field during the electrospinning. As investigated by some other researchers, the diameters of the nanofibers were determined mainly by voltage, distance, flow rate, collectors, and environmental conditions. [45, 46] Besides the collectors, the parameters mentioned above were constant, and this assured that the fibers were almost uniform throughout. The diameters of the fibers differed from about 200 nm to more than 1200 nm, and this demonstrated that both thick and fine fibers coexisted. This coexistence of thick and thin nanofibers better mimicked the fungi mycelia morphology.

M_{0.5-40} and M_{0.5-60} obtained by electrospinning with a flow rate of 0.5 mL h⁻¹ were uniform compared to 1.0 mL h⁻¹ under similar corresponding other conditions, and the deviation was relatively small. When the flow rate was reduced, the nanofibers could be fully stretched in the electric field and the electric field was more stable, resulting in the diameter distribution of the nanofiber being more uniform. [46, 47]

According to the LSCM 3D images (**Fig. 2-9**) and SEM images (**Fig. 2-8**), the three-dimensional structures of the four PU nanofiber membranes could be visually observed, and all have a concave–convex mesh structure.

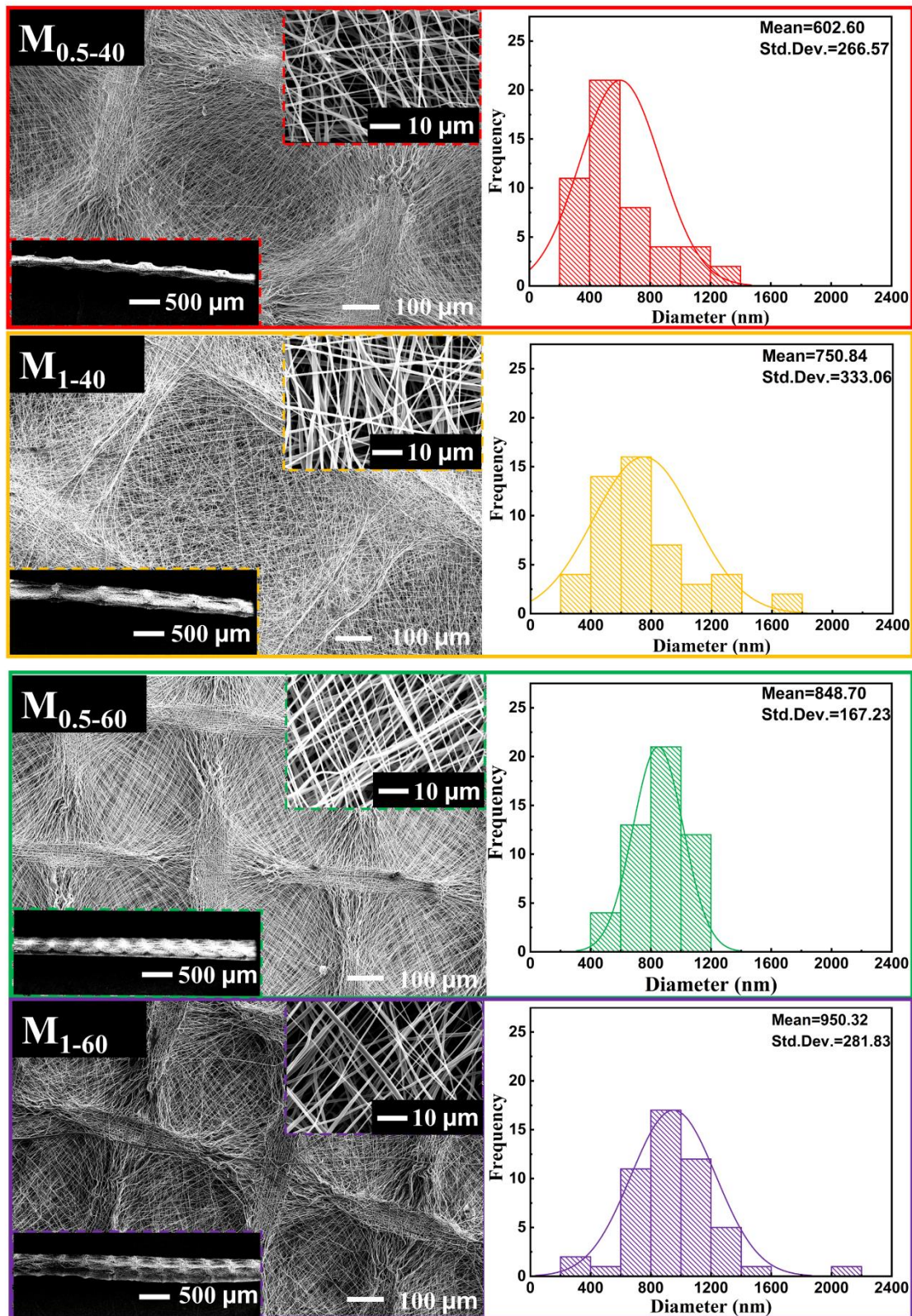


Fig. 2-8. SEM images (top right insets show larger magnification SEM images, bottom left insets show section of the mesh-like membranes), including diameter distribution.

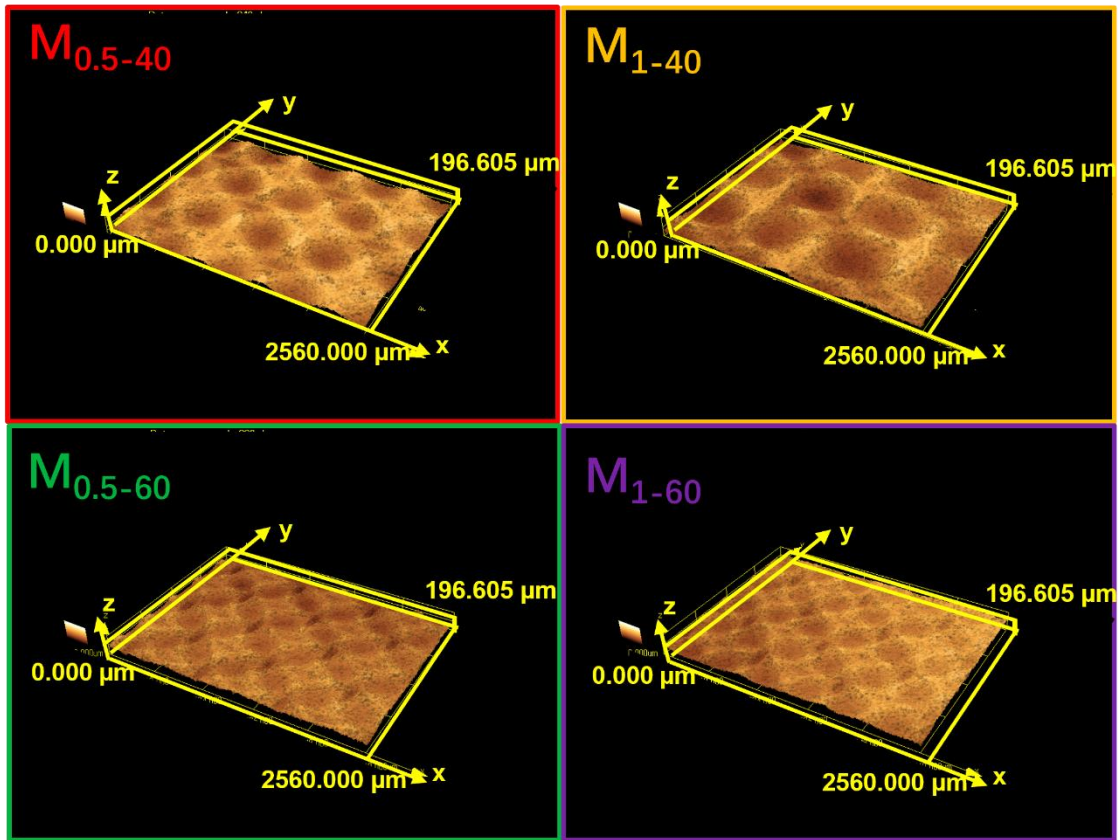


Fig. 2-9. LSCM 3D photographic images.

2.3.5 Surface Features and Wettability of Composite Amphipathic Materials

Fig. 2-10(a) shows the structure diagram of the expected composite material. Fig. 2-10(b) shows cross-section views of the composite materials. The water-harvesting performance of the composite materials also was tested with the system shown in Fig. 2-10(c), as well as the function of each envisioned layer and the process of water harvesting. Samples were clamped on a shelf.

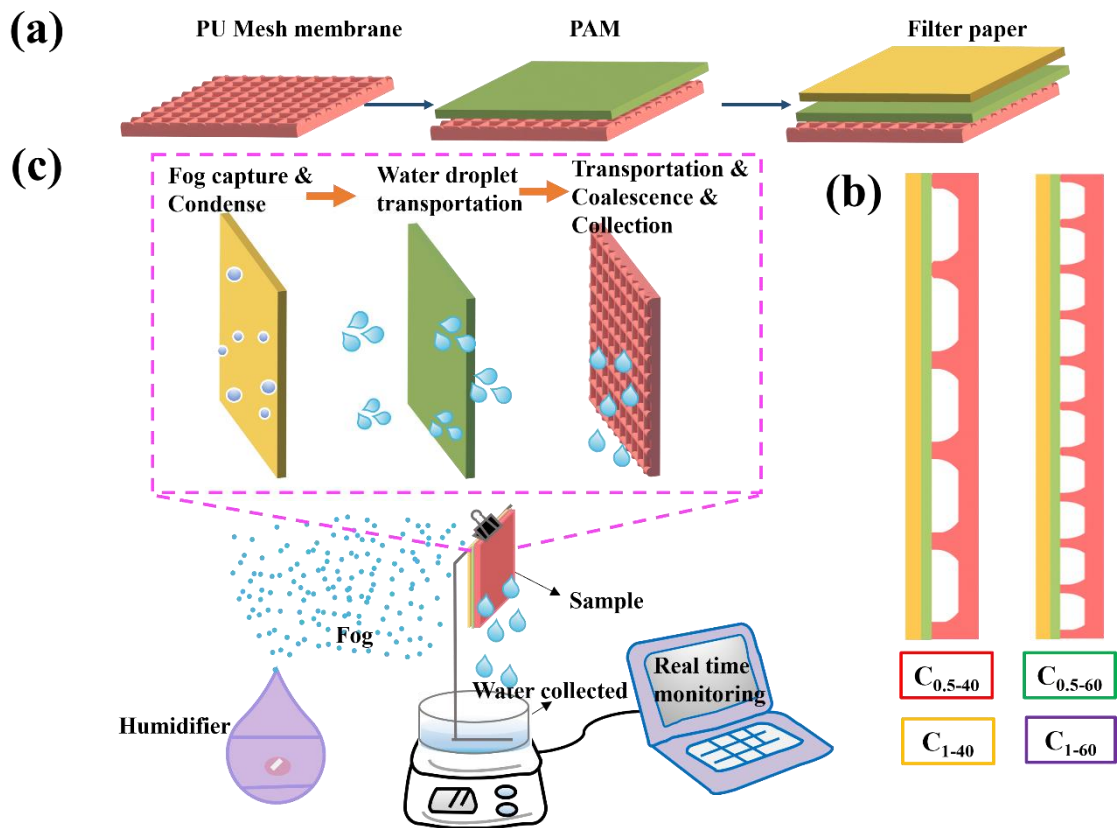


Fig. 2-10. Images and properties of composite materials: (a) envisioned composite material, (b) the cross-section views of composite materials, (c) schematic diagram of the water-collection device and process.

Originally, the filter paper was hydrophilic. After adding the hydrophobic mesh-like membrane, the WCA of the composite material was tested (**Fig. 2-11**). Diffusion within 0.1 s was recorded due to the hydrophilicity of the material. It was found that $C_{0.5-40}$ and C_{1-40} can absorb water faster than $C_{0.5-60}$ and C_{1-60} , and the initial WCAs were also smaller and more hydrophilic. Therefore, it was assumed that $C_{0.5-40}$ and C_{1-40} may perform better in the transportation of the collected water than $C_{0.5-60}$ and C_{1-60} .

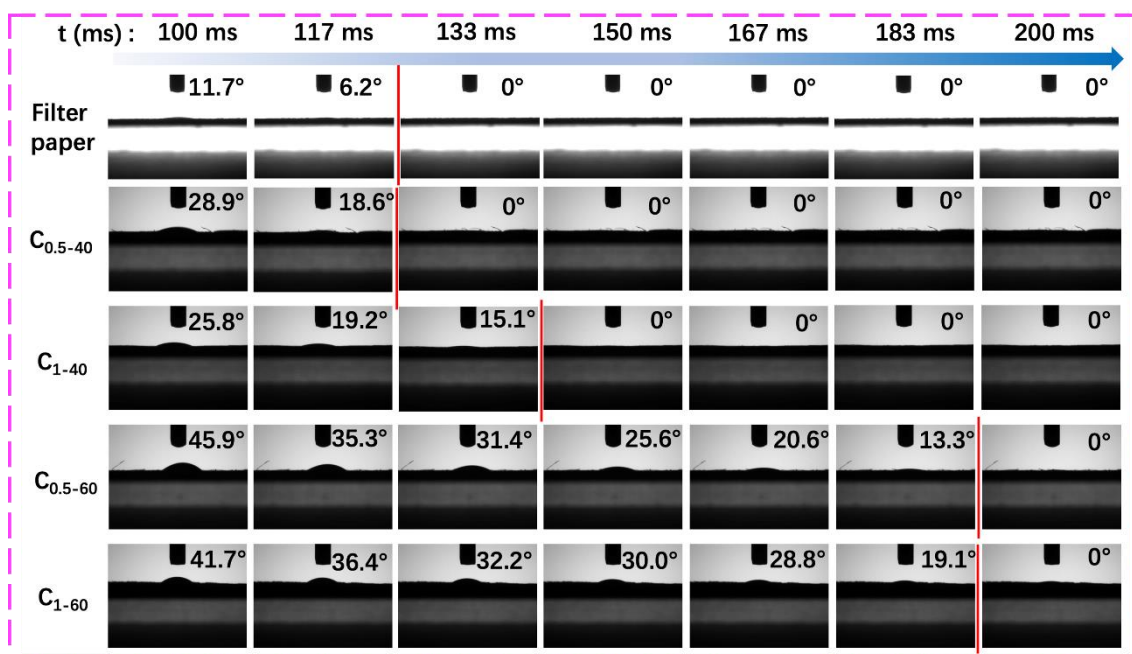


Fig. 2-11. Change of water contact angle of different material surface in 0.1 s.

The excellent water absorption of the filter paper is attributed to the cellulose-based chemistry and the fact that the filter paper structure itself has cavities. [48-50] The morphology and contact angle 0° of the filter paper are shown in (Fig. 2-12). According to these, it can be seen that the filter paper is composed of continuous fiber bundles with diameters ranging from a few nanometers to a few micrometers, and there are gaps between the bundles of fibers. From the perspective of practical application, filter paper is cost-effective as a hydrophilic, porous material, so the direct utilization of filter paper is a good choice as the hydrophilic part of the water-collecting material.

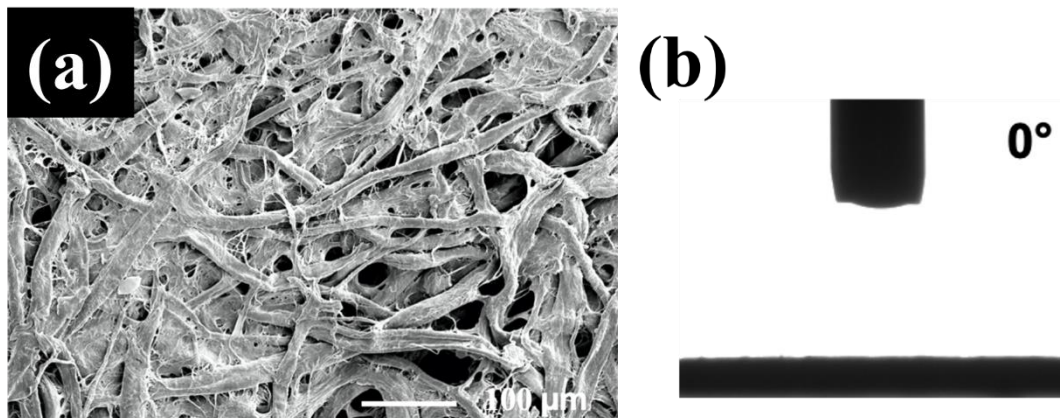


Fig. 2-12. The morphology (a) and WCA (b) of filter paper.

PAM was used as the connection between the filter paper and the PU membrane, i.e., the water-conducting layer of the water-harvesting material. Through the contact angle experiment, it was found that the surface of the filter paper of the composite material was not affected and that the hydrophilicity still was excellent, which means water droplets that fall on the surface would be absorbed immediately.

2.3.6 Water-Harvesting Properties of the Composite Materials

The mass of water collection at each measurement time was determined and is shown in **Fig. 2-13**. During the 1 h water-collection experiment, both the PU membrane and the filter paper absorbed water. After 30 min, the water-harvesting capacity of the filter paper gradually diminished, indicating that a single hydrophilic material was not very effective for the collection of water. The PU membrane also showed a saturation trend at 55 min, indicating that hydrophobic materials also have limitations in harvesting water. For the composite materials, the mass of the absorbed water increased with time. Moreover, the total amounts of the water of C_{0.5-40} and C₁₋₄₀ that were collected were higher than the sum of the water collected from the filter paper and the corresponding membranes. The difference in the total collected water mass was caused by the mesh structure of the

membrane. The amphiphilic materials with a wettability gradient have more advantages in harvesting water. It can be seen that the water-harvesting capacity of $C_{0.5-40}$ is excellent. However, at the end of the first hour during the water-collection experiment, the volume of water tended to be balanced, but the composite material made of the PU membrane and filter paper still had an upward trend. It is possible that a greater amount of water could be collected if the time of the experiment continues to be extended. This shows that materials with both hydrophilic and hydrophobic properties are better than pure hydrophilic or pure hydrophobic materials in the collection of water, which means that amphiphilic materials have superiority in harvesting water.

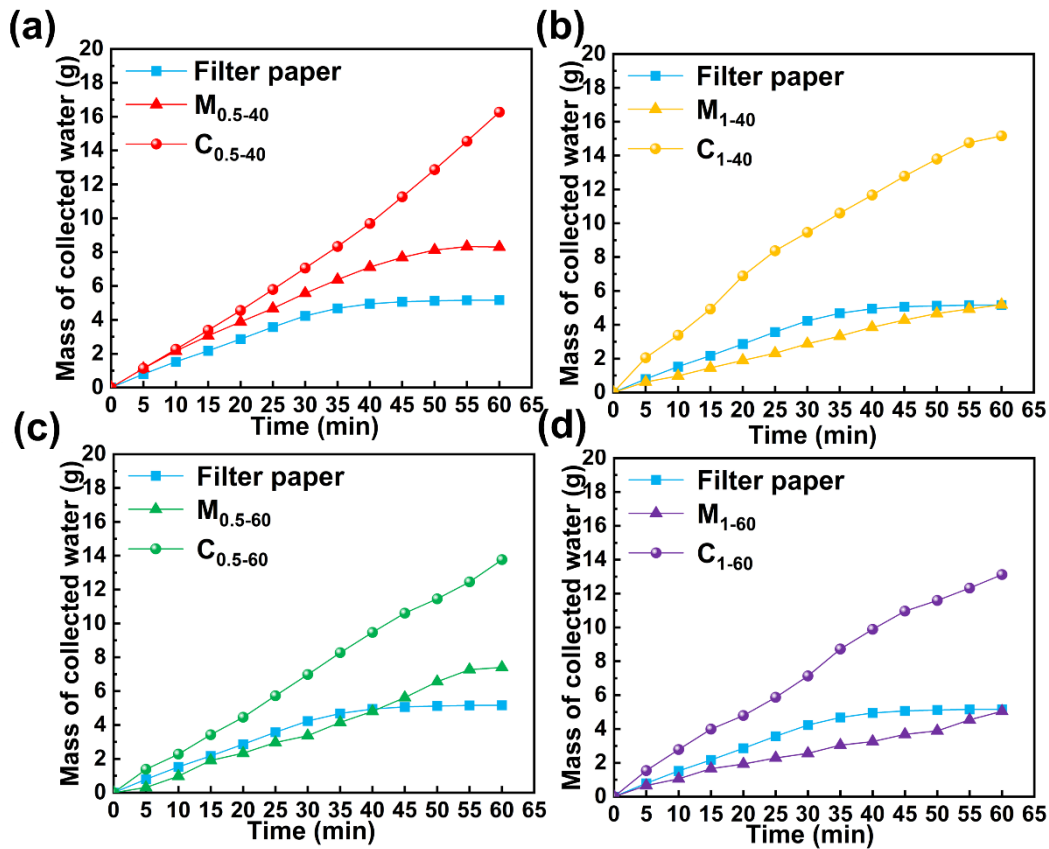


Fig. 2-13. Fog-harvesting performance of composite materials: (a) amount of water collected by (1) $M_{0.5-40}$, $C_{0.5-40}$, (2) M_{1-40} , C_{1-40} , (3) $M_{0.5-60}$, $C_{0.5-60}$, and (4) M_{1-60} , C_{1-60} during the process.

Considering that $C_{0.5-40}$ was the most prominent in the water-harvesting effect, it was observed and explored further. The surface of the composite material ($C_{0.5-40}$) was brushed with blue pigment powder with a soft brush for enhanced visualization. When the sample was not wetted, the surface was white and blue gradually appeared after wetting. **Fig. 2-14(a)** show the process of the fog-harvesting behavior of $C_{0.5-40}$. The results show that the droplets continue to form, increase in size, and drip rapidly after about 20 min. At the same time, as shown in **Fig. 2-14(b)**. It was found that $C_{0.5-40}$ collected water and water diffused rapidly. When the sample began to collect fog from 0 to 10 s due to the higher vapor pressure in the atmosphere, water molecules entered the sample and released heat, resulting in increasing the temperature to about 25 °C. However, when the sample continued to collect fog after 10 s, the heat was dispersed to the environment, and the temperature of the sample decreased gradually. At 90 s, the temperature had decreased to 20 °C and continued to stabilize. When the temperature of the water-collecting material is lower than the surrounding environment, the tiny water droplets can be condensed in time when they collide with the surface of the material; thus, the water-harvesting efficiency can be improved after increasing the condensation effect. It shows that $C_{0.5-40}$ quickly collected fog and was completely wet within 90 s.

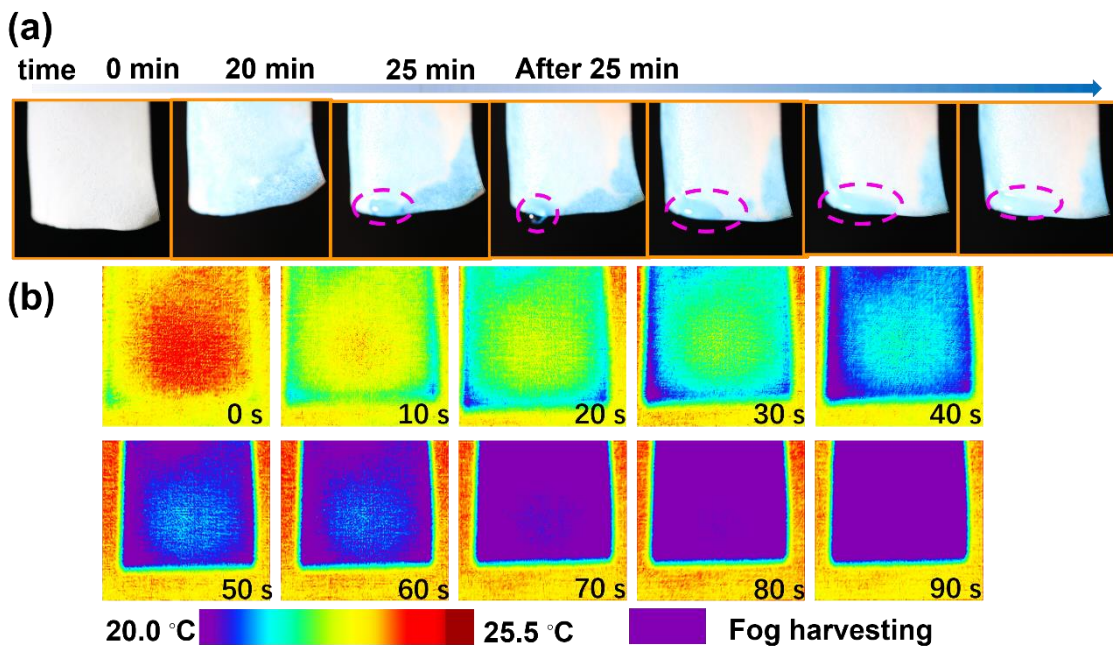


Fig. 2-14. (a) Fog-harvesting system at different time points; (b) thermal infrared images of the C_{0.5-40}.

Fig. 2-15(a) summarizes the water-collection rate of the filter paper, membranes, and composites. Even under the same humidification condition, the efficiency is different. Although the filter paper is a hydrophilic material, it is not very effective in collecting droplets. After the filter paper was saturated with water, a water film would also form on the surface, and it hindered further continuous collection of water. Even though the PU membrane is hydrophobic, there were condensed water droplets on the surface after a certain period of humidification, so the mass still increased. However, as long as the water-collection rate of the corresponding composite material increased greatly compared to the filter paper and PU membranes, it proves that the composite materials can improve the efficiency of water collection. It was observed that C_{0.5-40} and C₁₋₄₀ have higher water-collection efficiencies than C_{0.5-60} and C₁₋₆₀. The reason is that the meshes of C_{0.5-40} and C₁₋₄₀ are larger, which temporarily favors the deposition and collection of a larger volume of coalesced water, which then increases in size into a bigger droplet to drip off. The results indicate that the heterogeneity structure in layers has an effect on the efficiency of water collection. [51] When the surface of the filter paper kept collecting water, the collected water could be transported to the hydrophobic layer in time, so that the entire composite material was not easily saturated and could continue to collect water.

Fig. 2-15(b) shows how the C_{0.5-40} and the collected water look after 1 h of water collection. Notably, the water-collection performance of the composite membrane materials in this work was 1018.6 mg cm⁻² h⁻¹, superior to most existing 2D flat materials (**Fig. 2-15(c)** and **Table 2-1**). [13, 23, 32, 36, 52-55]

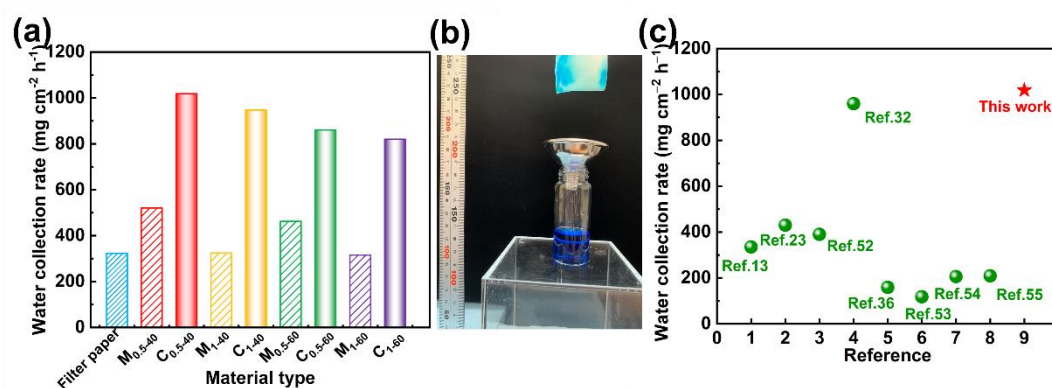


Fig. 2-15. (a) water-collection rates of different samples; (b) photo of the fog-collected in 1 h; and (c) comparison of the fog-harvesting performance of different 2D flat materials.

Table 2-1. Comparison of fog harvesting performance of different materials.

No.	Fabricated materials	Fog harvesting rate(mg·cm ⁻² ·h ⁻¹)	Ref.
1	Fluorinated PAN nanofiber.	~335	13
2	A superhydrophobic bulgy surface with superhydrophobic bulges on it.	~430	23
3	A thinner fiber created by electrospun CA on a thicker fiber of Nylon mesh.	~390	24
4	Superhydrophilic cotton absorbent and hydrophobic copper mesh.	~960	25
5	A (super)hydrophobically modified metal-based gauze onto the surface of a hydrophilic polystyrene (PS) flat sheet.	~159	26
6	PVDF-HFP electrospun nanomat impregnated with Krytox-1506 oil.	~118	45
7	Carbon fiber cloth with periodic superhydrophobic-hydrophilic patterns.	~206	46
8	Incorporate electrospun polyvinylidene fluoride (PVDF) fibers with commercial Raschel mesh.	~209	47
9	Polyurethane (PU) nanofiber mesh membrane and hydrophilic filter paper, adhered by PAM.	~1018.6	This work

2.3.7 Water-Harvesting Behavior

Fig. 2-16 describes the contemplated main water-harvesting steps and mechanism of the C_{0.5-40}. The first step is that micrometer water droplets were captured by the surface of the hydrophilic filter paper and condensed into a water film. The second step was to transfer the excess water through the PAM to the hydrophobic PU membrane. In the third step, micro water droplets coalesced on the hydrophobic membrane to form larger water

droplets that could drip and be-collected.

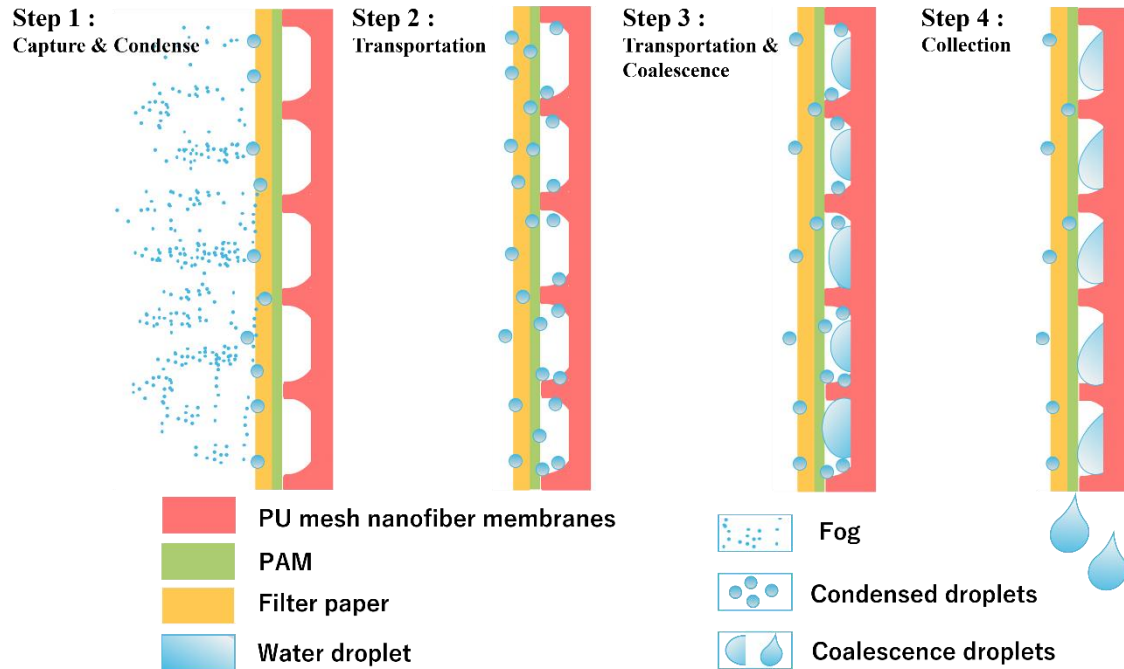


Fig. 2-16. Fog-harvesting steps of fog collection.

In order to verify the behavior of the water droplets on the PU membrane in the $C_{0.5-40}$, the whole process was recorded. As shown in **Fig. 2-17**, tiny water droplets appeared and were deposited on the mesh-like membrane. The water droplets gradually become larger and merged with the surrounding water droplets and moved, but they could still be retained temporarily on the recess of the membrane. As the water droplets continued to be transported and become larger, the temporarily deposited water droplets would reach a critical size and they could be-collected. The behavior of the water droplets on the mesh-like PU membrane can corroborate the above-expected water-collecting behavior of the water-harvesting material.

The fabricated water-harvesting material has a mesh-like hierarchical structure composed of coarse fibers and fine fibers, accompanied by both hydrophilicity and hydrophobicity, which successfully mimicked the water-collecting characteristics of

fungi. Accompanied by different sizes and densities of meshes, water-collection behaviors are different, leading to the composite material faster at transporting temporarily collected water. In addition to the asymmetric wettability of the hydrophilicity and hydrophobicity Janus materials benefit to water collection, the mesh-like hierarchical structure of this material also promotes the harvesting of water.

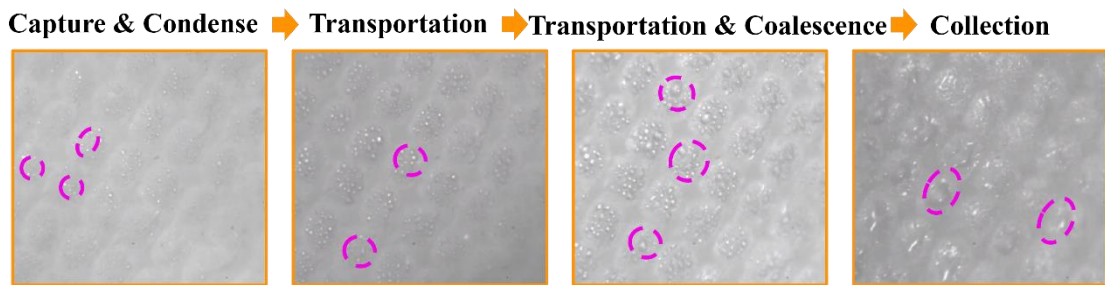


Fig. 2-17. Fog-collection mechanism.

2.4 Conclusion

Since fungi have the capacity to collect water from air, the main purpose of this study was to develop newly bioinspired water-harvesting materials that mimic water-collecting fungi. Several fungi, such as *Rhizopus delemar* and *Mucor hiemalis f. hiemalis* were cultivated over 1 week, and their morphologies were observed and analyzed. The results indicated that *Rhizopus delemar* could effectively collect water probably related to its uneven diameter of mycelia, as well as its hierarchical structure. Moreover, the heterogeneous mycelia were found to be both hydrophobic and hydrophilic.

Based on the structure and features of the fungi, several kinds of composite materials were fabricated using hydrophobic PU nanofiber membranes as mesh structures with different densities, with a hydrophilic filter paper layer pasted on its surface. Four kinds of PU nanofiber membranes were electrospun on the stainless mesh, by varying the flow rate and the density of the mesh. The results of the PU nanofiber membranes showed that, from a broad perspective, a hierarchical structure with a mesh-like structure was formed.

Meanwhile, coarse and fine PU nanofibers coexisted, which was similar to the mycelia. The SEM, WCA, and water-collection experiments proved that the composite material manufactured was able to collect droplets from fog. Hydrophilic–hydrophobic amphiphilic nanomaterials with thick and thin fibers that coexist have better water-collection performance than mesh membranes and filter paper. The hydrophilic filter paper on the surface performs well in capturing the water droplets in the air and making them coalesce, and then the mesh membrane with a mesh-like structure can transport the collected water. Composite materials with a lower mesh density collected a greater mass of water as a result of the puddles between the convexities being larger than the higher mesh density, which benefited the efficiency of the coalesce and collection of water, resulting in a water-collection efficiency as high as $1018.6 \text{ mg cm}^{-2} \text{ h}^{-1}$ in this work, which is more efficient than some membrane-like materials used in other research studies. In this study, an investigated bioinspired fog-harvesting material that can be applied to address serious contemporary water shortages in dry and underdeveloped areas of the globe was fabricated. Furthermore, the fabrication method is facile, has a low production cost, and efficient production, all of which ensure the possibility of good outcomes in practical applications.

Reference

- [1] Vörösmarty, C. J.; Green, P.; Salisbury, J.; Lammers, R. B. Global Water Resources: Vulnerability from Climate Change and Population Growth. *Science* 2000, 289 (5477), 284–288. <https://doi.org/10.1126/science.289.5477.284>.
- [2] Mekonnen, M. M.; Hoekstra, A. Y. Four Billion People Facing Severe Water Scarcity. *Sci. Adv.* 2016, 2 (2), e1500323. <https://doi.org/10.1126/sciadv.1500323>.
- [3] Rosegrant, M. W.; Cai, X.; Cline, S. A. *World Water and Food to 2025: Dealing with Scarcity*; International Food Policy Research Institute: Washington, DC, 2002.

- [4] Wang, X.; Liu, Q.; Wu, S.; Xu, B.; Xu, H. Multilayer Polypyrrole Nanosheets with Self-Organized Surface Structures for Flexible and Efficient Solar–Thermal Energy Conversion. *Adv. Mater.* 2019, 31 (19), 1807716. <https://doi.org/10.1002/adma.201807716>.
- [5] Fessehaye, M.; Abdul-Wahab, S. A.; Savage, M. J.; Kohler, T.; Gherezghiher, T.; Hurni, H. Fog-Water Collection for Community Use. *Renewable and Sustainable Energy Reviews* 2014, 29, 52–62. <https://doi.org/10.1016/j.rser.2013.08.063>.
- [6] Ju, J.; Bai, H.; Zheng, Y.; Zhao, T.; Fang, R.; Jiang, L. A Multi-Structural and Multi-Functional Integrated Fog Collection System in Cactus. *Nat Commun* 2012, 3 (1), 1247. <https://doi.org/10.1038/ncomms2253>.
- [7] Wang, B.; Zhou, X.; Guo, Z.; Liu, W. Recent Advances in Atmosphere Water Harvesting: Design Principle, Materials, Devices, and Applications. *Nano Today* 2021, 40, 101283. <https://doi.org/10.1016/j.nantod.2021.101283>.
- [8] Gad, H. E.; Hamed, A. M.; El-Sharkawy, I. I. Application of a Solar Desiccant/Collector System for Water Recovery from Atmospheric Air. *Renewable Energy* 2001, 22 (4), 541–556. [https://doi.org/10.1016/S0960-1481\(00\)00112-9](https://doi.org/10.1016/S0960-1481(00)00112-9).
- [9] Li, J.; Li, J.; Sun, J.; Feng, S.; Wang, Z. Biological and Engineered Topological Droplet Rectifiers. *Adv. Mater.* 2019, 31 (14), 1806501. <https://doi.org/10.1002/adma.201806501>.
- [10] Chen, G.; Wang, Y.; Qiu, J.; Cao, J.; Zou, Y.; Wang, S.; Jia, D.; Zhou, Y. A Facile Bioinspired Strategy for Accelerating Water Collection Enabled by Passive Radiative Cooling and Wettability Engineering. *Materials & Design* 2021, 206, 109829. <https://doi.org/10.1016/j.matdes.2021.109829>.
- [11] Zhang, Y.; Cai, Y.; Shi, J.; Morikawa, H.; Zhu, C. Multi-Bioinspired Hierarchical Janus Membrane for Fog Harvesting and Solar-Driven Seawater Desalination. *Desalination* 2022, 540, 115975. <https://doi.org/10.1016/j.desal.2022.115975>.
- [12] Zhu, H.; Guo, Z.; Liu, W. Biomimetic Water-Collecting Materials Inspired by Nature. *Chem. Commun.* 2016, 52 (20), 3863–3879. <https://doi.org/10.1039/C5CC09867J>.
- [13] Almasian, A.; Chizari Fard, Gh.; Mirjalili, M.; Parvinzadeh Gashti, M. Fluorinated-PAN Nanofibers: Preparation, Optimization, Characterization and Fog Harvesting Property. *Journal of Industrial and Engineering Chemistry* 2018, 62, 146–155. <https://doi.org/10.1016/j.jiec.2017.12.052>.

- [14] Xu, C.; Feng, R.; Song, F.; Wang, X.-L.; Wang, Y.-Z. Desert Beetle-Inspired Superhydrophilic/Superhydrophobic Patterned Cellulose Film with Efficient Water Collection and Antibacterial Performance. *ACS Sustainable Chem. Eng.* 2018, 6 (11), 14679–14684. <https://doi.org/10.1021/acssuschemeng.8b03247>.
- [15] Li, C.; Liu, Y.; Gao, C.; Li, X.; Xing, Y.; Zheng, Y. Fog Harvesting of a Bioinspired Nanocone-Decorated 3D Fiber Network. *ACS Appl. Mater. Interfaces* 2019, 11 (4), 4507–4513. <https://doi.org/10.1021/acsami.8b15901>.
- [16] He, X.-H.; Wang, W.; Liu, Y.-M.; Jiang, M.-Y.; Wu, F.; Deng, K.; Liu, Z.; Ju, X.-J.; Xie, R.; Chu, L.-Y. Microfluidic Fabrication of Bio-Inspired Microfibers with Controllable Magnetic Spindle-Knots for 3D Assembly and Water Collection. *ACS Appl. Mater. Interfaces* 2015, 7 (31), 17471–17481. <https://doi.org/10.1021/acsami.5b05075>.
- [17] Venkatesan, H.; Chen, J.; Liu, H.; Liu, W.; Hu, J. A Spider-Capture-Silk-Like Fiber with Extremely High-Volume Directional Water Collection. *Adv. Funct. Mater.* 2020, 30 (30), 2002437. <https://doi.org/10.1002/adfm.202002437>.
- [18] Marjanović, Ž.; Nehls, U. Ectomycorrhiza and Water Transport. In *Mycorrhiza*; Varma, A., Ed.; Springer Berlin Heidelberg: Berlin, Heidelberg, 2008; pp 149–159. https://doi.org/10.1007/978-3-540-78826-3_8.
- [19] Alexopoulos, C. J.; Mims, C. W.; Blackwell, M. *Introductory Mycology*, 4th ed.; Wiley: New York, 1996.
- [20] Xu, H.; Zwiazek, J. J. Fungal Aquaporins in Ectomycorrhizal Root Water Transport. *Front. Plant Sci.* 2020, 11, 302. <https://doi.org/10.3389/fpls.2020.00302>.
- [21] Huang, Z.-X.; Liu, X.; Wu, J.; Wong, S.-C.; Qu, J.-P. Electrospinning Water Harvesters Inspired by Spider Silk and Beetle. *Materials Letters* 2018, 211, 28–31. <https://doi.org/10.1016/j.matlet.2017.09.072>.
- [22] Feng, R.; Song, F.; Xu, C.; Wang, X.-L.; Wang, Y.-Z. A Quadruple-Biomimetic Surface for Spontaneous and Efficient Fog Harvesting. *Chemical Engineering Journal* 2021, 422, 130119. <https://doi.org/10.1016/j.cej.2021.130119>.
- [23] Zhong, L.; Zhu, H.; Wu, Y.; Guo, Z. Understanding How Surface Chemistry and Topography

Enhance Fog Harvesting Based on the Superwetting Surface with Patterned Hemispherical Bulges. *Journal of Colloid and Interface Science* 2018, 525, 234–242. <https://doi.org/10.1016/j.jcis.2018.04.061>.

[24] Shi, Y.-C.; Pan, T.-M. Beneficial Effects of *Monascus Purpureus* NTU 568-Fermented Products: A Review. *Appl Microbiol Biotechnol* 2011, 90 (4), 1207–1217. <https://doi.org/10.1007/s00253-011-3202-x>.

[25] Zhang, M.; Wang, C.; Wang, S.; Shi, Y.; Li, J. Fabrication of Coral-like Superhydrophobic Coating on Filter Paper for Water–Oil Separation. *Applied Surface Science* 2012, 261, 764–769. <https://doi.org/10.1016/j.apsusc.2012.08.097>.

[26] Kong, L.; Wang, Q.; Xiong, S.; Wang, Y. Turning Low-Cost Filter Papers to Highly Efficient Membranes for Oil/Water Separation by Atomic-Layer-Deposition-Enabled Hydrophobization. *Ind. Eng. Chem. Res.* 2014, 53 (42), 16516–16522. <https://doi.org/10.1021/ie502864u>.

[27] Fan, J.-B.; Song, Y.; Wang, S.; Meng, J.; Yang, G.; Guo, X.; Feng, L.; Jiang, L. Directly Coating Hydrogel on Filter Paper for Effective Oil-Water Separation in Highly Acidic, Alkaline, and Salty Environment. *Adv. Funct. Mater.* 2015, 25 (33), 5368–5375. <https://doi.org/10.1002/adfm.201501066>.

[28] d'Halluin, M.; Rull-Barrull, J.; Bretel, G.; Labrugère, C.; Le Grogneq, E.; Felpin, F.-X. Chemically Modified Cellulose Filter Paper for Heavy Metal Remediation in Water. *ACS Sustainable Chem. Eng.* 2017, 5 (2), 1965–1973. <https://doi.org/10.1021/acssuschemeng.6b02768>.

[29] Cheng, M.; Huang, L.; Wang, Y.; Zhao, Y.; Tang, J.; Wang, Y.; Zhang, Y.; Hedayati, M.; Kipper, M. J.; Wickramasinghe, S. R. Synthesis of Graphene Oxide/Polyacrylamide Composite Membranes for Organic Dyes/Water Separation in Water Purification. *J Mater Sci* 2019, 54 (1), 252–264. <https://doi.org/10.1007/s10853-018-2828-9>.

[30] Feng, W.; Gao, J.; Cen, R.; Yang, F.; He, Z.; Wu, J.; Miao, Q.; Liao, H. Effects of Polyacrylamide-Based Super Absorbent Polymer and Corn Straw Biochar on the Arid and Semi-Arid Salinized Soil. *Agriculture* 2020, 10 (11), 519. <https://doi.org/10.3390/agriculture10110519>.

[31] Ito, F.; Komatsubara, S.; Shigezawa, N.; Morikawa, H.; Murakami, Y.; Yoshino, K.; Yamanaka, S. Mechanics of Water Collection in Plants via Morphology Change of Conical Hairs. *Appl. Phys. Lett.* 2015, 106 (13), 133701. <https://doi.org/10.1063/1.4916213>.

- [32] Cao, M.; Xiao, J.; Yu, C.; Li, K.; Jiang, L. Hydrophobic/Hydrophilic Cooperative Janus System for Enhancement of Fog Collection. *Small* 2015, 11 (34), 4379–4384. <https://doi.org/10.1002/sml.201500647>.
- [33] Appels, F. V. W.; Camere, S.; Montalti, M.; Karana, E.; Jansen, K. M. B.; Dijksterhuis, J.; Krijgsheld, P.; Wösten, H. A. B. Fabrication Factors Influencing Mechanical, Moisture- and Water-Related Properties of Mycelium-Based Composites. *Materials & Design* 2019, 161, 64–71. <https://doi.org/10.1016/j.matdes.2018.11.027>.
- [34] Islam, M. R.; Tudryn, G.; Bucinell, R.; Schadler, L.; Picu, R. C. Morphology and Mechanics of Fungal Mycelium. *Sci Rep* 2017, 7 (1), 13070. <https://doi.org/10.1038/s41598-017-13295-2>.
- [35] Heaton, L.; Obara, B.; Grau, V.; Jones, N.; Nakagaki, T.; Boddy, L.; Fricker, M. D. Analysis of Fungal Networks. *Fungal Biology Reviews* 2012, 26 (1), 12–29. <https://doi.org/10.1016/j.fbr.2012.02.001>.
- [36] Wang, Y.; Zhang, L.; Wu, J.; Hedhili, M. N.; Wang, P. A Facile Strategy for the Fabrication of a Bioinspired Hydrophilic–Superhydrophobic Patterned Surface for Highly Efficient Fog-Harvesting. *J. Mater. Chem. A* 2015, 3 (37), 18963–18969. <https://doi.org/10.1039/C5TA04930J>.
- [37] Zhu, P.; Chen, R.; Zhou, C.; Tian, Y.; Wang, L. Asymmetric Fibers for Efficient Fog Harvesting. *Chemical Engineering Journal* 2021, 415, 128944. <https://doi.org/10.1016/j.cej.2021.128944>.
- [38] Havlíček, K.; Svobodová, L.; Bakalova, T.; Lederer, T. Influence of Electrospinning Methods on Characteristics of Polyvinyl Butyral and Polyurethane Nanofibres Essential for Biological Applications. *Materials & Design* 2020, 194, 108898. <https://doi.org/10.1016/j.matdes.2020.108898>.
- [39] Najafi, S. J.; Gharehaghaji, A. A.; Etrati, S. M. Fabrication and Characterization of Elastic Hollow Nanofibrous PU Yarn. *Materials & Design* 2016, 99, 328–334. <https://doi.org/10.1016/j.matdes.2016.02.111>.
- [40] Shrestha, B. K.; Shrestha, S.; Tiwari, A. P.; Kim, J.-I.; Ko, S. W.; Kim, H.-J.; Park, C. H.; Kim, C. S. Bio-Inspired Hybrid Scaffold of Zinc Oxide-Functionalized Multi-Wall Carbon Nanotubes Reinforced Polyurethane Nanofibers for Bone Tissue Engineering. *Materials & Design* 2017, 133, 69–81. <https://doi.org/10.1016/j.matdes.2017.07.049>.
- [41] Qi, L.; Ou, K.; Hou, Y.; Yuan, P.; Yu, W.; Li, X.; Wang, B.; He, J.; Cui, S.; Chen, X.

Unidirectional Water-Transport Antibacterial Trilayered Nanofiber-Based Wound Dressings Induced by Hydrophilic-Hydrophobic Gradient and Self-Pumping Effects. *Materials & Design* 2021, 201, 109461. <https://doi.org/10.1016/j.matdes.2021.109461>.

[42] Hongru, A.; Xiangqin, L.; Shuyan, S.; Ying, Z.; Tianqing, L. Measurement of Wenzel Roughness Factor by Laser Scanning Confocal Microscopy. *RSC Adv.* 2017, 7 (12), 7052–7059. <https://doi.org/10.1039/C6RA26897H>.

[43] Pang, Y.; Zhang, K.; Yang, Z.; Jiang, S.; Ju, Z.; Li, Y.; Wang, X.; Wang, D.; Jian, M.; Zhang, Y.; Liang, R.; Tian, H.; Yang, Y.; Ren, T.-L. Epidermis Microstructure Inspired Graphene Pressure Sensor with Random Distributed Spinosum for High Sensitivity and Large Linearity. *ACS Nano* 2018, 12 (3), 2346–2354. <https://doi.org/10.1021/acsnano.7b07613>.

[44] Wang, M.; Dong, L.; Wu, J.; Shi, J.; Gao, Q.; Zhu, C.; Morikawa, H. Leaf-Meridian Bio-Inspired Nanofibrous Electronics with Uniform Distributed Microgrid and 3D Multi-Level Structure for Wearable Applications. *npj Flex Electron* 2022, 6 (1), 34. <https://doi.org/10.1038/s41528-022-00171-x>.

[45] Xue, J.; Wu, T.; Dai, Y.; Xia, Y. Electrospinning and Electrospun Nanofibers: Methods, Materials, and Applications. *Chem. Rev.* 2019, 119 (8), 5298–5415. <https://doi.org/10.1021/acs.chemrev.8b00593>.

[46] Haider, A.; Haider, S.; Kang, I.-K. A Comprehensive Review Summarizing the Effect of Electrospinning Parameters and Potential Applications of Nanofibers in Biomedical and Biotechnology. *Arabian Journal of Chemistry* 2018, 11 (8), 1165–1188. <https://doi.org/10.1016/j.arabjc.2015.11.015>.

[47] Cramariuc, B.; Cramariuc, R.; Scarlet, R.; Manea, L. R.; Lupu, I. G.; Cramariuc, O. Fiber Diameter in Electrospinning Process. *Journal of Electrostatics* 2013, 71 (3), 189–198. <https://doi.org/10.1016/j.elstat.2012.12.018>.

[48] Wang, J.; Wong, J. X. H.; Kwok, H.; Li, X.; Yu, H.-Z. Facile Preparation of Nanostructured, Superhydrophobic Filter Paper for Efficient Water/Oil Separation. *PLoS ONE* 2016, 11 (3), e0151439. <https://doi.org/10.1371/journal.pone.0151439>.

[49] Liu, Z.; Yu, J.; Lin, W.; Yang, W.; Li, R.; Chen, H.; Zhang, X. Facile Method for the Hydrophobic

Modification of Filter Paper for Applications in Water-Oil Separation. *Surface and Coatings Technology* 2018, 352, 313–319. <https://doi.org/10.1016/j.surfcoat.2018.08.026>.

[50] Zhao, X.-Q.; Wahid, F.; Cui, J.-X.; Wang, Y.-Y.; Zhong, C. Cellulose-Based Special Wetting Materials for Oil/Water Separation: A Review. *International Journal of Biological Macromolecules* 2021, 185, 890–906. <https://doi.org/10.1016/j.ijbiomac.2021.06.167>.

[51] Zhang, Y.; Wang, T.; Wu, M.; Wei, W. Durable Superhydrophobic Surface with Hierarchical Microstructures for Efficient Water Collection. *Surface and Coatings Technology* 2021, 419, 127279. <https://doi.org/10.1016/j.surfcoat.2021.127279>.

[52] Shigezawa, N.; Ito, F.; Murakami, Y.; Yamanaka, S.; Morikawa, H. Development of Combination Textile of Thin and Thick Fiber for Fog Collection Bioinspired by *Burkheya Purpurea*. *The Journal of The Textile Institute* 2015, 1–8. <https://doi.org/10.1080/00405000.2015.1082740>.

[53] Lalia, B. S.; Anand, S.; Varanasi, K. K.; Hashaikeh, R. Fog-Harvesting Potential of Lubricant-Impregnated Electrospun Nanomats. *Langmuir* 2013, 29 (42), 13081–13088. <https://doi.org/10.1021/la403021q>.

[54] Chou, H.-T.; Chen, Y.-C.; Lee, C.-Y.; Chang, H.-Y.; Tai, N.-H. Biomimetic Structure of Carbon Fiber Cloth Grafted with Poly(N-Isopropylacrylamide) for Water Collection and Smart Gates. *RSC Adv.* 2017, 7 (72), 45799–45806. <https://doi.org/10.1039/C7RA05869A>.

[55] Knapczyk-Korczak, J.; Szewczyk, P. K.; Ura, D. P.; Bailey, R. J.; Bilotti, E.; Stachewicz, U. Improving Water Harvesting Efficiency of Fog Collectors with Electrospun Random and Aligned Polyvinylidene Fluoride (PVDF) Fibers. *Sustainable Materials and Technologies* 2020, 25, e00191. <https://doi.org/10.1016/j.susmat.2020.e00191>.

Chapter 3

Multi-bioinspired hierarchical Janus membrane for fog harvesting and solar- driven seawater desalination

Chapter 3: Multi-bioinspired hierarchical Janus membrane for fog harvesting and solar-driven seawater desalination

3.1 Introduction

Due to the impact of population growth, economic development and the COVID-19 outbreak, a large amount of clean water resources have been consumed, and the water crisis is getting worse year by year. How to alleviate the water crisis by means of energy conservation and environmental protection has also become the focus of people's attention [1], [2]. The sustainable development of clean water resources and the utilization of green energy are also the United Nations Sustainable Development Goals. The related research of water collection has become a hot spot of modern researchers [3], [4], [5], [6].

As we all know, the ocean occupies 71 % of the total surface area and accounts for more than 97 % of the total water on the earth [7]. Seawater desalination is one of the important methods to solve the current water crisis, mainly involving distillation-based mechanisms [8], [9], [10], [11]. In addition to the ocean, the air that accompanies us every day is also a large reservoir. The atmosphere contains about 12.7 cubic kilometers of water [12]. Even in deserts, which are often thought of as harsh environments, there is still more than 10 g m^{-3} of water in the atmosphere [13]. Therefore, in addition to desalination, harvesting water (moisture and fog) from the atmosphere is a promising way to solve the water crisis [14], [15]. Harvesting water from the air as a clean water resource is a feasible, sustainable, innovative and low-energy consuming technology [16]. Since 1976, when scientists discovered that insects in the Namib desert can extract water from fog, researchers have continued to investigate it further. In 2001, Parker and Lawrence elucidated how the beetle collects water from the fog to survive. The mechanism is that its back is a combination of hydrophilic bumps for capture droplets and the hydrophobic region for easy collected water drainage to the beetle's mouth [17], [18], [19].

Accompanied with theoretical researches of how animals and plants can use their own superior body structure and performance specially adapted to the surrounding environment to achieve fog-harvesting, the fabrications of bionic materials which can achieve good fog-harvesting effect emerge in an endless stream [20], [21], [22]. Inspired by the aforementioned insects in the desert, the hydrophilic-hydrophobic hybrid material surfaces with superior water concentration than either hydrophilic or hydrophobic surfaces. Fibrous network structures taken inspiration from spiders' webs meshes are also used for fog harvesting, as mesh-like structures can increase the Stokes' number of droplets flowing around the mesh which leads to more mesh-structured materials used for fog harvesting [23], [24]. Moreover, the multi-scale hierarchical functional materials formed by integrating micro/nano-scale structures onto the mesh-like macro-scale surface can improve the fog capture performance of the materials not only due to the surface wettability, but also the differences of Laplace pressure and surface free energy gradients [20], [21], [25], [26].

Fog harvesting mainly includes the initial capture of tiny droplets in the air, then the fusion of droplets, transportation and finally storage. In order to carry out material modification corresponding to these four steps to achieve higher fog harvesting efficiency, researchers no longer conduct bionics on a single creature, but combine different creatures as models to achieve considerable performance [27], [28], [29]. However, most of the current fog-harvesting materials can only be used for collecting fog alone in foggy environments or require additional energy to achieve a considerable water harvesting effect. The application of these materials is relatively sole. At present, few water collection materials are applied to implement on the ocean, where the moisture content of the air is also high. If the material can not only collect water in the air, but also be used for evaporating seawater and collecting purified water, it will be promising potential in addressing the water scarcity. Moreover, the production methods adopted, such as photolithography and inkjet printing [30], [31], are often time-consuming and complicated in preliminary design, and require multi-step delicate operations. The

technologies are often expensive, and it is difficult to control and adjust parameters, also the production scale is limited.

Electrospinning technology is a facile and scalable method to fabricate hierarchical structure nanofiber membranes. Polyurethane (PU) nanofiber membranes produced by electrospinning is an excellent base material which is frequently used for the fabrication of materials for water collection. Due to its hydrophobicity, excellent mechanical properties and porous air permeability, large specific surface area are often used as reinforced materials and high-performance filtering materials [32]. However, to make composite materials produced by some previous electrospinning technologies that can achieve hydrophilic or hydrophobic effects often need to add more polymers into the spinning solution, or some modification of the nanofiber membrane is often complicated or fails to achieve the expected biomimetic effect, while the more convenient and direct ultrasonication method can introduce other performance materials to the PU nanofiber.

Till now, to fabricate multiple biomimetic materials often have numerous and complex procedures and cannot be scaled up. At the same time, a large number of preliminary experiments are required, and many biomimetic researches also have not studied the mimicked objects. In this study, after the relevant culture and observation experiments were carried out on the cultured fungi, combining with the water-collective characteristics of spider webs, Namib desert beetles, termite wings, and emergent aquatic plants as inspiration, the mature, scalable electrospinning and ultrasonication technology were adopted which can easily and quickly achieve the hierarchical structure. A Janus membrane material with multi-bioinspired characteristics for fog harvesting and seawater desalination was successfully prepared. The mycelia of fungi are imitated by electrospinning, while change the receiving device to make PU membranes show a mesh-like structure to mimic spider webs. The irregular hydrophilic bumps of beetles provide references for the introduction of carbon nanospheres (CNSs), while the hair-like structure on termite wings and the pumping strategy of aquatic plants provide inspiration for the introduction of carbon nanotubes (CNTs).

The introduction of hydrophilic carbon nanotubes and carbon nanospheres on the surface of PU nanofiber mesh membrane not only achieve the biomimetic effect to improve the water collection performance contrast to the PU membrane, but also greatly improves the photothermal conversion of the original membrane. This novel hierarchical structure Janus membrane has excellent fog harvesting capacity and can reach $1666.2 \text{ mg cm}^{-2} \text{ h}^{-1}$ in foggy environment. It can also play the role of evaporation and purification in water sources such as the ocean. And it can effectively and rapidly generate solar steam with the evaporation rate of $1.05 \text{ kg m}^{-2} \text{ h}^{-1}$ under 1 sun.

This mechanism of Janus structure membrane material producing clean water under foggy or sunny conditions opens up new bionic ideas and new conceptions of material preparation and for water collecting materials that are suitable for more environments and occasions in the future.

3.2 Experimental section

3.2.1 Materials

Difco™ Potato Dextrose Agar (213400) was purchased from Becton, Dickinson and Company (Japan) for making culture medium. Ethanol (99.5), *N, N*-Dimethylformamide (DMF), multi-walled carbon nanotube (MWNT, 40-70 nm) (hydrophobic), and D(+)-Glucose, were provided by FUJIFILM Wako Pure Chemical Corporation (Japan). Polyurethane (PU, molecular weight $\sim 110,000 \text{ g mol}^{-1}$) was obtained from Sigma-Aldrich Co. LLC (USA). Fungi was supplied by the Biological Resource Center (NBRC), National Institute of Technology and Evaluation (Japan). The deionized water and distilled water were produced by WG250B, Yamato Scientific co., Ltd., (Japan). Stainless steel mesh (SUS304, 40 meshes/in.) was purchased from Q-ho Metal Works (Japan). Carboxylated MWNTs was supplied by XFNANO Materials Tech Co., Ltd. (China); it had a length of 0.5–2 μm and an average diameter of 10–20 nm (hydrophilic).

3.2.2 Fabrication of hydrophobic hierarchical mesh PU nanofiber membrane

PU pellets were put into DMF solution with a mass percentage of 20 wt% and dissolved at 60 °C under the action of magnetic stirrer to prepare the electrospinning solution. In order to construct the hierarchical macro-micro-nanoscale mesh structure, a stainless steel mesh was used as the receiving substrate during electrospinning, with the schematic diagram of the device shown in **Fig. 3-1(a)**. After several preliminary experiments and adjustment of relevant parameters, the voltage was kept at 15 kV, the needle was 15 cm set away from the receiving device substrate, and the solution feed rate was 0.5 ml h⁻¹. The entire electrospinning process was carried out in a general environment at temperature of 20 ± 2 °C and humidity of 60 ± 5 % RH. The electrospinning solution volume was 2 ml each time. After electrospinning, the whole receiving device (i.e., the mesh and the electrospun membrane on its surface) was removed and placed indoors for natural air drying for 24 h to remove residual solvents. Finally, the electrospun PU nanofiber membrane (PUM) was peeled off from the mesh for subsequent experiments. The cross-section SEM image of the mesh-like membrane is shown in **Fig. 3-1(b)**.

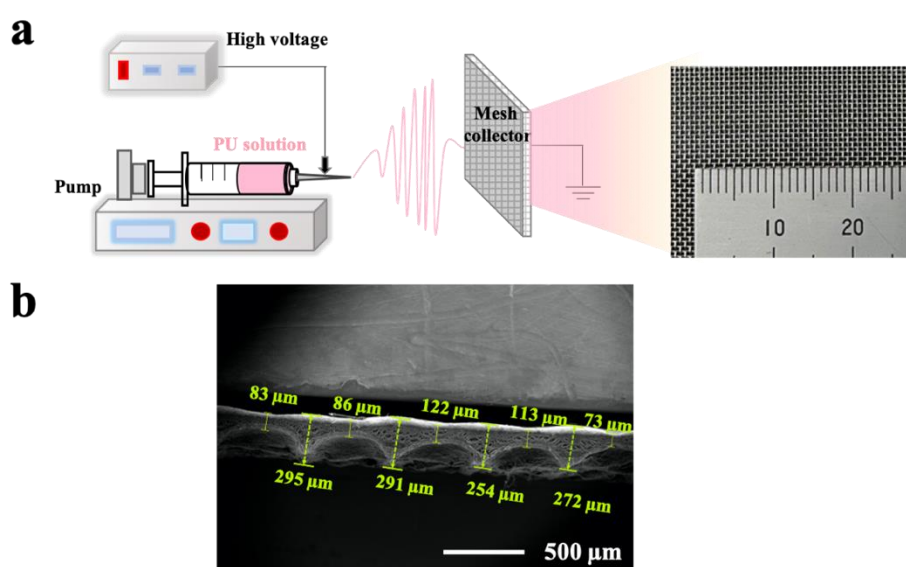


Fig. 3-1. (a) The schematic diagram of the electrospinning device. (b) The cross-section SEM image of the mesh-like membrane.

3.2.3 Fabrication of carbon nanospheres (CNSs)

Glucose was added into deionized water and dissolved by ultrasonic dispersion to produce a concentration of 0.3 mol L^{-1} glucose solution, which was then transferred to a reaction kettle with a filling degree of 40 %. Hydrothermal reaction was carried out at $190 \text{ }^\circ\text{C}$ for 4 h. After the reaction, the obtained product was repeatedly centrifuged and cleaned with 99.5 % ethanol, and finally dried into carbon hydrophilic nanospheres (HL-CNSs). Next, the HL-CNSs were calcinated in a tube furnace to $600 \text{ }^\circ\text{C}$ for 1 h at a heating rate of $2 \text{ }^\circ\text{C min}^{-1}$ under argon to destroy and eliminate the oxygen-containing groups on the surface of HL-CNSs and finally obtained the hydrophobic carbon nanospheres (HB-CNSs) [33].

3.2.4 Fabrication of different types of PU composite nanofiber membranes

0.1 g MWNTs were added into 100 ml ethanol and pure water with a volume ratio of 4:1 for ultrasonic dispersion (labeled as HB-CNTs dispersions). HL-CNTs dispersions, HB-CNSs dispersions, and HL-CNSs dispersions, were applied by the same steps. The same amount of HB-CNTs dispersion solution and HB-CNSs solution were mixed through ultrasonication to obtain the HB-CNTs/CNSs solution. The HL-CNTs/CNSs solution was prepared by the same procedure. Then the $4 \times 4 \text{ cm}^2$ PUm was immersed in the HB-CNTs dispersion solution for ultrasonication for 30 min. Finally, the membrane was taken out of the solution and repeatedly rinsed with deionized water. After being dried for 2 h in an oven at $40 \text{ }^\circ\text{C}$, the PU composite membrane coated with the HB-CNTs (labeled as HB-CNTs/PUm) was obtained, and then HL-CNTS/PUm, HL-CNSs/PUm, HB-CNSs /PUm, HL-CNTs/CNSs/PUm and HB-CNTs/CNSs/PUm were obtained by the

same ultrasonication as mentioned above.

3.2.5 Culture and observation of fungi

Potato Dextrose Agar powder in a quantity of 11.7 g and 300 ml of distilled water was stirred in a cone glass bottle, then sterilized at 120 °C for 1.5 h, and naturally cooled to 60 °C to pour into a petri dish for cultivation under an ultraviolet sterilization condition, and wrapped before placing at 2 °C for 24 h as a culture medium for fungi cultivation. Thawed fungi strains were transplanted on the culture medium. After the transplantation, fungi grew naturally in a temperature incubator at 28 °C for 1 week for the observation. Morphologies of cultivated fungi is shown in **Fig. 3-2**.

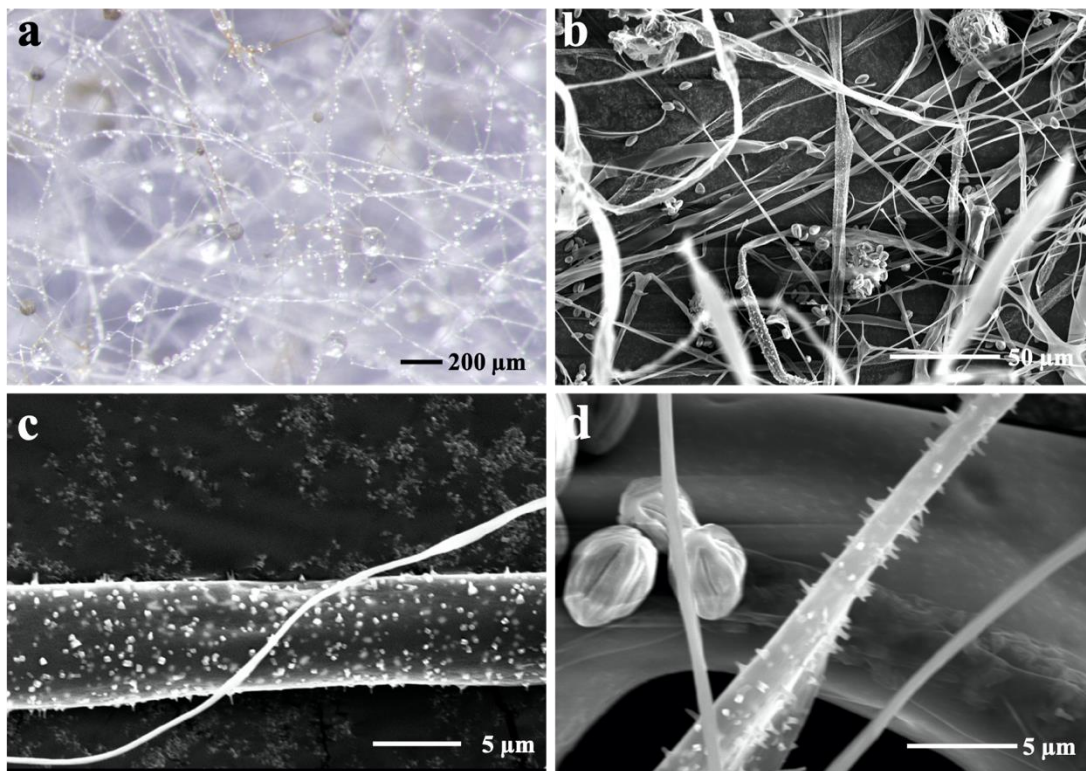


Fig. 3-2. (a) Stereomicroscopic images of fungi. (b) SEM images of fungi at low magnification. (c) and (d) are SEM images of different parts of fungi at different high magnifications.

3.2.6 Characterization

Morphological investigation, element composition and distribution of the samples were analyzed by using a scanning electron microscope with energy-dispersive X-ray spectroscopy (SEM, JSM-6010LA, JEOL Ltd., Japan) at 10 kV. Morphology observation at larger magnifications was observed using field emission scanning electron microscope (FE-SEM, S-5000, Hitachi High-Tech Corporation, Japan) at 20 kV. The microstructure images of the prepared materials were taken using transmission electron microscopy (TEM, JEM-2010, JEOL Ltd., Japan). Before the SEM and FE-SEM observation, a layer of gold was sputtered onto samples' surface to prevent the accumulation of electrons by auto fine coater (JFC-1600, JEOL Ltd., Japan). 3D topographical images were determined by laser scanning confocal microscopy (LSCM, OLS3000MS, OLYMPUS CORPORATION, Japan). Attenuated total reflectance Fourier transform infrared (ATR-FTIR) spectra were recorded by using Fourier Transform Infrared Spectrophotometer (FT/IR-6600•IRT-5200, JASCO Corporation, Japan). Contact angles were measured ten times on the different points of each sample by an automatic contact angle meter (DMs-400, Kyowa Interface Science Co., Ltd., Japan) at room temperature 20 ± 2 °C with a 1 μ L droplet every time. The change of temperature and temperature infrared images were recorded and analyzed by a FLIR thermal imaging camera and FLIR Tools application. The metal ions' concentrations in seawater and distilled water were determined with the help of ICP emission spectroscopic analyzer (SPS3100, Hitachi High-Tech Science Corporation, Japan). The fog-harvesting process video was taken by using an industrial camera system (PL3-05, Shinano Kenshi Co., Ltd., Japan).

3.2.7 Water harvesting performance measurements

The sample was fixed on the homemade shelf with the inclined angle of 90° in a plastic container. The temperature and relative humidity were 20 ± 2 °C and $75 \pm 5\%$ RH respectively. The humidifier (HTJS-007J-WH, MODERN DECO Co., Ltd., Japan) provided a fog flow was placed 5 cm away from the tested sample. The whole fog-harvesting device was placed on the electronic balance (GR-200, A&D Company, Japan) and the real-time fog-harvesting mass (m_{ht}) were recorded. Mass of harvested fog per unit area (mg) and fog-harvesting efficiency (η_h) were obtained by calculation through the following equations (eqs 1 and 2), respectively:

$$\Delta m_h = \frac{m_{ht} - m_{h0}}{S} \quad (1)$$

$$\eta_h = \frac{\Delta m_h}{t} \quad (2)$$

where m_h refers to the mass of composite membrane including harvested water (mg), m_{h0} is the mass of composite material before fog-harvesting (mg). S is surface area of the sample (4×4 cm²), and t is the water harvesting time (h).

3.2.8 Preparation of the Janus membrane solar evaporation device and performance measurements

In order to make the fabricated membrane better show the performance of evaporation, we adopted an effective and proper evaporation system[34]. The fabricated membrane was taken as solar absorber, the polystyrene foam was applied as the thermal insulation and water-trapped layer, the cotton layer can supply the water continuously. The whole device was applied for the following solar evaporation.

At 1 sun simulated by the solar simulator (XES-40S3-TT, SAN-EI Electric, Japan) the solar water evaporation and purification experiment was performed. The real-time interfacial solar evaporation with mass and temperature changes were recorded by the

GR-200 electronic balance and a FLIR thermal imaging camera. The water evaporation mass change per unit Δm_e and evaporation rate η_e can be calculated by the following equations (eqs 3 and 4):

$$\Delta m_e = \frac{m_{et} - m_{e0}}{S} \quad (3)$$

$$\eta_e = \frac{\Delta m_e}{t} \quad (4)$$

where m_{et} refers to the mass of the whole evaporation device recorded in real time (kg), m_{e0} is the mass of whole evaporation device before evaporation (kg). S is surface area of the sample, and t is the solar evaporation time (h). In order to be suitable for the evaporation device, the membrane was cut into a circle shape with a radius of 2.75 cm. The evaporation experiments of ordinary domestic water and natural seawater were carried out both with and without solar irradiation.

3.3 Results and discussion

3.3.1 Design and preparation of membranes

Currently, many biomimetic materials are based on the inspiration from a certain creature and there are few designs that combine different creature's features together to promote the fog harvesting. Therefore, a unique design approach has been suggested inspired by the cultivated mycelia of fungi, spider webs, Namib desert beetles, termite wings, and emergent aquatic plants (see **Fig. 3-3**), and a fog-harvesting and solar driven water purification Janus membrane materials were successfully prepared. Mycelia of fungi like the fibrous network are mimicked by electrospinning, then the mesh-like PU membrane shows a structure like spider webs. The introduction of CNSs mimicked the hydrophilic bumps of desert beetles. The microtrichia on termite wings and the pumping strategy of aquatic plants provide inspiration for the introduction of CNTs. There have been few reports on the structure of mimicking fungi, but according to the observation of

the cultured fungi (**Fig. 3-2** mentioned before) and some relevant prior studies [35], [36], the mycelia of fungi show fibrous network. It also can be speculated that the mycelia structure of fungi can effectively deposit water droplets.

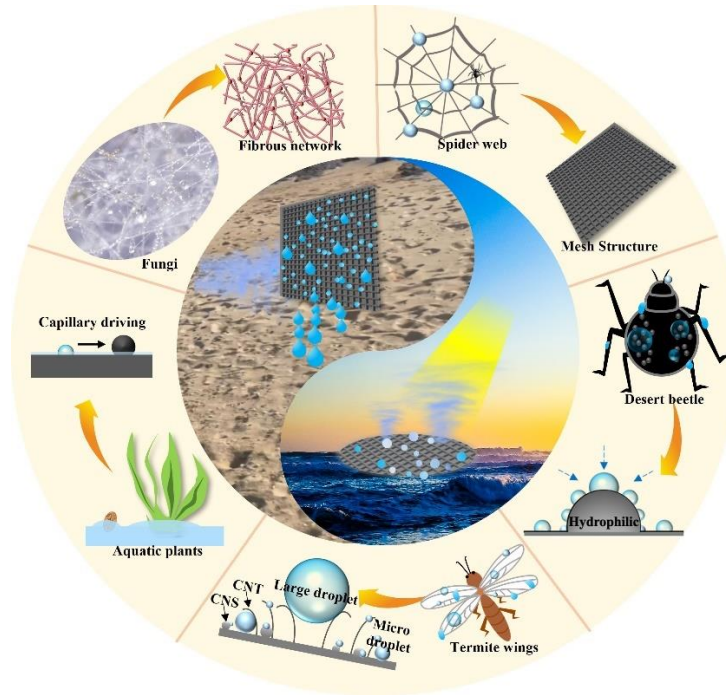


Fig. 3-3. A multi-bioinspired water harvesting system. Characteristics of spider web, desert beetle, termite wings, aquatic plants and fungi are integrated onto mesh-like Janus nanofiber membrane for synergistical optimization for water harvesting.

Fig. 3-4 is the schematic demonstration for the fabrication of different hierarchical nanofiber Janus membranes. The CNTs, or CNSs, or CNTs/CNSs were anchored onto the PU mesh nanofiber surface with the assistance of the ultrasonication. The carbon nanomaterials in the suspension were rapidly pushed towards the nanofibers in an instant under the action of ultrasound and interfacial collisions occurred between carbon nanomaterials and nanofiber surfaces during the process of induced modification of nanofibers by ultrasonication. Due to the collisions, the impacted parts of the PU nanofiber instantly softened or partially melted [37], [38], allowing the carbon nanomaterial to be anchored on the nanofiber. At the same time, the entire membrane

material can still maintain the structural integrity. The original PUM appeared white, but after CNTs and CNSs were introduced into the film surface, the entire material appeared black. On the other hand, before ultrasonic treatment, the surface of PU nanofibers was very smooth, while after ultrasonic treatment, a micro-nanoscale hierarchical structure was formed on the surface of nanofibers. The resulting PU composite membrane can maintain the softness and porous air permeability of the original nanofibers.



Fig. 3-4. Schematic demonstration for the preparation of PU composite membranes.

3.3.2 Structure characterizations and morphology of the membranes

The microscopic morphology of several membrane materials is shown in **Fig. 3-5**, **3-6**. As shown in **Fig. 3-5**, and **Fig. 3-1(b)**, membranes with clear mesh-like structure can be seen. Further in the SEM images (**Fig. 3-6**) even after ultrasonic treatment, the mesh-like structure of each membrane was still retained, proving that the fabricated carbon nanomaterials PU composite membranes can still maintain a mesh-like structure in terms of macroscopic structure. The surface of the PU nanofibers obtained by electrospinning was smooth as shown in **Fig. 3-7**. Through observing the microstructure of the PU composite membrane, it can be found that different carbon nanomaterials were anchored to the surface of the nanofibers (**Fig. 3-8**). The corresponding FE-SEM images of a larger magnification are inserted. Aggregation and dispersion varied depending on the nature of

the carbon nanomaterials, and the introduction and addition of these carbon nanomaterials constructed a hierarchical microstructure with secondary nanostructure. The formed hierarchical microstructure improved the surface roughness and specific surface area of the nanofibers. The TEM images (**Fig. 3-9 (a, b)**) further confirmed that both the carbon nanomaterials and PU nanofibers maintained their original appearance after ultrasonication, the part in the red circle was CNSs, and the surface of the PU nanofibers was also anchored with carbon nanotubes. **Fig. 3-9 (c)** is a stereomicroscopic image of fungi, the parts marked in red are spores. Besides, the mycelia are also thick and thin, and there are water droplets on both the spores and the mycelia. According to these pictures, the morphology of composite materials was consistent with the characteristics of predicted biomimetic objects. The CNSs bumps on the PU nanofibers are similar to the circular bumps on the back of the beetle in the desert, while the CNTs are like the microtrichia on the wings of the termite and emergent aquatic plants construction. Being viewed on a larger scale, the entire Janus composite material is also similar to a fibrous network structure with a mesh-like structure that mimics fungi mycelia networks and spider webs. The introduction of different carbon nanomaterials will affect the surface morphology, surface chemical properties and surface wettability of the composite membrane materials. The detailed wettability and chemical characteristics of the composite nanofiber membranes will be discussed in the following sections.

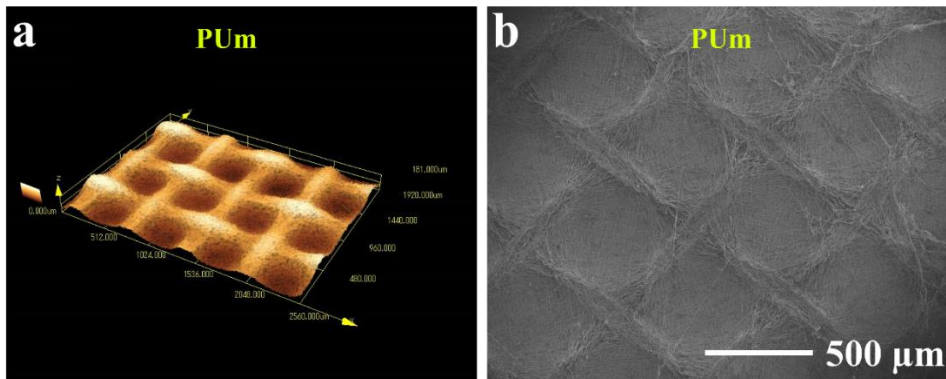


Fig. 3-5. (a) LSCM image of PUm. (b, c) SEM images of PUm.

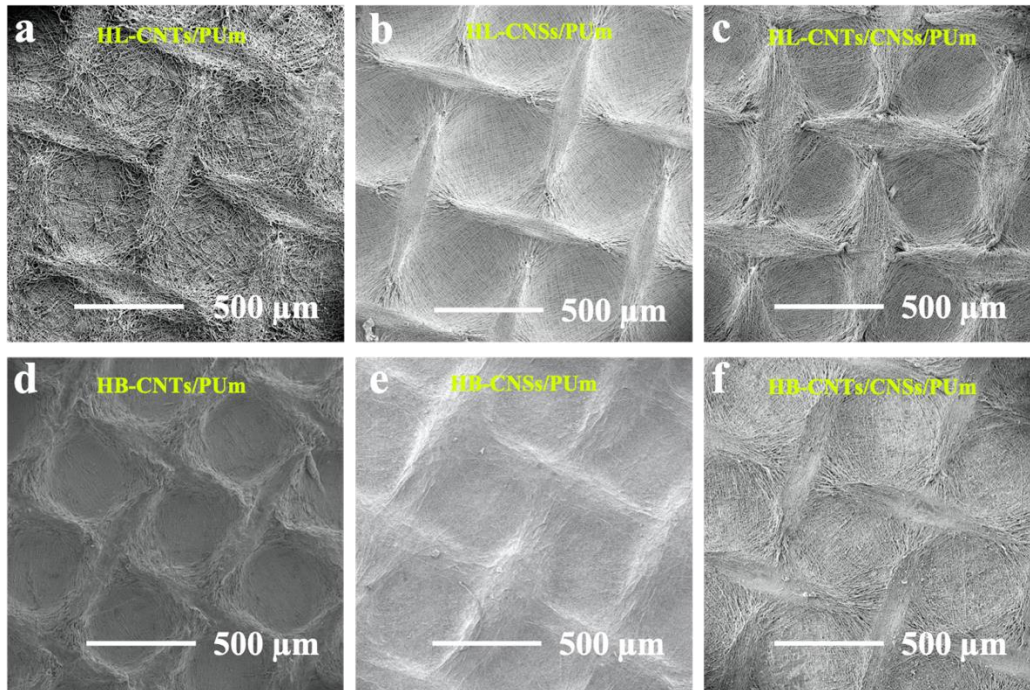


Fig. 3-6. SEM images showing same mesh-like structure of different membranes.

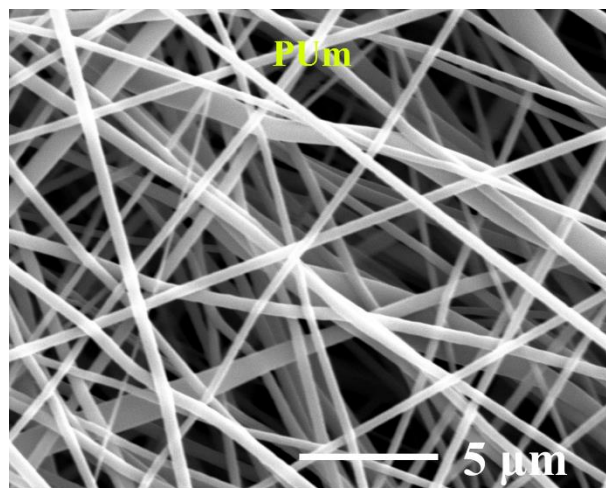


Fig. 3-7. SEM images of PUm.

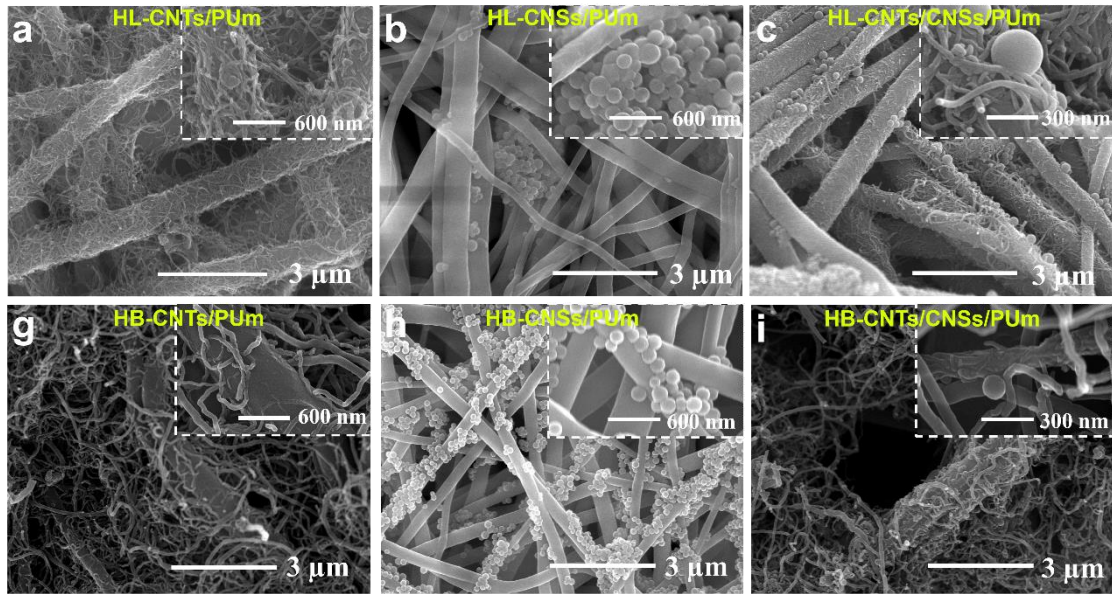


Fig. 3-8. FE-SEM images of different membranes. The insert images are the corresponding FE-SEM images at large magnifications.

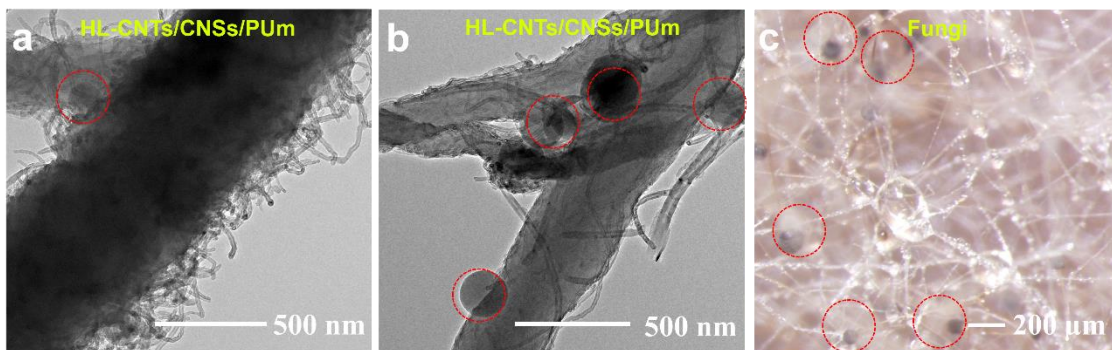


Fig. 3-9. (a, b) TEM images shown the distribution of different carbon nanomaterials on different parts of nanofibers of HL-CNTs/CNSs/PUm. (c) Stereomicroscopic image of water-collective fungi.

3.3.3 Chemical composition and surface wettability of membranes

In addition to the surface microstructure, the surface chemical composition of the nanofiber membrane also affects the surface wettability. **Fig. 3-10 (a)** shows the Fourier Transform infrared spectroscopy (FTIR) spectra of each membrane. For PUm, there is a

prominent peak at 3326 cm^{-1} , which is the unique N–H stretching vibration absorption peak in the molecular structure of PU nanofibers [39]. The peaks at 1726 cm^{-1} and 1528 cm^{-1} belong to the free and hydrogen bonding of carbonyl groups in the urethane linkage ($-\text{H}-\text{N}-\text{COO}-$) [37]. Then, the N–H in plane bending vibration is validated from the peak at 1595 cm^{-1} . Meanwhile, the peak at 1532 cm^{-1} is related to the combination of N–H bending and C–H stretching [40]. After the decoration of CNTs or CNSs or the both of them, the peaks of the functional groups mentioned above keeps nearly unchanged. This may be due to the overlap of stretching vibration absorption peak of N–H groups in PU molecular structure with those of oxygen-containing groups on the surfaces of CNTs and CNSs, and the hydrogen bonding between hydroxyl or carbonyl groups in PU and oxygen-containing groups in CNT and CNS. The carbon nanomaterials coated on the surface of PUM can shield the infrared spectrum signal to a certain extent.

In order to further verify the functional groups on the surface of self-made CNSs, FTIR test was conducted on CNSs. As shown in **Fig. 3-10 (b)**, the broadening peak of HL-CNSs at 3435 cm^{-1} belongs to the stretching vibration of $-\text{OH}$ in hydroxyl or carboxyl group, and the stretching vibration peak at 2933 cm^{-1} corresponds to the C–H in aliphatic or alkane. The stretching vibration peak of $\text{C}=\text{O}$ is located at 1700 cm^{-1} , and the peak at 1616 cm^{-1} is corresponding to the in-plane stretching vibration peak of $\text{C}=\text{C}$. The two peaks appear in the $1400\text{--}1000\text{ cm}^{-1}$ region are related with the bending vibration peaks of $-\text{OH}$ in aromatic hydroxyl groups or carboxyl groups, respectively. 798 cm^{-1} is the out-of-plane bending vibration peak of C–H. According to these peaks, HL-CNSs can be judged to contain hydrophilic polar groups such as $-\text{OH}$, $\text{C}=\text{O}$ and $\text{O}-\text{C}=\text{O}$ [33]. The HL-CNSs did not show the peaks mentioned above after the calcination, thus it can be considered that the hydrophilic groups on the HL-CNSs were destroyed or eliminated, which means that the hydrophilic carbon nanospheres were transformed into hydrophobic nanospheres, that is, the HL-CNSs were successfully transformed into HB-CNSs. It is proved that hydrophilic carbon spheres and hydrophobic carbon spheres were both successfully fabricated.

In consequence of the surface wettability of the fabricated membranes has great effect on the fog-harvesting properties [41], [42], [43], the water contact angles (WCAs) of the samples were measured. Each sample was tested ten times on the different places of the surface and the average value and standard deviation were obtained. As shown in **Fig. 3-10 (c)**, PUm, HB-CNTs/PUm, HB-CNSs/PUm, HB-CNTs/CNSs/PUm show hydrophobicity. HL-CNTs/PUm, HL-CNSs/PUm, HL-CNTs/CNSs/PUm show hydrophilicity. The WCA of original PUm was 120.8° . After the hydrophilic carbon nanomaterials were anchored on the nanofibers' surface after ultrasonication, the surface of composite nanofiber membrane became hydrophilic due to the introduction of polar groups on HL-CNTs and HL-CNSs and the hierarchical microstructure. The WCA of the material can be reduced to 61.7° due to the effect of hydrophilic macrotrichia and bumps structure. Owing to the introduction of hydrophobic carbon nanomaterials, the surface roughness of the composite film was reinforced, and the hydrophobicity could reach 140° . According to the above results, the introduction of hydrophilic carbon nanomaterials by the means of ultrasonication can make the composite surface hydrophilic, and similarly the introduction of hydrophobic carbon nanomaterials will strengthen hydrophobicity of PUm to transformed into the more hydrophobic PU composite membrane.

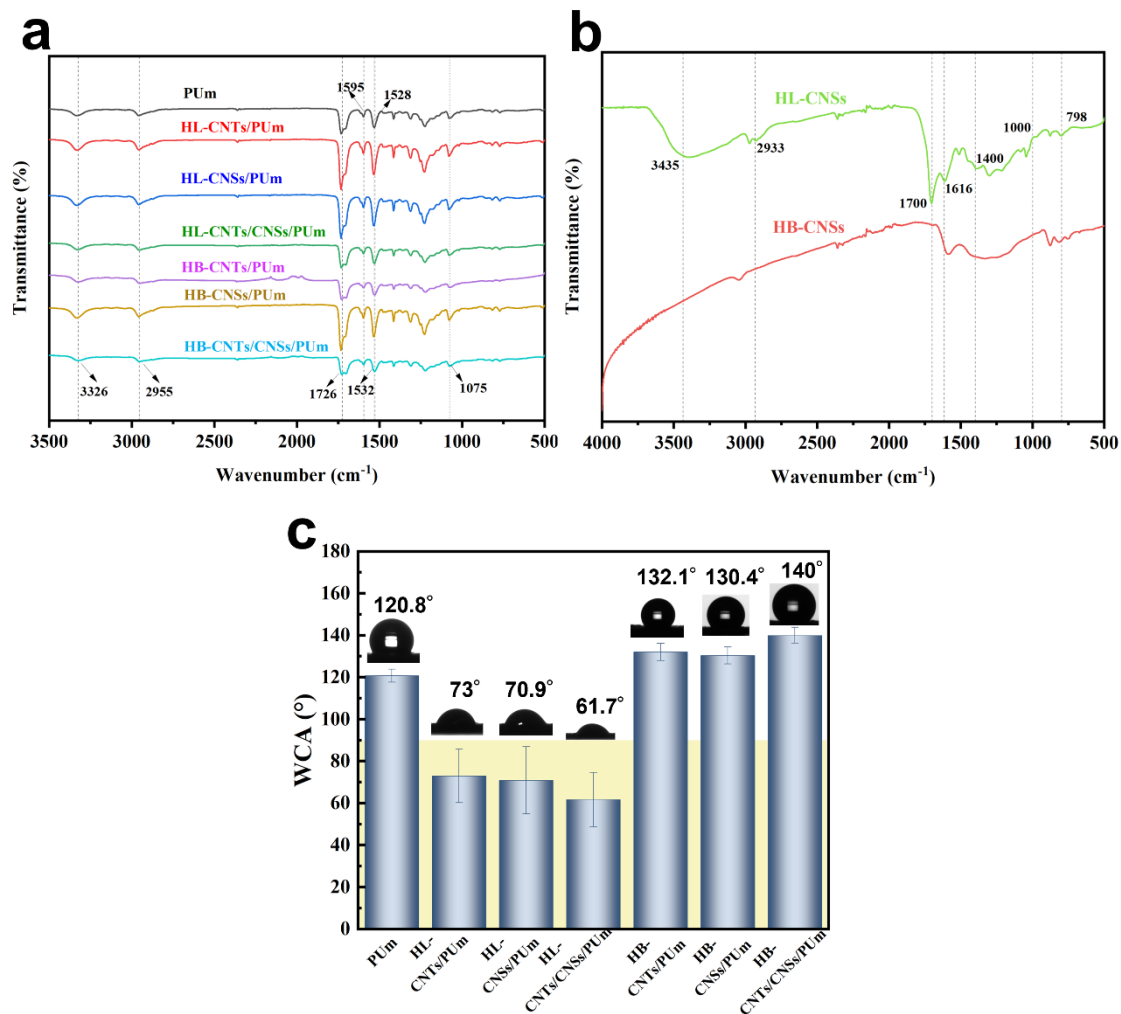


Fig. 3-10. (a) FTIR spectra of membranes. (b) FTIR spectra of HL-CNSs and HB-CNSs. (c) Static WCA of membranes. Insets show the corresponding WCA images.

3.3.4 Fog harvesting properties

To investigate the fog harvesting efficiency of the fabricated materials, fog collection experiments were carried out, and the experimental setup is shown in **Fig. 3-11**. The fog flow supply velocity was 40–50 cm s⁻¹ (determined by an anemometer, Model 6541–01, KANOMAX, Japan). **Fig. 3-12 (a)** shows the mass of water collected per unit area accumulated over time of seven different membranes. Accompanied with the fog

collection time increases, the mass of water harvested of all samples increased. However, the water harvesting rate was faster for membranes with apparently surface-anchored hydrophilic carbon nanomaterials than the hydrophobic ones. **Fig. 3-12 (b)** shows their water harvesting efficiency. It is found that the membranes with hydrophilic surface have higher water harvesting efficiency, which means the secondary hydrophilic structure constructed on the hydrophobic fibrous membrane can effectively enhance the fog capture ability and fog harvesting efficiency. The introduction of hydrophilic and hydrophobic carbon nanomaterials not only introduced the hydrophilicity and hydrophobicity of the material to the PUm, but their size also influenced the effects. The diameters of the two kinds of CNTs are different, while the size of HB-CNTs is 40–70 nm, and that of HL-CNTs is 10–20 nm. According to the Wenzel equation, the rougher the hydrophobic surface is, the more hydrophobic the surface would be [44], [45]. The larger the diameter of HB-CNTs is, the coarser and more hydrophobic the surface of nanofiber membrane became when they were introduced to PUm. On the other hand, as the HL-CNTs are smaller in size, more hydrophilic sites were introduced into the hydrophobic PUm to facilitate the capture of fog. Moreover, the structure and properties of hydrophobic mesh nanofibers can facilitate the transport and temporary deposition of droplets on a micro scale so that water droplets could form larger sizes and then fall off under the influence of gravity and be eventually collected. In addition, it is noteworthy that the water harvesting efficiency of HL-CNTs/CNSs/PUm is $1631.07 \text{ mg cm}^{-2} \text{ h}^{-1}$ about twice that of HB-CNTs/CNSs/PUm, which proves that a single hydrophobic material cannot easily achieve water harvesting. We speculated that the superior water harvesting efficiency of HL-CNTs/CNSs/PUm should be realized by the synergistic effect of the designed biomimetic fibrous network structure and the surface hydrophilicity and internal hydrophobic porous characteristics of the composite material [15], [46].

In order to prove the excellent stability and utilization rate of HL-CNTs/CNSs/PUm, water collection cycle tests were also carried out (**Fig. 3-12 (c)**), and it was found that the water harvesting efficiency remained at a high level each time even reached 1666.2 mg

$\text{cm}^{-2} \text{h}^{-1}$ to prove its sustainability. In addition, the comparison with the film-like materials in other studies (see **Fig. 3-12 (d)** and **Table 3-1**) also proved that the HL-CNTs/CNSs/PUM prepared in this work have relatively better water harvesting properties [14], [15], [20], [21], [26], [47], [48], [49], [50]. Considering the high humidity in the laboratory, in order to further test the water collecting capacity of the material at low humidity, we also carried out the fog collection experiment of HL-CNTs/CNSs/PUM at the relative humidity of $25 \pm 5 \%$. It was found that even in the dry environment, HL-CNTs/CNSs/PUM still had high water harvesting capacity (**Fig. 3-13 (a)**) and water harvesting efficiency (**Fig. 3-13 (b)**) and could be reused. The stability of HL-CNTs/CNSs/PUM has been tested under different conditions like the water washing, abrasives impact and longer period of water harvesting, the corresponding water harvesting performance was also tested (Fig. S5, S6 and S7).

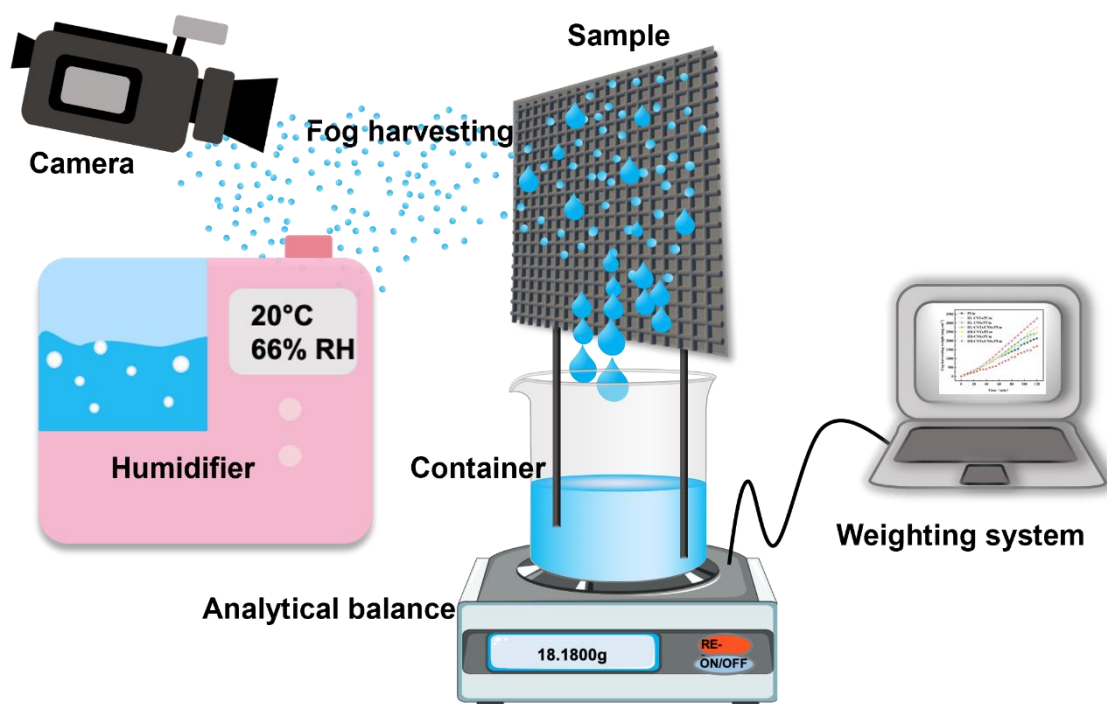


Fig. 3-11. Schematic illustration of the fog-harvesting system.

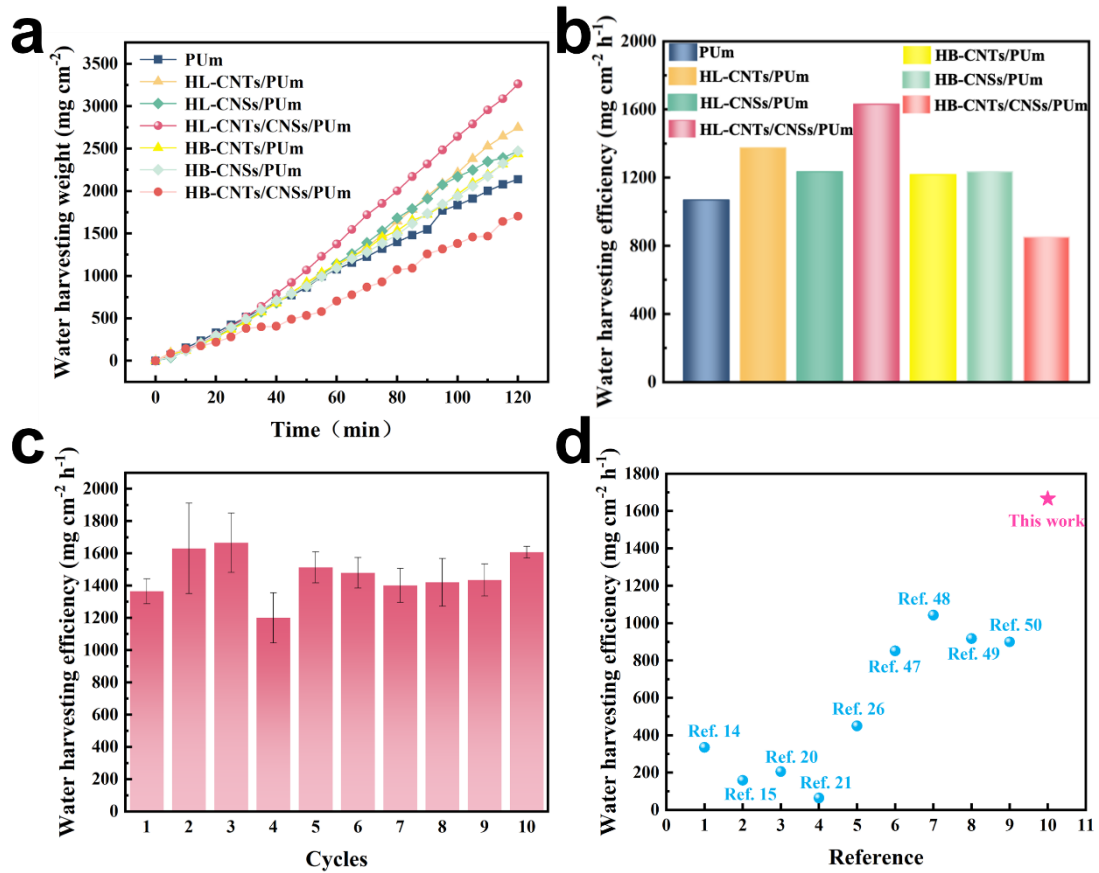


Fig. 3-12. (a) Water harvesting weight for membranes during a period of 2 h. (b) Water harvesting efficiency of membranes. (c) Water harvesting cycle tests of HL-CNTs/CNSs/PUM. Each cycle lasts 2 h. (d) Comparison of water harvesting efficiency of fog collectors between this work and other previous studies.

Table 3-1. Comparison of fog harvesting performance of different materials.

No.	Fabricated materials	Fog velocity (cm s ⁻¹)	Fog harvesting rate (mg cm ⁻² h ⁻¹)	Ref.
1	Fluorinated PAN nanofiber	0.60	~335	14
2	CuO-50-PFDT-PS-130	12	~159	15
3	PNIPAM-PD/TiO ₂ @CFC	12	~206	20
4	PVDF fibers directly on Raschel mesh	19	~64	21
5	Copper Oxide Microtufts on Natural Fractals	5-15	~450	26
6	Bioinspired MNS-SLIPS	45-50	~852	47
7	Ag/TiO ₂ -Dopa/CTA	25	~1043	48
8	SA-ZIF-8 ₄₀ @SPI	50	~917.6	49

9	Binary cooperative Janus fog collector	70	~900	50
10	HL-CNTs/CNSs/PUM	40-50	~1666.2	This work

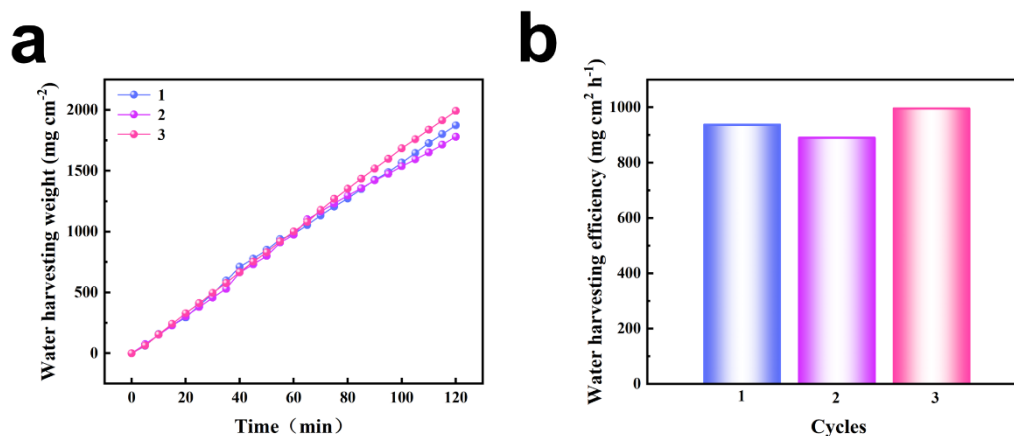


Fig. 3-13. (a) Water harvesting weight for HL-CNTs/CNSs/PUM during a period of 2 h in a low humidity environment and the corresponding water harvesting efficiency (b).

The wash fastness of HL-CNTs/CNSs/PUM was carried out with a commercial washing machine according to JIS L 1930. Each washing cycle was continued for 15min at room temperature. Samples can be obtained after 15 washing cycles. After washing, HL-CNTs/CNSs/PUM was dried at room temperature and the water harvesting property was evaluated.

According to the JISH8503, 0.5kg of WHITEMORUNDUM/WA (SHOWA DENKO K.K., Japan) abrasives were used to conduct abrasives impact test on HL-CNTs/CNSs/PUM. The schematic diagram of the experiment is shown in **Fig. 3-14**. After the abrasives impact test, HL-CNTs/CNSs/PUM was dried at room temperature and the water harvesting property was evaluated.

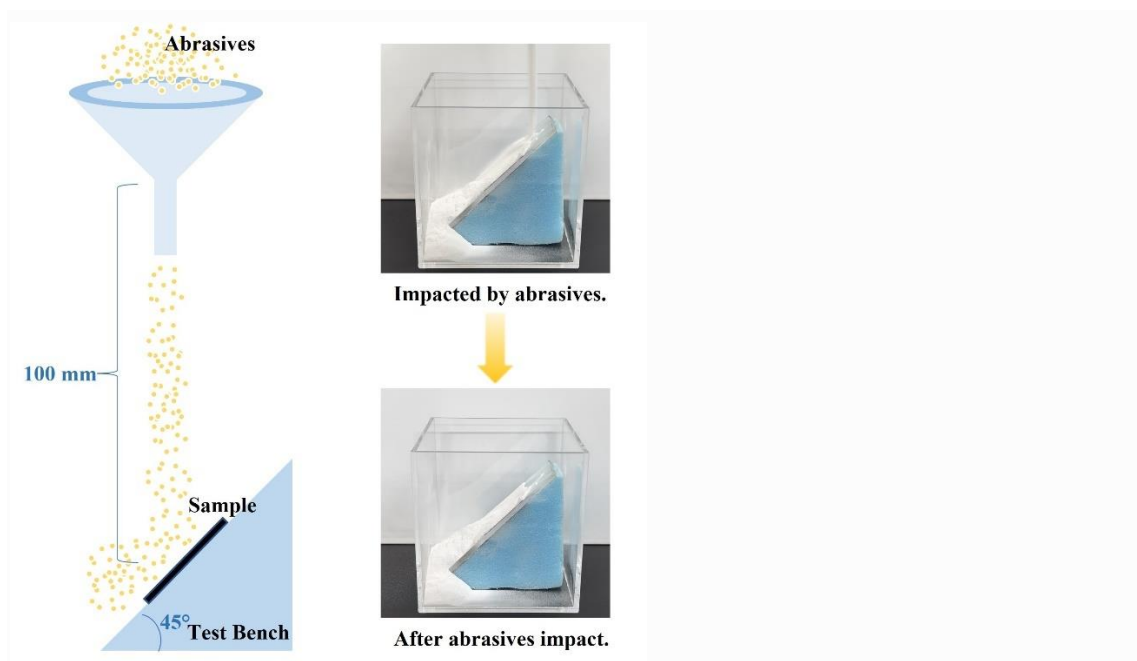


Fig. 3-14. The abrasives impacting test.

After water washing test and abrasives impact test, the water harvesting performance of HL-CNTs/CNSs/PUM is shown in **Fig. 3-15 (a)**. The water harvesting efficiency is slightly lower than that before treatment but still maintains relatively high water-harvesting efficiency. From **Fig. 3-15 (b)**, it can be seen that HL-CNTs/CNSs/PUM could still maintain high water harvesting efficiency for longer time, However, accompanied with the increase of experimental time, the water harvesting rate will become slightly lower, and tended to be balanced, but it can still maintain a relatively water harvesting trend.

The results of stability verification related experiments indicated that the HL-CNTs/CNSs/PUM could meet the requirement of the actual environment of water harvesting (wet, a small amount of sands in wind and durable utilization). Importantly, the fabricating process of HL-CNTs/CNSs/PUM is facile and the as-prepared HL-CNTs/CNSs/PUM can also achieve fog-harvesting property.

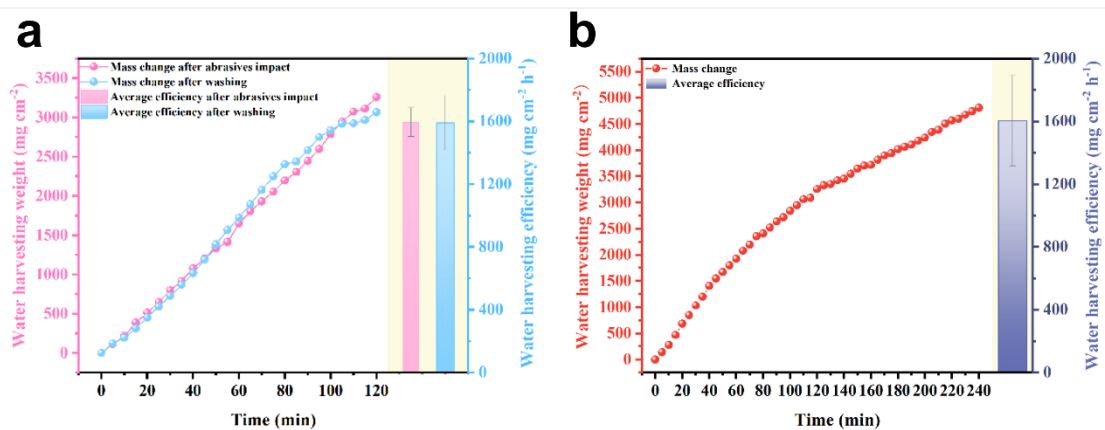


Fig. 3-15. (a) Investigations of mechanical robustness of HL-CNTs/CNSs/PUM surfaces. Water harvesting performance of HL-CNTs/CNSs/PUM during a period of 2h after the washing and abrasives impact. (b) Water harvesting weight for HL-CNTs/CNSs/PUM during a period of 4 h.

3.3.5 Fog harvesting mechanism of HL-CNTs/CNSs/Pum

In order to observe the water harvesting behavior of the material, the fog-collecting process on-site using an industrial camera was recorded. **Fig. 3-16** shows the fog collection process on the surface of HL-CNTs/CNSs/PUM within 1 min, including the captured nucleation of tiny fog droplets, the gradual condensation growth of water droplets, and the final sliding. When the fog was sprayed on the surface of HL-CNTs/CNSs/PUM, the tiny droplets were immediately adsorbed on the surface, and then the condensed droplets grew larger, and the hydrophilic CNTs and CNSs clusters made the droplets adhere and attract more tiny fog droplets. Finally, the water droplets on the mesh-like surface slid into the concaves and the water droplets temporarily deposited in the concaves also continued to accumulate. Growing droplets continued to coalesce with adjacent tiny droplets to reduce surface energy and also became bigger to be attracted to the concave [51], [52]. Such bulge-concave mesh allows for rapidly continuous droplets capture and collection. Then the large water droplets on the mesh-like membrane

slid off under the action of gravity hence be collected. This multiple biomimetic mesh-like membrane can realize rapid transport of water droplets on the plane and gradient wetting on the cross-section.

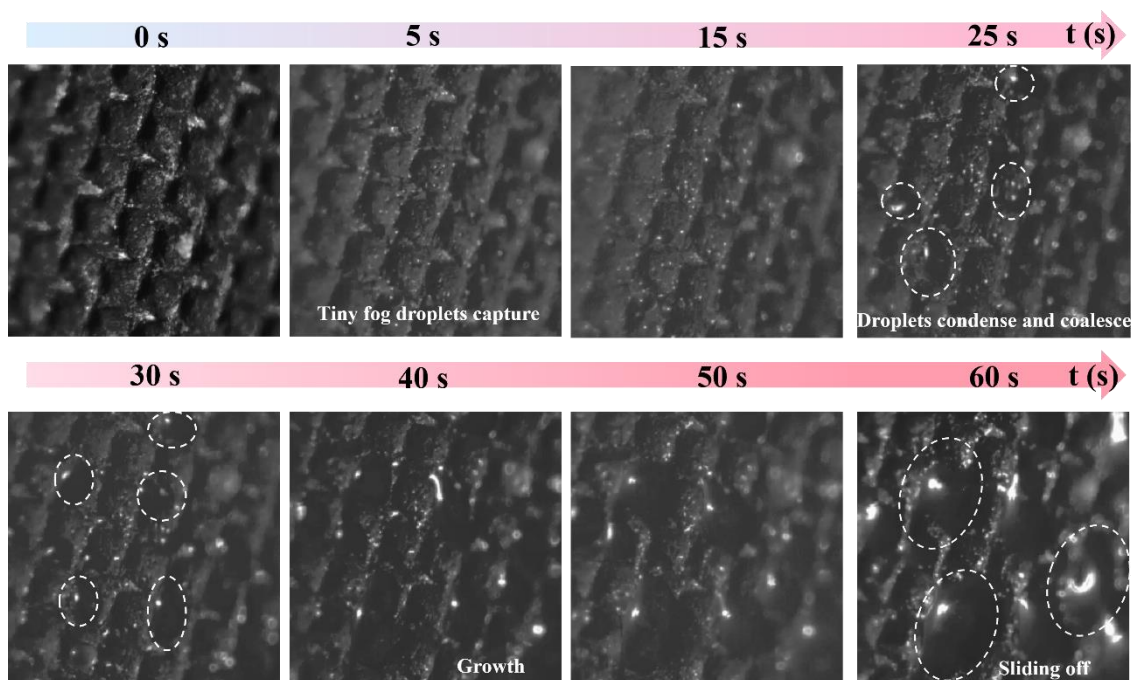


Fig. 3-16. Water collection behavior on HL-CNTs/CNSs/PUM surface in 1 min.

The content mentioned above is the fog-collection behavior that can be directly observed. Further study on the fog-collecting behavior on single nanofibers is also helpful to understand the water harvesting mechanism of HL-CNTs/CNSs/PUM. As shown in **Fig. 3-17**, the tiny fog droplets on a single nanofiber were firstly captured by the hydrophilic CNSs bumps, and when the water droplets coalesced to a critical size, the high dynamic pressure generated by the bumps stimulated the water droplets roll down to the hydrophobic nanofiber surface benefits from the back where hydrophilic and hydrophobic parts coexist of desert beetle. At the same time, due to the introduction of HL-CNTs, this needle-like structure has adhesion properties to water droplets similar to the structure on termite wings [53]. Likewise, the protrusions of CNSs and CNTs on

smooth hydrophobic nanofibers will generate upward capillary force to accelerate the coalescence of driven droplets, which is similar to the spontaneous aggregation phenomenon of floating particles driven by capillary force penetrating vegetation to the surface [29], [54], [55]. Therefore, introducing CNTs and CNSs on smooth hydrophobic PU nanofibers to form the Janus nanofibers can not only improve the fog capture ability, but also promote the self-driven coalescence of droplets so that the water droplets condense on the material with the maximum retention which helps to improve the water harvesting efficiency.

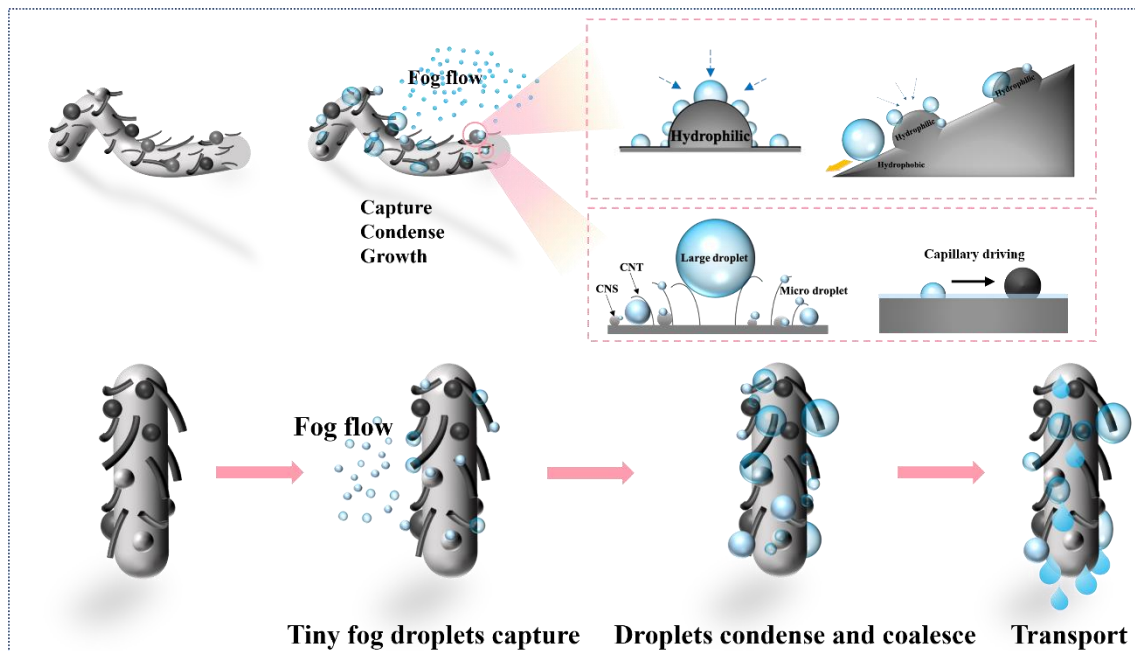


Fig. 3-17. Water harvesting behavior on single nanofiber of HL-CNTs/CNSs/PUm.

Surfaces with periodic peaks have been shown to exhibit enhanced performance in water harvesting [56]. As shown in **Fig. 3-18 (a)**, as the fog collection process proceeded, more and more fog droplets will collide the water droplets already condensed on the membrane and continued to spread and grow. When the droplet further grew bigger, it would coalesce with the adjacent droplets, leading to the droplets also spontaneously

enter the concaves and eventually form the large droplets that slide when gravity overcomes the adhesion of the water droplets to the surface structure. Since the fog capture and coalescence process is shortened and this kind of aggregation growth can reduce the re-evaporation of microdroplets.

The fog-collection behavior on a single nanofiber has been discussed. In order to further explore the fog-collection mechanism of the PU hierarchical structure composite membrane, not only the surface topography structure of the material needs to be analyzed, but also the fluid motion around the material and on the surface as well as the force of the droplets need to be discussed.

For the whole PU composite membrane with bulge-concave structure, the bulge microstructure distributed on the surface can affect the motion of fog droplets to promote the capture of fog. Therefore, for substrates with bulges structure, the bulges also affect the distribution of fog droplets, as shown in **Fig. 3-19 (a)**. Combined with relevant studies [27], [57], it can be speculated that the fog flow at the bulges will be relatively concentrated as shown in **Fig. 3-19 (b)**. And the continuously supplied fog flow can accelerate the growth rate of water droplets on the bulges. Meanwhile, the collection of water from the fog flow mainly relies on the collision between the fog droplets and the substrate [50]. At the same time, due to the non-negligible air resistance, the collision behavior of micro droplets is different from that of macro droplets. To further understand the dynamic process of fog collection, boundary layer theory should be considered [50], [58].

$$\frac{\delta}{x} = 5 \times Re^{-0.5} \quad (5)$$

δ is the thickness of the boundary layer, x is the length of the fog harvester along the direction of fog flow, see schematic **Fig. 3-20 (a)**, Re is the Reynolds number. When the droplets collide the membrane continuously, the x at the bulge is obviously smaller, while the x of the concave (i.e., at the condensed water film) is larger, that is, the thickness of the boundary layer can be reduced at the micron-scale bulges of the membrane, enabling

more droplets to collide and be collected **Fig. 3-20 (b)**). Furthermore, droplets are more likely to be concentrated on the bulges of the membrane that is closer to the source of the fog, also indicating that the bulge structure can improve the efficiency of fog collection. Due to boundary layer effects, when a fog droplet collides the plain water film, its kinetic energy should be dissipated before it can be successfully collected [50]. In contrast, the bulges on the membrane can effectively reduce the boundary layer effect, which reduces the velocity of bulges' nearby droplets. The bulges also promote droplet collision due to its thinner boundary, and the droplets tend to condense at the bulges or tips of the fog collection material [50], [59], [60], [61], [62], [63]. During the process of collecting fog, high-velocity droplets can be effectively collected regardless of their kinetic energy if they hit the bulge (**Fig. 3-18 (b)**), which means that the droplets will be successfully captured at the bulges regardless of whether they are moving at high or low speed (**Fig. 3-18 (b)**). However, to be collected at the flat places the droplets will slow down to a slower velocity onto the condensed water film. The present findings suggest that micron-scale or millimeter-scale bulges structures on the surface of material may be a possible factor to improve fog harvesting efficiency.

To further elucidate the effect of nanofiber meshes of HL-CNTs/CNSs/PUM on water harvesting and transport, we proposed droplets motion as shown in **Fig. 3-18 (c)**. The droplets captured by HL-CNTs and HL-CNSs would be transported along the nanofiber bundles on the plane, while the mesh-like structure with a height of more than 250 μm on the cross-section produced an additional Laplace pressure difference (ΔP) [64]:

$$\Delta P = P_d - P_D \quad (6)$$

The capillary pressure formed by the bulge macrostructure on the membrane surface is much smaller than that of the underlying micro-nano-scale pores, that is, P_d is much larger than P_D , and ΔP facilitates the transport of water droplets from the surface to the hydrophobic part.

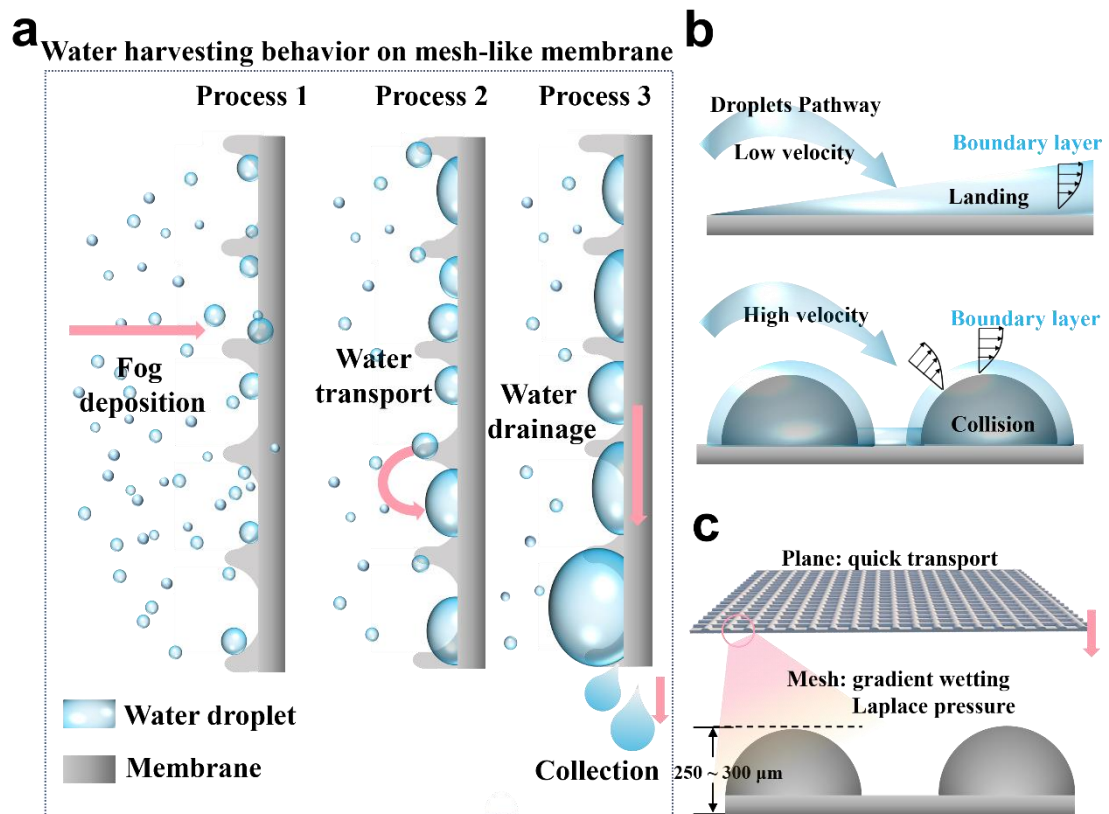


Fig. 3-18. Illustration of fog harvesting mechanism of HL-CNTs/CNSs/PUM. (a) Water harvesting behavior on mesh-like membrane. (b) The boundary layer effect on the fog collection of different parts of the surface. (c) Mechanism of directional transport of tiny droplets in mesh-like nanofiber networks, combining fast transport in the plane and gradient wetting in the cross-section.

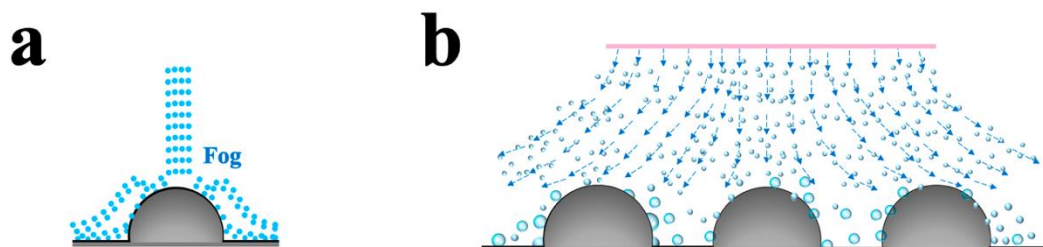


Fig. 3-19. (a) The schematic illustration of the fog flow and droplets growth. (a) Local distribution of fog microdroplets around the single bump. (b) Distribution of fog microdroplets around bumps and flats.

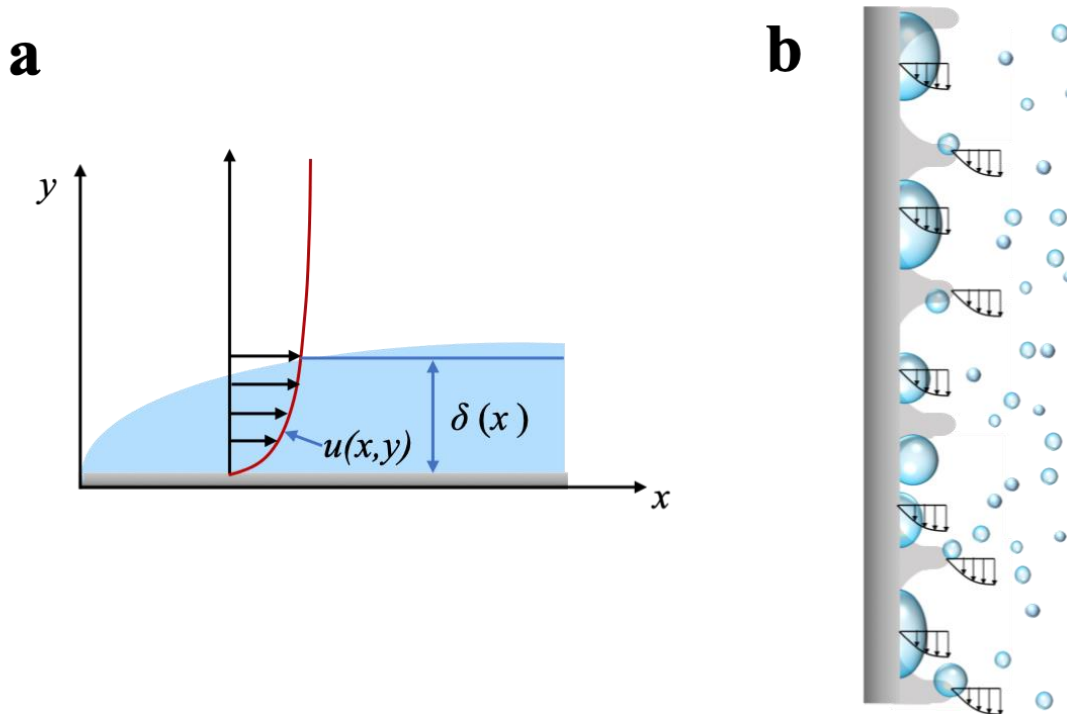


Fig. 3-20. Boundary layer schematics. (a) The schematic illustration for the boundary layer theory. (b) Schematic diagram of the boundary layers of different parts of the fog-harvesting HL-CNTs/CNSs/PUM.

In summary, the micro-nano structures enable the mesh surface to effectively capture droplets by altering the microscopic wetting and nucleation properties of the surface. Furthermore, in the surface energy gradient principle, water droplets tend to be driven towards more wettable regions, which have higher surface energy [59], [60]. Integrating micro-nanostructures on the mesh-like macroscale surface structure of HL-CNTs/CNSs/PUM due to the differences in Laplace pressure and surface free energy gradients contributed to increase the fog capture and transport rate.

3.3.6 Solar-heat conversion and evaporation performance

The excellent water harvesting performance of HL-CNTs/CNSs/PUM also reflects its excellent water transport performance, which can effectively affect solar evaporation.

On the one hand, its hydrophilicity and rapid water supply of the surface of HL-CNTs/CNSs/PUM can ensure the evaporation of the interface, on the other hand, the hydrophobic properties and porosity of PU nanofibers in the interior can ensure the passage of steam and can effectively desalt to achieve purification effect.

To explore the solar-heat conversion property, HL-CNTs/CNSs/PUM and PUM were exposed to 1 sun (1 kW m^{-2}) solar light irradiation (**Fig. 3-21 (a)**) at dry state tested under room temperature. IR camera is used to record the real-time temperature change. **Fig. 3-21 (b, c)** show the temperature increased rapidly under the simulated solar radiation and then basically stabilized after 300 s. HL-CNTs/CNSs/PUM can reach a high temperature of $72.7 \text{ }^{\circ}\text{C}$, however the temperature of PUM just changed to $31.0 \text{ }^{\circ}\text{C}$ under the same condition. Moreover, both of them were applied into a device in the following solar evaporation experiments to explore the evaporation performance and ability of desalination.

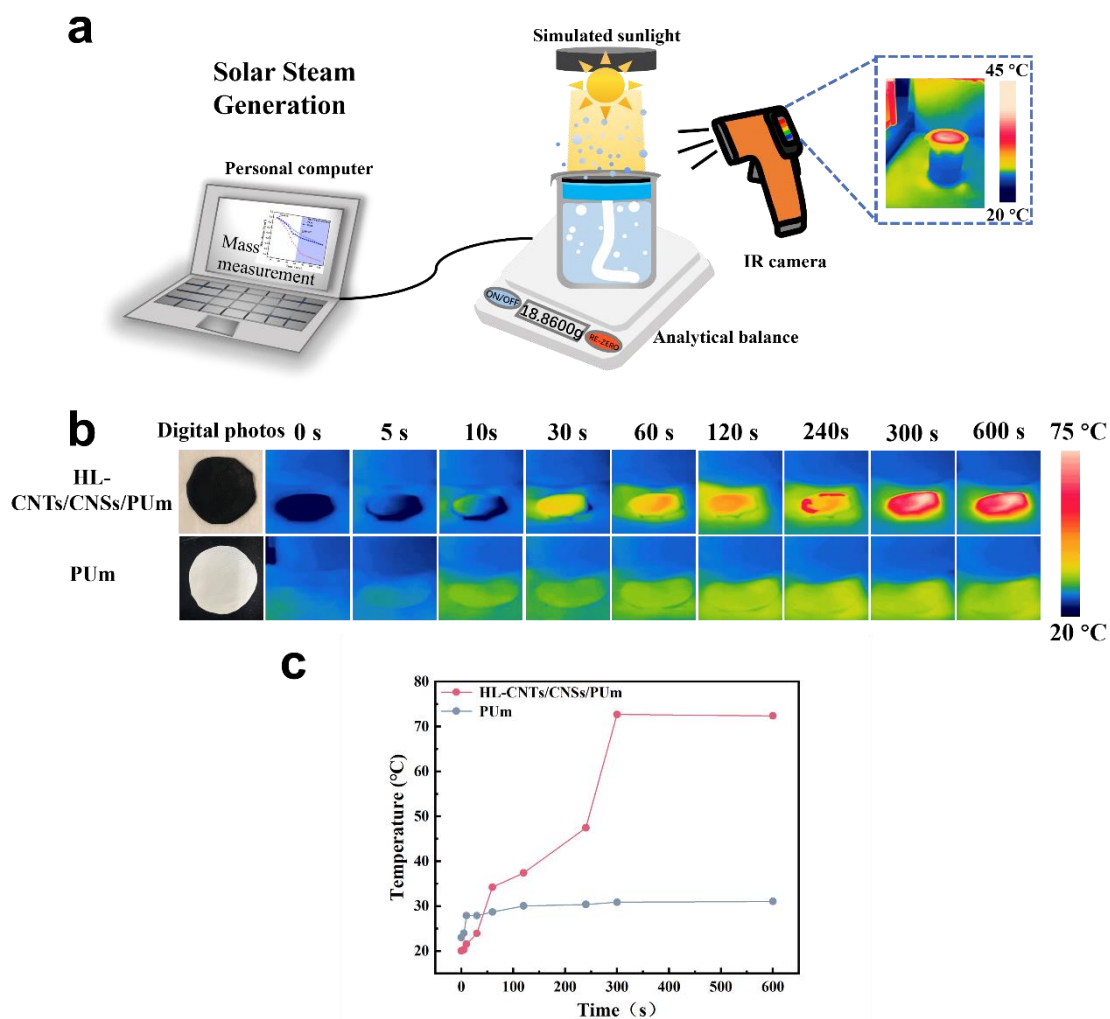


Fig. 3-21. (a) Schematic diagram of the solar-driven evaporation measurement system. (b) Thermal images of the HL-CNTs/CNSs/PUM and PUM. and (c) corresponding temperature change.

The membranes were assembled into the reasonable solar evaporation device based on some previous studies [34], [65]. Initially the polystyrene foam was applied as the thermal insulation layer. Secondly, inserted a cotton piece as the water-trapped layer, additionally the cotton can be the water supply channel. Thirdly, the different PU membrane was placed on the upper layer as the solar absorber. When the whole solar evaporation device floated on the water, water could be efficiently transported to the

upper PU membrane. Meanwhile, it can not only ensure the water transport to the membrane but also provide proper thermal management. The photothermal membranes could exert considerable evaporation potential by the means of this device.

According to the current researches, it is found that the evaporation efficiency of water through the certain system is much higher than that of the water directly irradiated by sunlight. Local concentrated and precise heating can improve the energy utilization efficiency and reduce unnecessary heat loss, thus promoting the efficient generation of solar steam. Therefore, the evaluation and comparison of the evaporation effect of the prepared membranes were all carried out in the designed system. Evaporation experiments were performed on PUm, HL-CNTs/CNSs/PUm and the blank control one (i.e., no membrane).

The temperature variation trend can be seen from the **Fig. 3-22 (a, b)**, the temperature of the HL-CNTs/CNSs/PUm in the device reached about 42.6 °C after 1 h of the radiation, while the blank device was 35.5 °C, the PUm was only 32.2 °C in the end. The results show that the heat from sunlight is significantly more concentrated in the evaporation interface of the HL-CNTs/CNSs/PUm device than the PUm device and blank device. Subsequently, the over-time mass changes and the evaporation rates of these three devices were measured under the presence and absence of sunlight with ultrapure water and natural seawater (from the Sea of Japan, Itoigawa City, Niigata Prefecture, Japan, the coordinate of latitude and longitude is 37.10806°N, 137.99304°E). For the all devices' results (**Fig. 3-23**), no matter whether pure water or seawater was evaporated, the mass change and rate of evaporation are not much different, which proved that the whole system can evaporate water with different compositions equally and effectively. Under the same irradiation conditions, due to the excellent broadband absorption capability of the whole HL-CNTs/CNSs/PUm device, the solar steam generation rates could reach 1.00 kg m⁻² h⁻¹ and 1.05 kg m⁻² h⁻¹ for ultrapure water and natural seawater, respectively. Even after the simulated sunlight was turned off, in the absence of heat provided by the simulated sunlight, the evaporation rates of all samples slowly decreased but the solar

steam generation rates of HL-CNTs/CNSs/PUM device were still higher than the others reached $0.64 \text{ kg m}^{-2} \text{ h}^{-1}$ and $0.67 \text{ kg m}^{-2} \text{ h}^{-1}$ even after 1 h in the darkness during a whole evaporation cycle containing with 1 h light on and 1 h light off.

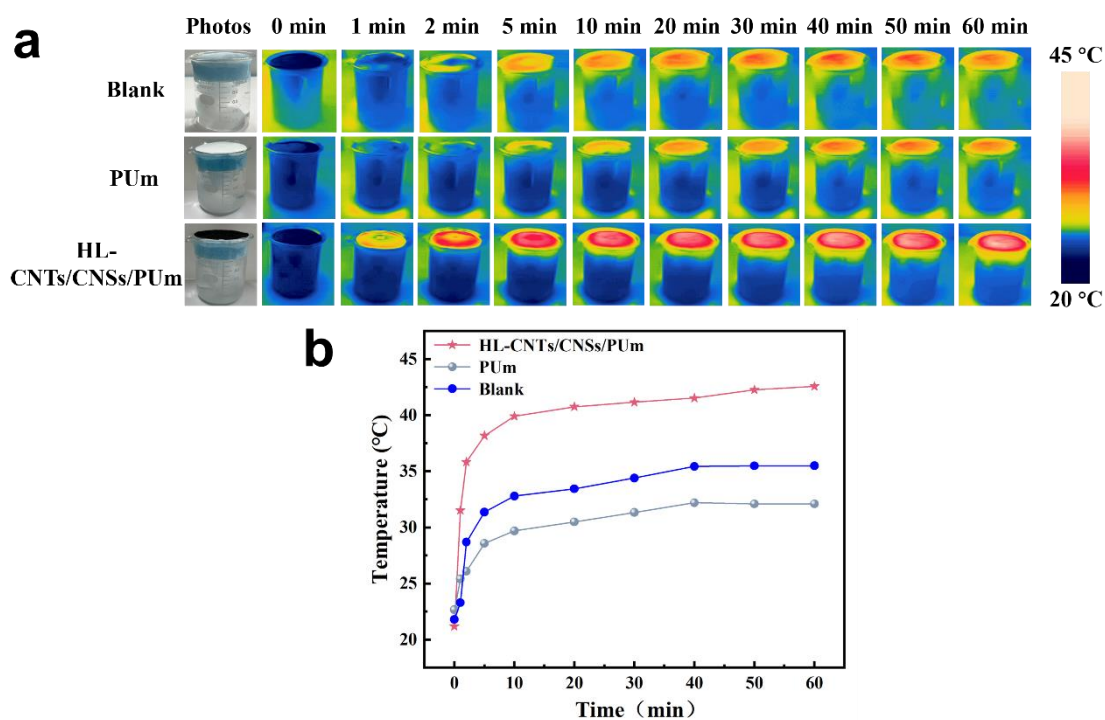


Fig. 3-22. (a) Thermal images of the blank device, the PUM device, and HL-CNTs/CNSs/PUM device under 1 sun irradiation at various time points and (b) corresponding temperature change.

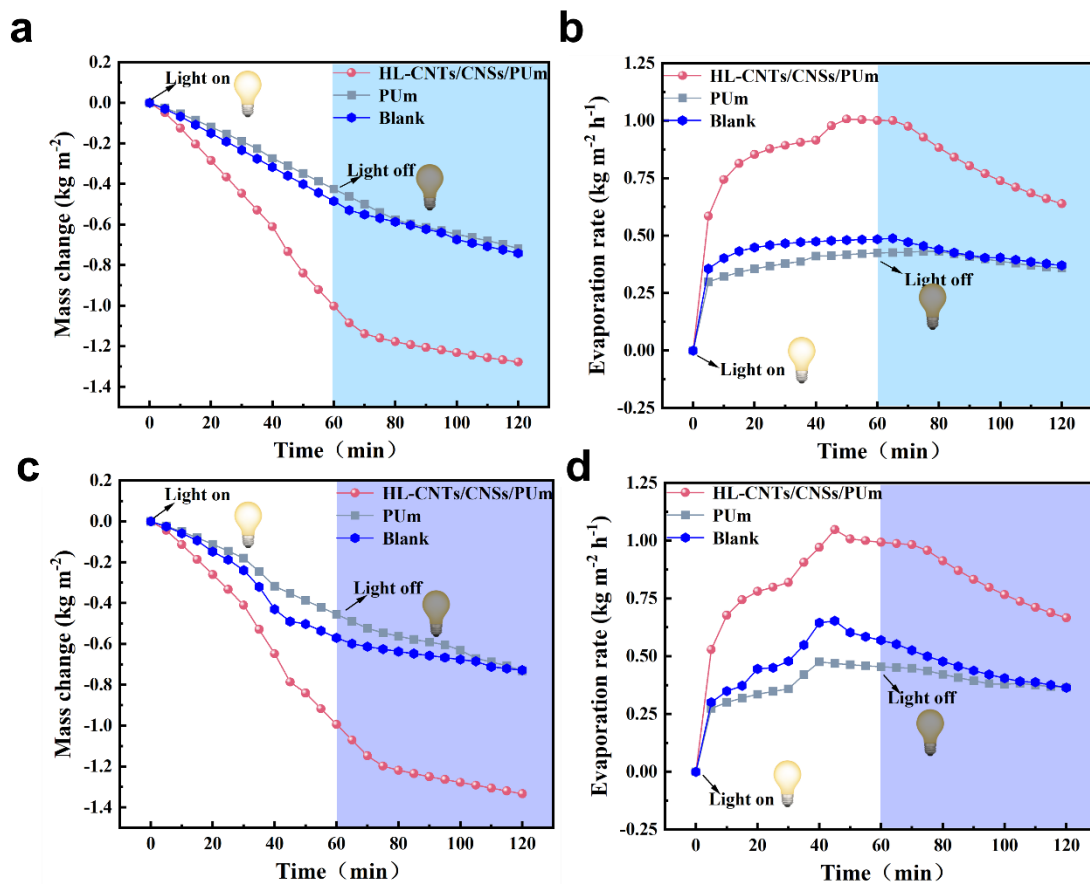


Fig. 3-23. (a) Curves of pure water mass change (b) and the average evaporation rate at each measurement time of the blank device, the PUM device, and HL-CNTs/CNSs/PUM system, respectively. (d) Curves of natural seawater mass change (e) and the average evaporation rate at each measurement time of the blank device, the PUM device, and HL-CNTs/CNSs/PUM system, respectively.

3.3.7 Practical applications of the HL-CNTs/CNSs/PUM device

As shown in **Fig. 3-24 (a, b)**, after 10 h of seawater evaporation, the HL-CNTs/CNSs/PUM remained black, and was not damaged, there was a small amount of salt deposition on the surface, and after the simulated sunlight was turned off the salt would dissolve at room temperature, and the surface could return to its original state, which can be used to continue the evaporation more times, proving to own excellent

chemical stability and stable photoaging stability. In order to verify the purification ability, the concentration variations of metal ions (including Na^+ , Mg^{2+} , K^+ , Ca^{2+} these four main metal ions containing other metals Fe^{3+} , Cd^{2+} , Mn^{2+} , Pb^{2+} , Zn^{2+} , **Fig. 3-24 (c)**) in seawater and purified water were determined by SPS3100. The four main metal ion concentrations in seawater were $11,102.6 \text{ mg L}^{-1}$ (Na^+), 552.81 mg L^{-1} (K^+), 789.67 mg L^{-1} (Ca^{2+}), and 890 mg L^{-1} (Mg^{2+}), notably, the corresponding concentration of the four ions in the purified water obviously decreased to 2.89, 0.4736, 0, and 0.0066 mg L^{-1} (Na^+ , K^+ , Ca^{2+} , and Mg^{2+}). The other metals were $3.81, 0.34, 0.07, 3.12, 0.52 \text{ mg L}^{-1}$ (Fe^{3+} , Cd^{2+} , Mn^{2+} , Pb^{2+} , Zn^{2+}) before and $0.279, 0.022, 0.002, 0.198, \text{ and } 0.043 \text{ mg L}^{-1}$ after solar evaporation. According to the results, the concentration of metal ions is much lower after the solar evaporation by means of the HL-CNTs/CNSs/PUM device, indicating that photothermal evaporation owns the outstanding ions purification and removal ability.

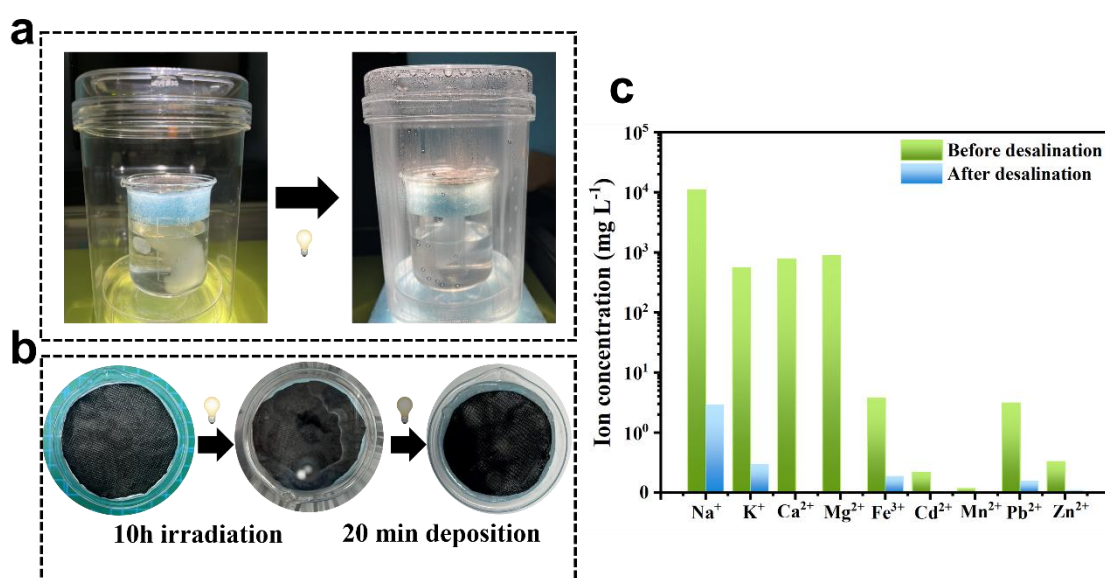


Fig. 3-24. (a) Diagram of the evaporation process. (b) The photos of HL-CNTs/CNSs/PUM device before and after 10 h solar irradiation and recovery condition. (c) Concentrations of Na^+ , Mg^{2+} , K^+ , Ca^{2+} , Fe^{3+} , Cd^{2+} , Mn^{2+} , Pb^{2+} , Zn^{2+} in natural seawater and purified water.

The energy dispersive spectrometer (EDS) can demonstrate the existence of element component. To further explore whether the membrane has the ability to adsorb ions, EDS scanning was performed on the HL-CNTs/CNSs/PUM before and after seawater evaporation to detect the composition of the membrane surface. According to the **Fig. 3-25 (a)**, it can be seen that the surface components of HL-CNTs/CNSs/PUM were C and O elements before seawater evaporation, and there were C, O, Na, Mg, S, Cl, and K on the membrane surface after evaporation (**Fig. 3-25 (b)**). Besides, the atomic and weight percentage of the of the HL-CNTs/CNSs/PUM surface before and after the solar evaporation respectively (**Fig. 3-25 (c, d)**).

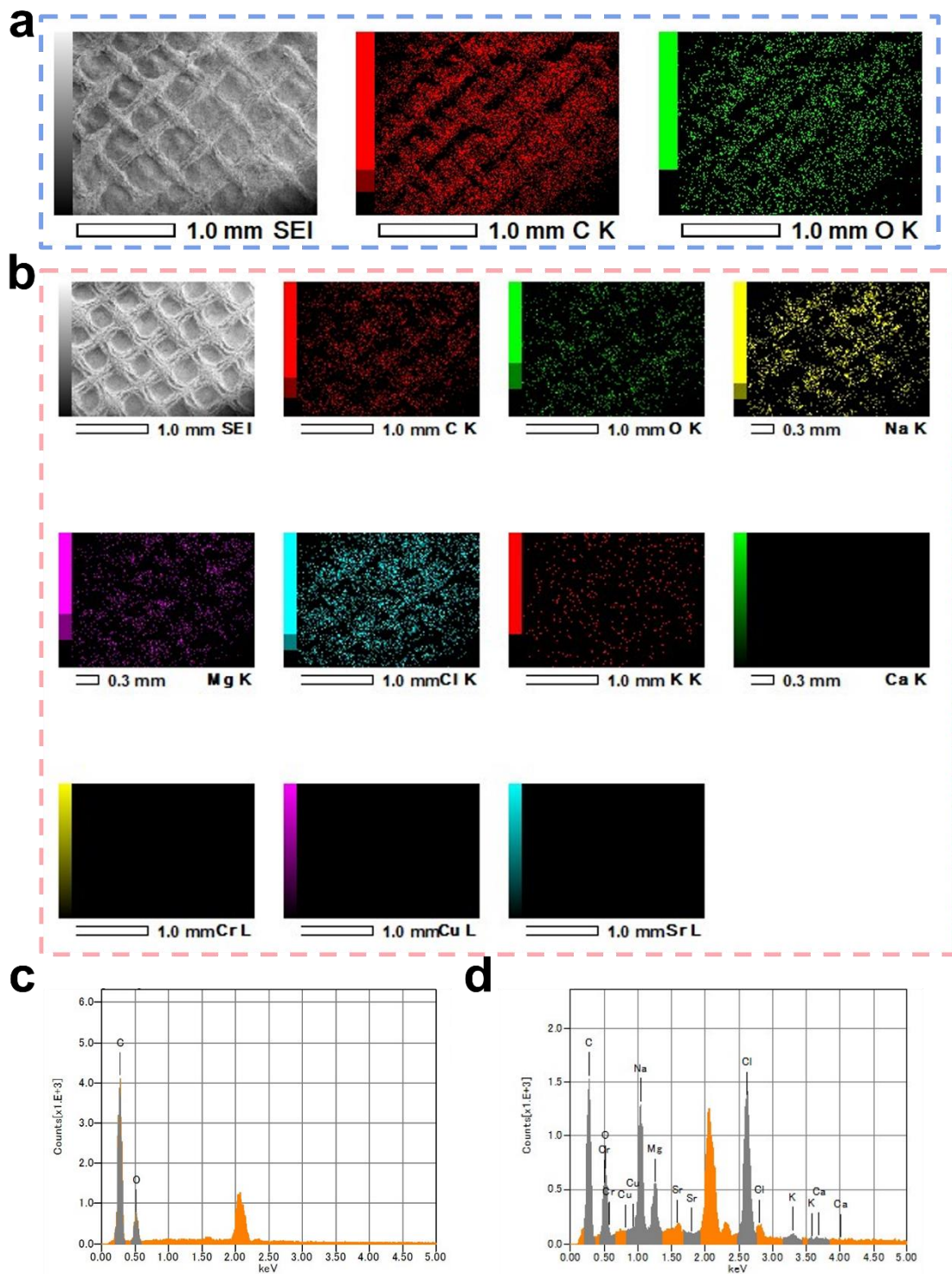


Fig. 3-25. (a) EDS images of HL-CNTs/CNSs/PUM before evaporation. (b) EDS images of HL-CNTs/CNSs/PUM after evaporation. (c) The atomic and weight percentage of the of the HL-CNTs/CNSs/PUM surface before the solar evaporation. (d) The atomic and

weight percentage of the of the HL-CNTs/CNSs/PUM surface after the solar evaporation respectively.

According to the results, we can infer that the fabricated HL-CNTs/CNSs/PUM can effectively adsorb ions in seawater to achieve the effect of desalination. All of the results show that the HL-CNTs/CNSs/PUM possesses steady and efficient solar-thermal evaporation capacity, accompanied with high application potential in seawater desalination to collect clean water.

3.4 Conclusion

In summary, a hierarchical multi-bioinspired Janus membrane was fabricated successfully by applying a feasible and scalable process combined the electrospinning and ultrasonication. HL-CNTs/CNSs/PUM with mesh and macro-micro-nanoscale hierarchical structure constructed by anchoring hydrophilic carbon nanospheres and carbon nanotubes on the surface of PU nanofiber membrane can not only be applied in fog-harvesting but also in solar-thermal water evaporation and seawater desalination.

The HL-CNTs and HL-CNSs attached on the hydrophobic PU nanofiber membrane changed the surface wettability. In this structure, the hydrophilic parts can easily capture the fog and form into a critical size, the mesh structure can make the bigger droplet deposit, then the hydrophobic nanofibers provide the channel to transport and drain the deposited water. The synergy of these structural and material properties enables the fog-harvesting goal to be achieved. The HL-CNTs/CNSs/PUM exhibited rapid water capture and efficient photothermal conversion, which makes it possess water harvesting efficiency of $1666.2 \text{ mg cm}^{-2} \text{ h}^{-1}$ and evaporation rate of $1.05 \text{ kg m}^{-2} \text{ h}^{-1}$. It is worth noting that this Janus composite membrane also showed outstanding effect in seawater desalination. In addition, it maintained high capacity in multiple cycle tests, showing durability and

reusability. Looking forward, further attempts could prove quite beneficial to harnessing different natural resources for potable water harvesting and broadening the way to address water scarcity.

Reference

- [1] S. Cairncross, C. Hunt, S. Boisson, K. Bostoen, V. Curtis, I.C. Fung, W.-P. Schmidt, Water, sanitation and hygiene for the prevention of diarrhoea, *International Journal of Epidemiology*. 39 (2010) i193–i205. <https://doi.org/10.1093/ije/dyq035>.
- [2] C.J. Vörösmarty, P. Green, J. Salisbury, R.B. Lammers, Global Water Resources: Vulnerability from Climate Change and Population Growth, *Science*. 289 (2000) 284–288. <https://doi.org/10.1126/science.289.5477.284>.
- [3] H. Kim, S.R. Rao, E.A. Kapustin, L. Zhao, S. Yang, O.M. Yaghi, E.N. Wang, Adsorption-based atmospheric water harvesting device for arid climates, *Nat Commun*. 9 (2018) 1191. <https://doi.org/10.1038/s41467-018-03162-7>.
- [4] L. Li, T. Hu, A. Li, J. Zhang, Electrically Conductive Carbon Aerogels with High Salt-Resistance for Efficient Solar-Driven Interfacial Evaporation, *ACS Appl. Mater. Interfaces*. 12 (2020) 32143–32153. <https://doi.org/10.1021/acsami.0c06836>.
- [5] L. Li, Q. Li, Y. Feng, K. Chen, J. Zhang, Melamine/Silicone Hybrid Sponges with Controllable Microstructure and Wettability for Efficient Solar-Driven Interfacial Desalination, *ACS Appl. Mater. Interfaces*. 14 (2022) 2360–2368. <https://doi.org/10.1021/acsami.1c20734>.
- [6] W. Zhou, C. Zhou, C. Deng, L. Chen, X. Zeng, Y. Zhang, L. Tan, B. Hu, S. Guo, L. Dong, S.C. Tan, High-Performance Freshwater Harvesting System by Coupling Solar Desalination and Fog Collection with Hierarchical Porous Microneedle Arrays, *Adv Funct Materials*. (2022) 2113264. <https://doi.org/10.1002/adfm.202113264>.
- [7] C.E. Herdendorf, Large Lakes of the World, *Journal of Great Lakes Research*. 8 (1982) 379–412. [https://doi.org/10.1016/S0380-1330\(82\)71982-3](https://doi.org/10.1016/S0380-1330(82)71982-3).

- [8] X. Zhou, F. Zhao, Y. Guo, B. Rosenberger, G. Yu, Architecting highly hydratable polymer networks to tune the water state for solar water purification, *Sci. Adv.* 5 (2019) eaaw5484. <https://doi.org/10.1126/sciadv.aaw5484>.
- [9] Y. Zhang, S.C. Tan, Best practices for solar water production technologies, *Nat Sustain.* (2022). <https://doi.org/10.1038/s41893-022-00880-1>.
- [10] S. Guo, Y. Zhang, H. Qu, M. Li, S. Zhang, J. Yang, X. Zhang, S.C. Tan, Repurposing face mask waste to construct floating photothermal evaporator for autonomous solar ocean farming, *EcoMat.* 4 (2022). <https://doi.org/10.1002/eom2.12179>.
- [11] L. Li, J. Zhang, Highly salt-resistant and all-weather solar-driven interfacial evaporators with photothermal and electrothermal effects based on Janus graphene@silicone sponges, *Nano Energy.* 81 (2021) 105682. <https://doi.org/10.1016/j.nanoen.2020.105682>.
- [12] H. Park, I. Haechler, G. Schnoering, M.D. Ponte, T.M. Schutzius, D. Poulikakos, Enhanced Atmospheric Water Harvesting with Sunlight-Activated Sorption Ratcheting, *ACS Appl. Mater. Interfaces.* 14 (2022) 2237–2245. <https://doi.org/10.1021/acsami.1c18852>.
- [13] H.E. Gad, A.M. Hamed, I.I. El-Sharkawy, Application of a solar desiccant/collector system for water recovery from atmospheric air, *Renewable Energy.* 22 (2001) 541–556. [https://doi.org/10.1016/S0960-1481\(00\)00112-9](https://doi.org/10.1016/S0960-1481(00)00112-9).
- [14] A. Almasian, Gh. Chizari Fard, M. Mirjalili, M. Parvinzadeh Gashti, Fluorinated-PAN nanofibers: Preparation, optimization, characterization and fog harvesting property, *Journal of Industrial and Engineering Chemistry.* 62 (2018) 146–155. <https://doi.org/10.1016/j.jiec.2017.12.052>.
- [15] Y. Wang, L. Zhang, J. Wu, M.N. Hedhili, P. Wang, A facile strategy for the fabrication of a bioinspired hydrophilic–superhydrophobic patterned surface for highly efficient fog-harvesting, *J. Mater. Chem. A.* 3 (2015) 18963–18969. <https://doi.org/10.1039/C5TA04930J>.
- [16] Y. Zhang, D.K. Nandakumar, S.C. Tan, Digestion of Ambient Humidity for Energy Generation, *Joule.* 4 (2020) 2532–2536. <https://doi.org/10.1016/j.joule.2020.10.003>.
- [17] A.R. Parker, C.R. Lawrence, Water capture by a desert beetle, *Nature.* 414 (2001) 33–34. <https://doi.org/10.1038/35102108>.

- [18] B. Wang, Y. Zhang, W. Liang, G. Wang, Z. Guo, W. Liu, A simple route to transform normal hydrophilic cloth into a superhydrophobic–superhydrophilic hybrid surface, *J. Mater. Chem. A*. 2 (2014) 7845–7852. <https://doi.org/10.1039/C4TA00833B>.
- [19] H. Yang, H. Zhu, M.M.R.M. Hendrix, N.J.H.G.M. Lousberg, G. de With, A.C.C. Esteves, J.H. Xin, Temperature-Triggered Collection and Release of Water from Fogs by a Sponge-Like Cotton Fabric, *Adv. Mater.* 25 (2013) 1150–1154. <https://doi.org/10.1002/adma.201204278>.
- [20] H.-T. Chou, Y.-C. Chen, C.-Y. Lee, H.-Y. Chang, N.-H. Tai, Biomimetic structure of carbon fiber cloth grafted with poly(N-isopropylacrylamide) for water collection and smart gates, *RSC Adv.* 7 (2017) 45799–45806. <https://doi.org/10.1039/C7RA05869A>.
- [21] J. Knapczyk-Korczak, P.K. Szewczyk, D.P. Ura, R.J. Bailey, E. Bilotti, U. Stachewicz, Improving water harvesting efficiency of fog collectors with electrospun random and aligned Polyvinylidene fluoride (PVDF) fibers, *Sustainable Materials and Technologies*. 25 (2020) e00191. <https://doi.org/10.1016/j.susmat.2020.e00191>.
- [22] F.V.W. Appels, S. Camere, M. Montalti, E. Karana, K.M.B. Jansen, J. Dijksterhuis, P. Krijgsheld, H.A.B. Wösten, Fabrication factors influencing mechanical, moisture- and water-related properties of mycelium-based composites, *Materials & Design*. 161 (2019) 64–71. <https://doi.org/10.1016/j.matdes.2018.11.027>.
- [23] J.K. Domen, W.T. Stringfellow, M.K. Camarillo, S. Gulati, Fog water as an alternative and sustainable water resource, *Clean Techn Environ Policy*. 16 (2014) 235–249. <https://doi.org/10.1007/s10098-013-0645-z>.
- [24] J. de D. Rivera, D. Lopez-Garcia, Mechanical characteristics of Raschel mesh and their application to the design of large fog collectors, *Atmospheric Research*. 151 (2015) 250–258. <https://doi.org/10.1016/j.atmosres.2014.06.011>.
- [25] Y. Zhang, N. Meng, A.A. Babar, X. Wang, J. Yu, B. Ding, Lizard-Skin-Inspired Nanofibrous Capillary Network Combined with a Slippery Surface for Efficient Fog Collection, *ACS Appl. Mater. Interfaces*. 13 (2021) 36587–36594. <https://doi.org/10.1021/acsami.1c10067>.

- [26] V. Sharma, H. Ali-Löyty, A. Koivikko, K. Yiannacou, K. Lahtonen, V. Sariola, Copper Oxide Microtufts on Natural Fractals for Efficient Water Harvesting, *Langmuir*. 37 (2021) 3370–3381. <https://doi.org/10.1021/acs.langmuir.0c03497>.
- [27] H. Zhou, X. Jing, S. Li, Z. Guo, Near-bulge oil meniscus-induced migration and condensation of droplets for water collection: Energy saving, generalization and recyclability, *Chemical Engineering Journal*. 417 (2021) 129215. <https://doi.org/10.1016/j.cej.2021.129215>.
- [28] R. Feng, F. Song, C. Xu, X.-L. Wang, Y.-Z. Wang, A Quadruple-Biomimetic surface for spontaneous and efficient fog harvesting, *Chemical Engineering Journal*. 422 (2021) 130119. <https://doi.org/10.1016/j.cej.2021.130119>.
- [29] X. Zhang, L. Sun, Y. Wang, F. Bian, Y. Wang, Y. Zhao, Multibioinspired slippery surfaces with wettable bump arrays for droplets pumping, *Proc. Natl. Acad. Sci. U.S.A.* 116 (2019) 20863–20868. <https://doi.org/10.1073/pnas.1912467116>.
- [30] C. Dorrer, J. Rühle, Mimicking the Stenocara Beetle—Dewetting of Drops from a Patterned Superhydrophobic Surface, *Langmuir*. 24 (2008) 6154–6158. <https://doi.org/10.1021/la800226e>.
- [31] A. Lee, M.-W. Moon, H. Lim, W.-D. Kim, H.-Y. Kim, Water harvest via dewing, *Langmuir*. 28 (2012) 10183–10191. <https://doi.org/10.1021/la3013987>.
- [32] J.-X. Wu, J. Zhang, Y.-L. Kang, G. Wu, S.-C. Chen, Y.-Z. Wang, Reusable and Recyclable Superhydrophilic Electrospun Nanofibrous Membranes with In Situ Co-cross-linked Polymer–Chitin Nanowhisker Network for Robust Oil-in-Water Emulsion Separation, *ACS Sustainable Chem. Eng.* 6 (2018) 1753–1762. <https://doi.org/10.1021/acssuschemeng.7b03102>.
- [33] Q. Sun, Y. Cai, L. Sun, W. Ye, X. Long, S. Xu, Y. Ji, R. Wang, Preparation of sandwich-like CNs@rGO nanocomposites with enhanced microwave absorption properties, *J Mater Sci.* 56 (2021) 1492–1503. <https://doi.org/10.1007/s10853-020-05350-7>.
- [34] Z. Lin, T. Wu, J. Shi, B. Zhou, C. Zhu, Y. Wang, R. Liang, M. Mizuno, Poly(N -phenylglycine)-Based Bioinspired System for Stably and Efficiently Enhancing Solar Evaporation, *ACS Sustainable Chem. Eng.* 9 (2021) 448–457. <https://doi.org/10.1021/acssuschemeng.0c07608>.

- [35] X. Zhang, J. Hu, X. Fan, X. Yu, Naturally grown mycelium-composite as sustainable building insulation materials, *Journal of Cleaner Production*. 342 (2022) 130784. <https://doi.org/10.1016/j.jclepro.2022.130784>.
- [36] E. Elsacker, S. Vandeloock, J. Brancart, E. Peeters, L. De Laet, Mechanical, physical and chemical characterisation of mycelium-based composites with different types of lignocellulosic substrates, *PLoS ONE*. 14 (2019) e0213954. <https://doi.org/10.1371/journal.pone.0213954>.
- [37] X. Huang, B. Li, X. Song, L. Wang, Y. Shi, M. Hu, J. Gao, H. Xue, Stretchable, electrically conductive and superhydrophobic/superoleophilic nanofibrous membrane with a hierarchical structure for efficient oil/water separation, *Journal of Industrial and Engineering Chemistry*. 70 (2019) 243–252. <https://doi.org/10.1016/j.jiec.2018.10.021>.
- [38] J. Gao, M. Hu, Robert.K.Y. Li, Ultrasonication induced adsorption of carbon nanotubes onto electrospun nanofibers with improved thermal and electrical performances, *J. Mater. Chem*. 22 (2012) 10867. <https://doi.org/10.1039/c2jm00035k>.
- [39] J. Gao, B. Li, X. Huang, L. Wang, L. Lin, H. Wang, H. Xue, Electrically conductive and fluorine free superhydrophobic strain sensors based on SiO₂/graphene-decorated electrospun nanofibers for human motion monitoring, *Chemical Engineering Journal*. 373 (2019) 298–306. <https://doi.org/10.1016/j.cej.2019.05.045>.
- [40] X. Huang, B. Li, L. Wang, X. Lai, H. Xue, J. Gao, Superhydrophilic, Underwater Superoleophobic, and Highly Stretchable Humidity and Chemical Vapor Sensors for Human Breath Detection, *ACS Appl. Mater. Interfaces*. 11 (2019) 24533–24543. <https://doi.org/10.1021/acsami.9b04304>.
- [41] X. Lou, Y. Huang, X. Yang, H. Zhu, L. Heng, F. Xia, External Stimuli Responsive Liquid-Infused Surfaces Switching between Slippery and Nonslippery States: Fabrications and Applications, *Adv. Funct. Mater*. 30 (2020) 1901130. <https://doi.org/10.1002/adfm.201901130>.
- [42] Y. Liu, L. Zhao, J. Lin, S. Yang, Electrodeposited surfaces with reversibly switching interfacial properties, *Sci. Adv*. 5 (2019) eaax0380. <https://doi.org/10.1126/sciadv.aax0380>.
- [43] Z. Yu, H. Zhang, J. Huang, S. Li, S. Zhang, Y. Cheng, J. Mao, X. Dong, S. Gao, S. Wang, Z. Chen, Y. Jiang, Y. Lai, Namib desert beetle inspired special patterned fabric with programmable and

- gradient wettability for efficient fog harvesting, *Journal of Materials Science & Technology*. 61 (2021) 85–92. <https://doi.org/10.1016/j.jmst.2020.05.054>.
- [44] X. Wang, Q. Zhang, Role of surface roughness in the wettability, surface energy and flotation kinetics of calcite, *Powder Technology*. 371 (2020) 55–63. <https://doi.org/10.1016/j.powtec.2020.05.081>.
- [45] Z. Liu, J. Yu, W. Lin, W. Yang, R. Li, H. Chen, X. Zhang, Facile method for the hydrophobic modification of filter paper for applications in water-oil separation, *Surface and Coatings Technology*. 352 (2018) 313–319. <https://doi.org/10.1016/j.surfcoat.2018.08.026>.
- [46] Y. Su, S. Cai, T. Wu, C. Li, Z. Huang, Y. Zhang, H. Wu, K. Hu, C. Chen, J. Li, Y. Hu, S. Zhu, D. Wu, Smart Stretchable Janus Membranes with Tunable Collection Rate for Fog Harvesting, *Adv. Mater. Interfaces*. 6 (2019) 1901465. <https://doi.org/10.1002/admi.201901465>.
- [47] R. Feng, C. Xu, F. Song, F. Wang, X.-L. Wang, Y.-Z. Wang, A Bioinspired Slippery Surface with Stable Lubricant Impregnation for Efficient Water Harvesting, *ACS Appl. Mater. Interfaces*. 12 (2020) 12373–12381. <https://doi.org/10.1021/acsami.0c00234>.
- [48] C. Xu, R. Feng, F. Song, X.-L. Wang, Y.-Z. Wang, Desert Beetle-Inspired Superhydrophilic/Superhydrophobic Patterned Cellulose Film with Efficient Water Collection and Antibacterial Performance, *ACS Sustainable Chem. Eng.* 6 (2018) 14679–14684. <https://doi.org/10.1021/acssuschemeng.8b03247>.
- [49] H. Liu, W.-Y. Xie, F. Song, X.-L. Wang, Y.-Z. Wang, Constructing hierarchically hydrophilic/superhydrophobic ZIF-8 pattern on soy protein towards a biomimetic efficient water harvesting material, *Chemical Engineering Journal*. 369 (2019) 1040–1048. <https://doi.org/10.1016/j.cej.2019.03.152>.
- [50] M. Cao, J. Xiao, C. Yu, K. Li, L. Jiang, Hydrophobic/Hydrophilic Cooperative Janus System for Enhancement of Fog Collection, *Small*. 11 (2015) 4379–4384. <https://doi.org/10.1002/smll.201500647>.
- [51] X. Li, Y. Liu, H. Zhou, C. Gao, D. Li, Y. Hou, Y. Zheng, Fog Collection on a Bio-inspired Topological Alloy Net with Micro-/Nanostructures, *ACS Appl. Mater. Interfaces*. 12 (2020) 5065–5072. <https://doi.org/10.1021/acsami.9b19756>.

- [52] Z. Yu, F.F. Yun, Y. Wang, L. Yao, S. Dou, K. Liu, L. Jiang, X. Wang, Desert Beetle-Inspired Superwetable Patterned Surfaces for Water Harvesting, *Small*. 13 (2017) 1701403. <https://doi.org/10.1002/sml.201701403>.
- [53] R. Nishimura, K. Hyodo, H. Mayama, S. Yokojima, S. Nakamura, K. Uchida, Dual wettability on diarylethene microcrystalline surface mimicking a termite wing, *Commun Chem*. 2 (2019) 90. <https://doi.org/10.1038/s42004-019-0192-6>.
- [54] P. Peruzzo, A. Defina, H.M. Nepf, R. Stocker, Capillary Interception of Floating Particles by Surface-Piercing Vegetation, *Phys. Rev. Lett.* 111 (2013) 164501. <https://doi.org/10.1103/PhysRevLett.111.164501>.
- [55] J. Jiang, J. Gao, H. Zhang, W. He, J. Zhang, D. Daniel, X. Yao, Directional pumping of water and oil microdroplets on slippery surface, *Proc. Natl. Acad. Sci. U.S.A.* 116 (2019) 2482–2487. <https://doi.org/10.1073/pnas.1817172116>.
- [56] B.T.W. Ang, C.H. Yap, W.S. Vincent Lee, J. Xue, Bioinspired Dual-Tier Coalescence for Water-Collection Efficiency Enhancement, *Langmuir*. 34 (2018) 13409–13415. <https://doi.org/10.1021/acs.langmuir.8b02474>.
- [57] L. Zhong, H. Zhu, Y. Wu, Z. Guo, Understanding how surface chemistry and topography enhance fog harvesting based on the superwetting surface with patterned hemispherical bulges, *Journal of Colloid and Interface Science*. 525 (2018) 234–242. <https://doi.org/10.1016/j.jcis.2018.04.061>.
- [58] M.-G. Medici, A. Mongruel, L. Royon, D. Beysens, Edge effects on water droplet condensation, *Phys. Rev. E*. 90 (2014) 062403. <https://doi.org/10.1103/PhysRevE.90.062403>.
- [59] H. Bai, X. Tian, Y. Zheng, J. Ju, Y. Zhao, L. Jiang, Direction Controlled Driving of Tiny Water Drops on Bioinspired Artificial Spider Silks, *Adv. Mater.* 22 (2010) 5521–5525. <https://doi.org/10.1002/adma.201003169>.
- [60] Y. Zheng, H. Bai, Z. Huang, X. Tian, F.-Q. Nie, Y. Zhao, J. Zhai, L. Jiang, Directional water collection on wetted spider silk, *Nature*. 463 (2010) 640–643. <https://doi.org/10.1038/nature08729>.
- [61] J. Ju, H. Bai, Y. Zheng, T. Zhao, R. Fang, L. Jiang, A multi-structural and multi-functional integrated fog collection system in cactus, *Nat Commun*. 3 (2012) 1247. <https://doi.org/10.1038/ncomms2253>.

- [62] J. Ju, Y. Zheng, L. Jiang, Bioinspired One-Dimensional Materials for Directional Liquid Transport, *Acc. Chem. Res.* 47 (2014) 2342–2352. <https://doi.org/10.1021/ar5000693>.
- [63] M. Cao, J. Ju, K. Li, S. Dou, K. Liu, L. Jiang, Facile and Large-Scale Fabrication of a Cactus-Inspired Continuous Fog Collector, *Adv. Funct. Mater.* 24 (2014) 3235–3240. <https://doi.org/10.1002/adfm.201303661>.
- [64] X. Wang, Z. Huang, D. Miao, J. Zhao, J. Yu, B. Ding, Biomimetic Fibrous Murray Membranes with Ultrafast Water Transport and Evaporation for Smart Moisture-Wicking Fabrics, *ACS Nano*. (2018) acsnano.8b08242. <https://doi.org/10.1021/acsnano.8b08242>.
- [65] Z. Lin, T. Wu, Y.-F. Feng, J. Shi, B. Zhou, C. Zhu, Y. Wang, R. Liang, M. Mizuno, Poly(N - phenylglycine)/MoS₂ Nanohybrid with Synergistic Solar-Thermal Conversion for Efficient Water Purification and Thermoelectric Power Generation, *ACS Appl. Mater. Interfaces*. 14 (2022) 1034–1044. <https://doi.org/10.1021/acсами.1c20393>.

Chapter 4

Multi-bioinspired hierarchical integrated hydrogel for passive fog harvesting and solar-driven seawater desalination

Chapter 4: Multi-bioinspired hierarchical integrated hydrogel for passive fog harvesting and solar-driven seawater desalination

4.1 Introduction

Owing to the impact of population growth, economic development, and the outbreak of the COVID-19 epidemic in recent years, a large amount of clean water resources is being consumed, the water crisis is getting worse year by year [1], [2]. Water scarcity is a huge challenge for the world as the demand for clean water continues to increase [3]. Two-thirds of the world's population lives under severe water shortage conditions for at least one month a year, and 500 million people in the world face serious water shortage problems throughout the year [4]. How to alleviate this crisis has also become the focus of attention, and now some effective methods have been proposed to collect and utilize the limited fresh water on the earth, such as seawater desalination, atmospheric water harvesting and sewage treatment [5], [6], [7], [8], [9], [10], [11]. Based on these, the related research of producing clean water has become a hotspot of modern researchers [12], [13], [14].

While freshwater accounts for around 2.5% of Earth's water resources, its proportion has declined in recent years due to pollution and climate change [15], [16]. The ocean makes up more than 97% of the total water on the earth, and the atmosphere that surrounds us is also a huge reservoir [17], [18]. Extracting fresh water from the atmosphere and seawater is a good choice. On the one hand, water harvesting technologies from the atmosphere include raindrop, dew, and fog collection as well as adsorption [19], [20], [21], [22], [23], [24], [25]. In addition, in virtue of the moisture in the air contains less bacteria and impurities, the collected water could be generally ready for further use

without complicated sterilization and purification processes [25], [26]. Over the past few years, researchers have tried plenty of approaches to optimize the key steps of fog collection including capture of tiny droplets in the air, followed by droplet fusion, transport and final storage [25]. At present, the water in the atmosphere is often collected by modifying the surface wettability or transforming the surface structure and morphology of the material to create biomimetic surface [27], [28], [29], [30]. However, due to the relatively low water collection efficiency of planar structure, and the delicate operation of multiple steps are often required during the preliminary design, the production scale is also relatively limited at the same time [29], [31].

On the other hand, common seawater desalination technologies include reverse osmosis (RO), multi-stage flash (MSF) desalination and multi-effect distillation (MED) [32]. However, how to carry out relevant researches through the way of carbon neutral and zero carbon is also a difficult problem. In recent years, solar energy, which is widely distributed on the earth and renewable green energy, has been attracted more and more attention [33], [34], [35], [36] and leads to development of solar-driven interfacial evaporation [37], [38], [39], [40], [41], [42], [43]. One of the most common solar-driven interfacial evaporation materials is photothermal film [44]. There are many studies on photothermal film's solar absorption and anti-pollution properties, however the flexibility and stability of materials have been ignored.

In order to solve these problems related to manufacturing and development mentioned above and to be more effectively developed for multiple scenarios under different conditions, such as the famous Sandwich Bay in Namibia known as the Sand Sea Symphony, which has attracted many researchers, and the frequent fog water is the source of life for this region's flora and fauna [45], [46], [47], [48]. Previous studies of clean water production inspired by these creatures have mostly been focused on the collection of fog only, there has been few subsequent research of how to release the water and be not only applied in the desert but also in the ocean nearby [49], [50], [51]. In this study, the hydrogel with biomimetic three-dimensional structure and excellent

performance which can be formed in one step, is also introduced into a system for producing clean water that can be applied to multiple scenarios.

Selaginella lepidophylla, a remarkable spike moss that can survive desiccation and even resurrect from an air-dried state, undergoes structural changes to adapt to different hydration states [52], [53]. Honeycomb structures in nature possess large surface areas, high structural stability, and excellent permeability, which accelerate the directional transport of coalesced tiny droplets and enhance heat and mass transfer for maximal adsorption and desorption rates [28], [54], [55], [56]. Pufferfish, a common ocean creature, can expand by absorbing water when threatened and return to its original shape when safe, with this transformation being repeatable [57], [58]. These three miraculous creatures served as inspiration for the design strategy of a biomimetic and multifunctional hydrogel suitable for producing clean water in various scenarios in this research. In particular, *Selaginella lepidophylla*'s drying resistance and morphological changes resemble the hydrogel's water absorption characteristics, its porous structure is also very similar to that of honeycomb to facilitate water transfer. Furthermore, the water absorption and spitting behavior of pufferfish inspired the hydrogel's water collection and release abilities. The high hydrophilicity, porous, and extensive hydrogen bond network of Polyvinyl alcohol and sodium alginate were utilized, accompanied by borax as a cross-linking agent to prepare functional hydrogels. As a novel polymer material with a three-dimensional network porous structure, hydrogel can make full use of high specific surface area, high porosity and surface activity to endow itself an ideal adsorption agent. The addition of MOFs and graphene not only improve the photothermal property of hydrogel, but also has higher ion adsorption capacity and removal ability of heavy metal ions [59], [60], [61]. Hence, it owns high evaporation efficiency, efficacious desalination ability, and durability.

The above advantages make the fabricated hydrogel not only owns the average water harvesting ratio up to 22.44 g g^{-1} under the condition of fog flow after 5 h, but also rapidly release water under solar with water release efficiency of $1.67 \text{ kg m}^{-2} \text{ h}^{-1}$ under 1 sun.

Meanwhile, with the help of reasonable and facile devices, it can perform seawater evaporation and desalination more effectively by the synergy to continuously transport seawater to the surface result in the evaporation rate over $1.89 \text{ kg m}^{-2} \text{ h}^{-1}$. The biomimetic 3D macro/micro/nano hierarchical porous structure of the hydrogel demonstrated in this study ensures rapid water transport and vapor escape. This scalable, modular hydrogel not only triggers new biomimetics ideas and concepts for composite functional material preparation, but also opens a new paradigm for producing clean water in more scenarios in the future as well as good for ecological sustainability.

4.2 Experimental section

4.2.1 Materials

Polyvinyl alcohol (PVA, $n = 1500 \sim 1800$), sodium alginate (SA, 300 ~ 400cP), nitric acid, sodium tetraborate (Borax), cobalt(II) nitrate hexahydrate and methanol were provided by FUJIFILM Wako Pure Chemical Corporation (Japan). Graphene nanoplatelets (6–8 nm thick \times 15 μm wide) was obtained from Strem Chemicals, Inc. (USA). 2-Methylimidazole was supplied by Tokyo Chemical Industry Co., Ltd. (Japan). The deionized water was produced by WG250B, Yamato Scientific co., ltd., (Japan).

4.2.2 Fabrication of ZIF-67 nanocrystal powder

In addition to their ability to provide nano-sized structures, metal–organic frameworks (MOFs) are also well-known for their outstanding adsorption capabilities and photothermal effects. This makes them an ideal component for composite materials with diverse applications. In this study, ZIF-67 was fabricated as one of the functional components in hydrogels. The cobalt(II) nitrate hexahydrate (1.746 g) and 2-methylimidazol (2-MeIM) (1.968 g) were added in 60 mL and 20 mL of methanol separately. Then the $\text{Co}(\text{NO}_3)_2 \cdot 6\text{H}_2\text{O}$ solution was added into 2-MeIM solution kept at

continuous stirring. The solution was stirred for 10 h at 600 rpm at room temperature (20 ± 2 °C). After that, ZIF-67 nanocrystals were collected by centrifugation at 600 rpm for 20 min and followed by four times methanol washing. The final nanocrystals were then dried in an oven at 60 °C for 12 h.

4.2.3 Treatment of graphene nanoplatelets

Graphene is a highly effective photothermal material, and its inclusion in the hydrogel can enable the hydrogel to release water under sunlight, akin to the way a pufferfish expels water. This property can be attributed to the excellent photothermal effect of graphene, which generates heat under sunlight and results in water being released from the hydrogel. To make graphene nanoplatelets more easily dispersed in the solution subsequently, graphene nanoplatelets (0.5 g) and nitric acid solution (50 mL, 3 mol L⁻¹) were mixed and stirred for 14 h at 100 °C at 300 rpm. After acidification, the graphene solution was cooled to room temperature and washed repeatedly with distilled water until the solution become neutral. It was finally put into the oven and dried at 45 °C for 12 h.

4.2.4 Preparation of different types of PVA/SA based hydrogels

A hydrogel matrix was chosen as the most suitable material to mimic the different states of *Selaginella lepidophylla*. To create the hydrogel, PVA and SA were utilized as the primary matrix components. PVA powder was dissolved in deionized water (10 wt%) at ~ 85 °C with continuous stirring for 4 h. The 3.5 wt% SA solution was prepared under the same condition. Different mass ratios of 1:2, 1:1 and 2:1 PVA/SA solutions were poured into beakers respectively, kept stirring at 80 °C for 3 h, then poured into molds. 10 wt% borax solution was dripped onto the PVA/SA solution, accompanied by keeping the mass ratio of PVA/SA solution to borax solution at 3:2. After being crosslinked 12 h at room temperature, the original PVA/SA hydrogel (PVA/SA) was obtained. Graphene nanoplatelets and ZIF-67 and the mixture of the two (1:1) were added into the PVA/SA

solution at a ratio of 1 wt% separately, and kept vigorous stirring at 80 °C for 4 h. Graphene/PVA/SA hydrogel, ZIF-67/PVA/SA hydrogel and graphene/ZIF-67/PVA/SA hydrogel (GZPS) were prepared according to the preparation method as same as the original PVA/SA hydrogel mentioned above.

4.2.5 Vacuum freeze-drying treatment for as-prepared hydrogels

Freeze-drying was utilized in this study to create a honeycomb-like porous structure in the hydrogel matrix. Liquid nitrogen was slowly poured into the paper cups that have been filled with four different hydrogels prepared before, so that the hydrogels can be quickly frozen in a short time to maintain their porous structure. Next, the frozen hydrogels (PVA/SA hydrogel, graphene/PVA/SA hydrogel, ZIF-67/PVA/SA hydrogel and graphene/ZIF-67/PVA/SA hydrogel) were vacuum freeze-dried for 24 h. The obtained biomimetic aerogels with honeycomb structure were called PVA/SA, graphene/PVA/SA, ZIF-67/PVA/SA and GZPS respectively.

4.2.6 Instruments and characterization

Morphological investigation was analyzed by using a field emission scanning electron microscope (FE-SEM, S-5000, Hitachi High-Tech Corporation, Japan). Element composition and distribution of the samples were analyzed by using a scanning electron microscope (SEM) equipped with an energy-dispersive spectroscopy (EDS) device (SEM, JSM-6010LA, JEOL Ltd., Japan). Before the morphological investigation, a layer of gold was sputtered onto samples' surface to prevent the accumulation of electrons by auto fine coater (JFC-1600, JEOL Ltd., Japan). The mechanical property test was carried out using a tensile tester (MCT-2150, A&D, Japan). TG-DTA curves were obtained by thermogravimetry analyzer (TG8120, Rigaku, Japan). The viscoelasticity of the sample was tested by dynamic viscoelasticity measuring device (DVA-225, itk dva, Japan). The chemical component was recorded by utilizing Attenuated total reflectance-Fourier

transform infrared (ATR-FTIR) (FT/IR-6600•IRT-5200, JASCO Corporation, Japan). The X-ray diffraction (XRD) patterns were recorded with a diffractometer (MiniFlex300, Rigaku Corporation and its Global Subsidiaries, Japan). X-ray photoelectron spectroscopy (XPS) analyses were performed using an X-ray photoelectron spectrometer (AXIS-ULTRA HAS SV, Kratos Analytical Ltd., Japan). UV–vis–NIR spectra was measured by a Shimadzu UV-3600 spectrophotometer (MPC-3100, SHIMADZU CORPORATION, Japan). Static water contact angles (WCA) were measured ten times on the different points of each sample by an automatic contact angle meter (DMs-400, Kyowa Interface Science Co., Ltd., Japan) at room temperature 20 ± 2 °C with a 1 μ L droplet each time. The temperature infrared images were recorded by a FLIR thermal imaging camera. The ions' concentrations in natural seawater and the collected water were determined with the help of ICP emission spectroscopic analyzer (SPS3100, Hitachi High-Tech Science Corporation, Japan).

4.2.7 Water harvesting and release assessments

The mass of the aerogel was recorded before the fog absorption experiments. The ambient temperature is 20 ± 2 °C and the relative humidity is 45 ± 5 %RH. The humidifier (HTJS-007 J-WH, MODERN DECO Co., Ltd., Japan) provided a fog flow was placed 15 cm away from the tested aerogel. To facilitate long-term water collection, a facile aerogel water collection device was settled up, and the detailed structure can refer to the **Fig. 4-1**. The whole fog-harvesting device was placed on the electronic balance (GR-200, A&D Company, Japan) and the real-time fog-harvesting mass were recorded. Simultaneously, to exclude the interference of other factors, and the device without aerogel was also tested for water collection. Finally, the results of each hydrogel water harvesting trend were also subtracted from the blank control group to obtain the results of water uptake by the hydrogel water harvesting device.

The water uptake rate (W_u) and water harvesting ratio (R_h) can be calculated by the following equations (eqs. (1) and (2)):

$$W_u = \frac{m_1 - m_0}{m_1} \times 100\% \quad (1)$$

$$R_h = \frac{m_1 - m_0}{m_0} \quad (2)$$

where m_0 is the mass of the initial mass of the hydrogel before the water harvesting behavior (g), m_1 is the mass of the current mass of the water harvesting system (g) (after removing the water harvesting mass of the blank device).

The water release experiment was performed at 20 ± 2 °C and $45 \pm 5\%$ RH, accompanied by being exposed to solar simulator (XES-40S3-TT, SAN-EI Electric, Japan) of 1 sun irradiation. The mass of the irradiated hydrogel was recorded by the weighing system in real time. Water release unit gram mass (W_r) and water release efficiency (η_r) were obtained by calculation through the following equations (eqs. (3), (4)), respectively:

$$W_r = \frac{m_b - m_a}{S_r} \quad (3)$$

$$\eta_r = \frac{W_r}{t} \quad (4)$$

where m_a is the mass of the initial mass of the hydrogel before the water release behavior (kg), m_b is the mass of the current mass of the hydrogel (kg). t is the irradiation time (h), S_r is the area of the irradiated top surface of the hydrogel (m²).

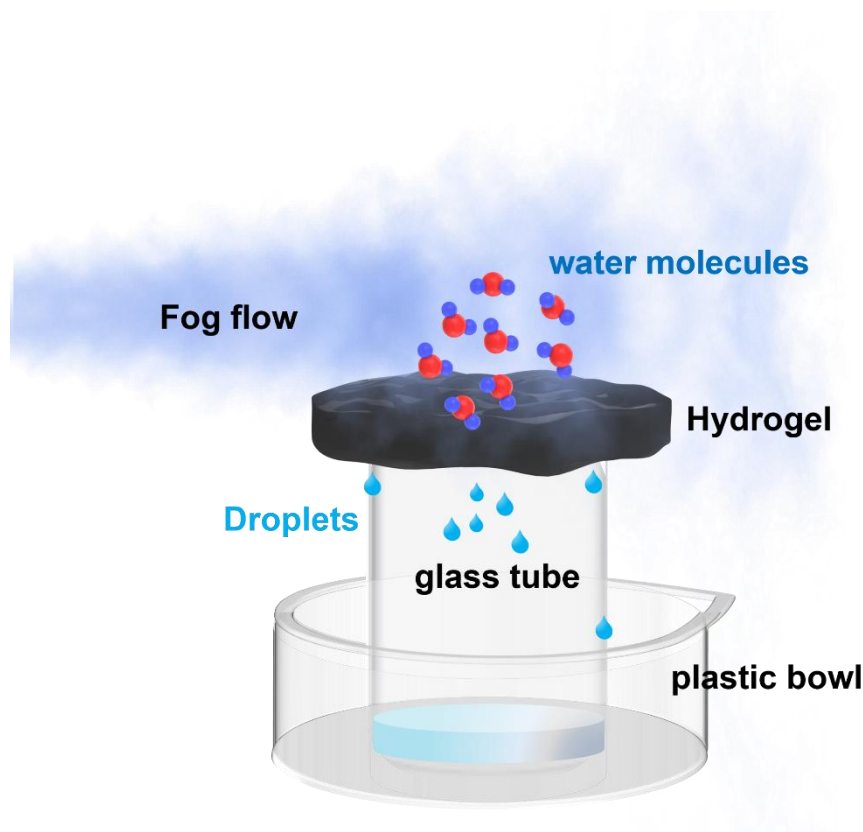


Fig. 4-1. Schematic diagram of a facile water harvesting device.

4.2.8 Preparation of the solar-driven seawater evaporation device system and performance measurements

In order to enhance the evaporation effect of the hydrogel based on previous related researches, a proper evaporation system was adopted [29], [44]. In order to distinguish materials in different hydration states, PVA/SA, graphene/PVA/SA, ZIF-67/PVA/SA and GZPS aerogel after water harvesting were labeled as PVA/SA gel, graphene/PVA/SA gel, ZIF-67/PVA/SA gel and GZPS gel. The gel was taken as solar irradiation functional absorber, the polystyrene foam was applied as the thermal insulation and seawater-trapped layer, cotton was used as a channel to transport seawater. In subsequent experiments, the device system without the gel was also tested to determine the role of the solar irradiation absorber in solar-driven water collection and release.

The device system was applied for the following solar-driven evaporation and desalination experiments under the simulated 1 sun. The real-time mass and temperature changes were recorded during the evaporation experiment. The water evaporation mass change per area (Δm_e), evaporation rate (R_e) and solar-thermal conversion efficiency (η_e) can be calculated by the following equations (eqs. (5), (6) and (7)):

$$\Delta m_e = m_a - m_\beta \quad (5)$$

$$R_e = \frac{\Delta m_e}{S_e T} \quad (6)$$

$$\eta_e = \frac{(R_{e1} - R_{e0})h_v}{C_{opt}P_0} \quad (7)$$

where m_a refers to the current mass of the whole evaporation device (kg), m_β is the mass of whole evaporation device before evaporation (kg). S_e is the area of the top evaporation surface of the hydrogel (m^2), and T is the solar evaporation time (h). where R_{e1} represents the solar-driven evaporation rate, R_{e0} is the dark natural evaporation rate, h_v donates to the liquid-vapor phase transition enthalpy, C_{opt} is the optical density, and P_0 donates to the power density of 1 sun radiation.

4.3 Results and discussion

4.3.1 Design and synthesis of biomimetic hydrogel

Bioinspired by the hydro-responsive behavior and morphological changes of *Selaginella lepidophylla* at various hydration states, as well as the hierarchical capillary water-collecting structure of honeycomb and the ability of pufferfish to absorb water, expand, and release water to shrink, the concept of biomimetic composite hydrogel was developed in this study has been proposed. As mentioned above, the water response behavior and morphological changes of *Selaginella lepidophylla* in different hydration states and the hierarchical capillary porous structure of the honeycomb that is conducive to water transmission and the use of polyvinyl alcohol and sodium alginate supplemented

with borax as a cross-linker. The properties of the functional hydrogel matrix prepared by the agent are very close. In addition, the addition of ZIF-67 and graphene will make the hydrogel have the performance of photothermal conversion, so that the composite hydrogel can release water and improve evaporation performance. This bioinspired composite hydrogel owns a macro/micro/nano hierarchical structure and is capable of producing clean water in various scenarios and under different water conditions. (**Fig. 4-2**).

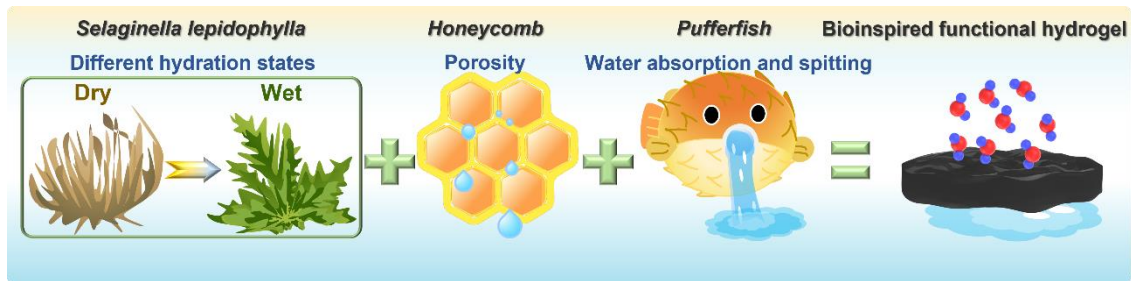


Fig. 4-2. (a) Scheme of integrating the features of the *Selaginella lepidophylla*, pufferfish and honeycomb to inspire the fabrication of hydrogel.

The main matrix materials of hydrogels are PVA and SA. To determine the appropriate ratio of PVA to SA and the minimum amount of cross-linking agent required, the physical fluid gel PVA/SA in different mass ratios (1:2, 1:1, 2:1) that have been thoroughly mixed before were prepared. The same mass of borax solution was dropped to the pre-gel solutions' surfaces. After the cross-linking reaction overnight, the state of the gels with three ratios is shown in **Fig. 4-3**. From the states of the cross-linked hydrogels, it can be seen that the 1:2 pre-gel still presents a very strong fluid state. When the ratio is 1:1, although it has reached the cross-linked state, the degree of cross-linking in some areas with bubbles is not sufficient. Finally, the ratio of PVA/SA of 2:1 was used for subsequent preparation and applications. **Fig. 4-4 (a)** shows the specific details of the biomimetic hydrogel preparation process, using GZPS as an example. To investigate the effect of added functional nanomaterials, four types of hydrogels were prepared: PVA/SA

hydrogel without any added pre-gel, PVA/SA hydrogel with only graphene, PVA/SA hydrogel with only ZIF-67, and pre-gels added with both. At the same time, the chemical mechanism has also been elucidated. The -OH groups in PVA and SA reacted with tetrahydroxyborate anions (B(OH)_4^-) and formed bis(diol)-borax complexes as cross-linking points, then formed an interpenetrating polymer network hydrogel. The fabricated hydrogels were pre-frozen to maintain the porous state and then vacuum freeze-dried to enable the formation of a complete hierarchical porous structure. Specifically for its application, this hydrogel can effectively collect the fog when there is a fog flow in the surroundings in its dry state. After collecting water, it can release the water collected under solar irradiation. Simultaneously, it could also be applied in its wet state wet state for solar-driven seawater desalination (**Fig. 4-4 (b)**). All of these functions in different scenarios can be applied to produce clean water.

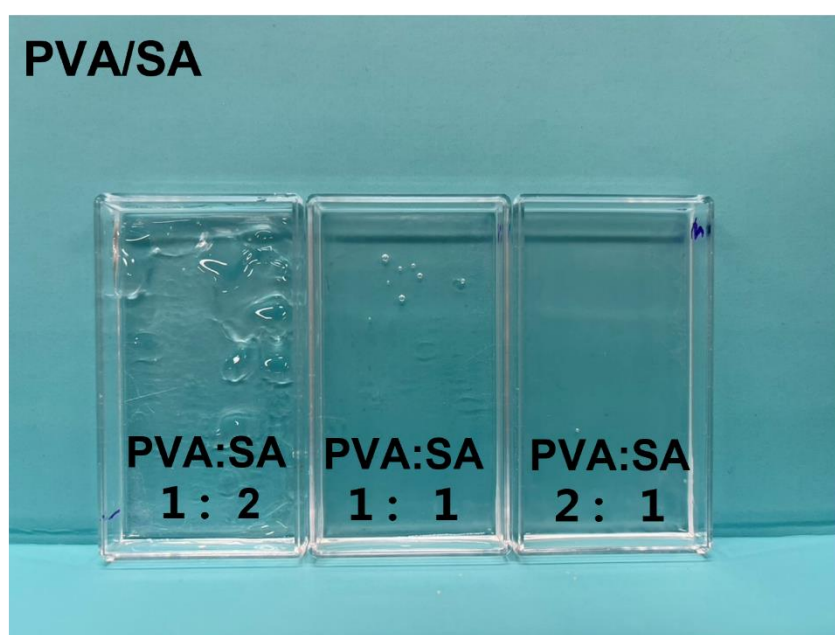


Fig. 4-3. The photo of the states of different ratios of PVA/SA pre-gel after one night cross-linked.

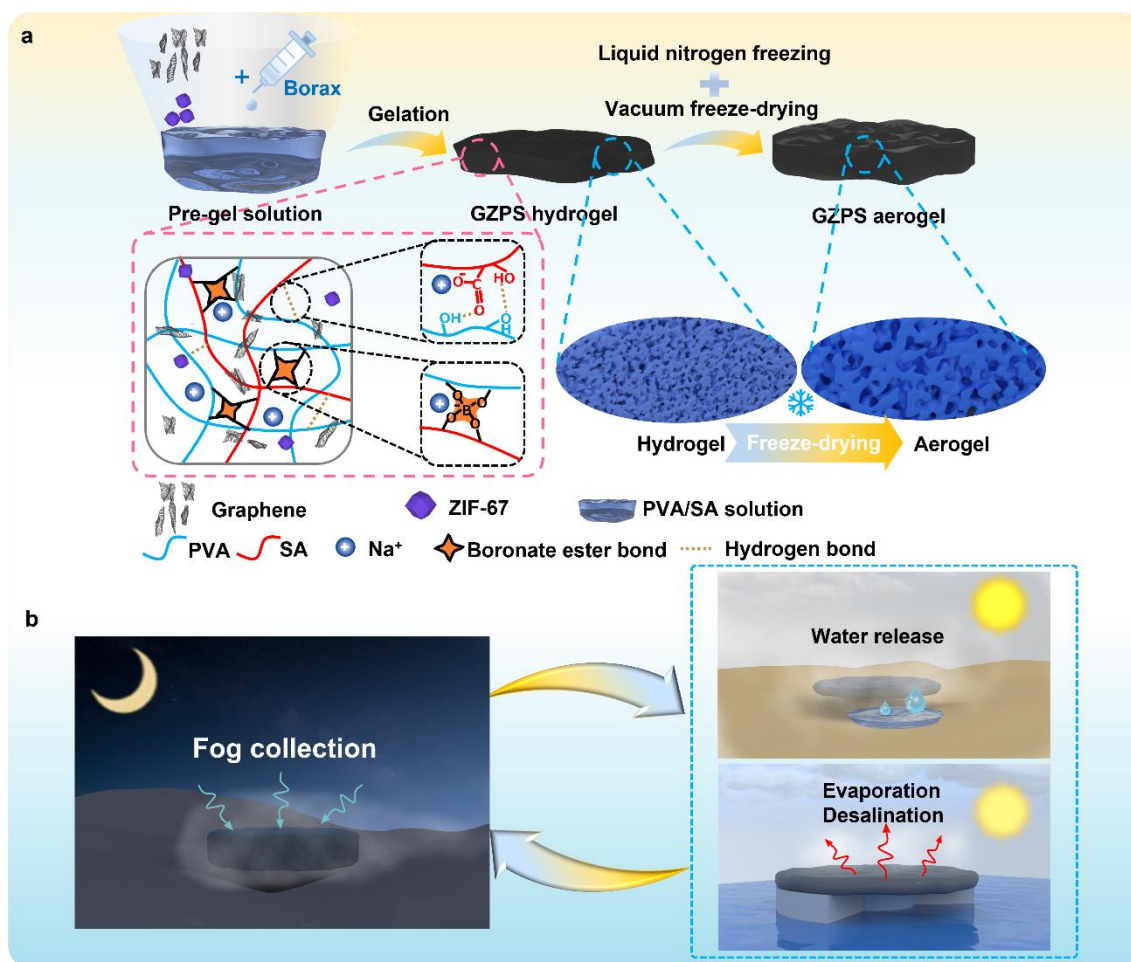


Fig. 4-4. (a) A flow chart of fabrication of GZPS hydrogels. (b) Schematic illustration of water harvesting, water release and solar-driven evaporation.

4.3.2 Appearance, performance characteristics and microscopic hierarchical structure of functionalized hydrogels

Fig. 4-5 (a) shows that the original PVA/SA hydrogel dyed with edible red and blue pigments, undyed hydrogel and GZPS hydrogels can be molded into various shapes, showing its softness and moldable, which can be used according to different scenarios or assembled containers. **Fig. 4-5 (b-e)** demonstrate the self-healing properties of hydrogels, even after being stretched, twisted, frozen and thawed, as well as chopped.

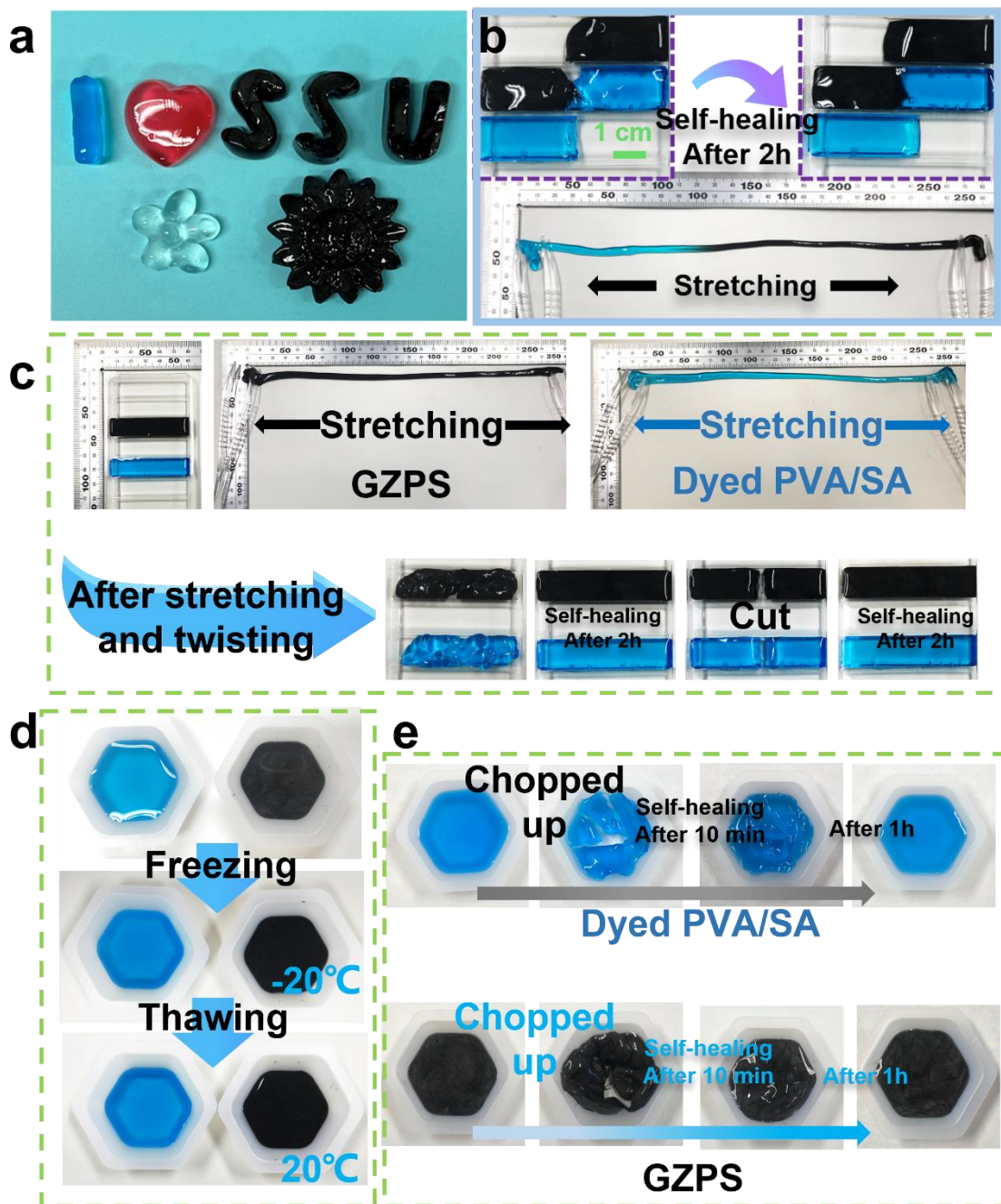


Fig. 4-5. (a) Different fabricated hydrogels of various shapes. (b-e) Self-healing behaviors in different conditions and situations.

These phenomena can be attributed to the reversible boronic ester bonds and the bis(di-ol)-borax complexation went through the PVA and SA networks, forming reversible dynamic covalent bonds, which made the PVA/SA-based hydrogels own self-healing

properties [17]. The appearance of small-sized aerogels formed after pre-frozen and vacuum freeze-drying and the lightweight characteristic can be seen in **Fig. 4-6**. It further hinted that it can be easily carried and applied at anhydrous state. The morphology and EDS distribution of self-made ZIF-67 nanocrystal powder and treated graphene are shown in **Fig. 4-7** and **4-8**. **Fig. 4-9** show the morphological structures of four aerogels. It can be observed that all four hydrogels have a honeycomb-like structure and a macro/micro/nano hierarchical structure. This peculiar macro-porous structure owning dense graded microstructure will affect the photothermal effect, steam escape, water transport performance and salt diffusion [62]. No matter whether the functional nanomaterials were added or not, the biomimetic structure of the honeycomb were not be affected. Graphene possesses multi-layers sheet structure, so it cannot be directly observed on the Graphene/PVA/SA skeleton structure. On the contrary, ZIF-67 could be clearly observed which are marked in purple (enlarged views inserted in **Fig. 4-9 (g, h)**). EDS distribution of **Fig. 4-10** and **Fig. 4-11** exhibit that B, C, O, and Na elements evenly distributed in each hydrogel at the microstructure level, and Co element also appeared uniformly in the added hydrogel of ZIF-67, which means each component material was uniformly distributed throughout the hydrogel and formed a network structure. Strategies such as multi-hierarchical structure can maintain stable evaporation rate and inhibit salt precipitation [62]. In addition to demonstrating the water absorption and release properties of the GZPS gel, it is also important to evaluate its mechanical properties, as they are crucial for its practical application. In **Fig. 4-12(a)** and **(b)**, the tensile stress–strain curve and 50 cyclic compressive loading/unloading cycles of the GZPS gel were shown, respectively. Furthermore, dynamic rheological testing was also performed on the GZPS gel (**Fig. 4-12(c)**), which showed its viscoelastic properties.

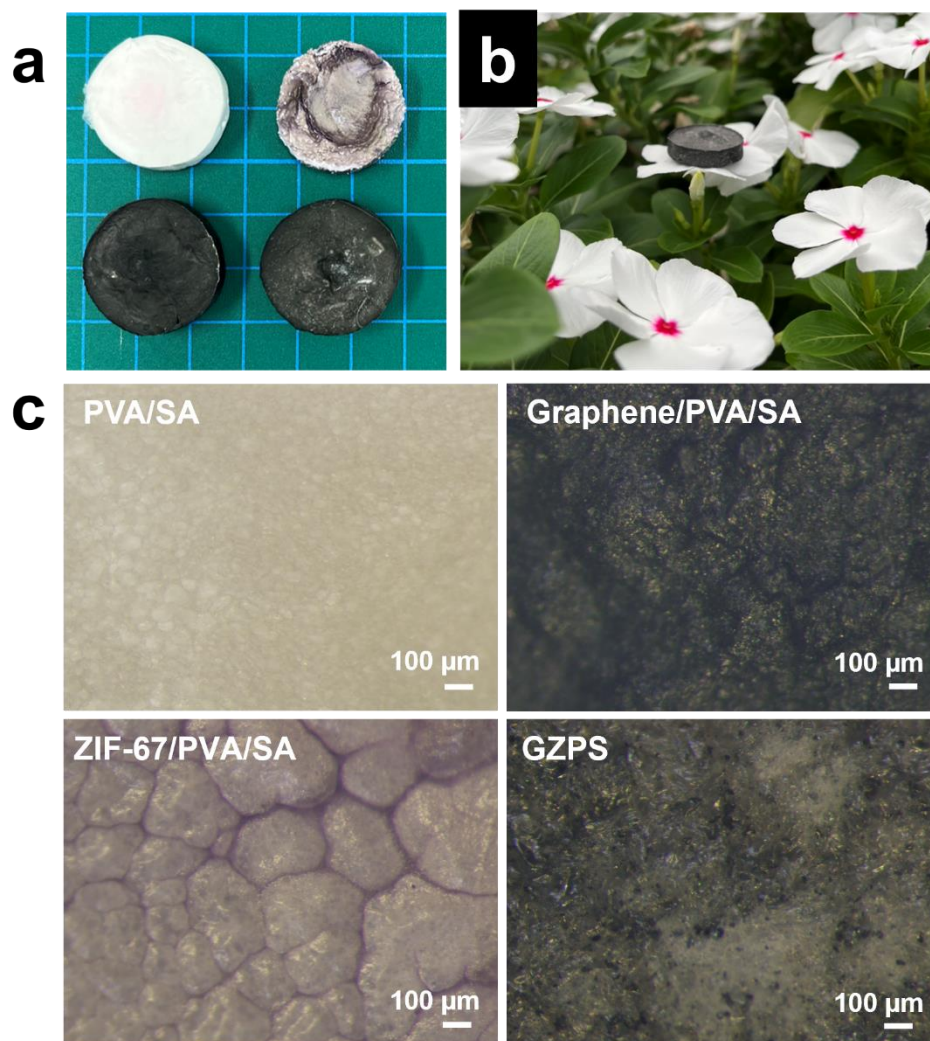


Fig. 4-6. (a) Small-sized aerogels' appearances, and the lightweight demonstration (b). (c) Aerogel surface viewed through optical microscope.

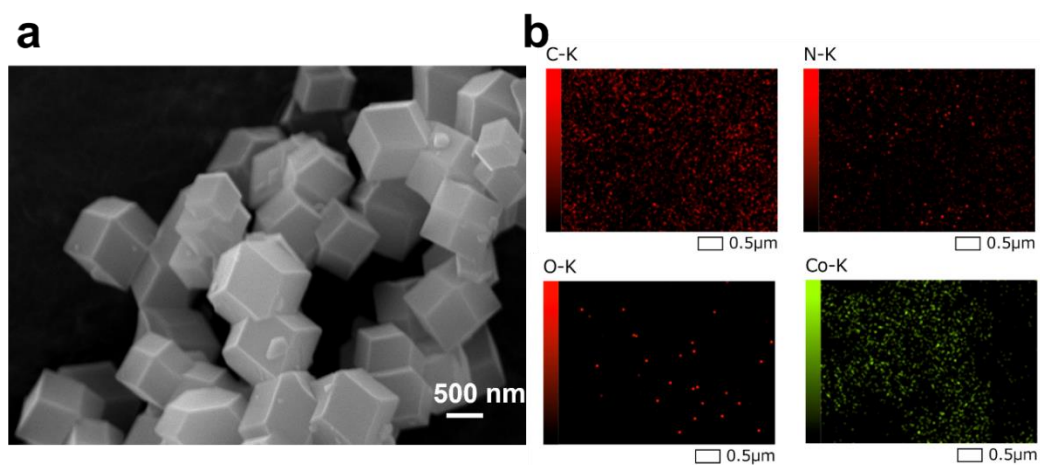


Fig. 4-7. FE-SEM image and elemental distribution images of ZIF-67.

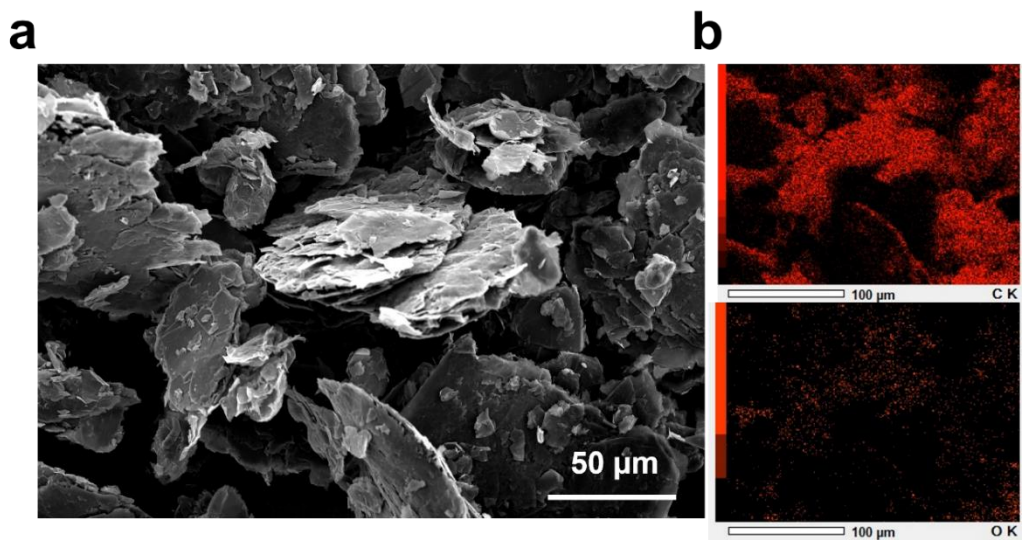


Fig. 4-8. FE-SEM image and elemental distribution images of treated graphene.

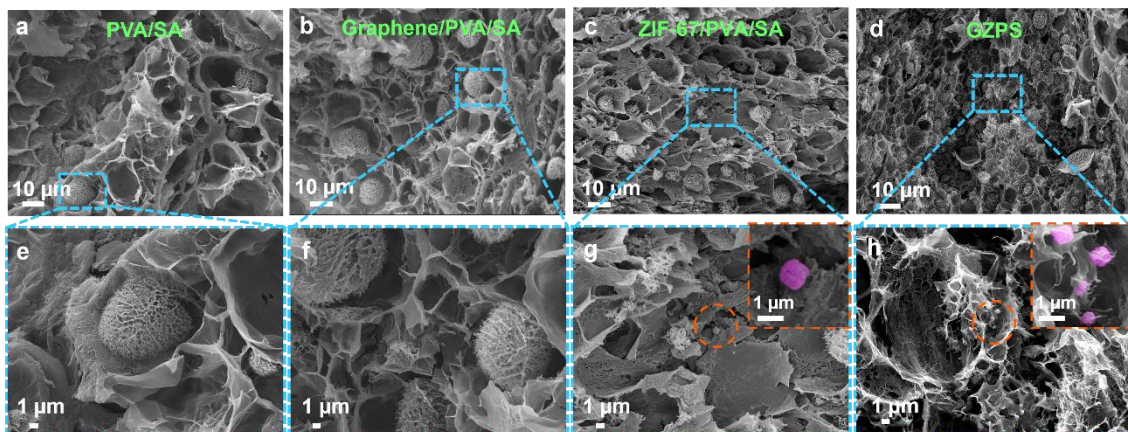


Fig. 4-9. FE-SEM images of different aerogels. The corresponding enlarged images inserted reveal hierarchical biomimetic structures.

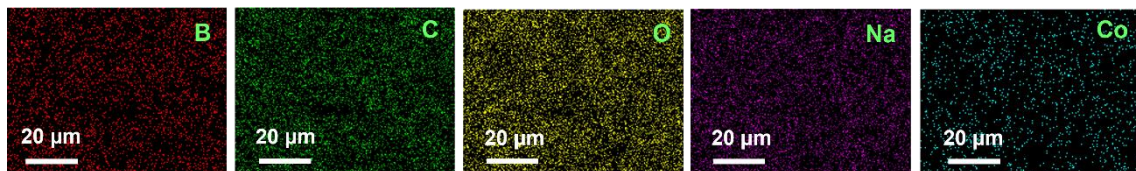


Fig. 4-10. Elemental distribution on GZPS hydrogels.

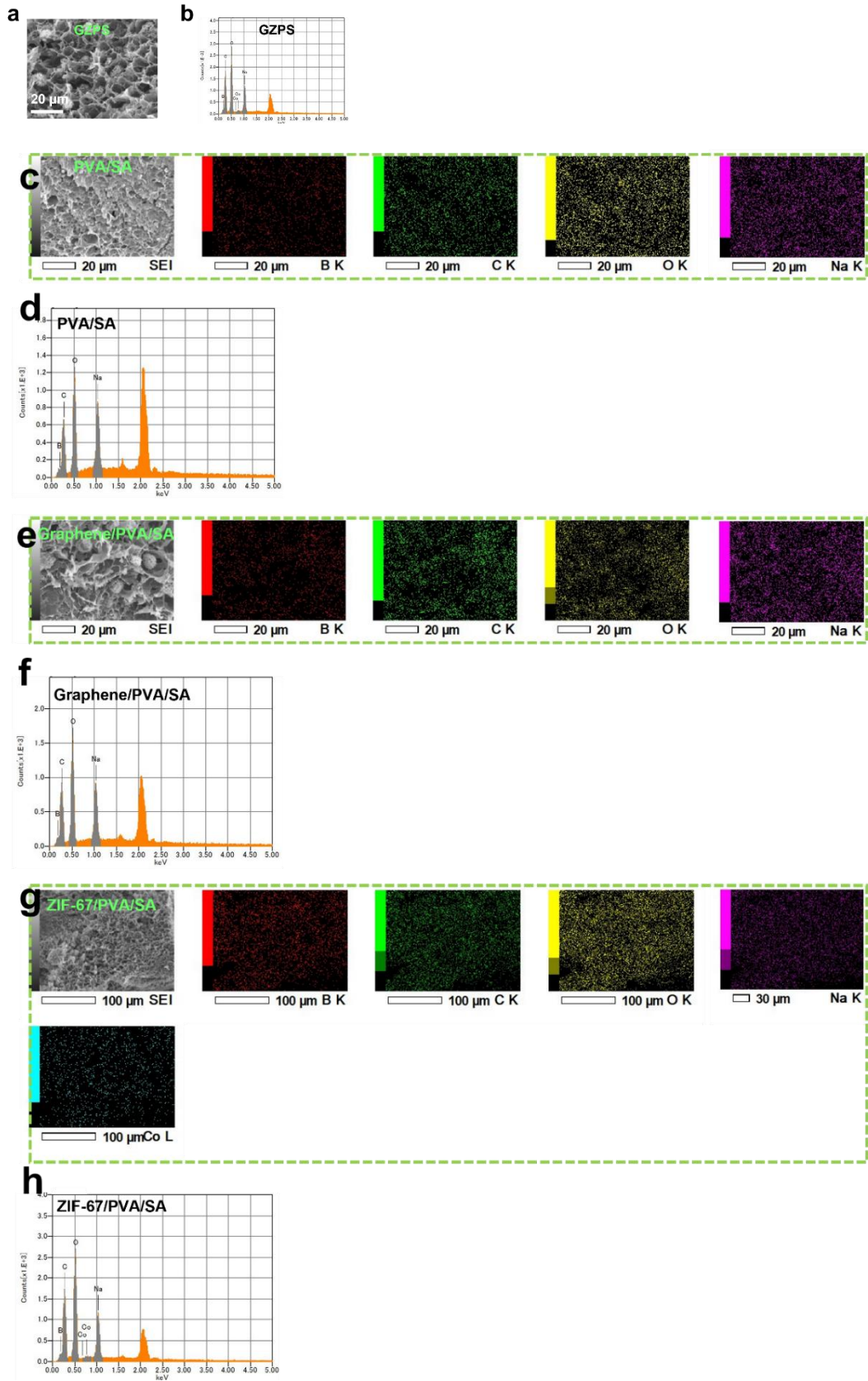


Fig. 4-11. FE-SEM images and corresponding elemental distributions of four kinds of hydrogels. (a) FE-SEM image, atomic and weight percentage (b) of the of the GZPS. (c) FE-SEM and EDS images of PVA/SA with atomic and weight percentage (d). (e) FE-SEM and EDS images of graphene/PVA/SA with atomic and weight percentage (f). (g) FE-SEM and EDS images of ZIF-67/PVA/SA with atomic and weight percentage (h).

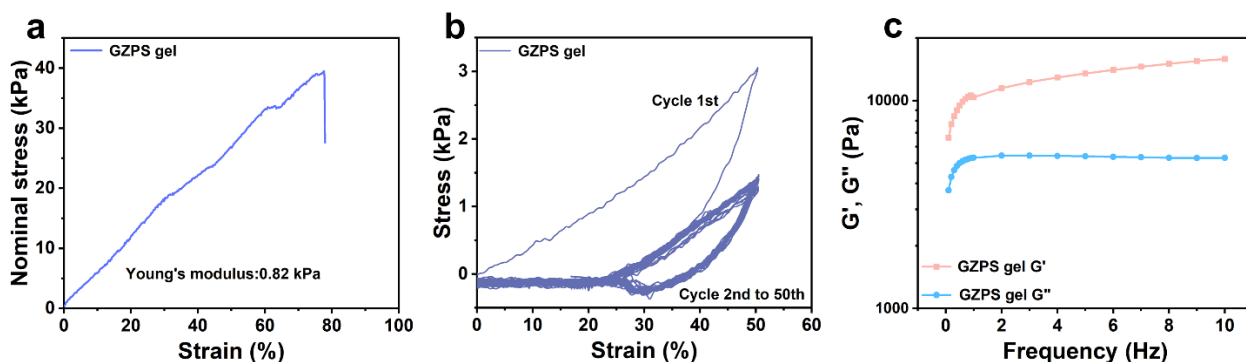


Fig. 4-12. Mechanical properties of GZPS gel. (a) Tensile stress-strain curve and Young's modulus of GZPS gel. (b) Compressive loading/unloading cycles curves of GZPS gel. (c) Storage modulus (G') and loss modulus (G'') versus frequency of GZPS gel.

4.3.3 Chemical composition and surface wettability of hydrogels in different hydration states

Chemical structures and compositions of the four hydrogels were characterized, and the results are presented in **Fig. 4-13~16**. FTIR spectra in **Fig. 4-13 (a)** and **Fig. 4-14** demonstrate the chemical components of hydrogels. The broad peak at 3502 cm^{-1} corresponds to the stretching vibration of O–H. The peak at 1356 cm^{-1} is the characteristic absorption peak of the B–O group from borax. Broad absorption bands at $3200\text{--}3600\text{ cm}^{-1}$ corresponding to the O–H stretching vibrations from the –OH groups of PVA and SA were found in four different hydrogels. The sharp peaks at 1027 cm^{-1} and 1600 cm^{-1}

correspond to the C–O stretching vibration of the –COOH groups and the symmetric stretching vibration of the C–O–C linkages of SA.

The characteristic peaks of borax, PVA, and SA were observed in all four hydrogels, implying that these materials' components were incorporated into the hydrogels successfully.[63] Further, in order to confirm that ZIF-67 was successfully introduced, XRD characterization was introduced (**Fig. 4-13 (b), 4-15**), and the characteristic diffraction peaks of other substances were indeed not observed in the original PVA/SA without any functional nanomaterials being added. The characteristic diffraction peak of graphene appears in both graphene/PVA/SA and GZPS, and the characteristic peaks of ZIF-67 nanocrystal powder also appears in ZIF-67/PVA/SA, but the characteristic peak of graphene was not obvious, so the XPS was relatively sensitive to perform analysis on GZPS, it can be deduced that GZPS has successfully incorporated graphene and ZIF-67 from its scanned full spectrum as well as the full surveys of added graphene and ZIF-67 (**Fig. 4-13 (c), 4-16**).

Considering that the surface wettability of prepared hydrogels in different hydration status has a great influence on the fog collection performance and seawater evaporation, [49, 64] the water contact angles of the samples were measured. Each sample was tested ten times at different positions on the surface, and since the samples were found to be hydrophilic and swiftly absorbed 1 μL of testing water droplets, WCAs of the samples at 100ms were recorded, and the average value and standard deviation were calculated.

From **Fig. 4-13 (d)**, it can be found that the four aerogels formed by freeze-drying are all hydrophilic, and the average WCA of GZPS in the aerogel state is 42.4° . The aerogels with hydrophilicity are also conducive to the subsequent water collection effect. Furthermore, after becoming wet during the water harvesting experiment, the WCAs became smaller, leading to the surface of the substrate of material more hydrophilic. As a result, the average WCA of GZPS gel is reduced to 13.3° . The hydrophilic matrix can ensure that the surface of the gel material will be more hydrophilic during evaporation, which is beneficial to fast water transfer to the evaporation surface as well as facilitates

the diffusion of salts to reduce the impact of salt precipitation on seawater evaporation efficiency thus improving lifespan and solar-to-steam conversion efficiency.

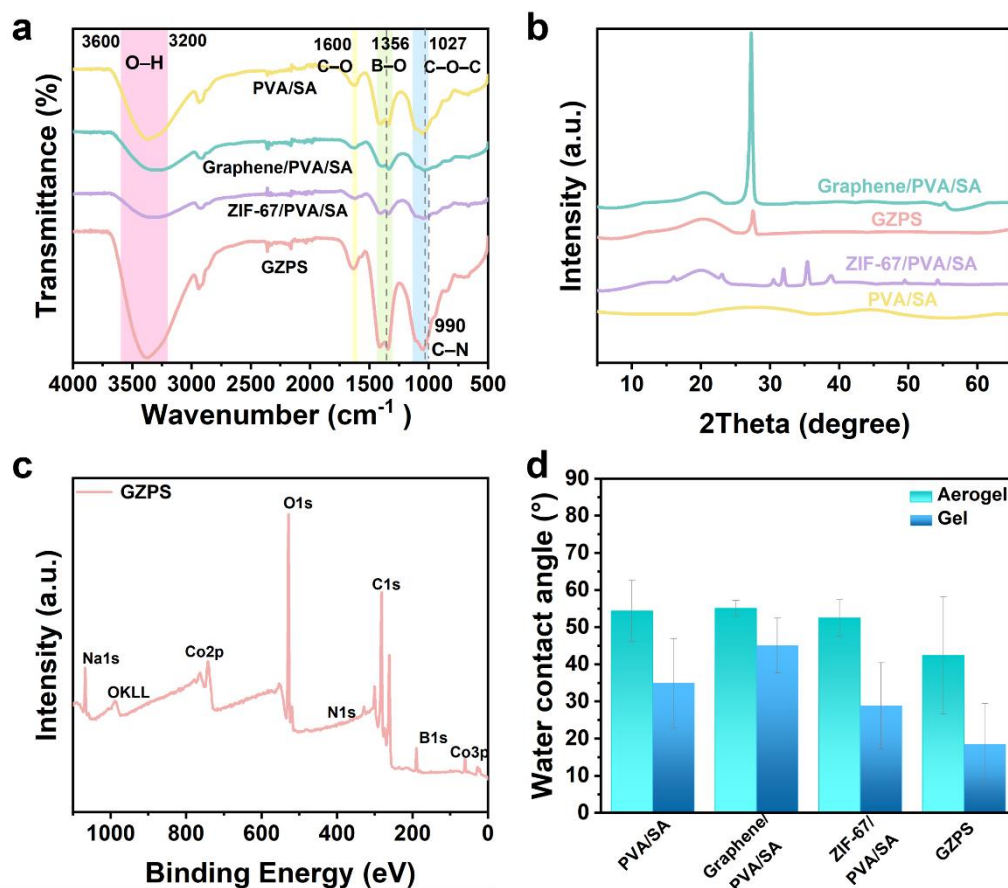


Fig. 4-13. (a) FTIR spectra, (b) XRD patterns of all samples, (c) survey XPS spectra of GZPS, and (d) Static WCAs of hydrogels in different hydration states.

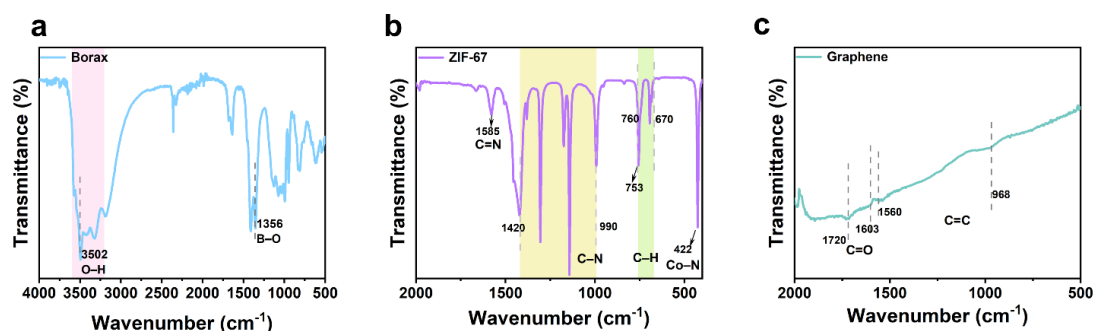


Fig. 4-14. FTIR spectra of (a) Borax, (b) ZIF-67, and (c) graphene.

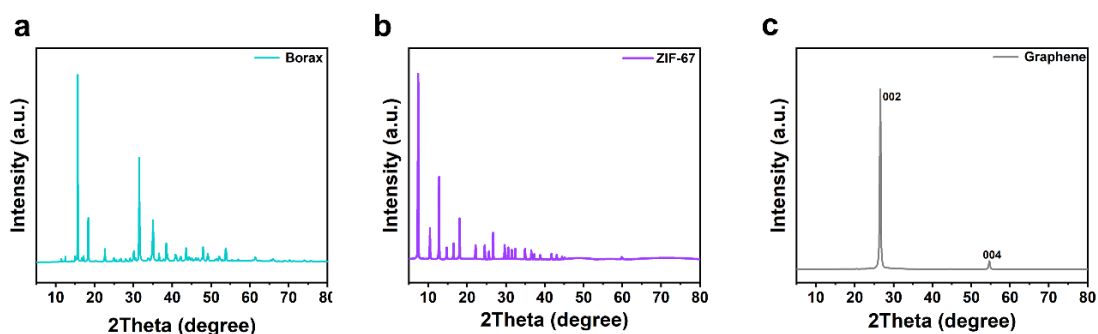


Fig. 4-15. XRD patterns of (a) borax, (b) ZIF-67, and (c) graphene.

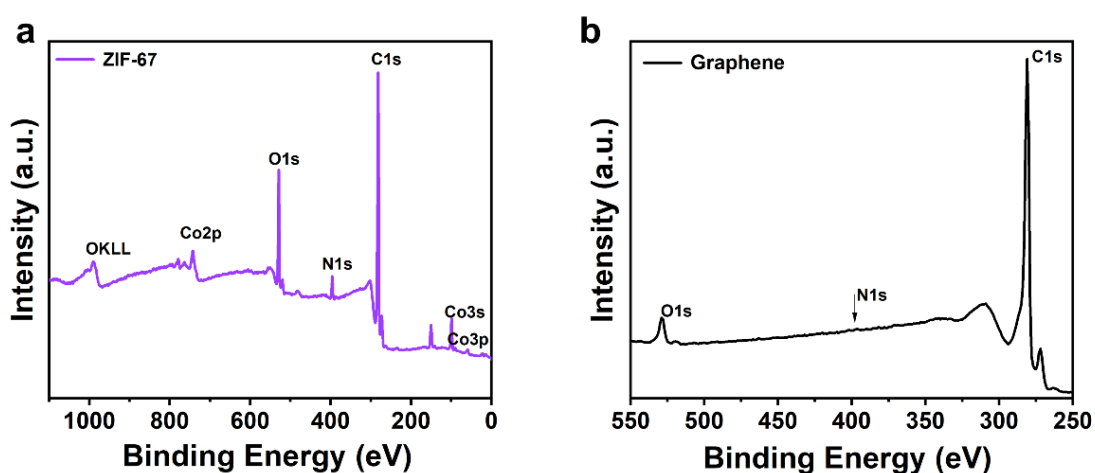


Fig. 4-16. Survey XPS spectra of (a) ZIF-67 and (b) graphene.

4.3.4 Photothermal conversion properties of hydrogels in different hydration states

The excellent photothermal performance of the hydrogel matrix is not only conducive to the subsequent water release but also beneficial to the evaporation and desalination of seawater driven by solar. Graphene and ZIF-67 were introduced into the hydrogel matrix because of their excellent photothermal performance and adsorption capacity, [65] while ZIF-67 is also often exploited in water treatment, visible light-driven catalysis and thermal decomposition applications [66].

The aerogel nearly contains no water, however it would be filled with water after the water harvesting experiment. These two states (dry and wet) lead to corresponding influences and differences on the solar-to-heat conversion performance. With the

intention of exploring the performance of solar-heat conversion, the temperature changes of the four kinds of aerogels and the aerogels after being implemented the water harvesting processes were monitored under 1 sun, when the ambient temperature is 20 ± 2 °C and the relative humidity is $65 \pm 5\%$. According to **Fig. 4-17 (a)**, although the temperature of PVA/SA aerogel rose slightly only to 32.4 °C within 10 min, the graphene/PVA/SA rose to 54.8 °C because of the addition of graphene, the solar-heat conversion ability has been significantly improved. Although the ZIF-67/PVA/SA aerogel rose to 47.8 °C, the GZPS aerogel with the same total mass ratio of the added functionalized nanomaterials with the ratio of graphene:ZIF-67 (1:1) could also rise to 54.7 °C in 10 min, which indicating that even if the amount of added graphene of GZPS was reduced to only half compared to the graphene/PVA/SA also been given the synergistic photothermal effect of ZIF-67. GZPS aerogel maintains good solar-heat conversion ability, and the synergistic effect of ZIF-67 and graphene accelerates the temperature change of GZPS. **Fig. 4-17 (b)** directly demonstrates the infrared imaging of surface temperature of four kinds of aerogels under 1 sun.

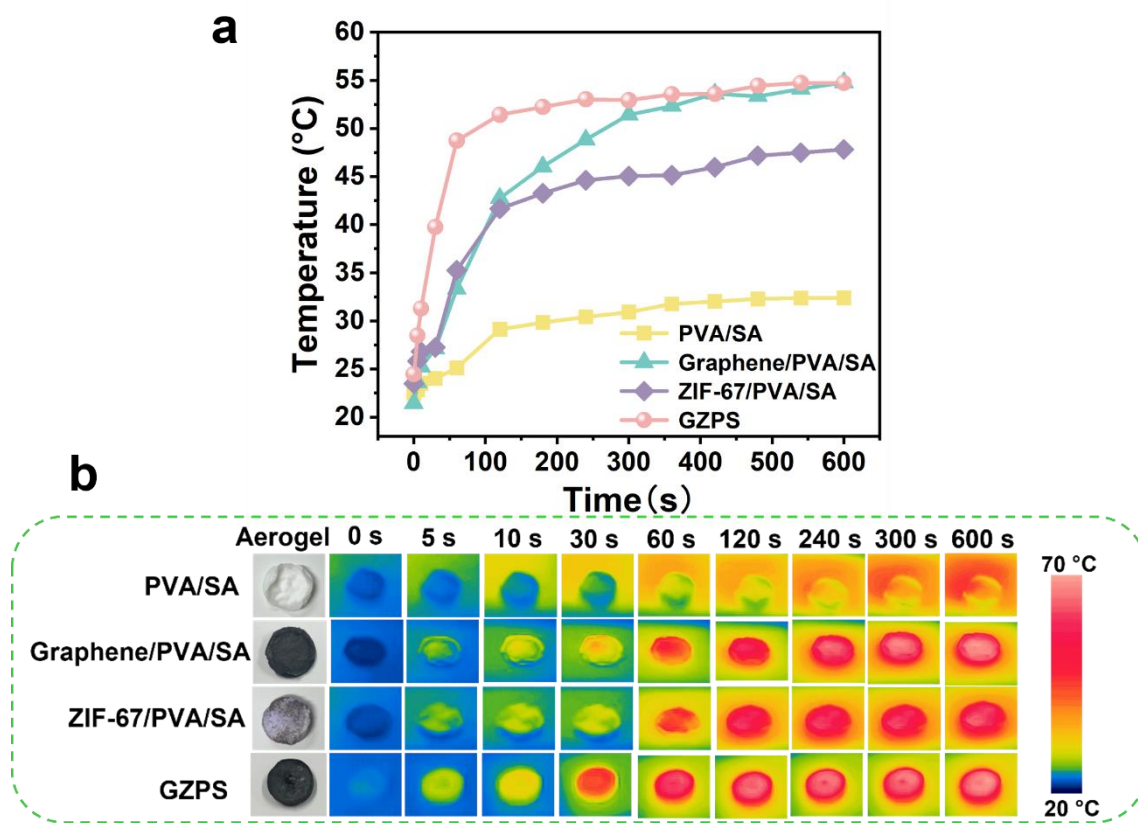


Fig. 4-17. (a) Surface temperature change of four kinds of aerogels (PVA/SA, graphene/PVA/SA, ZIF-67/PVA/SA, GZPS) under 1 sun. (b) IR images of four gels under 1 sun irradiation at various time points.

To verify whether the hydrogel molded into other irregular shapes could also maintain excellent solar-heat conversion performance, it was shaped like a flower. The flower-shaped one was also tested for light-heat conversion. It was found that the flower-shaped GZPS aerogel can also exhibit almost consistent temperature changes under solar radiation within 10 min (**Fig. 4-18 (a)**). The composite aerogel owns stable photothermal conversion performance no matter what shape it is. While maintaining the room temperature, when the external humidity was changed to 40 ± 5 °C, the cycle experiments with or without solar irradiation (**Fig. 4-18 (b)**) also proved its excellent photothermal conversion performance and implied that it can be utilized when the ambient humidity is lower, leading to photothermal effect even be better represented.

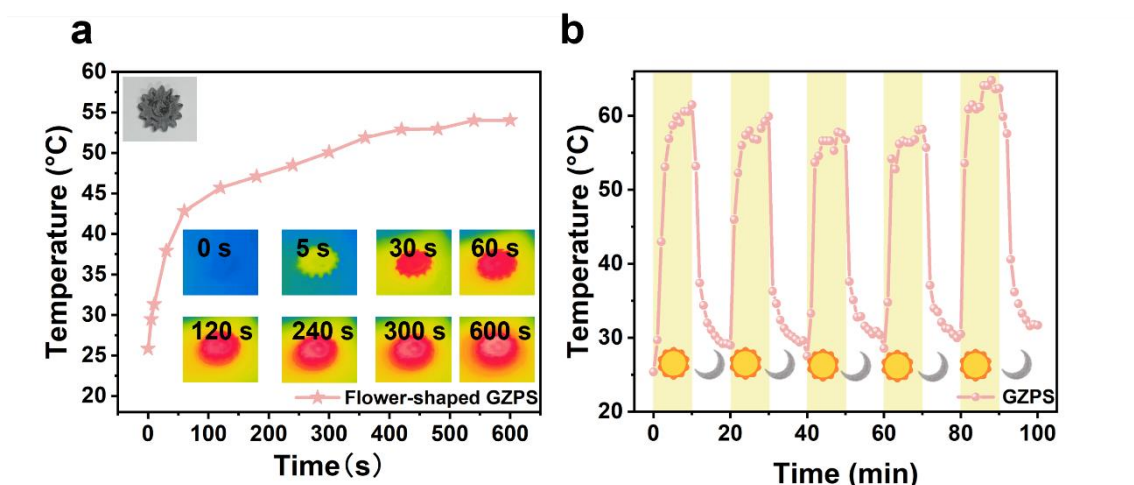


Fig. 4-18. (a) Surface temperature change of flower-shaped GZPS aerogel under 1 sun with the IR images inserted. (b) The temperature curves of photothermal cycle test for GZPS aerogel.

In addition to the excellent photothermal performance of the fabricated material in dry state without moisture, which proves that it can effectively absorb solar energy, whether it still has excellent photothermal conversion ability after the water harvesting is still worth being checked. After the water collection behavior of the four aerogels, similar characterization experiments were carried out to explore the solar-heat conversion capabilities of the four gels in the wet state. The full band absorption performance of four kinds of gels was investigated by the UV–vis–NIR spectrum. As shown in **Fig. 4-19 (a)**, PVA/SA gel reflects the worst absorption of solar light. However, neither with the addition of ZIF-67 or graphene or both, the totality solar light absorption rate is significantly improved, showing full-band absorption range from 300 nm to 2500 nm, thanks to ZIF-67 as well as the efficient photothermal conversion of graphene. It also proves that graphene/PVA/SA gel, ZIF-67/PVA/SA gel and GZPS gel can absorb sunlight effectively. Meanwhile, the solar absorption efficiency of the GZPS gel was calculated to be 95.25%, demonstrating its superior solar absorption capability. The temperature of the four gels all increased within 30 min under the solar radiation (**Fig. 4-19 (b)**). When the simulated

sunlight was turned on, the temperature rose rapidly, then the temperature increased slowly after 10 min. Considering that the gels were in the state of being irradiated by solar light, the water in the matrix was evaporated and absorbed heat from the matrix, the gels were taken away part of the heat. The upper limit temperature will be much lower than that of aerogel when it was dry, however graphene/PVA/SA gel and GZPS gel still maintain proper photothermal conversion capabilities, both reached about 36.4 °C. Correspondingly, when there is no light source the temperature of the gels would also decline rapidly, demonstrating its ability to respond rapidly to solar heat. In addition, the cycle photothermal test performed on GZPS gel showed its high photostability and stable energy conversion ability (Fig. 4-19 (c). Fig. 4-19 (d) directly shows the temperature distribution and temperature change of GZPS gel when it was irradiated by solar light during the cycle test. The results above indicate that the hydrogels added with graphene and ZIF-67 own good solar-heat conversion ability in both dry and wet states and can be utilized as desorption host materials for collected water and efficient solar absorbers for interfacial solar driven evaporation.

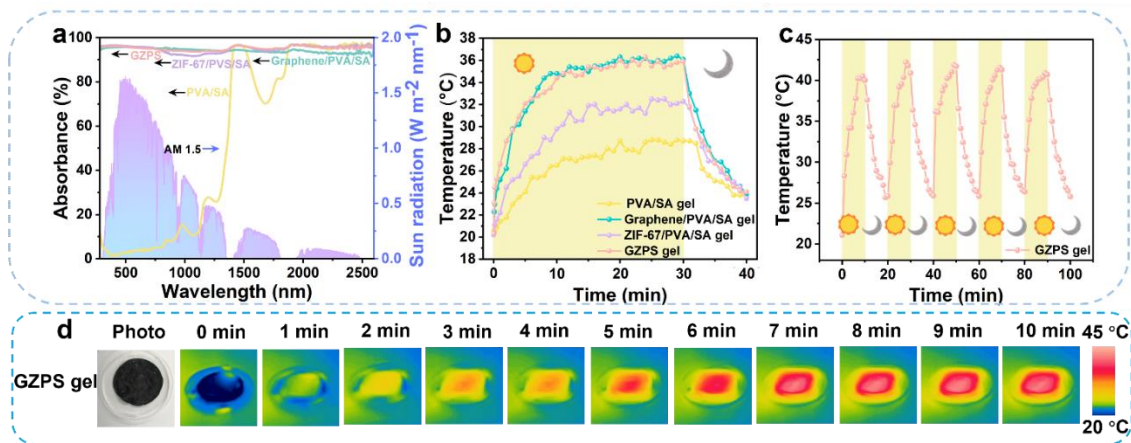


Fig. 4-19. (a) The UV–vis–NIR spectra of four gels (PVA/SA, graphene/PVA/SA, ZIF-67/PVA/SA, GZPS). (b) Surface temperature change of four kinds of gels under 1 sun and in dark. (c) The temperature curves of photothermal cycle test for GZPS gel under 1 sun. (d) IR images of GZPS gel under 1 sun irradiation at various time points.

4.3.5 Water harvesting and release performance

Four kinds of aerogels that have been fabricated were utilized to explore their water absorption and water release ability, the schematic diagram of the experimental setup is shown in **Fig. 4-20 (a)**. The fog flow velocity is $50\text{--}70\text{ cm s}^{-1}$ (tested by an anemometer, Model 6541-01, KANOMAX, Japan). After a period of water collection experiment, the gel enriched with collected water was placed under simulated sunlight. The desorption behavior was monitored, and its temperature change and real-time mass change were also recorded simultaneously. Regarding the water absorption capacity, two calculation methods are adopted to measure their water harvesting capacity. First, according to the Eq. (1), the ratio value of the real-time change mass to the real-time total mass (i.e., dry hydrogel mass plus collected water mass) can be used to measure the degree of water uptake, that is, the moisture content of the material overall. From **Fig. 4-20 (b)**, it is evident that all four aerogels were capable of effectively collecting water. However, PVA/SA hydrogel only captures water molecules through the matrix containing hydrophilic groups, resulting in a water uptake rate of only 78.73% after 3 h of water collection behavior. However, after adding the functional nanomaterials containing hydrophilic groups, the water uptake ratio of the hydrogel containing both of graphene and ZIF-67 reached 94.06% after a 3 h water harvesting test, which proved its relatively high-water content.

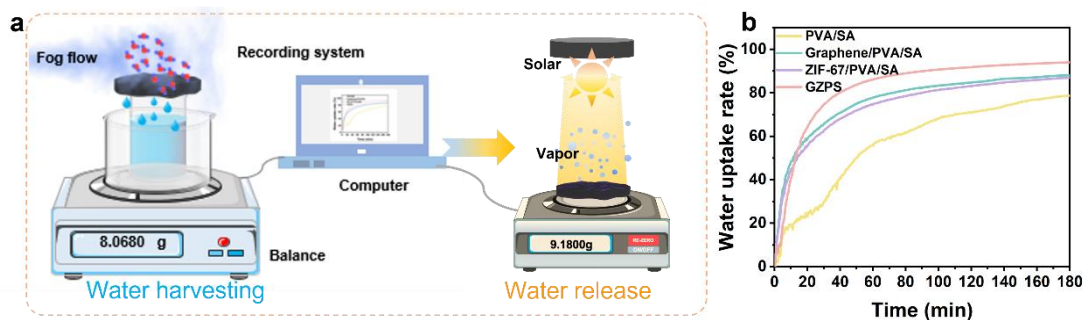


Fig. 4-20. (a) Schematic diagram of the water harvesting and release experiments. (b) Water uptake rate change of four aerogels during the 3 h water harvesting test.

According to Eq. (2), the mass of the aerogel when it did not contain water was used to measure how much water can be harvested per unit mass of the aerogel (**Fig. 4-21 (a)**). It can be seen intuitively that GZPS aerogel continued to harvest water within 3 h with the cooperation of a facile water collection device, the water harvesting ratio can reach 15.84 g g^{-1} , which is the highest among the four samples. In order to test whether GZPS aerogel possesses stable and excellent water harvesting characteristics and fabricating repeatability, ten GZPS aerogels produced at different times were subjected to water harvesting experiments, the experiment time was also extended to 5 h (**Fig. 4-21 (b)**). The water uptake ratio of different ten batches of the GZPS aerogels could reach above 95% approximately after 5 h, and the average water harvesting ratio even reached 22.45 g g^{-1} , which shows its excellent water absorption ability. Henceforth, only the GZPS series hydrogels were applied for the subsequent water release experiments and the following solar-driven seawater evaporation experiment.

The gels that have collected water were placed under simulated sunlight to explore their water release performance. According to Eq. (3), the water released per unit area of the irradiated gel under 1 sun is calculated over time. From the cumulative mass change (**Fig. 4-21 (c)**), it is apparent that the GZPS gel can release water rapidly in response to solar radiation, and the amount of released water significantly reduces in the absence of radiation. The real-time water release efficiency every 5 min (**Fig. 4-21 (d)**) was also obtained according to the Eq. (6). Under solar radiation, the GZPS gel exhibited rapid water release with a maximum efficiency of about $1.67 \text{ kg m}^{-2} \text{ h}^{-1}$. Although the efficiency decreased with the prolonged radiation time, it remained relatively high, possibly due to the hydration effect (**Fig. 4-21 (e)**). The polymer chains in the hydrogel can capture nearby water molecules by interactions such as hydrogen bonds to form bound water, while water molecules separated from the polymer chains are free water,

presenting same properties with those in bulk water. The intermediate area between bound water and free water owns intermediate water. This kind of intermediate water is considered as activated water which can be evaporated with less energy than bulk water [67]. Therefore, it is speculated that the activated water in the hydrogel should be evaporated firstly. As the evaporation time was prolonged, the remaining bound water and free water could not be easily evaporated, so the efficiency was reduced over time. However, relying on the excellent photothermal properties of graphene and ZIF-67 enabled it still release water under solar radiation. At the same time, to investigate the sustainability of its water harvesting and release efficiency, continuous cycle experiments were conducted. The experiment involved passive water collection for 3 h and solar-driven water release for 1 h, which was considered as one cycle (as shown in **Fig. 4-21 (f)**). The mass of the hydrogel was measured during each cycle to compare the water collection and release characteristics of the material. The unit weight was calculated based on the hydrogel matrix itself, without the aid of any additional device, to provide a more intuitive comparison. The calculation was based on the initial mass of each experiment of dry gel (for harvesting) or wet gel (for releasing). It can be seen that the water harvesting efficiency is relatively high at the beginning due to the aerogel state, which can reach 7.66 g g^{-1} . The water release ratio maintained at the same level, but as the number of cycles increases, its water absorption capacity decreased. This may due to the water release time of 1 h is not enough to release the all collected water, when the inside space of the gel is filled with water, the water collection ratio will be lower than when it starts to collect water in a dry state. As the number of cycle experiments increased, the GZPS gel was able to maintain a relatively stable water harvesting and release performance, even when it already contained water. To provide a more intuitive comparison with the original aerogel, the mass of water released by the GZPS gel was also calculated and plotted as a negative value against the weight of the original dry gel (**Fig. 4-22 (a)**). The fluctuations in a certain range prove its coherence, stability and durability in water harvesting and release. These behaviors and performance can be attributed to the synergistic effect of the

hydrogel matrix and the added ZIF-67 and graphene. By utilizing bionic structures (porous structures similar to honeycombs) and characteristics (Selaginella lepidophylla's ability to adapt to different conditions), the gel was fabricated to mimic the water absorption and spitting behavior of pufferfish. This achievement demonstrates the potential of biomimetic and multifunctional hydrogels for producing clean water in a variety of scenarios. The stable water harvesting and release performance of the GZPS gel, even after repeated cycle experiments, suggests that the material has good durability and can withstand long-term use, making it a promising candidate for practical applications. At the same time, a simple self-healing test on GZPS gel in different states was conducted. The GZPS aerogel with cracks in the dry state even could recover a certain degree of self-healing effect after water collection for 4 h ((**Fig. 4-22 (b)**)).

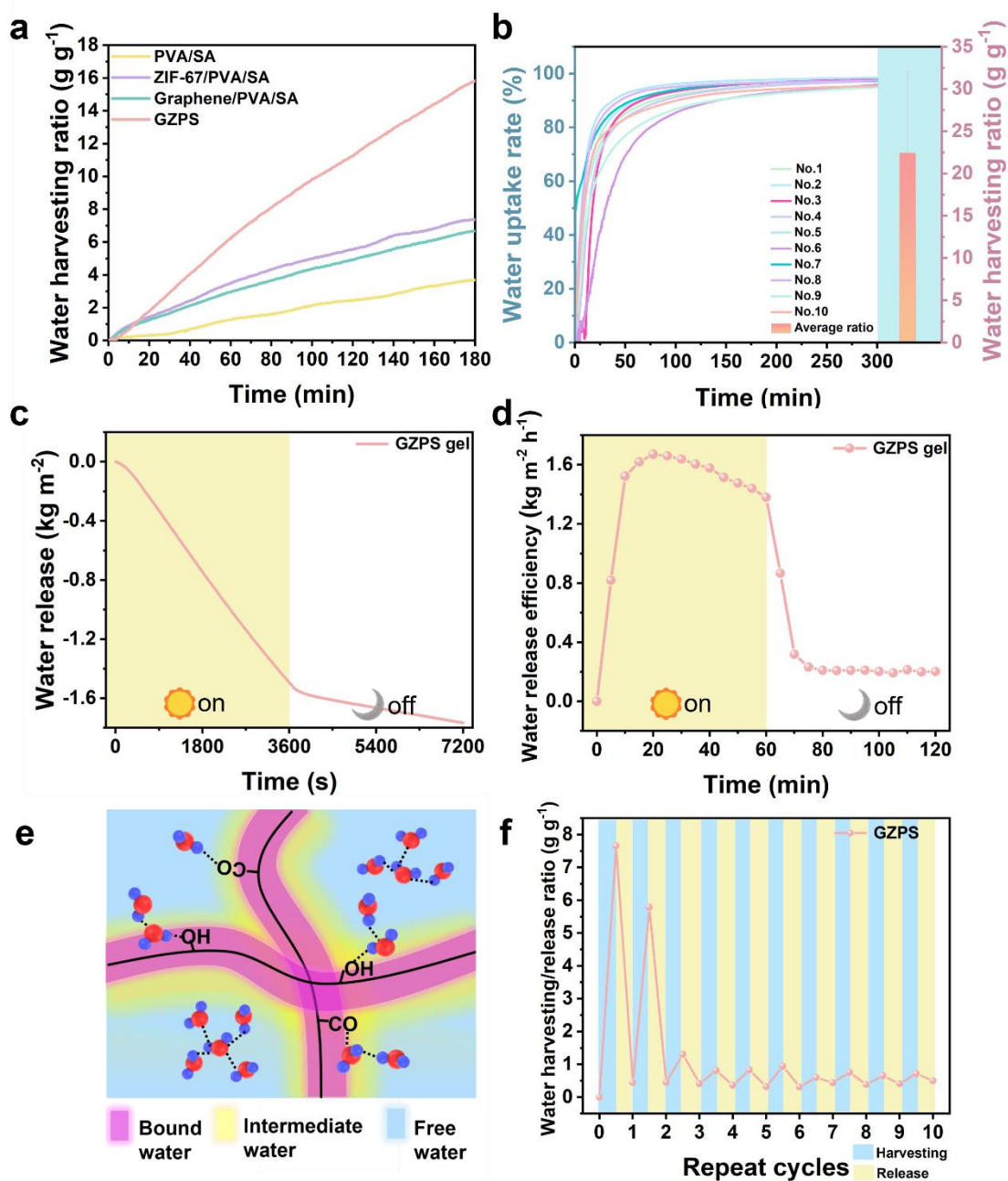


Fig. 4-21. (a) water harvesting ratio change of four aerogels during the 3 h water harvesting test. (b) Water harvesting performance of 10 GZPS aerogels during 5 h water collection tests. (c) Water release change of per unit area and water release efficiency (d) of GZPS gel under 1 sun or in the dark. (e) Schematic illustrating different water types—bound water, free water, and intermediate water in the hydrogel. (f) Continuous water harvesting and release cycle tests.

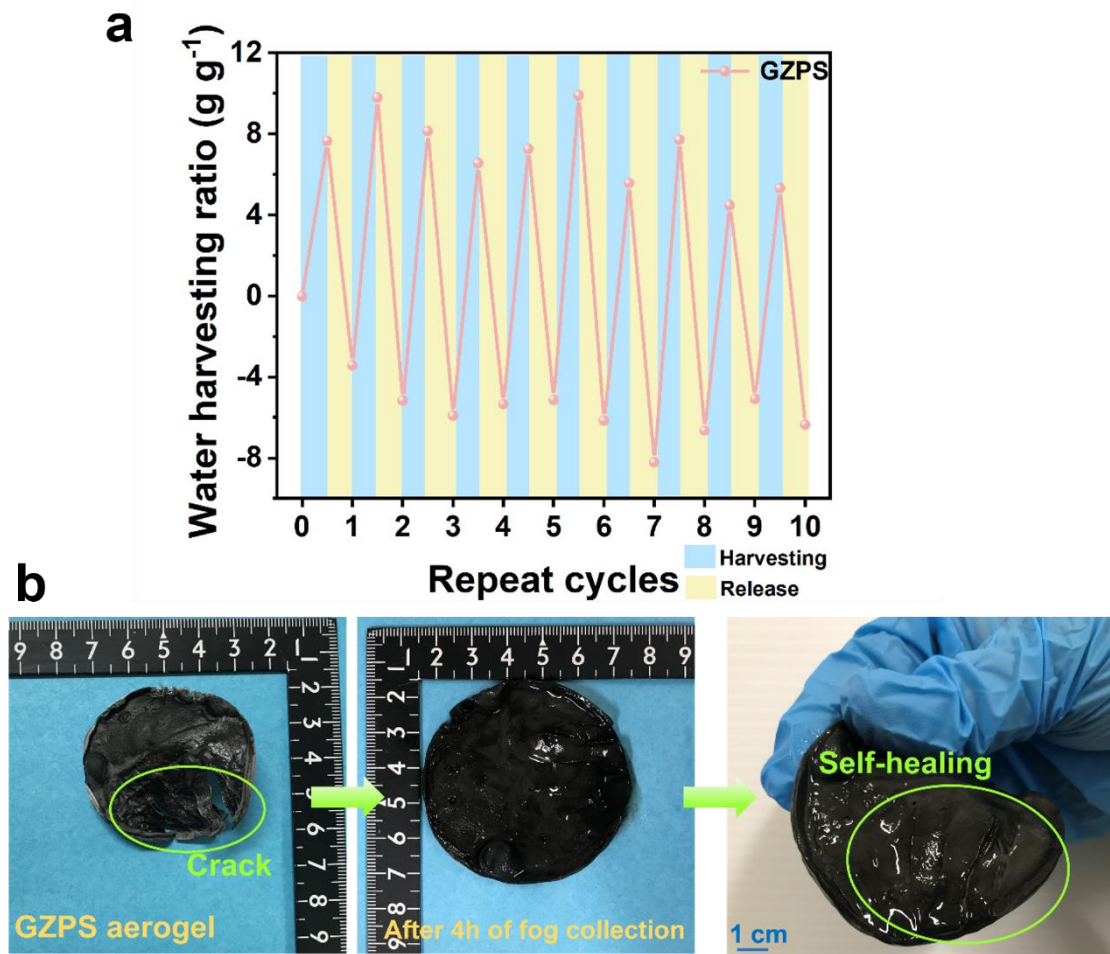


Fig. 4-22. (a) Cyclic stability test of the GZPS gel. (b) Self-healing of GZPS aerogel after water collection.

4.3.6 Solar-driven seawater evaporation performance

The excellent water transmission performance of GZPS gel can ensure the interfacial evaporation when it is driven by solar energy. On the other hand, its internal biomimetic porous hierarchical structure can also ensure the smooth passage of steam and effective desalination to purify seawater [62]. The schematic diagram of the seawater evaporation experimental device and recording concept system is shown in **Fig. 4-23 (a)**. To fully exert the function of the prepared hydrogel and prolong the service life, according to some previous studies [29], [37], [44], the specific appearance of the evaporator device system is shown in **Fig. 4-23 (b)**. It shows that hydrogel is used as the uppermost solar absorber

to convert the absorbed sunlight into heat energy to drive seawater evaporation. The thickness of GZPS is 5×10^{-3} m, the diameter is 2.5×10^{-2} m, and the surface area is about 1.9625×10^{-3} m². Polystyrene foam is applied as a heat insulation layer, and a cotton piece is inserted in the middle as seawater supply channel. When the entire facile evaporation device floats on the sea surface, seawater can be directly and effectively transported to the upper GPZS gel. Accompanied by proper heat management, GZPS can perform considerable evaporation potential. This entire device is called GZPS device system. For the sake of comparing the effectiveness of the GZPS in seawater evaporation, only natural seawater (from the Sea of Japan, Kamakura City, Kanagawa Prefecture, Japan, the coordinate of latitude and longitude is 35.30487°N, 139.50995°E), seawater configured with only the device system without GZPS and GZPS device system were used for seawater evaporation experiments. The temperature change IR images can be seen from **Fig. 4-23 (c)**. Correspondingly, the temperature change curves of 1 h radiation were also shown in **Fig. 4-23 (d)**. The temperature of the GZPS gel in the GZPS device system reaches about 42.5 °C, the surface temperature of the device system is 33.1 °C, and the natural seawater is 28.5 °C after 1 h. The results exhibit that the heat of solar radiation on the interface of the GZPS device system evaporator is significantly more concentrated than the other two, which can reduce unnecessary heat loss and improve energy utilization efficiency, thus promoting the efficient generation of solar steam. The mass change of GZPS device system, device system and natural seawater over time under different conditions is shown in **Fig. 4-24 (a)**. The natural seawater and device system are only 0.31 and 0.38 kg m⁻² h⁻¹ under 1 sun, but the GZPS device system is 1.34 kg m⁻² h⁻¹, three times higher than the natural seawater and device system. The GZPS device system, device system and natural seawater were tested continuously under the condition of the simulated sunlight being switched on and off (**Fig. 4-24 (b)**). It can be found that the evaporation speed of these three evaporation systems is faster under sunlight than dark condition, proving that the strong broadband absorption ability of GZPS gel can effectively promote the evaporation of seawater by solar. Then the corresponding real-

time evaporation efficiency and solar thermal conversion efficiency during each five minutes were calculated according to the Eqs. (6), (7), respectively (**Fig. 4-24 (c)**). The evaporation efficiency of GZPS device system can reach $1.47 \text{ kg m}^{-2} \text{ h}^{-1}$, and its solar thermal conversion efficiency even reached 92.32%, while the highest evaporation efficiency of natural seawater and device system without GZPS gel is only 0.44 and $0.55 \text{ kg m}^{-2} \text{ h}^{-1}$, respectively, and the solar thermal conversion efficiency is only 18.91% and 30.67%, respectively. Comparing these three evaporation behaviors, GZPS device system achieves satisfactory solar steam generation rate and efficiency. It should be noted that in such calculation steps, the energy loss like convection with air (q_{conv}), radiation to the environment (q_{rad}), and conduction to underlying bulk water (q_{cond}) was ignored [36]. By taking all the energy loss as well as the sunlight reflection and transmission into account, the energy efficiency is determined. (See detailed calculation **procedure A**). It is worth noting that a complex polymeric network could cause reduce the evaporation enthalpy, so the corresponding efficiency was also calculated [11]. (See detailed calculation **procedure B** and **Fig. 4-25**).

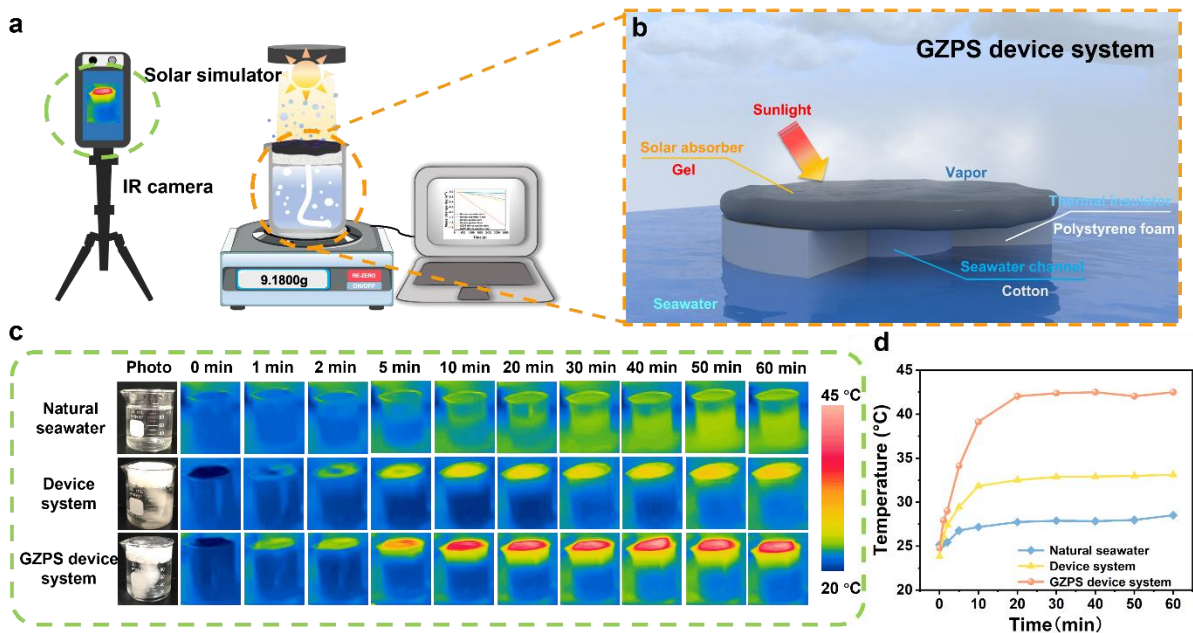


Fig. 4-23. (a) Schematic diagram of the solar-driven evaporation measurement system. (b) Specific appearance of the evaporator device system. (c) Thermal images of the natural seawater, the device system, and GZPS device system under 1 sun irradiation at various time points and (d) corresponding temperature changes.

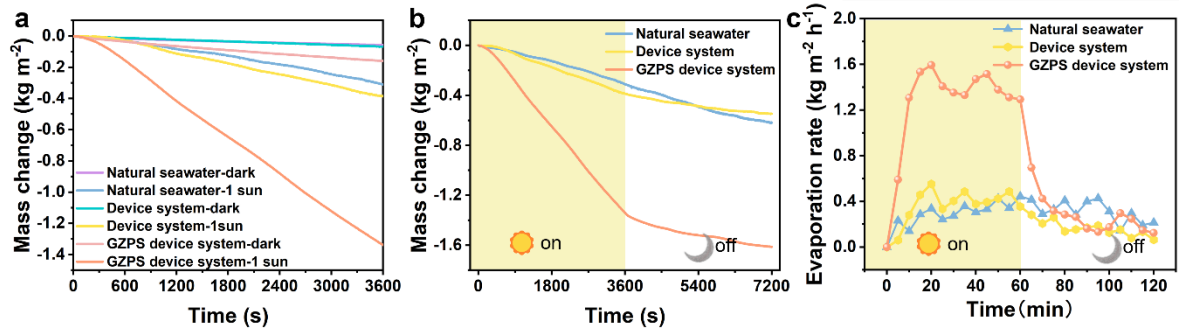


Fig. 4-24. (a) Mass change curves depending on the time of the natural seawater, the device system, and GZPS device system under different conditions. (b) Mass change curves of the natural seawater, the device system, and GZPS device system under 1 sun and in dark and the corresponding evaporation rate (c).

A. Heat losses and the corresponding energy efficiency

The incident sunlight (q_{solar}) is efficiently absorbed by the GZPS gel and converted to thermal energy during solar water purification (α is the solar absorptance ratio of the absorber, which is 0.9525 for GZPS gel). Most of the thermal energy produced is used for water evaporation (q_{evap}), whereas a small portion is lost by convection with air (q_{conv}), radiation to the environment (q_{rad}), and conduction to underlying bulk water (q_{cond}). Therefore, assume that the effect of cotton channel can be negligible, the input and output thermal energy can be described as:

$$\alpha q_{solar} = q_{evap} + q_{conv} + q_{rad} + q_{cond} \quad (1)$$

The convection heat loss is given by:

$$q_{conv} = h_{conv}(T_{evap} - T_0) \quad (2)$$

where h_{conv} is the convection heat transfer coefficient. The heat convection of air in the static condition is generally in the range of $5 \sim 10 \text{ W m}^{-2} \text{ K}^{-1}$. By taking h_{conv} as $5 \text{ W m}^{-2} \text{ K}^{-1}$, the convection heat loss is calculated to be $q_{conv} = 5 \times (315.65 - 304.35) = 56.5 \text{ W m}^{-2}$ (energy efficiency $\eta_A = 5.65\%$)

The radiation loss (q_{rad}) can be expressed as:

$$q_{rad} = \varepsilon\sigma(T_{evap}^4 - T_0^4) \quad (3)$$

where ε is the radiation emittance of the evaporation surface (ε is taken as 1 by assuming that GZPS gel is a black body). σ is the Steven-Boltzmann constant (i.e., $5.67 \times 10^{-8} \text{ W m}^{-2} \text{ K}^{-4}$). T_{evap} and T_0 are the temperature of the evaporation surface and the ambient environment, respectively. T_{evap} is tested as 315.65 K ($42.5 \text{ }^\circ\text{C}$, absorber surface equilibrium temperature), while T_0 is 304.35 K ($31.2 \text{ }^\circ\text{C}$, the ambient temperature near the evaporation surface). Thus, the radiation heat loss for GZPS gel is calculated to be $q_{rad} = 1 \times 5.67 \times 10^{-8} \times (315.65^4 - 304.35^4) \approx 76.37 \text{ W m}^{-2}$ ($\eta_A = 7.64\%$).

The conduction heat loss can be determined by:

$$q_{cond} = A_{path}/A_{evap} (T_{evap} - T_0)/(d/k_{abs} + 1/h_c) \quad (4)$$

where A_{evap} is the area of the evaporation surface, which is taken as $1.9625 \times 10^{-3} \text{ m}^2$ (actual evaporation area of GZPS gel samples), and A_{path} is the area of the water path ($1.1304 \times 10^{-4} \text{ m}^2$). k_{abs} is the effective thermal conductivity of the absorber with water inside (k_{abs} of the absorber is very close to the thermal conductivity of water, which is measured as $0.59 \text{ W m}^{-1} \text{ K}^{-1}$), and d is thickness of the absorber (0.005 m). h_c is the heat transfer coefficient between the bottom surface of the absorber and the bulk water ($50 \text{ W m}^{-2} \text{ K}^{-1}$). Therefore, the conduction heat loss is determined to be $q_{cond} = \frac{1.1304 \times 10^{-4}}{1.9625 \times 10^{-3}} (315.65 - 304.35) / (\frac{0.005}{0.59} + \frac{1}{50}) = 22.8 \text{ W m}^{-2}$ ($\eta_A = 2.28\%$).

In terms of all the above-mentioned heat loss, the q_{evap} for the vapor generation is:

$$q_{evap} = \alpha q_{solar} - q_{conv} - q_{rad} - q_{cond} = 0.9525 \times 1000 - 56.5 - 76.3749 - 22.8096 = 796.8251 \text{ W m}^{-2}$$

Finally, the energy efficiency (η_A) of GZPS gel is calculated to be:

$$\eta_A = \frac{h_{evap}(T_{evap}-T_0)}{q_{solar}} = \frac{q_{evap}}{q_{solar}} = \frac{796.8251}{1000} \times 100\% = 79.68\% \quad (5)$$

Overall, by taking all the energy loss as well as the sunlight reflection and transmission into account, the energy efficiency is determined to be 79.68% (radiation heat loss ~7.64%, convection heat loss ~5.65%, conduction heat loss ~2.28%, and the reflection and transmission energy loss ~4.75%).

B. Evaporation enthalpies and the corresponding energy efficiency

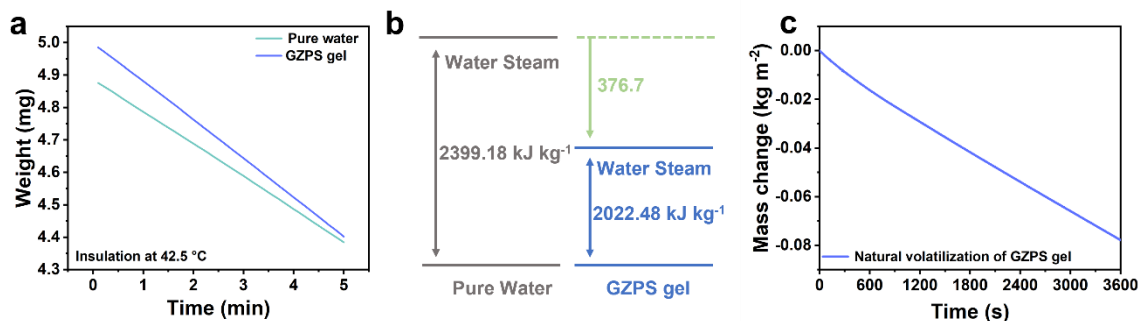


Fig. 4-25. TG curves (a) and evaporation enthalpies (b) of pure water and GZPS gel at 42.5 °C. (c) Natural volatilization of GZPS gel.

To estimate the water evaporation enthalpy of GZPS, TG measurements were performed and the weight changing curves were recorded at a constant temperature of 42.5 °C, which is the balanced temperature of GZPS. For comparison, the pure water was also tested and showed 0.49141 mg weight loss in 5 min. The weight loss of GZPS gel was 0.58294 mg in 5 min. Assuming that the evaporation is driven by identical energy input (U_{in}), the evaporation enthalpies can be calculated by the following Eq. (6) and (7):

$$U_{in} = \Delta H_w \dot{m}_w = \Delta H_{ev} \dot{m}_{ev} \quad (6)$$

$$\Delta H_w = \alpha + \beta T + \gamma T^{1.5} + \delta T^{2.5} + \varepsilon T^3 \quad (7)$$

where ΔH_w and ΔH_{ev} are the evaporation enthalpies of pure water and GZPS gel, respectively. \dot{m}_w and \dot{m}_{ev} refer to the weight change rates of pure water and GZPS gel. where $\alpha = 2500.304$, $\beta = -2.2521025$, $\gamma = -0.021465847$, $\delta = 3.1750136 \times 10^{-4}$, $\varepsilon = -2.8607959 \times 10^{-5}$ are constants, and T is temperature (°C). Thus, the ΔH_w of pure water can be calculated to be 2399.18 kJ kg⁻¹ at 42.5 °C (Eq. 7). The \dot{m}_w of pure water and \dot{m}_{ev} of GZPS gel have been measured in TG (**Fig. 4-25 (a)**). Thus, the ΔH_{ev} of GZPS gel can be calculated to be 2022.48 kJ kg⁻¹, which is lower than that of pure water (**Fig. 4-25 (b)**). Lower evaporation enthalpy facilitated water molecules easier to be diffused from the evaporator, and thus result in higher evaporation rate.

Based on the obtained evaporation enthalpy, the solar evaporation efficiency (η_B) can be calculated by the following Eq. (8):

$$\eta_B = \frac{\dot{m}\Delta H_{ev}}{P_{in}} \quad (8)$$

where \dot{m} represents the evaporation rate, which should exclude the natural volatilization rate in dark. ΔH_{ev} is the interfacial water evaporation enthalpy. P_{in} refers to the incident solar intensity (kW m^{-2}). The natural volatilization rate of GZPS gel have been measured to be $0.078 \text{ kg m}^{-2} \text{ h}^{-1}$ (**Fig. 4-25 (c)**). Thus the \dot{m} should be $1.392 \text{ kg m}^{-2} \text{ h}^{-1}$ (minimum value) and $1.822 \text{ kg m}^{-2} \text{ h}^{-1}$ (maximum value) for GZPS gel. Based on the measured value of ΔH_{ev} , the solar evaporation efficiencies can be calculated to be 78.2% ~102.4%. These data confirm that the GZPS gel can work as high-efficient evaporator for solar-driven seawater desalination.

The excellent photothermal performance of GZPS device system benefits from its macro/micro/nano hierarchical structures that increase the optical path and reduce reflection through multiple scattering of incident light [68], as well as the excellent solar absorption and photothermal effect of ZIF-67 and graphene.

4.3.7 Practical application of GZPS evaporation device system

GZPS device system was tested for long-term usability and practical application effect. It has been carried out the cycle seawater evaporation experiment in solar light and darkness as well as long-term seawater evaporation experiment. To confirm the material's responsiveness to sunlight for photothermal conversion and its stability under different light conditions, a cyclic evaporation experiment was conducted. The experiment involved five cycles of turning on simulated solar radiation for one hour, followed by turning it off for one hour. The results show that the GZPS device system exhibited stable mass change trends during seawater evaporation, whether in the presence or absence of solar radiation. (**Fig. 4-26 (a)**). It may be that the salt in the seawater is stored in the GZPS

gel, which affects the subsequent long-term evaporation. According to the real-time efficiency, it can also be assumed that the highest efficiency can even reach over $1.89 \text{ kg m}^{-2} \text{ h}^{-1}$ at the beginning (**Fig. 4-26 (b)**). In the subsequent continuous cycle evaporation experiment, even if the evaporation rate dropped to $1.03 \text{ kg m}^{-2} \text{ h}^{-1}$ when exposed to solar radiation, which still proves its durability and stability. The evaporated seawater was collected in a glass container in order to evaluate the effect of seawater desalination. As can be seen from **Fig. 4-26 (c)**, there were obviously small water droplets of water vapor condensation in the glass container after evaporating for 3 min, and the photothermal effect is still significant when it evaporates even in the presence of the glassware. Ion concentration test was performed on the water collected after 12 h of continuous seawater evaporation, to verify the purification ability, including the four main metal ions of Na^+ , Ca^{2+} , Mg^{2+} , K^+ and other metal ions including heavy metal ions (Mn^{2+} , Fe^{3+} , Co^{2+} , Ni^{2+} , Zn^{2+} , Pb^{2+} , Cd^{2+} , Cu^{2+} , Cr^{3+}). The concentrations of Na^+ , Ca^{2+} , Mg^{2+} and K^+ sharply decreased to 6.61, 1.80, 5.61, and 2.95 mg L^{-1} , respectively, after solar purification (**Fig. 4-26 (d)**). The concentration of other metal ions is also much lower than that of the original seawater (**Fig. 4-26 (e)**), demonstrating that photothermal evaporation has a strong removal effect on heavy metal ions.

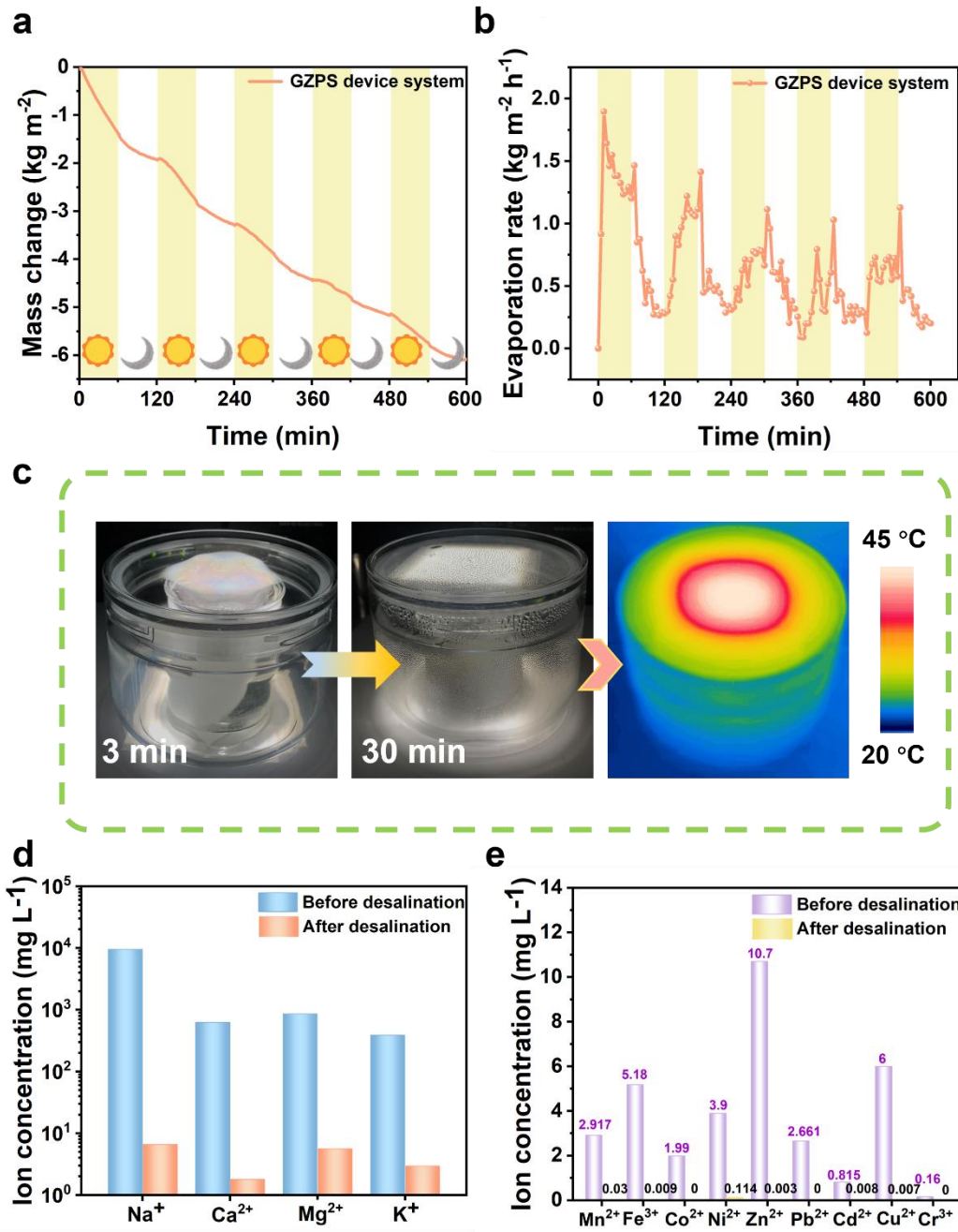


Fig. 4-26. (a) Mass change curve of the GZPS device system during the solar-driven seawater evaporation cyclic test, and the corresponding evaporation rate (b). (c) Photographs about the water droplets formation and the IR image during the evaporation. (d) The four main ion concentrations and other mental ion concentrations (e) in purified water and seawater.

The results show that the GZPS device system has excellent seawater purification and ion removal capabilities in solar-driven seawater evaporation. After a long term of evaporation, there is no obvious salt on the surface of GZPS gel. It is inferred that the hydrogel interior may contain salt, but this phenomenon does not strongly affect the surface appearance (**Fig. 4-27**). This inference is verified by EDS distribution that a large amount of Na and Cl elements do appear in the hydrogel after long-term seawater evaporation experiment. Simultaneously, small amounts of other elements were also detected (**Fig. 4-28**), which proves its ability to adsorb ions.



Fig. 4-27. The photos of GZPS device system before and after 12 h solar irradiation.

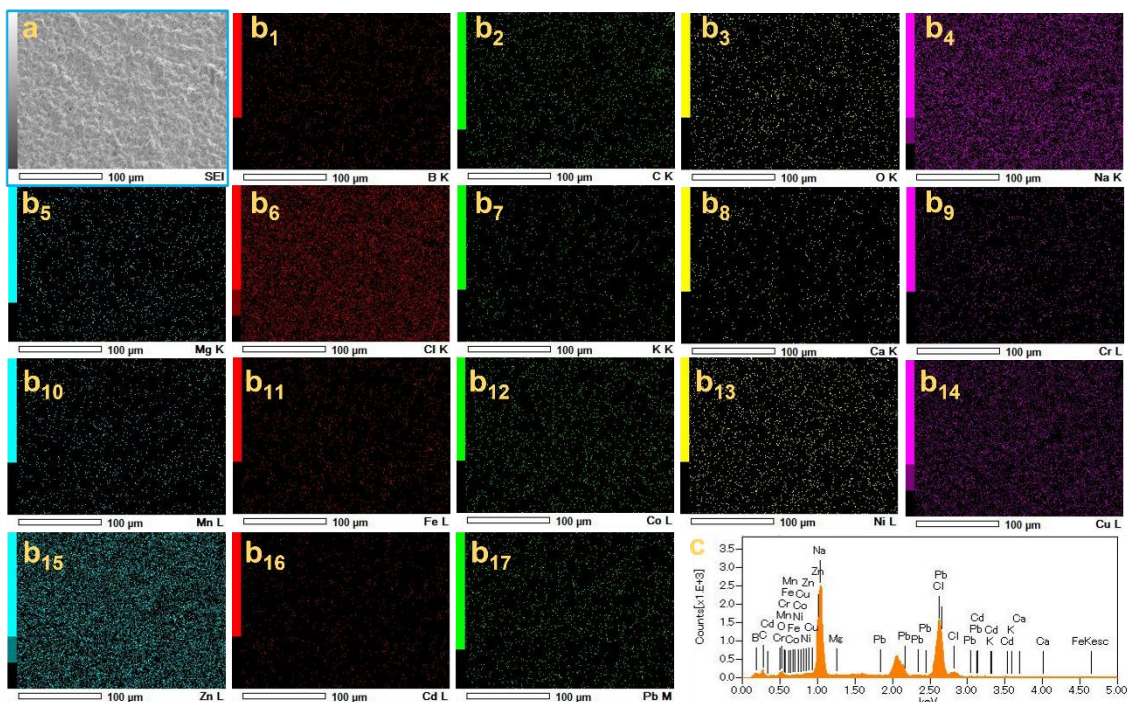


Fig. 4-28. Appearance and element distribution of GZPS after seawater evaporation. (a) FE-SEM image of GZPS after evaporation. (b1-b17) EDS images of GZPS after evaporation. (c) The atomic and weight percentage of the GZPS after evaporation.

According to the results, it can be inferred that the prepared GZPS hydrogel owns great potential in seawater desalination to produce clean water. The water production capacity of GZPS hydrogel, including water collection and evaporation, was compared with that of some recent research studies respectively, which demonstrated its excellent performance (Table 4-1 and 4-2).

4.4. Conclusion

In this study, a multifunctional macro/micro/nano hierarchical structure composite hydrogel (graphene/ZIF-67/PVA/SA) bioinspired by various organisms (*Selaginella lepidophylla*, honeycomb, pufferfish) has been successfully prepared after being assisted

by facile water collection and evaporation enhancement device. It not only has outstanding performance in passive fog flow collection, accompanied by the collected water could be effectively released, but also has been successfully applied to solar-driven seawater desalination.

The synergistic effect of the hydrophilicity of the PVA/SA hydrogel matrix itself and the excellent solar absorption performance and ion adsorption capacity of the added functional nanomaterials graphene and ZIF-67 endow the composite hydrogel no matter in the dry or wet state produce clean water effectively. In the case of fog flow, the water uptake rate can reach 94.06% after 3 h, and the water release efficiency can reach up to $1.67 \text{ kg m}^{-2} \text{ h}^{-1}$ under the subsequent 1 sun irradiation. During natural seawater evaporation, with the integration of a rationally designed evaporation device system, the seawater evaporation rate even reached up to $1.89 \text{ kg m}^{-2} \text{ h}^{-1}$ with solar-heat conversion efficiency of 92.32%. This study facilitates scalable and modular applications for harvesting and purifying water from various sources assisted by clean renewable energy. Its special biomimetic strategy and structure as well as combination with facile and common props provide potential value for the application of functional materials, soft matter, gas adsorption and flexible power generation materials.

References

- [1] S.H. Antwi, D. Getty, S. Linnane, A. Rolston, COVID-19 water sector responses in Europe: A scoping review of preliminary governmental interventions, *Sci Total Environ* 762 (2021) 143068. <https://doi.org/10.1016/j.scitotenv.2020.143068>.
- [2] C.J. Vorosmarty, P. Green, J. Salisbury, R.B. Lammers, Global water resources: vulnerability from climate change and population growth, *Science* 289(5477) (2000) 284-8. <https://doi.org/10.1126/science.289.5477.284>.

- [3] D. Wang, Y. Chen, M. Jarin, X. Xie, Increasingly frequent extreme weather events urge the development of point-of-use water treatment systems, *npj Clean Water* 5(1) (2022). <https://doi.org/10.1038/s41545-022-00182-1>.
- [4] M.M. Mekonnen, A.Y. Hoekstra, Four billion people facing severe water scarcity, *Sci Adv* 2(2) (2016) e1500323. <https://doi.org/10.1126/sciadv.1500323>.
- [5] Z. Zhang, H. Fu, Z. Li, J. Huang, Z. Xu, Y. Lai, X. Qian, S. Zhang, Hydrogel materials for sustainable water resources harvesting & treatment: Synthesis, mechanism and applications, *Chemical Engineering Journal* 439 (2022). <https://doi.org/10.1016/j.cej.2022.135756>.
- [6] G. Liu, T. Chen, J. Xu, G. Yao, J. Xie, Y. Cheng, Z. Miao, K. Wang, Salt-Rejecting Solar Interfacial Evaporation, *Cell Reports Physical Science* 2(1) (2021). <https://doi.org/10.1016/j.xcrp.2020.100310>.
- [7] H. Lu, W. Shi, Y. Guo, W. Guan, C. Lei, G. Yu, Materials Engineering for Atmospheric Water Harvesting: Progress and Perspectives, *Adv Mater* 34(12) (2022) e2110079. <https://doi.org/10.1002/adma.202110079>.
- [8] J. Yang, J.B. van Lier, J. Li, J. Guo, F. Fang, Integrated anaerobic and algal bioreactors: A promising conceptual alternative approach for conventional sewage treatment, *Bioresour Technol* 343 (2022) 126115. <https://doi.org/10.1016/j.biortech.2021.126115>.
- [9] N. Li, L. Luo, C. Guo, J. He, S. Wang, L. Yu, M. Wang, P. Murto, X. Xu, Shape-controlled fabrication of cost-effective, scalable and anti-biofouling hydrogel foams for solar-powered clean water production, *Chemical Engineering Journal* 431 (2022) 134144. <https://doi.org/https://doi.org/10.1016/j.cej.2021.134144>.
- [10] L. Yang, N. Li, C. Guo, J. He, S. Wang, L. Qiao, F. Li, L. Yu, M. Wang, X. Xu, Marine biomass-derived composite aerogels for efficient and durable solar-driven interfacial evaporation and desalination, *Chemical Engineering Journal* 417 (2021) 128051. <https://doi.org/https://doi.org/10.1016/j.cej.2020.128051>.
- [11] C. Li, B. Zhu, Z. Liu, J. Zhao, R. Meng, L. Zhang, Z. Chen, Polyelectrolyte-based photothermal hydrogel with low evaporation enthalpy for solar-driven salt-tolerant desalination, *Chemical Engineering Journal* 431 (2022) 134224. <https://doi.org/https://doi.org/10.1016/j.cej.2021.134224>.

- [12] M.S. Irshad, N. Arshad, X. Wang, Nanoenabled Photothermal Materials for Clean Water Production, *Glob Chall* 5(1) (2021) 2000055. <https://doi.org/10.1002/gch2.202000055>.
- [13] P. Zhang, Q. Liao, H. Yao, Y. Huang, H. Cheng, L. Qu, Direct solar steam generation system for clean water production, *Energy Storage Materials* 18 (2019) 429-446. <https://doi.org/10.1016/j.ensm.2018.10.006>.
- [14] R. Li, Y. Shi, M. Wu, S. Hong, P. Wang, Improving atmospheric water production yield: Enabling multiple water harvesting cycles with nano sorbent, *Nano Energy* 67 (2020). <https://doi.org/10.1016/j.nanoen.2019.104255>.
- [15] G. Baggio, M. Qadir, V. Smakhtin, Freshwater availability status across countries for human and ecosystem needs, *Sci Total Environ* 792 (2021) 148230. <https://doi.org/10.1016/j.scitotenv.2021.148230>.
- [16] X. Xu, N. Bizmark, K.S.S. Christie, S.S. Datta, Z.J. Ren, R.D. Priestley, Thermoresponsive Polymers for Water Treatment and Collection, *Macromolecules* 55(6) (2022) 1894-1909. <https://doi.org/10.1021/acs.macromol.1c01502>.
- [17] F. Li, N. Li, S. Wang, L. Qiao, L. Yu, P. Murto, X. Xu, Self-Repairing and Damage-Tolerant Hydrogels for Efficient Solar-Powered Water Purification and Desalination, *Advanced Functional Materials* 31(40) (2021). <https://doi.org/10.1002/adfm.202104464>.
- [18] Y. Tu, R. Wang, Y. Zhang, J. Wang, Progress and Expectation of Atmospheric Water Harvesting, *Joule* 2(8) (2018) 1452-1475. <https://doi.org/10.1016/j.joule.2018.07.015>.
- [19] A. Lee, M.W. Moon, H. Lim, W.D. Kim, H.Y. Kim, Water harvest via dewing, *Langmuir* 28(27) (2012) 10183-91. <https://doi.org/10.1021/la3013987>.
- [20] H. Park, I. Haechler, G. Schnoering, M.D. Ponte, T.M. Schutzius, D. Poulikakos, Enhanced Atmospheric Water Harvesting with Sunlight-Activated Sorption Ratcheting, *ACS Appl Mater Interfaces* 14(1) (2022) 2237-2245. <https://doi.org/10.1021/acsami.1c18852>.
- [21] B. Wang, X. Zhou, Z. Guo, W. Liu, Recent advances in atmosphere water harvesting: Design principle, materials, devices, and applications, *Nano Today* 40 (2021). <https://doi.org/10.1016/j.nantod.2021.101283>.

- [22] H. Lu, W. Shi, J.H. Zhang, A.C. Chen, W. Guan, C. Lei, J.R. Greer, S.V. Boriskina, G. Yu, Tailoring the Desorption Behavior of Hygroscopic Gels for Atmospheric Water Harvesting in Arid Climates, *Adv Mater* 34(37) (2022) e2205344. <https://doi.org/10.1002/adma.202205344>.
- [23] Y. Lin, K. Shao, S. Li, N. Li, S. Wang, X. Wu, C. Guo, L. Yu, P. Murto, X. Xu, Hygroscopic and Photothermal All-Polymer Foams for Efficient Atmospheric Water Harvesting, Passive Humidity Management, and Protective Packaging, *ACS Applied Materials & Interfaces* 15(7) (2023) 10084-10097. <https://doi.org/10.1021/acsami.3c00302>.
- [24] J. He, N. Li, S. Wang, S. Li, C. Wang, L. Yu, P. Murto, X. Xu, Hygroscopic photothermal beads from marine polysaccharides: demonstration of efficient atmospheric water production, indoor humidity control and photovoltaic panel cooling, *Journal of Materials Chemistry A* 10(15) (2022) 8556-8567. <https://doi.org/10.1039/D2TA00594H>.
- [25] H. Zhu, Z. Guo, W. Liu, Biomimetic water-collecting materials inspired by nature, *Chem Commun (Camb)* 52(20) (2016) 3863-79. <https://doi.org/10.1039/c5cc09867j>.
- [26] Y. Wang, S. Gao, W. Xu, Z. Wang, Nanogenerators with Superwetting Surfaces for Harvesting Water/Liquid Energy, *Advanced Functional Materials* 30(26) (2020). <https://doi.org/10.1002/adfm.201908252>.
- [27] S. Wang, K. Liu, X. Yao, L. Jiang, Bioinspired Surfaces with Superwettability: New Insight on Theory, Design, and Applications, *Chem Rev* 115(16) (2015) 8230-93. <https://doi.org/10.1021/cr400083y>.
- [28] Y. Zhang, N. Meng, A.A. Babar, X. Wang, J. Yu, B. Ding, Multi-bioinspired and Multistructural Integrated Patterned Nanofibrous Surface for Spontaneous and Efficient Fog Collection, *Nano Lett* 21(18) (2021) 7806-7814. <https://doi.org/10.1021/acs.nanolett.1c02788>.
- [29] Y. Zhang, Y. Cai, J. Shi, H. Morikawa, C. Zhu, Multi-bioinspired hierarchical Janus membrane for fog harvesting and solar-driven seawater desalination, *Desalination* 540 (2022). <https://doi.org/10.1016/j.desal.2022.115975>.
- [30] Y. Zhang, N. Meng, A.A. Babar, X. Wang, J. Yu, B. Ding, Lizard-Skin-Inspired Nanofibrous Capillary Network Combined with a Slippery Surface for Efficient Fog Collection, *ACS Appl Mater Interfaces* 13(30) (2021) 36587-36594. <https://doi.org/10.1021/acsami.1c10067>.

- [31] Y. Zhang, C. Zhu, J. Shi, S. Yamanaka, H. Morikawa, Bioinspired Composite Materials used for Efficient Fog Harvesting with Structures that Consist of Fungi-Mycelia Networks, *ACS Sustainable Chemistry & Engineering* 10(38) (2022) 12529-12539. <https://doi.org/10.1021/acssuschemeng.2c01816>.
- [32] D. Curto, V. Franzitta, A. Guercio, A Review of the Water Desalination Technologies, *Applied Sciences* 11(2) (2021). <https://doi.org/10.3390/app11020670>.
- [33] C. Zhu, A. Mochizuki, J. Shi, M. Ishimori, S. Koyama, H. Ishizawa, J. Yan, H. Morikawa, Photocatalytic self-cleaning coatings to remove oleic acid, an organic pollutant, from cotton fabrics, *Cellulose* 28(12) (2021) 8139-8152. <https://doi.org/10.1007/s10570-021-04004-4>.
- [34] C. Zhu, J. Shi, S. Xu, M. Ishimori, J. Sui, H. Morikawa, Design and characterization of self-cleaning cotton fabrics exploiting zinc oxide nanoparticle-triggered photocatalytic degradation, *Cellulose* 24(6) (2017) 2657-2667. <https://doi.org/10.1007/s10570-017-1289-7>.
- [35] Q. Zhao, J. Liu, Z. Wu, X. Xu, H. Ma, J. Hou, Q. Xu, R. Yang, K. Zhang, M. Zhang, H. Yang, W. Peng, X. Liu, C. Zhang, J. Xu, B. Lu, Robust PEDOT:PSS-based hydrogel for highly efficient interfacial solar water purification, *Chemical Engineering Journal* 442 (2022) 136284. <https://doi.org/https://doi.org/10.1016/j.cej.2022.136284>.
- [36] Q. Zhao, Z. Wu, X. Xu, R. Yang, H. Ma, Q. Xu, K. Zhang, M. Zhang, J. Xu, B. Lu, Design of poly(3,4-ethylenedioxythiophene): polystyrene sulfonate-polyacrylamide dual network hydrogel for long-term stable, highly efficient solar steam generation, *Separation and Purification Technology* 300 (2022) 121889. <https://doi.org/https://doi.org/10.1016/j.seppur.2022.121889>.
- [37] Z. Lin, T. Wu, Y.F. Feng, J. Shi, B. Zhou, C. Zhu, Y. Wang, R. Liang, M. Mizuno, Poly(N-phenylglycine)/MoS₂ Nanohybrid with Synergistic Solar-Thermal Conversion for Efficient Water Purification and Thermoelectric Power Generation, *ACS Appl Mater Interfaces* 14(1) (2022) 1034-1044. <https://doi.org/10.1021/acscami.1c20393>.
- [38] Z. Lin, T. Wu, B. Jia, J. Shi, B. Zhou, C. Zhu, Y. Wang, R. Liang, M. Mizuno, Nature-inspired poly(N-phenylglycine)/wood solar evaporation system for high-efficiency desalination and water purification, *Colloids and Surfaces A: Physicochemical and Engineering Aspects* 637 (2022). <https://doi.org/10.1016/j.colsurfa.2022.128272>.

- [39] L. Li, T. Hu, A. Li, J. Zhang, Electrically Conductive Carbon Aerogels with High Salt-Resistance for Efficient Solar-Driven Interfacial Evaporation, *ACS Appl Mater Interfaces* 12(28) (2020) 32143-32153. <https://doi.org/10.1021/acsami.0c06836>.
- [40] C. Ge, D. Xu, H. Du, Z. Chen, J. Chen, Z. Shen, W. Xu, Q. Zhang, J. Fang, Recent Advances in Fibrous Materials for Interfacial Solar Steam Generation, *Advanced Fiber Materials* (2022). <https://doi.org/10.1007/s42765-022-00228-6>.
- [41] J. Han, W. Xing, J. Yan, J. Wen, Y. Liu, Y. Wang, Z. Wu, L. Tang, J. Gao, Stretchable and Superhydrophilic Polyaniline/Halloysite Decorated Nanofiber Composite Evaporator for High Efficiency Seawater Desalination, *Advanced Fiber Materials* 4(5) (2022) 1233-1245. <https://doi.org/10.1007/s42765-022-00172-5>.
- [42] Z. Liu, Z. Zhou, N. Wu, R. Zhang, B. Zhu, H. Jin, Y. Zhang, M. Zhu, Z. Chen, Hierarchical Photothermal Fabrics with Low Evaporation Enthalpy as Heliotropic Evaporators for Efficient, Continuous, Salt-Free Desalination, *ACS Nano* 15(8) (2021) 13007-13018. <https://doi.org/10.1021/acsnano.1c01900>.
- [43] D. Xu, Z. Zhu, J. Li, Recent Progress in Electrospun Nanofibers for the Membrane Distillation of Hypersaline Wastewaters, *Advanced Fiber Materials* 4(6) (2022) 1357-1374. <https://doi.org/10.1007/s42765-022-00193-0>.
- [44] Z. Lin, T. Wu, J. Shi, B. Zhou, C. Zhu, Y. Wang, R. Liang, M. Mizuno, Poly(N-phenylglycine)-Based Bioinspired System for Stably and Efficiently Enhancing Solar Evaporation, *ACS Sustainable Chemistry & Engineering* 9(1) (2020) 448-457. <https://doi.org/10.1021/acssuschemeng.0c07608>.
- [45] SEDIMENTOLOGY AND PALEOHYDROLOGY OF LATE QUATERNARY LAKE DEPOSITS IN THE NORTHERN NAMIB SAND SEA, NAMIBIA.
- [46] F. Mvondo Owono, M.-J. Ntamak-Nida, O. Dauteuil, F. Guillocheau, B. Njom, Morphology and long-term landscape evolution of the South African plateau in South Namibia, *Catena* 142 (2016) 47-65. <https://doi.org/10.1016/j.catena.2016.02.012>.
- [47] S.E. Evans, M.E. Dueker, J.R. Logan, K.C. Weathers, The biology of fog: results from coastal Maine and Namib Desert reveal common drivers of fog microbial composition, *Sci Total Environ* 647 (2019) 1547-1556. <https://doi.org/10.1016/j.scitotenv.2018.08.045>.

- [48] A. Roth-Nebelsick, M. Ebner, T. Miranda, V. Gottschalk, D. Voigt, S. Gorb, T. Stegmaier, J. Sarsour, M. Linke, W. Konrad, Leaf surface structures enable the endemic Namib desert grass *Stipagrostis sabulicola* to irrigate itself with fog water, *J R Soc Interface* 9(73) (2012) 1965-74. <https://doi.org/10.1098/rsif.2011.0847>.
- [49] Z. Yu, H. Zhang, J. Huang, S. Li, S. Zhang, Y. Cheng, J. Mao, X. Dong, S. Gao, S. Wang, Z. Chen, Y. Jiang, Y. Lai, Namib desert beetle inspired special patterned fabric with programmable and gradient wettability for efficient fog harvesting, *Journal of Materials Science & Technology* 61 (2021) 85-92. <https://doi.org/10.1016/j.jmst.2020.05.054>.
- [50] D. Gurera, B. Bhushan, Optimization of bioinspired conical surfaces for water collection from fog, *J Colloid Interface Sci* 551 (2019) 26-38. <https://doi.org/10.1016/j.jcis.2019.05.015>.
- [51] N. Kyong Kim, D. Hee Kang, H. Eom, H. Wook Kang, Biomimetic fog harvesting surface by photo-induced micro-patterning of zinc-oxide silver hierarchical nanostructures, *Applied Surface Science* 470 (2019) 161-167. <https://doi.org/10.1016/j.apsusc.2018.11.132>.
- [52] A. Yobi, B.W. Wone, W. Xu, D.C. Alexander, L. Guo, J.A. Ryals, M.J. Oliver, J.C. Cushman, Metabolomic profiling in *Selaginella lepidophylla* at various hydration states provides new insights into the mechanistic basis of desiccation tolerance, *Mol Plant* 6(2) (2013) 369-85. <https://doi.org/10.1093/mp/sss155>.
- [53] A. Rafsanjani, V. Brule, T.L. Western, D. Pasini, Hydro-responsive curling of the resurrection plant *Selaginella lepidophylla*, *Sci Rep* 5 (2015) 8064. <https://doi.org/10.1038/srep08064>.
- [54] Y. Zhang, L. Wu, A.A. Babar, X. Zhao, X. Wang, J. Yu, B. Ding, Honeycomb-Inspired Robust Hygroscopic Nanofibrous Cellular Networks, *Small Methods* 5(11) (2021) e2101011. <https://doi.org/10.1002/smt.202101011>.
- [55] L. Heng, X. Meng, B. Wang, L. Jiang, Bioinspired design of honeycomb structure interfaces with controllable water adhesion, *Langmuir* 29(30) (2013) 9491-8. <https://doi.org/10.1021/la401991n>.
- [56] J. Wang, C. Deng, G. Zhong, W. Ying, C. Li, S. Wang, Y. Liu, R. Wang, H. Zhang, High-yield and scalable water harvesting of honeycomb hygroscopic polymer driven by natural sunlight, *Cell Reports Physical Science* 3(7) (2022). <https://doi.org/10.1016/j.xcrp.2022.100954>.

- [57] P.C. Wainwright, R.G. Turingan, Evolution of Pufferfish Inflation Behavior, *Evolution* 51(2) (1997) 506-518. <https://doi.org/10.1111/j.1558-5646.1997.tb02438.x>.
- [58] X. Wang, S. Zhao, C. Li, X. Liu, J. Song, Neural basis of the stress response in a pufferfish, *Takifugu obscurus*, *Integr Zool* 10(1) (2015) 133-40. <https://doi.org/10.1111/1749-4877.12103>.
- [59] J. Fan, Z. Shi, M. Lian, H. Li, J. Yin, Mechanically strong graphene oxide/sodium alginate/polyacrylamide nanocomposite hydrogel with improved dye adsorption capacity, *Journal of Materials Chemistry A* 1(25) (2013). <https://doi.org/10.1039/c3ta10639j>.
- [60] W. Li, Y.Y. Liu, Y. Bai, J. Wang, H. Pang, Anchoring ZIF-67 particles on amidoximerized polyacrylonitrile fibers for radionuclide sequestration in wastewater and seawater, *J Hazard Mater* 395 (2020) 122692. <https://doi.org/10.1016/j.jhazmat.2020.122692>.
- [61] H.U. Rehman Shah, K. Ahmad, H.A. Naseem, S. Parveen, M. Ashfaq, A. Rauf, T. Aziz, Water stable graphene oxide metal-organic frameworks composite (ZIF-67@GO) for efficient removal of malachite green from water, *Food Chem Toxicol* 154 (2021) 112312. <https://doi.org/10.1016/j.fct.2021.112312>.
- [62] L. Li, Q. Li, Y. Feng, K. Chen, J. Zhang, Melamine/Silicone Hybrid Sponges with Controllable Microstructure and Wettability for Efficient Solar-Driven Interfacial Desalination, *ACS Appl Mater Interfaces* 14(1) (2022) 2360-2368. <https://doi.org/10.1021/acsami.1c20734>.
- [63] D. Fatma Tugce Senberber, A.S. Kipcak, E.M. Derun, Microwave Dehydration of Borax: Characterization, Dehydration Kinetics, and Modelling, *Glass Physics and Chemistry* 48(3) (2022) 210-218. <https://doi.org/10.1134/s1087659622030087>.
- [64] X. Lou, Y. Huang, X. Yang, H. Zhu, L. Heng, F. Xia, External Stimuli Responsive Liquid-Infused Surfaces Switching between Slippery and Nonslippery States: Fabrications and Applications, *Advanced Functional Materials* 30(10) (2020). <https://doi.org/10.1002/adfm.201901130>.
- [65] S. Yan, H. Song, Y. Li, J. Yang, X. Jia, S. Wang, X. Yang, Integrated reduced graphene oxide/polypyrrole hybrid aerogels for simultaneous photocatalytic decontamination and water evaporation, *Applied Catalysis B: Environmental* 301 (2022). <https://doi.org/10.1016/j.apcatb.2021.120820>.

- [66] S. Bibi, E. Pervaiz, M. Ali, Synthesis and applications of metal oxide derivatives of ZIF-67: a mini-review, *Chemical Papers* 75(6) (2021) 2253-2275. <https://doi.org/10.1007/s11696-020-01473-y>.
- [67] X. Zhou, F. Zhao, Y. Guo, B. Rosenberger, G. Yu, Architecting highly hydratable polymer networks to tune the water state for solar water purification, *Sci Adv* 5(6) (2019) eaaw5484. <https://doi.org/10.1126/sciadv.aaw5484>.
- [68] N. Li, L. Qiao, J. He, S. Wang, L. Yu, P. Murto, X. Li, X. Xu, Solar-Driven Interfacial Evaporation and Self-Powered Water Wave Detection Based on an All-Cellulose Monolithic Design, *Advanced Functional Materials* 31(7) (2020). <https://doi.org/10.1002/adfm.202008681>.

Table 4-1. Comparison of solar evaporation rate for previously reported interfacial photothermal materials under 1 sun.

No.	Solar absorbers	Evaporation rate (kg m ⁻² h ⁻¹)	Energy efficiency (%)	Ref.
1	PVA/PVP/PAM/ATP	1.20	~85	S1
2	Ti ₃ C ₂ /PVA	1.41	~88.7	S2
3	PVA/PPy/Si	1.35	~92.6	S3
4	PPy/KFs/SA/CaCl ₂	1.37	~82.4	S4
5	PVA/PPy/Ti ₂ O ₃	2.60	~91	S5
6	G@ZIF nanohybrid	1.78	~96	S6
7	Mesoporous Wood	1.15	~80	S7
8	3D-printed CNT/GO/NFC	1.25	~85.6	S8
9	RGO-SA-CNT aerogel	1.62	~83	S9
10	CACH	1.33	~90.6	S10
11	Self-regenerating evaporator	1.04	~75.1	S11
12	RGO-bamboo paper	2.94	~80	S12
13	MDPC	1.222	~84.3	S13
14	Carbon fabric	0.90	~60.2	S14
15	h-G foam	1.40	~93.4	S15
16	Black Gold Film	1.51	~94.5	S16
17	Au-GO	1.34	~84.1	S17
18	AuNP/PBONF	1.424	~83	S18
19	PEDOT:PSS-PAAm hydrogel	2.15	~97.2	S19
20	GZPS	~1.89	~92.32	This work

Table 4-2. Comparison of fog harvesting performance of different materials.

No.	Fabricated materials	Fog harvesting rate	Ref.
1	PAAS–PNIPAAm Hydrogel	~2.76 g g ⁻¹	S20
2	PDMAPS/CNT/LiCl	~1.30 g g ⁻¹	S21
3	LCP hydrogel	~ 2.56 kg kg ⁻¹ day ⁻¹	S22
4	PAN/AM/graphene/CaCl ₂	~ 1.04 L kg ⁻¹	S23
5	PVA/PPy hydrogel membrane	~34 L m ⁻² day ⁻¹	S24
6	Binary/FCNT sorbent	~ 5.6 g g ⁻¹	S25
7	Gel	~10 L kg ⁻¹ day ⁻¹	S26
8	PAETA–Ac/CNT hydrogel	~ 0.53 g g ⁻¹	S27
9	PCLG	~ 2.9 L m ⁻² day ⁻¹	S28
10	PAM–LiCl	~ 7 g g ⁻¹	S29
11	GZPS with device	~22.44 g g ⁻¹	This work

Reference in Table 4-1 and 4-2

[S1] J. Jia, W. Liang, H. Sun, Z. Zhu, C. Wang, A. Li, Fabrication of bilayered attapulgite for solar steam generation with high conversion efficiency, *Chemical Engineering Journal* 361 (2019) 999-1006. <https://doi.org/https://doi.org/10.1016/j.cej.2018.12.157>.

[S2] X. Zhao, X.-J. Zha, J.-H. Pu, L. Bai, R.-Y. Bao, Z.-Y. Liu, M.-B. Yang, W. Yang, Macroporous three-dimensional MXene architectures for highly efficient solar steam generation, *Journal of Materials Chemistry A* 7(17) (2019) 10446-10455. <https://doi.org/10.1039/C9TA00176J>.

[S3] S. Cheng, Z. Yu, Z. Lin, L. Li, Y. Li, Z. Mao, A lotus leaf like vertical hierarchical solar vapor generator for stable and efficient evaporation of high-salinity brine, *Chemical Engineering Journal* 401 (2020) 126108. <https://doi.org/https://doi.org/10.1016/j.cej.2020.126108>.

[S4] P. Mu, W. Bai, Y. Fan, Z. Zhang, H. Sun, Z. Zhu, W. Liang, A. Li, Conductive hollow kapok fiber-PPy monolithic aerogels with excellent mechanical robustness for efficient solar steam generation, *Journal of Materials Chemistry A* 7(16) (2019) 9673-9679. <https://doi.org/10.1039/C8TA12243A>.

[S5] Y. Guo, F. Zhao, X. Zhou, Z. Chen, G. Yu, Tailoring Nanoscale Surface Topography of Hydrogel for Efficient Solar Vapor Generation, *Nano Letters* 19(4) (2019) 2530-2536. <https://doi.org/10.1021/acs.nanolett.9b00252>.

[S6] X. Han, L.V. Besteiro, C.S.L. Koh, H.K. Lee, I.Y. Phang, G.C. Phan-Quang, J.Y. Ng, H.Y.F. Sim, C.L. Lay, A. Govorov, X.Y. Ling, Intensifying Heat Using MOF-Isolated Graphene for Solar-Driven

Seawater Desalination at 98% Solar-to-Thermal Efficiency, *Advanced Functional Materials* 31(13) (2021) 2008904. <https://doi.org/https://doi.org/10.1002/adfm.202008904>.

[S7] T. Li, H. Liu, X. Zhao, G. Chen, J. Dai, G. Pastel, C. Jia, C. Chen, E. Hitz, D. Siddhartha, R. Yang, L. Hu, Scalable and Highly Efficient Mesoporous Wood-Based Solar Steam Generation Device: Localized Heat, Rapid Water Transport, *Advanced Functional Materials* 28(16) (2018) 1707134. <https://doi.org/https://doi.org/10.1002/adfm.201707134>.

[S8] Y. Li, T. Gao, Z. Yang, C. Chen, W. Luo, J. Song, E. Hitz, C. Jia, Y. Zhou, B. Liu, B. Yang, L. Hu, 3D-Printed, All-in-One Evaporator for High-Efficiency Solar Steam Generation under 1 Sun Illumination, *Advanced Materials* 29(26) (2017) 1700981. <https://doi.org/https://doi.org/10.1002/adma.201700981>.

[S9] X. Hu, W. Xu, L. Zhou, Y. Tan, Y. Wang, S. Zhu, J. Zhu, Tailoring Graphene Oxide-Based Aerogels for Efficient Solar Steam Generation under One Sun, *Advanced Materials* 29(5) (2017) 1604031. <https://doi.org/https://doi.org/10.1002/adma.201604031>.

[S10] J. Yuan, X. Lei, C. Yi, H. Jiang, F. Liu, G.J. Cheng, 3D-printed hierarchical porous cellulose/alginate/carbon black hydrogel for high-efficiency solar steam generation, *Chemical Engineering Journal* 430 (2022) 132765. <https://doi.org/https://doi.org/10.1016/j.cej.2021.132765>.

[S11] Y. Kuang, C. Chen, S. He, E.M. Hitz, Y. Wang, W. Gan, R. Mi, L. Hu, A High-Performance Self-Regenerating Solar Evaporator for Continuous Water Desalination, *Advanced Materials* 31(23) (2019) 1900498. <https://doi.org/https://doi.org/10.1002/adma.201900498>.

[S12] Y. Wang, X. Wu, B. Shao, X. Yang, G. Owens, H. Xu, Boosting solar steam generation by structure enhanced energy management, *Science Bulletin* 65(16) (2020) 1380-1388. <https://doi.org/https://doi.org/10.1016/j.scib.2020.04.036>.

[S13] S. Ma, W. Qarony, M.I. Hossain, C.T. Yip, Y.H. Tsang, Metal-organic framework derived porous carbon of light trapping structures for efficient solar steam generation, *Solar Energy Materials and Solar Cells* 196 (2019) 36-42. <https://doi.org/https://doi.org/10.1016/j.solmat.2019.02.035>.

[S14] M.W. Higgins, A.R. Shakeel Rahmaan, R.R. Devarapalli, M.V. Shelke, N. Jha, Carbon fabric based solar steam generation for waste water treatment, *Solar Energy* 159 (2018) 800-810. <https://doi.org/https://doi.org/10.1016/j.solener.2017.11.055>.

- [S15] H. Ren, M. Tang, B. Guan, K. Wang, J. Yang, F. Wang, M. Wang, J. Shan, Z. Chen, D. Wei, H. Peng, Z. Liu, Hierarchical Graphene Foam for Efficient Omnidirectional Solar–Thermal Energy Conversion, *Advanced Materials* 29(38) (2017) 1702590. <https://doi.org/https://doi.org/10.1002/adma.201702590>.
- [S16] Y. Zhang, Y. Wang, B. Yu, K. Yin, Z. Zhang, Hierarchically Structured Black Gold Film with Ultrahigh Porosity for Solar Steam Generation, *Advanced Materials* 34(21) (2022) 2200108. <https://doi.org/https://doi.org/10.1002/adma.202200108>.
- [S17] J. Zhou, Y. Gu, Z. Deng, L. Miao, H. Su, P. Wang, J. Shi, The dispersion of Au nanorods decorated on graphene oxide nanosheets for solar steam generation, *Sustainable Materials and Technologies* 19 (2019) e00090. <https://doi.org/https://doi.org/10.1016/j.susmat.2018.e00090>.
- [S18] M. Chen, Y. Wu, W. Song, Y. Mo, X. Lin, Q. He, B. Guo, Plasmonic nanoparticle-embedded poly(p-phenylene benzobisoxazole) nanofibrous composite films for solar steam generation, *Nanoscale* 10(13) (2018) 6186-6193. <https://doi.org/10.1039/C8NR01017J>.
- [S19] Q. Zhao, Z. Wu, X. Xu, R. Yang, H. Ma, Q. Xu, K. Zhang, M. Zhang, J. Xu, B. Lu, Design of poly(3,4-ethylenedioxythiophene): polystyrene sulfonate-polyacrylamide dual network hydrogel for long-term stable, highly efficient solar steam generation, *Separation and Purification Technology* 300 (2022) 121889. <https://doi.org/https://doi.org/10.1016/j.seppur.2022.121889>.
- [S20] Z. Zhang, Y. Wang, Z. Li, H. Fu, J. Huang, Z. Xu, Y. Lai, X. Qian, S. Zhang, Sustainable Hierarchical-Pored PAAS–PNIPAAm Hydrogel with Core–Shell Structure Tailored for Highly Efficient Atmospheric Water Harvesting, *ACS Applied Materials & Interfaces* 14(49) (2022) 55295-55306. <https://doi.org/10.1021/acsami.2c19840>.
- [S21] S. Aleid, M. Wu, R. Li, W. Wang, C. Zhang, L. Zhang, P. Wang, Salting-in Effect of Zwitterionic Polymer Hydrogel Facilitates Atmospheric Water Harvesting, *ACS Materials Letters* 4(3) (2022) 511-520. <https://doi.org/10.1021/acsmaterialslett.1c00723>.
- [S22] T. Lyu, Z. Wang, R. Liu, K. Chen, H. Liu, Y. Tian, Macroporous Hydrogel for High-Performance Atmospheric Water Harvesting, *ACS Applied Materials & Interfaces* 14(28) (2022) 32433-32443. <https://doi.org/10.1021/acsami.2c04228>.

- [S23] M.N. Uddin, M.F. Rab, A.K.M.N. Islam, E. Asmatulu, M.M. Rahman, R. Asmatulu, Nanostructured Hybrid Hydrogels for Solar-Driven Clean Water Harvesting from the Atmosphere, *Materials*, 2022.
- [S24] Y. Shi, O. Ilic, H.A. Atwater, J.R. Greer, All-day fresh water harvesting by microstructured hydrogel membranes, *Nature Communications* 12(1) (2021) 2797. <https://doi.org/10.1038/s41467-021-23174-0>.
- [S25] A. Entezari, M. Ejeian, R. Wang, Super Atmospheric Water Harvesting Hydrogel with Alginate Chains Modified with Binary Salts, *ACS Materials Letters* 2(5) (2020) 471-477. <https://doi.org/10.1021/acsmaterialslett.9b00315>.
- [S26] D.K. Nandakumar, Y. Zhang, S.K. Ravi, N. Guo, C. Zhang, S.C. Tan, Solar Energy Triggered Clean Water Harvesting from Humid Air Existing above Sea Surface Enabled by a Hydrogel with Ultrahigh Hygroscopicity, *Advanced Materials* 31(10) (2019) 1806730. <https://doi.org/https://doi.org/10.1002/adma.201806730>.
- [S27] M. Wu, R. Li, Y. Shi, M. Altunkaya, S. Aleid, C. Zhang, W. Wang, P. Wang, Metal- and halide-free, solid-state polymeric water vapor sorbents for efficient water-sorption-driven cooling and atmospheric water harvesting, *Materials Horizons* 8(5) (2021) 1518-1527. <https://doi.org/10.1039/D0MH02051F>.
- [S28] J. Wang, C. Deng, G. Zhong, W. Ying, C. Li, S. Wang, Y. Liu, R. Wang, H. Zhang, High-yield and scalable water harvesting of honeycomb hygroscopic polymer driven by natural sunlight, *Cell Reports Physical Science* 3(7) (2022) 100954. <https://doi.org/https://doi.org/10.1016/j.xcrp.2022.100954>.
- [S29] H. Lu, W. Shi, J.H. Zhang, A.C. Chen, W. Guan, C. Lei, J.R. Greer, S.V. Boriskina, G. Yu, Tailoring the Desorption Behavior of Hygroscopic Gels for Atmospheric Water Harvesting in Arid Climates, *Advanced Materials* 34(37) (2022) 2205344. <https://doi.org/https://doi.org/10.1002/adma.202205344>.

Chapter 5

Conclusion and outlook

Chapter 5: Conclusion and outlook

5.1 Conclusion

The growing need for clean water has driven research and initiatives related to atmospheric water harvesting (AWH). Inspired by nature's ingenious solutions, the development and enhancement of AWH materials and systems have become a primary focus. Bionic AWH harnesses the structural and material characteristics of natural systems to efficiently collect water in foggy environments.

In the initial stages of our research, we employed electrospun nanofibers combined with other materials to create a 2D sandwich-shaped water collection material. However, as our research progressed, we recognized the need for an improved and more scalable fabrication process. This realization led to the development of a composite nanofiber membrane created through electrospinning and ultrasonic treatment. This versatile membrane draws inspiration from various biological structures and properties, making it suitable for clean water production in multiple scenarios, including desalination through sunlight-driven interfacial evaporation.

As our research deepened, we identified a limitation in the water collection efficiency due to the 2D planar structure of the material, which could only passively intercept fog. This prompted our exploration of 3D hydrogel materials, capable of leveraging the distinct characteristics of hydrogels in both dry and wet states. By incorporating functional materials, these hydrogels demonstrated the potential to collect water in high humidity conditions at night and release water during sunny days. This innovation also extended their utility to seawater desalination, enhancing the overall efficiency of clean water production.

The followings provide conclusions of each relevant sub research:

(1) Since fungi have the capacity to collect water from air, the main purpose of this study was to develop newly bioinspired water-harvesting materials that mimic water-

collecting fungi. Several fungi, such as *Rhizopus delemar* and *Mucor hiemalis* f. *hiemalis* were cultivated over 1 week, and their morphologies were observed and analyzed. The results indicated that *Rhizopus delemar* could effectively collect water probably related to its uneven diameter of mycelia, as well as its hierarchical structure. Moreover, the heterogeneous mycelia were found to be both hydrophobic and hydrophilic.

Based on the structure and features of the fungi, several kinds of composite materials were fabricated using hydrophobic PU nanofiber membranes as mesh structures with different densities, with a hydrophilic filter paper layer pasted on its surface. Four kinds of PU nanofiber membranes were electrospun on the stainless mesh, by varying the flow rate and the density of the mesh. The results of the PU nanofiber membranes showed that, from a broad perspective, a hierarchical structure with a mesh-like structure was formed. Meanwhile, coarse and fine PU nanofibers coexisted, which was similar to the mycelia. The SEM, WCA, and water-collection experiments proved that the composite material manufactured was able to collect droplets from fog. Hydrophilic–hydrophobic amphiphilic nanomaterials with thick and thin fibers that coexist have better water-collection performance than mesh membranes and filter paper. The hydrophilic filter paper on the surface performs well in capturing the water droplets in the air and making them coalesce, and then the mesh membrane with a mesh-like structure can transport the collected water. Composite materials with a lower mesh density collected a greater mass of water as a result of the puddles between the convexities being larger than the higher mesh density, which benefited the efficiency of the coalesce and collection of water, resulting in a water-collection efficiency as high as $1018.6 \text{ mg cm}^{-2} \text{ h}^{-1}$ in this work, which is more efficient than some membrane-like materials used in other research studies. In this study, an investigated bioinspired fog-harvesting material that can be applied to address serious contemporary water shortages in dry and underdeveloped areas of the globe was fabricated. Furthermore, the fabrication method is facile, has a low production cost, and efficient production, all of which ensure the possibility of good outcomes in practical applications.

(2) A hierarchical multi-bioinspired Janus membrane was fabricated successfully by applying a feasible and scalable process combined the electrospinning and ultrasonication. HL-CNTs/CNSs/PUm with mesh and macro-micro-nanoscale hierarchical structure constructed by anchoring hydrophilic carbon nanospheres and carbon nanotubes on the surface of PU nanofiber membrane can not only be applied in fog-harvesting but also in solar-thermal water evaporation and seawater desalination.

The HL-CNTs and HL-CNSs attached on the hydrophobic PU nanofiber membrane changed the surface wettability. In this structure, the hydrophilic parts can easily capture the fog and form into a critical size, the mesh structure can make the bigger droplet deposit, then the hydrophobic nanofibers provide the channel to transport and drain the deposited water. The synergy of these structural and material properties enables the fog-harvesting goal to be achieved. The HL-CNTs/CNSs/PUm exhibited rapid water capture and efficient photothermal conversion, which makes it possess water harvesting efficiency of $1666.2 \text{ mg cm}^{-2} \text{ h}^{-1}$ and evaporation rate of $1.05 \text{ kg m}^{-2} \text{ h}^{-1}$. It is worth noting that this Janus composite membrane also showed outstanding effect in seawater desalination. In addition, it maintained high capacity in multiple cycle tests, showing durability and reusability. Looking forward, further attempts could prove quite beneficial to harnessing different natural resources for potable water harvesting and broadening the way to address water scarcity.

(3) A multifunctional macro/micro/nano hierarchical structure composite hydrogel (graphene/ZIF-67/PVA/SA) bioinspired by various organisms (*Selaginella lepidophylla*, honeycomb, pufferfish) has been successfully prepared after being assisted by facile water collection and evaporation enhancement device. It not only has outstanding performance in passive fog flow collection, accompanied by the collected water could be effectively released, but also has been successfully applied to solar-driven seawater desalination.

The synergistic effect of the hydrophilicity of the PVA/SA hydrogel matrix itself and the excellent solar absorption performance and ion adsorption capacity of the added

functional nanomaterials graphene and ZIF-67 endow the composite hydrogel no matter in the dry or wet state produce clean water effectively. In the case of fog flow, the water uptake rate can reach 94.06% after 3 h, and the water release efficiency can reach up to $1.67 \text{ kg m}^{-2} \text{ h}^{-1}$ under the subsequent 1 sun irradiation. During natural seawater evaporation, with the integration of a rationally designed evaporation device system, the seawater evaporation rate even reached up to $1.89 \text{ kg m}^{-2} \text{ h}^{-1}$ with solar-heat conversion efficiency of 92.32%. This study facilitates scalable and modular applications for harvesting and purifying water from various sources assisted by clean renewable energy. Its special biomimetic strategy and structure as well as combination with facile and common props provide potential value for the application of functional materials, soft matter, gas adsorption and flexible power generation materials.

5.2 Outlook

In this work, we successfully designed and manufactured bioinspired 2D and 3D functional materials to achieve the goal of atmospheric water harvesting (AWH). Additionally, we cleverly expanded the applications of these materials, including seawater desalination, by harnessing clean energy sources such as solar power. However, despite significant progress, there are still some issues that require optimization and improvement:

(1) In Chapters 2 and 3, while 2D AWH materials have been successfully used for fogwater collection, their efficiency may be more pronounced when encountering heavy fog, and they are relatively dependent on external conditions.

(2) In Chapter 4, although hydrogel materials show relatively good AWH performance, there are still uncertainties about their water collection efficiency in low-humidity environments.

(3) The materials produced have been tested only in laboratory settings, and their practical outdoor performance still needs validation. Furthermore, the development of suitable water collection containers for complementary use is necessary.

(4) Currently, there are various standards and definitions for AWH materials research, so it is essential to establish a widely accepted set of standards to evaluate the performance of AWH materials using standardized experimental equipment and control methods.

Alleviating the worldwide water crisis demands continued research and exploration in the advancement of water harvesting materials. The path ahead is challenging, yet we find both enjoyment and purpose in this endeavor.

Published papers

The dissertation based on the following papers:

- [1] **Yi Zhang**, Chunhong Zhu, Jian Shi, Shigeru Yamanaka, Hideaki Morikawa, Bioinspired Composite Materials used for Efficient Fog Harvesting with Structures that Consist of Fungi-Mycelia Networks, *ACS Sustainable Chemistry & Engineering*, 10, 38, 12529–12539, 2022, <https://doi.org/10.1021/acssuschemeng.2c01816>
- [2] **Yi Zhang**, Yingying Cai, Jian Shi, Hideaki Morikawa, Chunhong Zhu, Multi-bioinspired hierarchical Janus membrane for fog harvesting and solar-driven seawater desalination, *Desalination*, 540, 115975, 2022, <https://doi.org/10.1016/j.desal.2022.115975>
- [3] **Yi Zhang**, Feifei Wang, Yongtao Yu, Jiajia Wu, Yingying Cai, Jian Shi, Hideaki Morikawa, Chunhong Zhu, Multi-bioinspired hierarchical integrated hydrogel for passive fog harvesting and solar-driven seawater desalination, *Chemical Engineering Journal*, 466, 143330, 2023, <https://doi.org/10.1016/j.cej.2023.143330>

Conference:

- (1) **張芸**, 山中 茂, 朱 春紅, 森川 英明, バイオインスパイアード水捕集ナノ繊維材料の開発, 日本繊維機械学会第 75 回年次大会 (2022 年 6 月, 口頭発表.)
- (2) **Yi Zhang**, Jian Shi, Hideaki Morikawa, Chunhong Zhu, Bioinspired nanofiber membrane for fog harvesting and solar-driven seawater desalination, The 49th Textile Research Symposium (2022), Kyoto Institute of Technology, Japan. (October 2022, Oral presentation)
- (3) **Yi Zhang**, Hideaki Morikawa, Chunhong Zhu, Multi-bioinspired hierarchical integrated hydrogel for passive fog harvesting and solar-driven seawater desalination,

The 14th Japan-China-Korea International Symposium on High-Tech Fiber Engineering for Young Researcher, Soochow, China. (August 2023, Oral presentation)

- (4) **Yi Zhang**, Hideaki Morikawa, Chunhong Zhu, Multi-bioinspired hierarchical integrated hydrogel for fog harvesting and seawater desalination, The 5th Japan-China Textile & Composite Symposium, Nantong, China. (September 2023, Oral presentation)

Other papers published by author:

- (1) Feifei Wang, **Yi Zhang**, Jian Shi, Lei Sun, Azeem Ullah, Chunhong Zhu, Ick Soo Kim, Bioinspired and Biodegradable Functionalized Graphene Oxide/Deacetylated Cellulose Acetate Composite Janus Membranes for Water Evaporation-Induced Electricity Generation, *ACS Sustainable Chemistry & Engineering*, 11, 26, 9792–9803, 2023, <https://doi.org/10.1021/acssuschemeng.3c01952>
- (2) Jiajia Wu, Mingxu Wang, Li Dong, **Yi Zhang**, Jian Shi, Masatoshi Ohyama, Yasuhiro Kohsaka, Chunhong Zhu, Hideaki Morikawa, Highly integrated, breathable, metalized phase change fibrous membranes based on hierarchical coaxial fiber structure for multimodal personal thermal management, *Chemical Engineering Journal*, 465, 142835, 2023, <https://doi.org/10.1016/j.cej.2023.142835>
- (3) Tingting Wu, Zhaoxing Lin, **Yi Zhang**, Nobuhiro Kanazawa, Takao Komiyama, Chunhong Zhu, Eiji Kikuchi, Jian Shi, Ruilu Liang, Poly-N-phenylglycine@ multi-walled carbon nanotubes composite membrane for improvement of Au (III) adsorption, *Separation and Purification Technology*, 304, 122404, 2023, <https://doi.org/10.1016/j.seppur.2022.122404>

Acknowledgments

大学卒業後、私は信州大学に入学しました。2018年9月に信州大学に入学し、日本語の学習と初期研究を始め、2019年3月に修士課程の学生となりました。その後、新型コロナウイルスの封鎖期間を経験しましたが、2021年3月に博士課程の学生となりました。信州大学に在籍してから、すでに5年以上が経過し、この5年間で多くの成長を遂げました。また、感謝すべき人々がたくさんおり、生活と研究の両面で多大な支援を受けています。

最初に、森川教授には深く感謝の意を表します。彼は私の指導教員であり、学業、生活、そして価値観の教育において、私に非常に肯定的な影響を与えました。また、故山中教授にも大きな感謝の意を捧げます。山中先生は私の研究への理解を深め、私が何も知らなかった時期にも辛抱強く指導してくれました。朱准教授にも大変感謝しており、日常生活や論文の修正に対して多くの支援をしていただきました。また、施准教授にも研究と生活の両方で多くの指導をしていただいたことに感謝します。そして、金教授にも、日常の指導に感謝の意を表します。

頻繁にご指導いただく教員以外にも、繊維学部の技術スタッフに特に感謝しています。武田先生は私に不慣れな装置の使用方法を辛抱強く教えてくれ、私に信頼を寄せてくれたことに感謝しています。また、岡田先生、武藤先生、中村先生、篠塚先生、山辺先生、林先生などの技術スタッフも、テストの際に私に手を差し伸べてくれたことに非常に感謝しています。伊藤先生と、すでに退職された宇佐美さんにも、SVBLで多くの装置と器具を使用する機会を提供してくれたことに感謝します。

さらに、初期の実験で協力してくれた掛川さんに特に感謝します。掛川さんは今でも私を自身の娘のように大切に扱い、コミュニケーションを続けてくれました。生活の面では、学務の片山さんに多くの問題を解決していただき、他の学務担当者も非常に親切で熱心に接してくれたことに感謝しています。

生活面で特に、千曲会館事務所の石坂さん、宮坂さん、佐藤さんに感謝の意を表します。彼らは私の家族のように、素晴らしい居住環境とオフィス環境を提供してくれました。経済的な面では、ロータリー米山記念奨学金に特に感謝し、私が所属するクラブ、蓼科ロータリーRC のメンバー全員、特に私のカウンセラーである木村様に感謝します。木村様は私にやさしく接していただき、まるで父親のようでした。

上記の方達以外にも、研究室の学生たちに感謝したいと思います。Kailun Chen 先輩には初めてのお世話をしていただき、Hanjing Li 先輩には生活のサポートをしていただきました。信州大学を卒業してから 2 年以上経った友達である王倩雨、別新宇、そして東北大学で博士課程を続けている Yu Yaonan にも感謝しています。修士課程時代の素晴らしい思い出があります。中国にいる王さん、別さんそして Chenshujun Feng は私の特別な精神的な支えであり、森川研究室の Mingxu Wang、Jiajia Wu、Li Dong、Yingying Cai には研究へのインスピレーションをいただき、Wu さんと Cai さんは普段から優しく接してくれました。一緒に勉強した同期の巖さんにも五年間はお疲れ様です。また、森川・朱研究室の日本の友達たち、前田さん、大崎さん、鹿島君、木村君、前君、ともうすぐ卒業する海水淡水化実験を一緒に行った渡辺君にも、日常の励まし、手助け、優しさに感謝しています。他の研究室にも感謝したい人がいます。卒業した木下君、金研究室の Feifei Wang、Lei Sun、施研究室の Chunqing Niu、鮑研究室の Chao Luo、Xueqin Lu、Yujun Zhuang などです。

最後に、私の彼氏である Fengyu Li にも感謝します。そして、私の最も可愛らしく、素晴らしい両親、親戚、中国にいる友達にも感謝します。